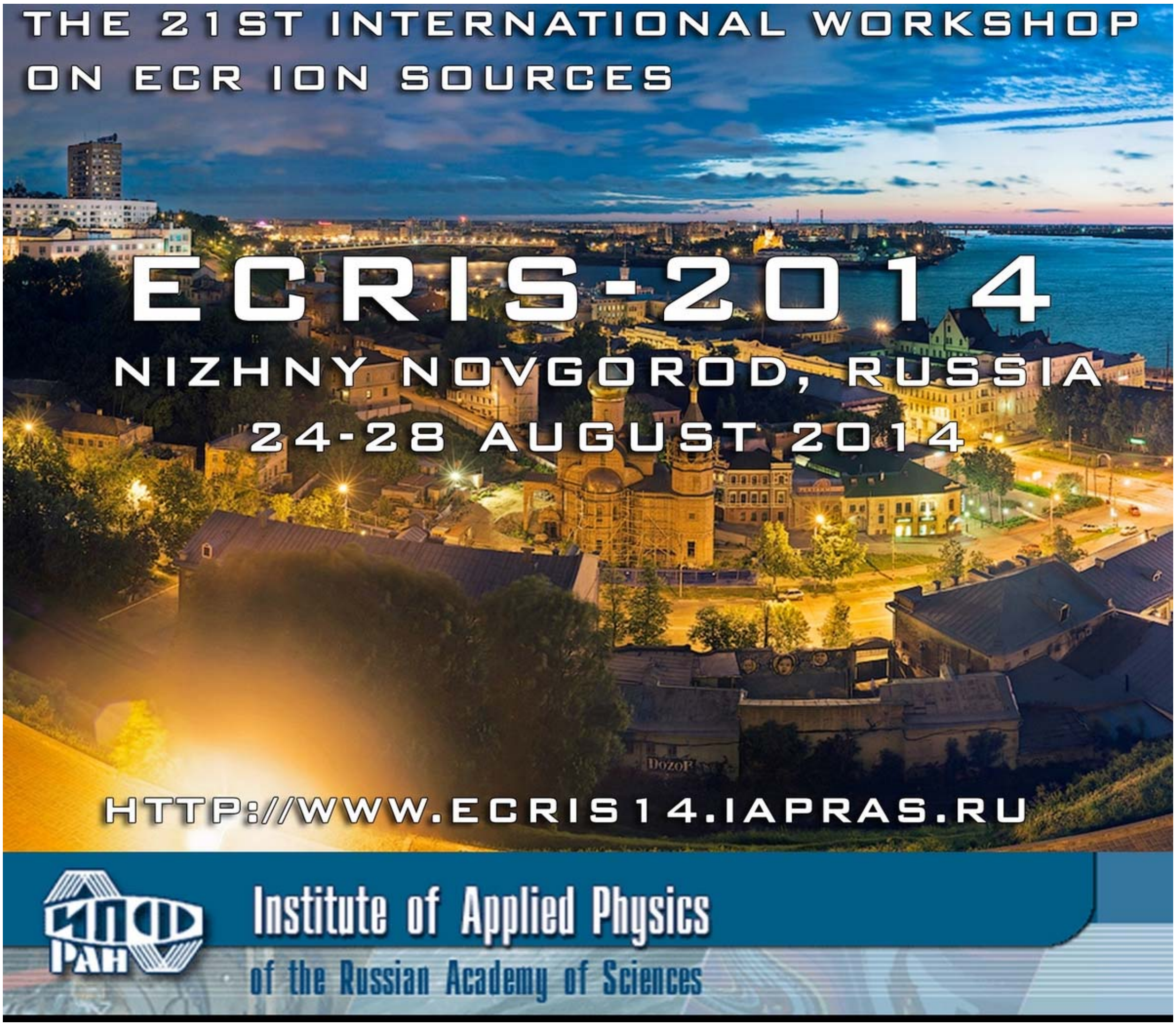
THE 21ST INTERNATIONAL WORKSHOP
ON ECR ION SOURCES
ECRIS-2014
NIZHNY NOVGOROD, RUSSIA
24-28 AUGUST 2014
HTTP://WWW.ECRIS14.IAPRAS.RU
Institute of Applied Physics
of the Russian Academy of Sciences

Preface

The 21st International Workshop on ECR Ion Sources was held by Institute of Applied Physics and Gycom Ltd., on 24 - 28 August 2014. The Workshop was held in Nizhny Novgorod (Russia) - one of the biggest cities situated in the central-European part of Russia at the confluence of two great rivers, the Volga and the Oka, founded in 1221.

ECRIS Workshop is a well-known event being excellent for new result presentation, fruitful discussions and warm communication. The workshop was focused on the latest advances and breakthroughs in ECR ion sources performance, its modeling and applications, as well as plasma physics and related technologies, presented in 31 oral and 19 poster presentations by 58 participants from all over the world.

In recognition of outstanding contributions to the development of ECR (Electron Cyclotron Resonance) ion sources and to encourage promising young scientists, PANTECHNIK – the world leader in commercial ECR ion sources – awarded the 4th "Richard Geller PRIZE" – a biennial award for promising young scientists in the field of ECR ion sources – on the occasion of ECRIS workshops.

Contents

Preface **i**

Foreword . . . iii
Contents . . . v
Committees . . . vii
Pictures . . . viii

Papers **1**

MOOMMH03 – First Results At 24 GHz With The Superconducting Source For Ions (SuSI) . . . 1
MOOBMH01 – Periodic Beam Burrent Oscillations Driven By Electron Cyclotron Instabilities In ECRIS Plasmas 5
MOOBMH02 – Emittance Measurements For RIKEN 28 GHz SC-ECRIS . . . 10
MOOBMH03 – Frequency Tuning Effect On The Bremsstrahlung Spectra, Beam Intensity And Shape In An ECR Ion Source . . . 15
MOOBMH04 – Emission Spectroscopy Diagnostic of Plasma Inside 2.45 GHz ECR Ion Source at PKU . . . 20
MOOAMH01 – Simulation Of The CERN GTS-LHC ECR Ion Source Extraction System With Lead And Argon Ion Beams . . . 23
MOOAMH02 – High Current Proton and Deuteron Beams for Accelerators and Neutron Generators . . . 30
MOOAMH03 – Optimization Of Low-Energy Beam Transport . . . 33
MOOAMH05 – Combination of Two ECRIS Calculations: Plasma Electrons and Extracted Ions . . . 38
MOPPH002 – Production Of Metallic Stable Ion Beams For GANIL And SPIRAL2 . . . 45
MOPPH004 – Status Report at the Heidelberg Ion-Beam Therapy (HIT) Ion Sources and the Testbench . . . 49
MOPPH006 – Direct Injection of Intense Heavy Ion Beams from a High Field ECR Ion Source into an RFQ . . 52
MOPPH007 – Current Developments for Increasing the Beam Intensities of the RIKEN 18-GHz Superconductiong ECR Ion Source . . . 57
MOPPH011 – Development of Interface and Diagnostic System for ECR ion source At KBSI . . . 61
MOPPH015 – Production and Acceleration of Titanium-50 Ion Beam at the U-400 Cyclotron . . . 64
MOPPH016 – Modernization of the mVINIS Ion Source . . . 68
MOPPH017 – LEGIS Facility for Study of Reactor Steels Radiation Resistance . . . 71
MOPPH018 – A Microwave Ion Source for Pulsed Proton Beam Production at ESS-Bilbao . . . 75
MOPPH019 – Metallic Beam Development with an ECR Ion Source at Michigan State University (MSU) . . . 79
TUOMMH01 – Improvement of Beam Intensities for ion beams with Charge-to-Mass Ratio of 1/3 with Two-Frequency Heating Technique . . . 83
TUOMMH02 – ECR Ion Source Developments at INFN-LNS . . . 87
TUOMMH03 – Status Report of SECRAL II Ion Source Development . . . 94
TUOMMH05 – HIISI, New 18 GHz ECRIS for the JYFL Accelerator Laboratory . . . 99
WEOMMH01 – The Installation of the 28GHz Superconducting ECR Ion Source At KBSI . . . 104
WEOMMH02 – First Commissioning Results of An Evaporative Cooling Magnet ECRIS-LECR4 . . . 107
WEOMMH03 – Development of the Magnetic System for New DECRIS-PM Ion Source. . . . 111
WEOMMH04 – Thermal Design of Refridgerated Hexapole 18 GHz ECRIS HIISI . . . 114
WEOBMH01 – Experimental Activities with the LPSC Charge Breeder in the European Context . . . 120
WEOBMH03 – Investigation on the Origin of High Energy X-Rays Observed in 3rd Generation ECRIS . . . 127
THOMMH01 – Boron Ion Beam Production with the Supernanogan ECR Ion Source for the CERN BIO-LEIR Facility 132
THOMMH02 – Application of an ECR Ion Source for Ionic Functionalization of Implant Materials on the Nanoscale 135
THOMMH03 – A Point-like Source of Extreme Ultraviolet Radiation Based on Non-equilibrium Discharge, Sustained by Powerful Radiation of Terahertz Gyrotron . . . 140
THOBMH01 – Closing Remarks for ECRIS'14 . . . 144

Appendices **147**

List of Authors . . . 147
Institutes List . . . 151
Participants List . . . 155

International Advisory Committee

A.Efremov, JINR, Russia

S.Gammino, LNS, Italy

H. Koivisto, JYFL, Finland

T. Lamy, LPSC, France

T.Thuillier, LPSC, France

P. Jardin , GANIL, France

D. Xie, LBNL, USA

T. Nakagawa, RiKEN, Japan

R. Vondrasek, ANL, USA

H. Zhao, IMP, China

M. Hotchkis, ANSTO, Australia

A. Kitagawa, NIRS, Chiba

LOC

Vadim Skalyga, Chair

Ivan Izotov

Sergey Golubev

Alexander Sidorov

Mikhail Viktorov

Dmitry Mansfeld

Sergey Razin

Maria Safronova

Igor Dubinov

FIRST RESULTS AT 24 GHZ WITH THE SUPERCONDUCTING SOURCE FOR IONS (SUSI)

Guillaume Machicoane, Dallas Cole, Kent Holland, Daniela Leitner, Dan Morris, Derek Neben and Larry Tobos, National Superconducting Cyclotron Laboratory, Michigan State University, East Lansing, MI, USA

Abstract

The first commissioning results at 24 GHz of the Superconducting Source for Ions (SuSI) from Michigan State University (MSU) are reported. Although SuSI has been designed to operate primarily at 18 GHz, the superconducting magnet has been able to reach a field sufficient for operation at 24 GHz. Very exciting new results have been obtained during the commissioning of SuSI at 24 GHz for oxygen and argon. For oxygen 1.4emA of O^{7+} was measured when injecting 5.2 kW of microwave power. For argon, 220euA of Ar^{16+} was measured with 6kW injected. In most cases, the performances don't seem to saturate yet with the injected power. Some surprising observations were also made regarding the coupling of 18 GHz in parallel with the operation of the ion source at 24 GHz as well as the impact of the frequency on performances.

INTRODUCTION

The Electron Cyclotron Resonance (ECR) ion source SuSI is a fully superconducting ion source that has been operated at 18GHz for the last five years for injection into the Coupled Cyclotron Facility (CCF). Excellent performance have been reported with SuSI at this frequency for medium charge state ions of light to heavy ion beams [1] In particular after coupling as much as 3.4 kW using two klystrons, performances were found to be still limited only by the amount of microwave power available. Trying to push further the performances of SUSI a 24GHz gyrotron was installed and tested with the ion source. The choice of 24GHz was solely based on the maximum magnetic field that can be achieved with SuSI. Although, the superconducting magnet structure was initially designed to be compatible with operation up to 28 GHz, quenches of SuSI sextupole magnet have set a limit that in accordance with the field requirement in the high-B mode would correspond to a maximum frequency somewhat above 24 GHz [2]. Even so energizing the SuSI magnet requires a careful ramping of the current. First it is necessary to ramp both solenoids and sextupole coils together to avoid a quench. Second, it is also necessary to first ramp the current in the coils 10 to 15% higher than what is required for a given field configuration before ramping the current down to their nominal values. This procedure has been found to be very important to reach a stable operating point for extended period of time. Therefore to establish a stable field configuration for operation at 24 GHz does require to first push the current in the coils close to the known limits of the magnet. To be safe during the commissioning of the gyrotron, both axial and radial field were kept somewhat below the expected high-B mode values for 24 GHz operation. For instance the radial field did not exceed 1.5 tesla. Likewise, the injection field was kept around 3 tesla most of the time. As a result, no quench occured during the commissioning period. Some promising and exciting results at 24GHz have been obtained. After a technical description of the 24 GHz system, the ion source, experimental results will be presented and followed by a discussion.

24 GHZ SYSTEM

A 24 GHz gyrotron system was purchased from GYCOM, a Russia based vendor. Although rated for 10 kW, the maximum output power transmitted from the tube to a water-cooled load during the commissioning tests was 8.8kW which is more than sufficient for operation with the ion source. The high voltage power supply (HVPS) was directly purchased from a domestic supplier and a filter circuit added between the HVPS and the gyrotron. This filter includes a 50 nF capacitance that limits the ripple to less than 2% and a set of four 20 Ohm resistance used to limit the stored energy to a maximum of 5 Joules to protect the gyrotron tube. The 24GHz transmission line and RF coupling system to SuSI is similar to the one developed for the SECRAL source [3]. The 24 GHz microwave propagates in an over-moded circular waveguide. The initial TE02 mode produced by the gyrotron is converted to TE01 using a mode converter because of the low attenuation of this mode. Coupling with the ion source can cause unwanted modes to propagate back in direction of the gyrotron so that a mode filter is also included in the transmission line. Diagnostics at the exit of the gyrotron include an arc detector and a bi-directional coupler. Although the gyrotron tube and the ion source are under vacuum, the transmission line is simply left at atmospheric pressure filled with the air that was trapped during assembly of the waveguide A 10 kW rated, boron nitride window is used at each end to define the vacuum/air interface. Finally, a high voltage break rated for 50 kV was also provided by GYCOM. Because of space limitation, the gyrotron was installed in a room above the ion source and two 90-degree bend were added to the transmission line to connect the gyrotron to the ion source. Figure 1 shows a layout of the gyrotron and ion source together. All components of the transmission line are water cooled. The control system provided with the equipment include a PID loop to regulate the output power using the read-back signal from the bi-directional coupler. A few important features help protect the equipment. First, the circuit used with the arc detector can send a fast signal (<10us) to inhibit the HVPS. Second

ISBN 978-3-95450-158-8

should the signal read from the bi-directional fails, the gyrotron control program allows to set a maximum value for the HVPS output voltage which limits the output power available.

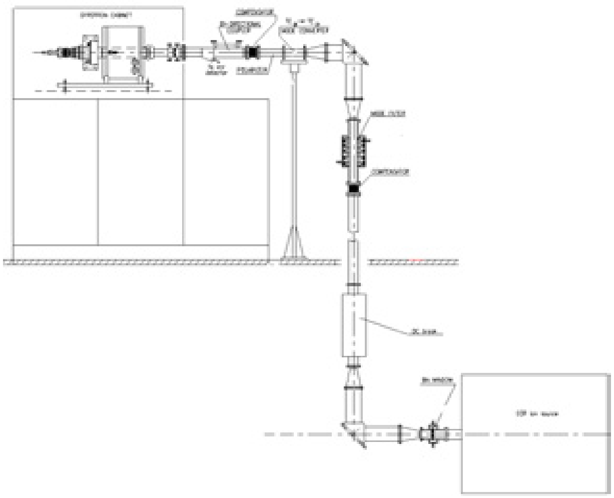

Figure 1: Layout of 24 GHz gyrotron and transmission line to SuSI ECR ion source.

The plasma chamber of SuSI is 101mm in diameter and is made of Aluminum. Because of the small diameter of the chamber, the over-moded waveguide take a significant portion of the injection flange. Figure 2 shows a layout of the baffle at the injection end. Space was made to include an oven, but it was necessary to tilt slightly the tube supporting it in order to maximize the oven diameter.

Figure 2: SuSI 24 GHz injection flange (baffle). It includes 1- gas tube; 2-WR62 Waveguide; 3- oven tube; 4-24 GHz circular waveguide.

The baffle also includes a tube for gas injection and a WR62 waveguide. The bias disk, the baffle itself and the WR62 waveguide are all independently cooled. A larger cooling line is used to cool both the 24 GHz waveguide and the oven tube.

SuSI has several interesting features [4]. First the axial magnetic profile is defined using 6 solenoids which provide some flexibility to adjust parameters such as field gradient at the resonance, B-minimum or plasma length. Second with a diameter of only 101mm, SuSI plasma chamber has a nominal volume of about 3.5 l which raise the possibility to reach power density between 1.5 to 2 kW/l with the gyrotron system. Another interesting feature of SuSI relates to the design of the superconducting magnet cold mass and cryostat. The magnet is directly connected to the laboratory cryoplant so that liquid helium is continuously injected in the cold mass. Recent boil-off measurements have shown that the static heat load at 4.2K is close to 30W. Therefore the ion source magnet is not sensitive to the dynamic heat load generated by the plasma which would only amount to a few watts.

SUSI COMMISSIONING TEST RESULTS AT 24GHZ/5.6KW

Acceptance tests of the 24 GHz system were completed successfully in February 2014 on a water-cooled calorimetric load. Tests included characterization of the tube operational parameters, long term stability at high power (5kW) as well as measurements of the ripple amplitude and frequency. Injection of microwave power started in April 2014 at relatively low power (<1 kW) and lead to a strong outgassing for several weeks. Following this initial conditioning period, commissioning continued using argon gas in May 2014. Finally additional work was done in July 2014 with oxygen and high charge state of argon as detailed below.

The initial work with argon gas started by optimizing SuSI for Ar^{11+} and Ar^{12+}. After two days spent optimizing the tuning parameters, such as magnetic field, gas, microwave power and biased disc an optimum of 905euA of Ar^{11+} and 860euA of Ar^{12+} were obtained with over 5kW of microwave power injected. Performances were not found to be saturating with the power as shown in figure 3 below.

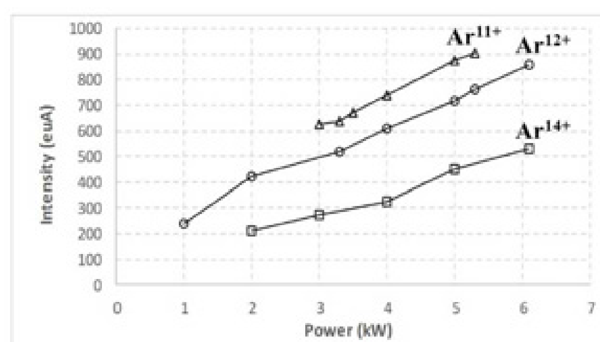

Figure 3: Electrical current of Ar^{11+}, Ar^{12+} and Ar^{14+} for various microwave power level of 24 GHz. None or little 18 GHz used.

It should be noted that the plot above was not obtained while keeping gas and magnetic field constant. Instead gas and field were adjusted for each power level. Power was not initially increased beyond 5.5kW as a safety precaution to protect the plasma chamber. The power density was then about 1.57 kW/l. The corresponding

ISBN 978-3-95450-158-8

axial magnetic field profile for Ar^{12+} was: B-injection= 3.1T and B-extraction =1.56T while B-minimum= 0.48T. The field at the plasma chamber wall was B-radial= 1.48T. The work continued with Ar^{14+} and in this case the microwave power was pushed up to 6.1 kW and 530euA of Ar^{14+} was measured. As observed with Ar^{11+} and Ar^{12+} and shown in figure 3, the current was not found to saturate even at this power level which corresponds to a power density 1.74 kW/l. The magnetic field was very similar to the one used with Ar^{12+}. Optimizing for very high charge states of Argon was however more difficult. Initial tuning on Ar^{16+} did not yield intensity exceeding 150euA and the intensity was clearly saturating with the microwave power injected beyond 4kW and is shown in figure 4. Also Ar^{16+} did require large amount of support gas (oxygen). After more conditioning was done for several weeks with the gyrotron system at a power between one and two kilowatt, a noticeable improvement in the current of Ar^{16+} was observed. Figure 4 shows the difference in the performance of Ar^{16+} function of the microwave power before and after conditioning the ion source. In both case the radial field was about 1.48T at the plasma chamber wall and the extraction field about 1.57T. The injection peak was higher in the first set of measurements with 3.2 T compare to 3.01 T in the second set. A significant difference also existed for the B-minimum which was at 0.63T initally and in principle more optimized for operation at 24 GHz. In the second set of measurement the B-minimum was adjusted to B=0.50T.

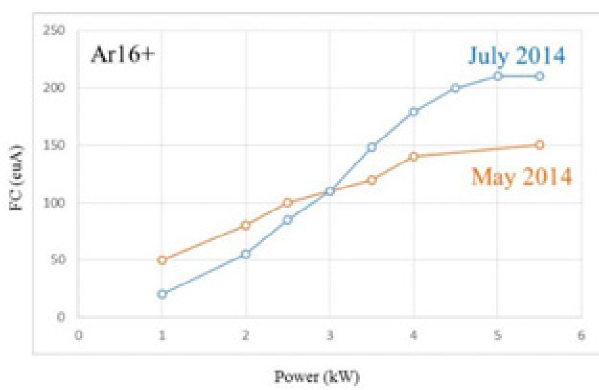

Figure 4: Comparison between two optimization of Ar^{16+} both done with power injected from 24 GHz gyrotron. The first run (Orange curve) was done in May 2014 and while the second run (Blue curve) was done in July 2014 after further conditioning of the source with the gyrotron.

The charge state distribution (CSD) of Ar^{16+} obtained after further conditioning of the ion source is shown in figure 5. The distribution is peaked on Ar^{14+} and large amount of oxygen were used to optimize the current. It is difficult to evaluate the amount of Ar^{17+} is present next to the peak of 0^{7+}.

After working with Argon, the ion source was then switched to oxygen and optimized for the production of 0^{6+} and 0^{7+}. As for Argon, the current did not saturate with the microwave power injected but it was difficult to optimize the current of 0^{6+} beyond 2.3 emA partly because SuSI beamline is not optimized for the transmission of high current but to inject low emittance beam into the coupled cyclotron. The optimized charge state distribution for 0^{6+} and 0^{7+} is shown in figure 6 below. The characteristic magnetic field is very similar between the two charge states and is detailed in figure 6. Mostly the optimization of the ion source on 0^{7+} was done by reducing the gas load.

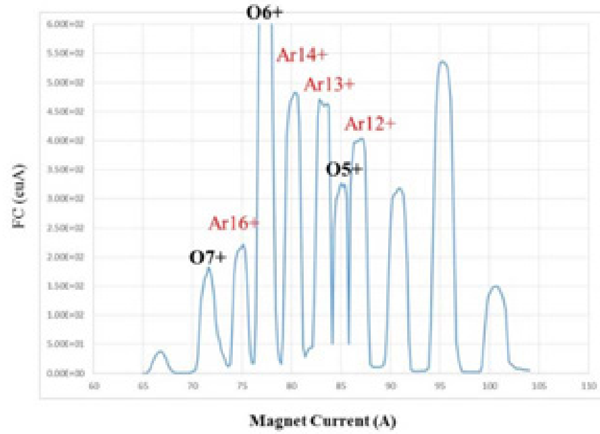

Figure 5: Argon distribution optimized for Ar^{16+}. Power 24GHz=5.7kW; Power 18GHz=500W; Drain current=4.5emA. Pressure extraction=2.5 E-8 Torr. B-radial=1.46T; B-injection=3.01T; B-minimum=0.49T; B-extraction=1.54T.

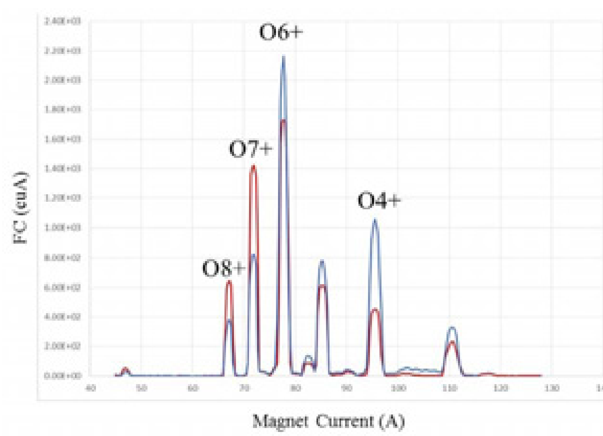

Figure 6: Oxygen distribution optimized for $0^{7+}/0^{6+}$. Power 24GHz=5.2/5.2kW; Power 18GHz=0/300W; Drain current=3.9/7.3emA. Pressure injection =7E-8/3E-7 Torr Pressure extraction=3.3E-8/3.7E-8 Torr. B-radial=1.46/1.49 T; B-injection=3.05/2.97T; B-minimum=0.52/0.46T; B-extraction=1.57/1.53.

DISCUSSION

First it is important to note that the commissioning results shown in the previous section have been obtained over a short period of time and that operation of SuSI at 24 GHz did require significant amount of conditioning as was also previously noted for SECRAL [3]. However a

ISBN 978-3-95450-158-8

few surprising observations were made during the measurements. First, although an 18 GHz/2kW klystron was also available during commissioning, it was observed that injecting even low level of power at 18 GHz did not help improve the ion source performance and mostly led to the current falling down by a few percent. The only noticeable exception was Ar^{16+} where 500 W of 18 GHz was used and helped improve the current by 10 to 15%. To dispel any doubts regarding the 18 GHz system, the ion source was then operated at a lower field and injected with microwave power from the klystron only. In this configuration, the performance of SuSI were similar to previous results. Factoring the transmission through the waveguide, the forward power at 18 GHz read at the bi-directional coupler at the injection of the ion source was in good agreement with the output power generated at the klystron while the reflected power stayed very low in all cases (< 10 Watt). Also it is unlikely that it is due to a critical density effect because the situation was the same for lower level of 24 GHz power injected. May be the fact that the radial and the peak values of the axial magnetic field were not optimized yet for operations at 24 GHz impacted the coupling of the 18 GHz. However, the minimum of the magnetic field was slightly below 0.5T in most cases, which is a value commonly used when injecting microwave power at 18 GHz. More work is needed to understand the conditions to optimize dual injection heating of 18 and 24 GHz. The second surprising observations was that the performances of the ion source at 18 GHz and 24 GHz appear equivalent for a similar level of microwave power injected into the ion source. A good example is shown for Ar^{14+} in figure 7. It is clear from the figure that for a range of microwave power extending from 2 to 3 kW the performance are very similar for both 18 GHz and 24 GHz. A clear advantage of the 24 GHz system is that it can provide much larger amount of microwave power to the ion source.

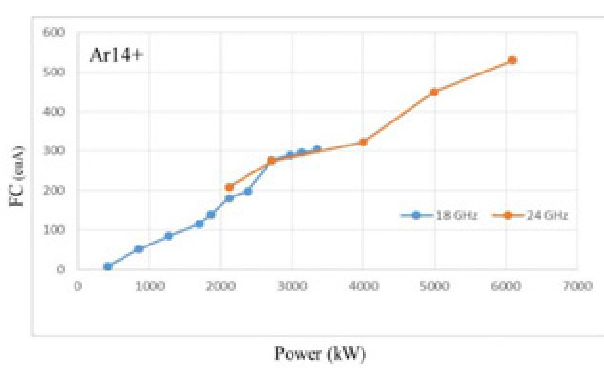

Figure 7: Comparison between 2010 run when only 18 GHz was used (Blue) and 2014 with only 24 GHz injected. Performances are very similar for equivalent amount of power injected in the source.

This observation was also true for Ar^{11+} and Ar^{12+}. However for Ar^{16+} the current obtained at 24 GHz was higher than the one at 18 GHz for similar power injected. Of course it could be that the source need more conditioning before the scaling of the performances with the frequency can be observed clearly. Finally, as it is difficult to know how much power is injected in the ion source with the gyrotron, we monitored the return temperature of the plasma chamber cooling water. Although it does not provide a precise calibration of the forward power, it was at least observed that the temperature of the water did increase for each increase of the ouptput power of the gyrotron demonstrating that more power get coupled into the ion source. Interestingly, we compared the return temperature of the plasma chamber cooling water for 1kW of 18 GHz as measured at the ion source bi-directional coupler with the return temperature for also 1kW of power injected from the 24 GHz gyrotron. Surprisingly, the increase in temperature was measured to be about 1 degree Fahrenheit with the 24 GHz system while it was only about 0.66 degree with the 18 GHz. Although this effect is not at present completely understood one possible explanation would be to consider that operation of an ECR ion source at higher frequency results in higher radial losses due to the more energetic electrons present in the plasma.

CONCLUSION

The first commissioning results at 24 GHz of SuSI were presented. Very good performances have been obtained for oxygen and argon and it was possible to couple very high level of microwave power to SuSI without problems. The magnet structure also was able to operate at a higher field without triggering any quenches. Work will continue in the future with SuSI to investigate the performances for heavier elements such as Xenon and Bismuth. Conditioning at 24 GHz takes time and better results are expected in the future. A Systematic study of the magnetic field need to be conducted to better understand the source behavior. Future work will also address measurements of the beam stability and emittance.

REFERENCES

[1] L.T. Sun et al., proceedings of the 19th international workshop on ECR ion source, Grenoble, France (2010).

[2] G.Machicoane, D.Cole, P.A.Zavodszky, proceedings of the 18th international workshop on ECR ion source, Chicago, USA (2008).

[3] H.W. Zhao et al. proceedings of the 19th international workshop on ECR ion source, Grenoble, France (2010).

[4] P.A. Závodszky et al., Rev. Sci. Instr.79 02A302 (2008).

ISBN 978-3-95450-158-8

PERIODIC BEAM CURRENT OSCILLATIONS DRIVEN BY ELECTRON CYCLOTRON INSTABILITIES IN ECRIS PLASMAS*

O. Tarvainen†, T. Kalvas, H. Koivisto, J. Komppula, R. Kronholm, J. Laulainen,
University of Jyväskylä, Department of Physics, 40500 Jyväskylä, Finland
I. Izotov, D. Mansfeld, V. Skalyga,
Institute of Applied Physics - Russian Academy of Sciences (IAP-RAS), Nizhny-Novgorod, Russia
V. Toivanen, CERN, Geneva, Switzerland

Abstract

Experimental observation of cyclotron instabilities in electron cyclotron resonance ion source plasma operated in cw-mode is reported. The instabilities are associated with strong microwave emission and a burst of energetic electrons escaping the plasma, and explain the periodic oscillations of the extracted beam currents. The instabilities are shown to restrict the parameter space available for the optimization of high charge state ion currents.

INTRODUCTION

Plasma instabilities can be categorized to magnetohydrodynamic (MHD) instabilities driven by the topology of the magnetic field (see e.g. Ref. [1]) and kinetic instabilities triggered by the anisotropy of the electron energy distribution function (EEDF) (see e.g. Ref. [2]). The magnetic field topology of a minimum-B ECRIS is effective in suppressing MHD instabilities [3]. Due to the resonant interaction between the incident microwave radiation the EEDF of an ECRIS plasma is strongly anisotropic and is considered to consist of several 'electron populations' - cold, warm and hot electrons with average energies of 10 - 100 eV, 1 - 10 keV and 10 - 100 keV, respectively [4, 5]. Such non-equilibrium plasmas are prone to kinetic instabilities driven by the hot electrons whose transverse velocities $\vec{v} \perp \vec{B}$ dominate over the longitudinal velocities $\vec{v} \parallel \vec{B}$.

We have recently reported [6] an experimental observation of electron cyclotron instabilities in a minimum-B ECRIS plasma sustained by 14 GHz microwave radiation in cw-mode. The instabilities lead to ms-scale oscillation of the extracted beam current reported earlier in Refs. [7] and [8]. In this paper we present a review of earlier work [6] and provide new data explaining the nature of the instabilities.

THEORETICAL BACKGROUND

Electron cyclotron instabilities are driven by hot electrons interacting resonantly with electromagnetic plasma waves. Whistlers or slow extraordinary (Z-mode) waves propagating to (quasi)parallel direction with respect to the external magnetic field, i.e. $\vec{k} \parallel \vec{B}$, can be excited inside the ECR-zone where the plasma oscillation frequency ω_{pe} can exceed the electron gyrofrequency ω_{ce} [9]. The (quasi)perpendicular extraordinary X- or Z-modes with $\vec{k} \perp \vec{B}$ can be excited when $\omega_{pe} < \omega_{ce}$ [10].

A characteristic feature of electron cyclotron plasma instabilities is the emission of microwaves. The energy of the microwave emission E_μ can be described by mode-dependent growth and damping rates γ and δ as

$$\frac{dE_\mu}{dt} \approx \langle \gamma - \delta \rangle E_\mu. \tag{1}$$

The solution of the differential equation shows that the intensity of the microwave emission is an exponential function of the difference of the growth and damping rates, which depend on the mode of the microwave emission. Since the instabilities are triggered by the anisotropy of the EEDF, their (volumetric) growth rate is proportional to the ratio of hot and cold electron densities. The damping rate is determined by volumetric absorption of the wave energy by the collisional background plasma and external (wall) losses.

The balance equation [11] for the hot electron (number) density $N_{e,hot}$ can be written as

$$\frac{dN_{e,hot}}{dt} \approx -\kappa N_{e,hot} E_\mu + S(t) - L(t), \tag{2}$$

where κ is a coefficient [12] describing the amplification of the electromagnetic wave and corresponding decrease in the hot electron component due to direct energy loss, $S(t)$ is the source term of hot electrons, i.e. stochastic heating, and $L(t)$ is their loss term due to collisional velocity space diffusion, inelastic collisions and rf-induced pitch angle scattering [13, 14]. In quiescent steady-state ECRIS plasma the damping rate exceeds the growth rate and the source and loss terms of hot electrons cancel out. In unstable operation conditions $S(t) > L(t)$, which causes the anisotropy of the EEDF to increase until the condition $\gamma > \delta$ is met. At this threshold the hot electrons interacting with the resulting plasma wave emit microwave radiation and are expelled into the loss cone directly as a result of the interaction with the amplified plasma wave or shortly after the perturbation via stochastic cooling and/or collisional scattering. The increased flux of electrons from the trap results in a burst of wall bremsstrahlung. The process stabilizes the plasma due to reduced density of hot electrons. However, the instability

* Work supported by by the EU 7th framework program 'Integrating Activities - Transnational Access', project number: 262010 (ENSAR), Magnus Ehrnrooth foundation, the Academy of Finland under the Finnish Centre of Excellence Program 2012–2017 (Nuclear and Accelerator Based Physics Research at JYFL) and researcher mobility grants 267174 and 267227, and the Russian Foundation for Basic Research grants 12-02-31206 and 13-02-00951.

† olli.tarvainen@jyu.fi

ISBN 978-3-95450-158-8

appears again at a periodic interval corresponding to the characteristic time required to create necessary anisotropy of the EEDF and leads to oscillations of the extracted ion currents.

EXPERIMENTAL SETUP

The experimental data discussed in this article were taken with the A-ECR type JYFL 14 GHz ECRIS [15] operated in continuous (CW) mode. The following is a list of diagnostics tools that have been used for characterizing the instabilities and their effect on the extracted beam currents. Detailed description of each diagnostics method can be found from the given reference.

- Microwave detector diode (0.01 - 50 GHz, 10 ns resolution) connected to a WR75 waveguide port [6].
- 25 GHz oscilloscope (Tektronix, MSO72504DX), connected to a WR75 waveguide port.
- Bismuth germanate (BGO) scintillator coupled with a Na-doped CsI (300 - 600 nm) current-mode photomultiplier tube (PMT) with < 4 μs temporal resolution [6].
- Off-axis visible light collector coupled with Na-doped CsI PMT (300 - 600 nm) [6].
- Sectored Faraday cup ~5 m downstream in the beam line (< 5 μs resolution) [6, 8, 16].

These complementary signals yield information on the hot electrons interacting with the plasma EM-wave, bremsstrahlung (power) flux induced by electrons escaping the confinement, plasma dynamics and extracted, m/q-analyzed, beam currents.

RESULTS AND DISCUSSION

Ion beams extracted from ECR ion sources often suffer from periodic ripple at ms-scale. Figure 1 shows a representative example of O^{6+} beam current signal recorded with the JYFL 14 GHz ECRIS together with the corresponding Fourier spectrum. The source was operated with pure oxygen and 650 W of power at 14 GHz resulting to average O^{6+} current of 175 μA with a fluctuation of +8.6 /-12.4 μA i.e. total of 12% at 860 Hz.

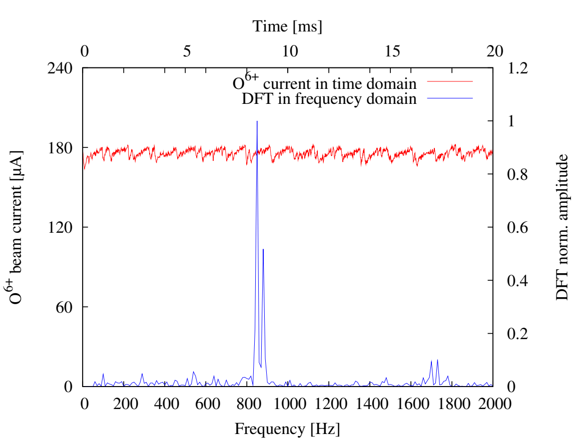

Figure 1: An example of O^{6+} beam current signal and corresponding Fourier transform (DFT) spectrum.

The ‘sawtooth’ behaviour shown in Fig. 1 consists of periodic drops followed by slower recovery phases of the beam current. An example of the diagnostics signals associated with the periodic plasma perturbations and drop of the beam current are presented in Fig. 2. The sequence of observable events is started at $t = 0$ by strong microwave emission from the plasma (a) lasting some hundreds of ns, coinciding with the leading edge of a bremsstrahlung burst (b) decaying in ~100 μs. The observed microwave signal associated with a burst of bremsstrahlung (electrons) is a signature of cyclotron instability, driven by hot electrons interacting resonantly with electromagnetic plasma waves, as described in the previous section.

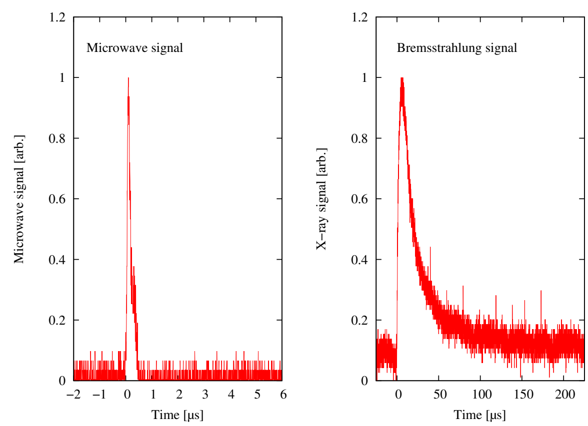

Figure 2: Microwave and X-ray (bremsstrahlung) signals associated with an onset of the periodic plasma instability.

The most critical tuning parameter affecting the occurrence of the cyclotron instabilities is the (solenoid) magnetic field strength. In the following we adopt the commonly used practice to quantify the strength of the ECRIS B-field by the ratio of the minimum field to the resonance field B_{min}/B_{ECR}. The effect of the magnetic field strength on the stability of the plasma is demonstrated in Fig. 3 showing the instability threshold value of B_{min}/B_{ECR} as a function of microwave power for different gaseous elements (He, Ar, Xe). The data for Fig. 3 were taken by adjusting the total extracted currents of different plasma species to be equal i.e. approximately 1.2 mA at 10 kV source potential suggesting that the plasma densities are approximately the same in each case. The error bars represent the step used for adjusting the magnetic field i.e. 5 A step in solenoid currents. The source potential (extraction high voltage) was not applied during the data taking. Increasing the magnetic field strength above the given threshold results in periodic onsets of the instabilities. This is most likely due to the fact that increasing the minimum-B lowers the gradient of the magnetic field at the resonance near the axis of the plasma chamber, which in turn results in increased energy gain in a single resonance crossing [17] and substantiates the anisotropy of the electron velocity distribution (EVD) triggering the instabilities. The shift of the instability threshold towards higher B_{min}/B_{ECR} (at given incident power level) with increasing mass number

ISBN 978-3-95450-158-8

could be due to increased electron energy loss in inelastic collisions.

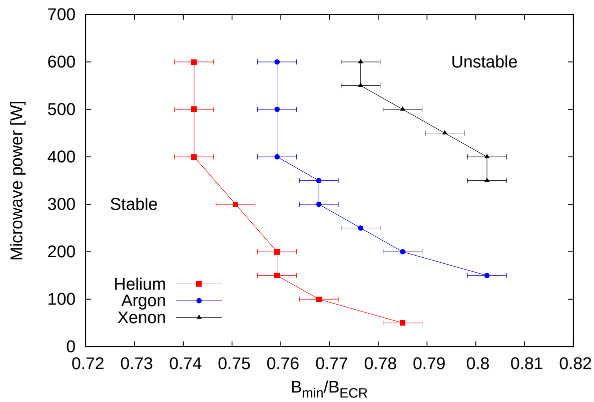

Figure 3: The instability threshold B_{min}/B_{ECR}-ratio of different plasmas as a function of incident microwave power.

The effect of neutral gas pressure on the threshold B_{min}/B_{ECR}-ratio, i.e. reduction of the instability threshold field with decreasing neutral gas pressure, is shown in Fig. 4. It was also observed that the high voltage applied for extracting the ions caused the threshold B-field to shift towards lower B_{min}/B_{ECR}-ratio. The effect of the high voltage is also demonstrated in Fig. 4 showing the threshold B_{min}/B_{ECR}-ratio for oxygen as a function of the applied source potential at three different neutral gas pressures and constant microwave power of 350 W. The error bars represent the step used for adjusting the magnetic field (5 A step). The given pressures are gas calibrated readings of an ionization gauge located outside the plasma chamber and connected to it through a radial diagnostics port.

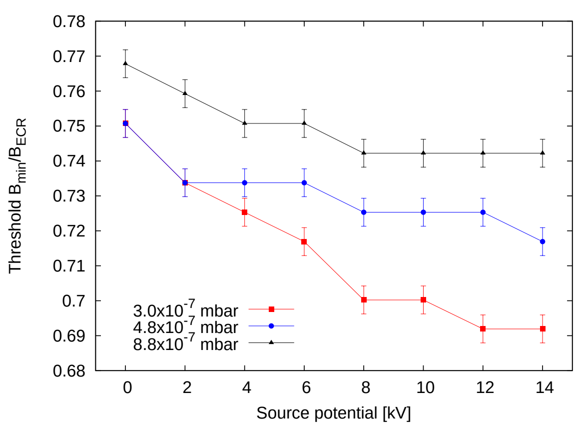

Figure 4: The instability threshold B_{min}/B_{ECR}-ratio of oxygen plasma as a function of the source potential.

The reduction of the threshold B_{min}/B_{ECR}-ratio with increasing source potential is believed to be due to the 'ion pumping effect', i.e. reduction of the neutral gas pressure and plasma density in the plasma chamber due to extracted ion beam, and subsequent decrease in the instability damping rate (reduced collision rate). This explanation is supported by the data in Fig. 5 showing the integrated visible light signal and total beam current extracted from the ion source as a function of applied high voltage. The recorded light emission of oxygen at 300 – 600 nm is dominated by emission lines of neutrals and ions up to the charge state O^{3+}. Thus, the visible light signal reflects the change in neutral gas balance (and density of low charge state ions). The presented example of the 'ion pumping' highlights the fact that the effect of source potential should always be taken into account in diagnostics of ECRIS plasmas.

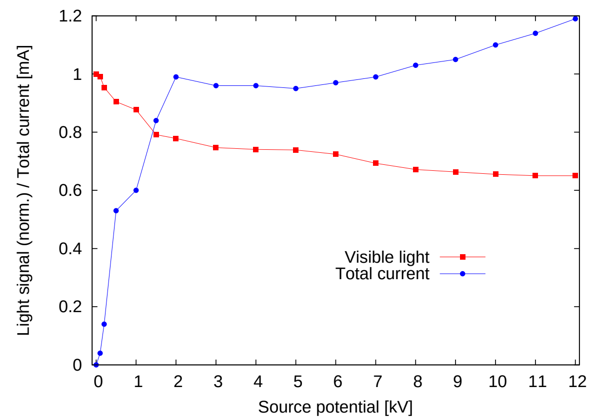

Figure 5: The visible light signal and total extracted current as a function of the source potential.

The repetition rate of the periodic instabilities at various B_{min}/B_{ECR}-ratios, incident microwave powers and neutral oxygen (O_2) pressures is presented in Fig. 6. The repetition rate increases substantially with increasing B_{min}/B_{ECR}-ratio and microwave power and decreases with increasing neutral gas pressure. The error bars represent the temporal fluctuation of the instability repetition rate at the given ion source setting. The tendencies shown in Fig. 6 can be explained qualitatively by interpreting the instability repetition rate as a measure of the stochastic electron heating rate as discussed in Ref. [6].

Finally, let us bring the discussion back to the beam current oscillations caused by the cyclotron instabilities. It is evident that the instability-induced burst of negative charge, expelled from the plasma, perturbs the density and charge state distribution of the extracted ion flux. The process differs fundamentally from the well-known afterglow burst of ECRIS plasmas [18] enhancing the high charge state ion flux to the extraction. The afterglow burst is caused by increased flux of cold electrons while the instabilities expel hot and warm electrons whose flux cannot be balanced only by a modest variation of the ambipolar potential. This claim is supported by the measurement [6] of the ion beam energy spread, $\Delta E/E$ of ~ 15% corresponding to a plasma potential V_p > 1 kV, during the instability-driven electron burst. The result was obtained by sweeping the m/q-analyzing magnet B-field and recording the corresponding current signals at μs-resolution with the Faraday cup. Thus, the observed drop of beam currents associated with the instabilities can

ISBN 978-3-95450-158-8

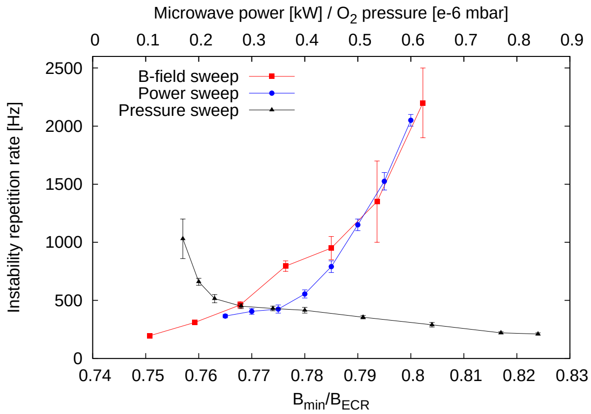

Figure 6: The repetition rate of the instabilities as a function of (i) B_{min}/B_{ECR}-ratio (350W, $3{\cdot}10^{-7}$ mbar), (ii) microwave power ($B_{min}/B_{ECR} = 0.77$, $3{\cdot}10^{-7}$ mbar) and (iii) oxygen pressure ($B_{min}/B_{ECR} = 0.77$, 350 W).

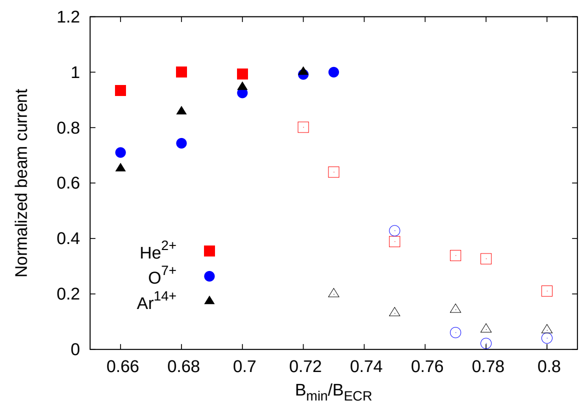

Figure 7: Normalized average beam currents of He^{2+}, O^{7+} and Ar^{14+} as a function of B_{min}/B_{ECR}-ratio. Solid symbols refer to stable operation and open symbols to existence of periodic cyclotron instabilities.

be explained at least partially by incorrect ion optics. A systematic quantification of the ion beam energy spread during the instability-driven electron burst at different ion source settings is one of the priorities of future experiments. This is due to the fact that such severe fluctuations of the plasma potential can cause degradation of the plasma chamber walls [19] by sputtering especially in afterglow operation mode in which instabilities are systematically observed [20] (independent of the source settings).

The cyclotron instabilities are detrimental to plasma confinement and extracted currents of highly charged ions as discussed in Ref. [6]. The ion source is typically tuned maximizing the temporally averaged beam current of a given charge state and, thus, the beam current oscillations at ~kHz frequencies are often obscured. For high charge state ion production improving the ion confinement time and enhancing the plasma density by increasing the magnetic field strength and/or microwave power are considered beneficial. However, such conditions make the plasma prone to instabilities that can limit the average extracted currents of highly charged ions and, hence, set restrictions for the parameter space available for their optimization. This is demonstrated in Fig. 7 showing an example of the normalized average currents of He^{2+}, O^{7+} and Ar^{14+} (high charge states) as a function of the B_{min}/B_{ECR}-ratio. The average beam current increases with the magnetic field strength until the instability threshold is reached and drops drastically as the magnetic field strength is increased further. Above this threshold the periodic disturbances of the plasma confinement occurring at temporal interval, which is shorter than the production time of the high charge state ions [21], limit the ion source performance. The presented example was obtained with 600 W microwave power and neutral gas pressures of $5.0{\cdot}10^{-7}$ mbar (He), $3.0{\cdot}10^{-7}$ mbar (O_2) and $3.4{\cdot}10^{-7}$ mbar (Ar).

Our future plans include a comprehensive study of the effects of cyclotron instabilities on the optimization of different charge states of various elements as well as analysis of the frequencies emitted during the plasma perturbations (data analysis in progress). Measurement of the instability frequency spectrum could help to identify the mode of the electromagnetic plasma waves.

REFERENCES

[1] J.B. Taylor, Phys. Fluids, 6, (1963), p. 1529.

[2] S.V. Golubev and A.G. Shalashov, Phys. Rev. Lett. 99, 205002, (2007).

[3] T. Antaya and S. Gammino, Rev. Sci. Instrum. 65, (1994), p. 1060.

[4] C. Barue, M. Lamoreux, P. Briand, A. Girard and G. Melin, J. Appl. Phys. 76, 5, (1994).

[5] G. Douysset, H. Khodja, A. Girard and J.P. Briand, Phys. Rev. E 61, 3, (2000).

[6] O. Tarvainen, I. Izotov, D. Mansfeld, V. Skalyga, S. Golubev, T. Kalvas, H. Koivisto, J. Komppula, R. Kronholm, J. Laulainen and V. Toivanen, Plasma Sources Sci. Technol. 23, 025020, (2014).

[7] O. Tarvainen, T. Kalvas, H. Koivisto, J. Komppula, V. Toivanen, C.M. Lyneis and M.M. Strohmeier, Proc. 20th Intl. Workshop on ECRIS (Sydney, Australia), TUXO02, `http://accelconf.web.cern.ch/AccelConf/ECRIS2012/papers/tuxo02.pdf`.

[8] V. Toivanen, O. Tarvainen, J. Komppula and H. Koivisto, J. Inst., JINST 8, T02005, (2013).

[9] A.G. Demekhov and V. Yu. Trakhtengerts, Radiophys. Quantum Electron. 29, (1986), p. 848.

[10] A. G. Demekhov, Radiophys. Quantum Electron. 30, (1987), p. 547.

[11] A.G. Shalashov, S.V. Golubev, E.D. Gospodchikov, D.A. Mansfeld and M.E. Viktorov, Plasma Phys. Control. Fusion 54, 085023, (2012).

[12] A.V. Vodopyanov, S.V. Golubev, A.G. Demekhov, V.G. Zorin, D.A. Mansfeld, S.V. Razin and A.G. Shalashov, J. Exp. Theor. Phys. 104, 2, (2007).

ISBN 978-3-95450-158-8

[13] C. Perret, A. Girard, H. Khodja and G. Melin, Phys. Plasmas 73, 3408, (1999).

[14] A. Girard, C. Pernot and G. Melin, Phys. Rev. E 62, 1, (2000).

[15] H. Koivisto, P. Heikkinen, V. Hänninen, A. Lassila, H. Leinonen, V. Nieminen, J. Pakarinen, K. Ranttila, J. Ärje and E. Liukkonen, Nucl. Instrum. Methods B 174, (2001), p. 379.

[16] O. Tarvainen, V. Toivanen, J. Komppula, T. Kalvas and H. Koivisto, Rev. Sci. Instrum. 85, 02A909, (2014).

[17] M.C. Williamson, A.J. Lichtenberg and M.A. Lieberman, J. Appl. Phys. 72, 1, (1992).

[18] F. Bourg, R. Geller and B. Jacquot, Nucl. Instrum. Methods A, 254, 13, (1987).

[19] D. Küchler, G. Bellodi, A. Lombardi, M. O'Neil, R. Scrivens, J. Stafford-Haworth and R. Thomae Proc. 20th Intl. Workshop on ECRIS (Sydney, Australia), TUPP10, `http://accelconf.web.cern.ch/AccelConf/ECRIS2012/papers/tupp10.pdf`

[20] I. Izotov, D. Mansfeld, V. Skalyga, V. Zorin, T. Grahn, T. Kalvas, H. Koivisto, J. Komppula, P. Peura, O. Tarvainen and V. Toivanen, Phys. Plasmas 19, 122501 (2012).

[21] R.C. Vondrasek, R.H. Scott, R.C. Pardo and D. Edgell, Rev.

ISBN 978-3-95450-158-8

EMITTANCE MEASUREMENTS FOR RIKEN 28 GHZ SC-ECRIS

Y. Higurashi, J. Ohnishi, K. Ozeki, and T. Nakagawa,
RIKEN Nishina Center for Accelerator Based Science, Wako, Japan

Abstract

In 2012, intense beams of highly charged uranium ions (180 eμA for U^{35+}, 230 eμA for U^{33+}) were extracted from RIKEN SC-ECRIS. Following this success, an intense beam of U^{35+} ions was used for the radioisotope beam factory (RIBF) experiment for a long period (about one month). It is obvious that production of high quality beams (characterized by smaller emittance and good stability etc) is also important for the RIKEN RIBF project. Therefore, in 2014, we systematically measured the emittance and beam intensity of highly charged uranium ions under varying conditions of magnetic field configuration, extracted beam intensity, beam stability etc. to obtain the optimal condition for the production of high-quality beams. In these experiments, we observed that the extent of emittance strongly depends on the magnetic field configuration, especially on B_{ext}.

.

INTRODUCTION

During the last several years, we have been working on increasing the intensity of highly charged uranium (U) ion beams and we have produced intense beams (~180 eμA for U^{35+} and ~230 eμA for U^{33+}) using the sputtering method [1]. In 2013, we produced ~90 eμA of U^{35+} for long-term usage in RIKEN radioisotope beam factory (RIBF) experiments. Consequently, in the course of the last several years, the intensity of U ion beams had dramatically increased. As an external ion sources for heavy ion accelerators, it is obvious that improving the quality of the beam characteristics, such as emittance and stability, is also important. Production of intense beams from the accelerator is key in producing intense RI beams, especially in the RIKEN RIBF project. For example, the overall design power of a U ion beam (beam intensity of 1 pμA) at the energy of 345 MeV/u is 82 kW. In this case, beam loss has to be minimized to avoid damaging the accelerator. It is obvious that the emittance of highly charged U ion beams should be sufficiently smaller than the acceptance of the accelerators of the RIKEN RIBF for safety acceleration. Therefore, to minimize the extent of emittance for intense beams of U ions, we intensively studied the effect of the ion source parameters on the emittance. As described in a previous paper [2], if the magnetic field distribution affects the ion dynamics and the trajectory of the extracted beams, it may also affect the emittance of highly charged heavy ions.

In this paper, we describe the experimental results regarding the effect of various ion source parameters (drain current, position of the beam extraction electrode, and magnetic field distribution) on the emittance of highly charged U ion beams.

EMITTANCE MEASUREMENT FOR U ION BEAMS

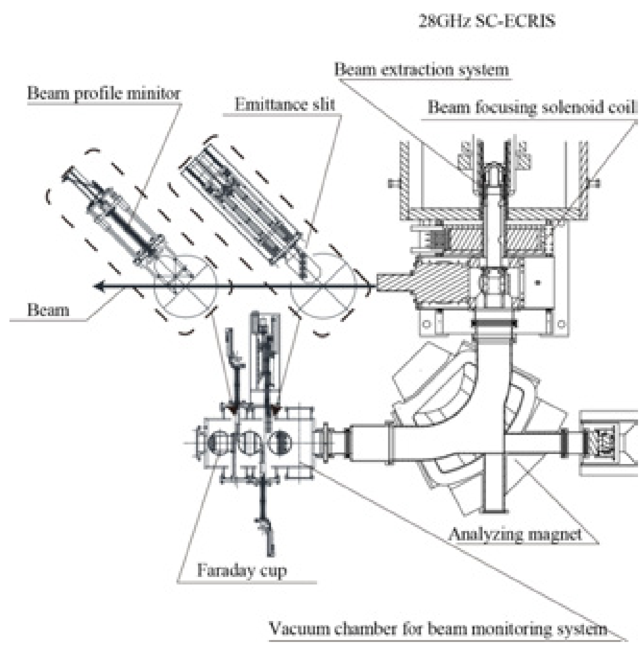

Figure 1: Schematic drawing of of the beam extraction system of the ion source and Low energy line with beam-monitoring system.

The sputtering method was used for production of highly charged U ion beams. The method is described in detail in ref. [3]. The main feature of the ion source is that it has six solenoid coils for producing the mirror magnetic field. Using this configuration, one can produce so-called "flat B_{min}" [4] and classical B_{min}. In this experiment, the extraction voltage was fixed at 22 kV.

Figure 1 shows the schematic drawing of the beam extraction system of the ion source and the low-energy beam line (analyzing magnet and beam monitoring system). Emittance was measured using the emittance monitor, which consists of a movable thin slit (emittance slit in Fig. 1) and wires (beam profile monitor in Fig. 1). We also installed the beam slit and Faraday cup in the vacuum chamber of the beam monitoring system.

The root mean square (rms) emittance is defined as

$$\begin{aligned} \varepsilon_{x-rms} &= \sqrt{\langle x^2\rangle\langle x'^2\rangle - \langle xx'\rangle^2} \\ \varepsilon_{y-rms} &= \sqrt{\langle y^2\rangle\langle y'^2\rangle - \langle yy'\rangle^2} \end{aligned} \quad (1)$$

ISBN 978-3-95450-158-8

In these equations, the averages of the phase-space coordinates of position (x, y) and divergence (x', y') are weighted by the beam intensity [5].

Effect of the Drain Current

In general, space charge strongly affects the beam trajectory and the extent of emittance. To study the effect, we measured the emittance of U^{35+} ions for various drain currents. Magnetic field distribution was the same as that in Fig. 1. Figure 2 shows the rms emittance as a function of the ion source drain current, which is proportional to the extraction current. The error bars (emittance spread) are the standard deviations. The emittance slightly increased from 0.07 to 0.08 π mm mrad as the drain current increased from ~2.5 mA to ~4.7 mA. We conclude that the space charge mostly compensates in this experiment. Furthermore, we observed the emittance spread for the same drain current as that shown in Fig. 2. This may be attributed to the plasma instabilities. Further investigation is needed to understand this phenomenon.

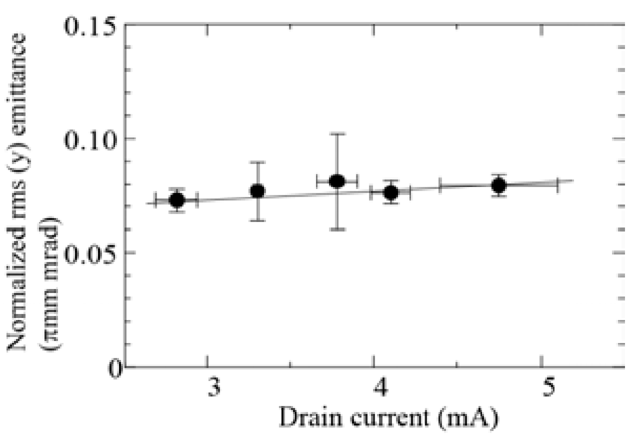

Figure 2: Normalized rms emittance as a function of drain current.

Effect of the Extraction Electrode Position

The position of the extraction electrode should affect the beam trajectory in the beam extraction region. Consequently, the emittance may depend on the electrode position. To study the effect of the electrode position on the emittance, we measured the emittance as a function of the extraction electrode position that ranged from ~25 mm to ~45 mm. Figure 3 shows the schematic of the beam extraction side. The position of the extraction electrode (L) is defined in Fig. 3. Magnetic field distribution was fixed at B_{inj}~3.1 T, B_{min}~0.65 T, B_{ext}~1.78 T and B_r~1.82 T. Figure 4 shows the normalized rms y-emittance of U^{35+} ions beam as a function of extraction electrode position (L). We observed that the effect of electrode position was very weak and the emittance slightly increased with decreasing L.

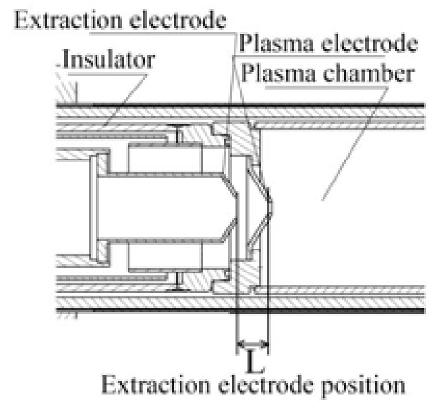

Figure 3: Schematic of the beam extraction side.

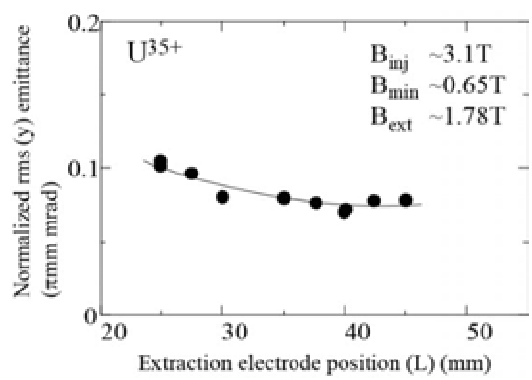

Figure 4: Rms emittance as a function of extraction electrode position (L).

Effect of the Magnetic Field Distribution

To investigate the magnetic field distribution effect, we measured the emittance for various magnetic field distributions with 18- and 28-GHz microwaves.

Figure 5 shows the magnetic field distribution for investigating the B_{ext} effect with 28GHz microwaves. The magnitude of B_{ext} was changed from ~1.8 T to ~1.4 T, while keeping the other magnetic fields strengths constant (B_{inj}~3.1 T, B_{min}~0.65 T and B_r~1.8 T). The RF power and the extraction voltage were ~1.5 kW and 22 kV, respectively. Figure 6 shows the normalized rms y-emittance as a function of B_{ext}. The emittance drastically changed from ~0.07 to ~0.17 π mm mrad as B_{ext} decreased from ~1.4 T to ~1.8 T. The beam intensity also depended on B_{ext}. It changed from ~60 eμA to 40 eμA as B_{ext} decreased from ~1.8 T to ~1.4 T.

In this figure, open circles denote the averaged emittance for various drain currents (2.5~4.5 mA), which is proportional to the extraction current. The error bars (emittance spread ~0.015 π mm mrad) are the standard deviations.

ISBN 978-3-95450-158-8

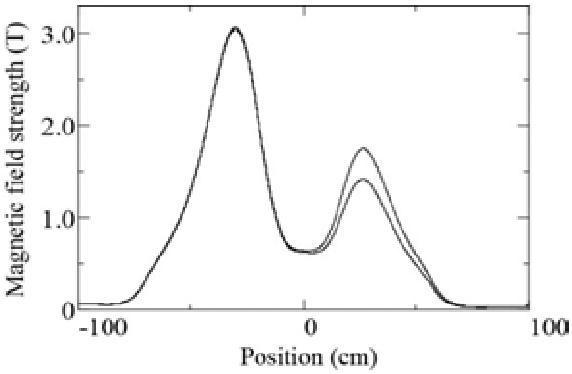

Figure 5: Magnetic field distribution for the B_{ext} effect with 28-GHz microwaves.

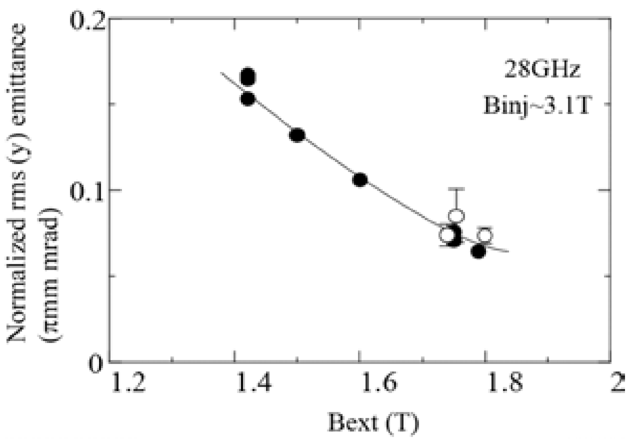

Figure 6: Normalized rms y-emittance as a function of B_{ext}.

Figure 7 shows the magnetic field distribution for investigating the B_{inj} effect. The magnitude of B_{inj} was changed from ~1.5 T to 3.1 T while keeping the other magnetic fields strengths constant (B_{ext} ~1.45 T, B_{min} ~0.65 T, B_r ~1.8 T). Figure 8 shows the results for rms y-emittance. Emittance increased from ~0.09 to ~0.17 π mm mrad as B_{inj} increased.

It should be noted that the B_{ext} in Fig. 7 was much lower than the typical magnetic field strength (so-called "high B mode operation" [6]) that is required to produce intense beams of highly charged heavy ions.

The "high B mode operation" takes B_{ext}~$2B_{ecr}$, which is higher than B_{ext}~1.45 T. In this condition, the emittance would be almost constant and independent of B_{inj}, as shown in Fig. 9. In Figure 9, the open circles are averaged emittance for B_{ext}~1.75 T. The error bars (emittance spread) are the standard deviations.

In the previous section, we presented the effect of the extraction electrode position on the emittance for the specific condition (B_{inj}~3.1 T, B_{min}~0.65 T, B_{ext}~1.78 T and B_r~1.82 T). To determine the extraction electrode position effect for additional magnetic field distributions, we measured the emittance as a function of electrode position for two conditions.

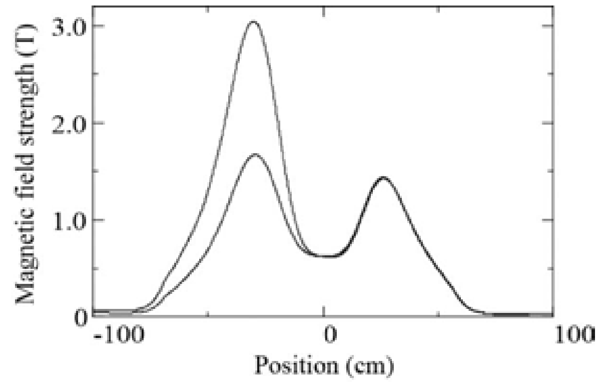

Figure 7: Magnetic field distribution for the B_{inj} effect with 28-GHz microwaves.

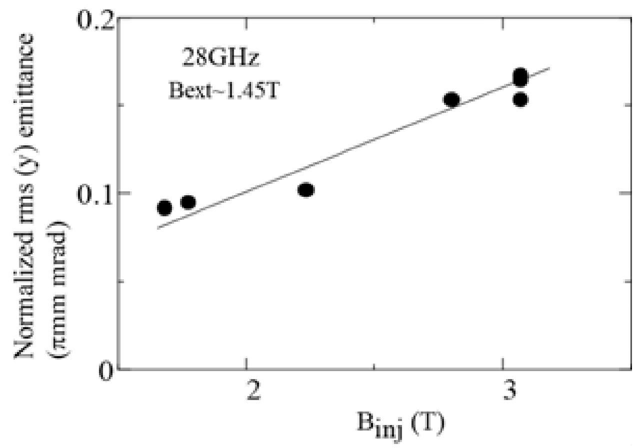

Figure 8: Magnetic field distribution for the B_{inj} effect with 28-GHz microwaves, for B_{ext} ~1.45 T.

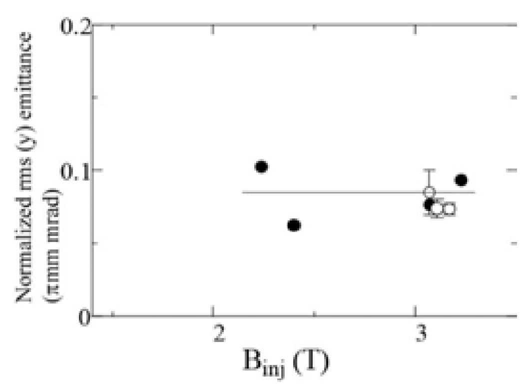

Figure 9: Magnetic field distribution for the B_{inj} effect with 28 GHz microwaves, for B_{ext}~1.75 T.

Figures 10 a) and b) show the effect of the extraction electrode position. Emittance was almost constant and ndependent of the position. Therefore, the emittance for U^{35+} ions beams might not be dependent on the extraction electrode position for the magnetic field distribution in

ISBN 978-3-95450-158-8

these test experiments. For these experimental results, we may conclude that ion dynamics in the plasma may be affected by B_{inj}; consequently, the emittance was changed by changing the B_{inj}.

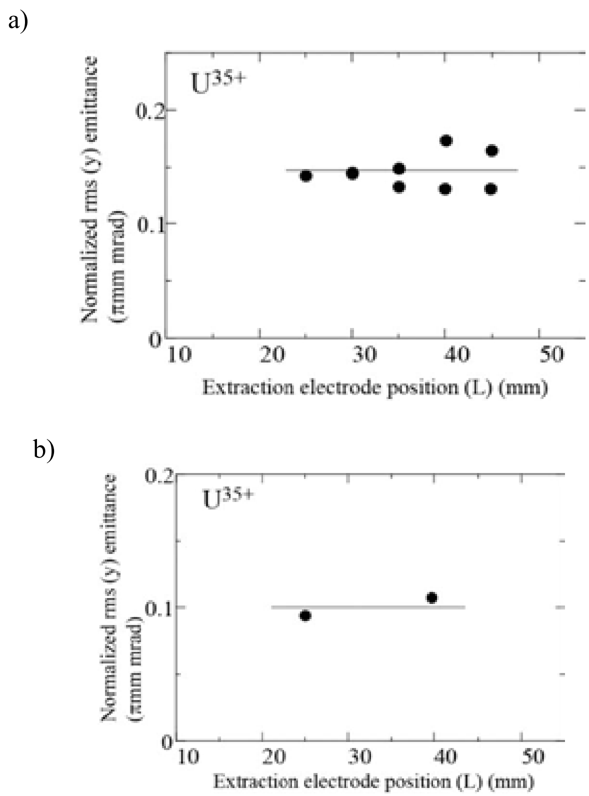

Figure 10: Normalized rms y-emittance as a function of extraction electrode position. a) B_{inj}~3.1 T, B_{min}~0.65 T, B_{ext} ~1.45 T, and B_r~ 1.8 T; b) B_{inj}~ 1.6 T, B_{min}~0.65 T, B_{ext}~1.45 T, and B_r~1.8 T.

We also observed the same phenomena for magnetic field distribution with 18-GHz microwaves. To study the B_{ext} effect, the magnitude of B_{ext} was changed from 0.9 T to 1.6 T. The RF power and extraction voltage were 500 W and 22 kV, respectively.

Figures 11 a) and b) show the magnetic field distribution for studying the effect of B_{ext} with 18-GHz microwaves and the normalized rms y-emittance as a function of B_{ext}, respectively. The emittance decreased as B_{ext} increased up to ~1.4 T and then saturated for B_{ext} above ~1.4 T. In this experiment, the minimal emittance of ~0.06 π mm mrad was obtained.

Figures 12 a) and b) show the magnetic field distribution for studying the effect of B_{inj} with 18-GHz microwaves and the normalized rms y-emittance as a function of B_{inj}, respectively. B_{ext} was fixed at 0.9 T. B_{min} values of 0.4 T and 0.5 T were chosen for this experiment. The emittance was changed from ~ 0.1 to ~0.2 π mm mrad up to 2 T, and then saturated. The maximal emittance was ~0.2 π mm mrad.

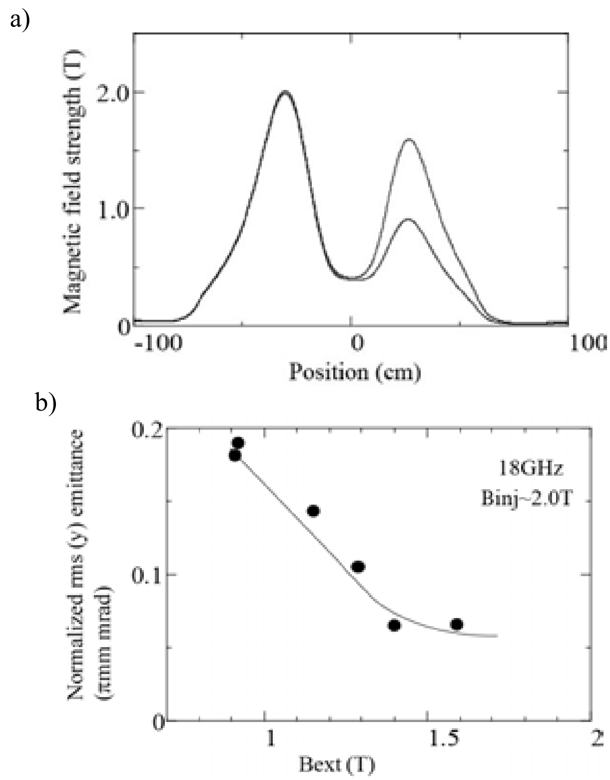

Figure 11: a) Magnetic field distribution for studying the effect of B_{ext}, b) Rms emittance as a function of extraction electrode position.

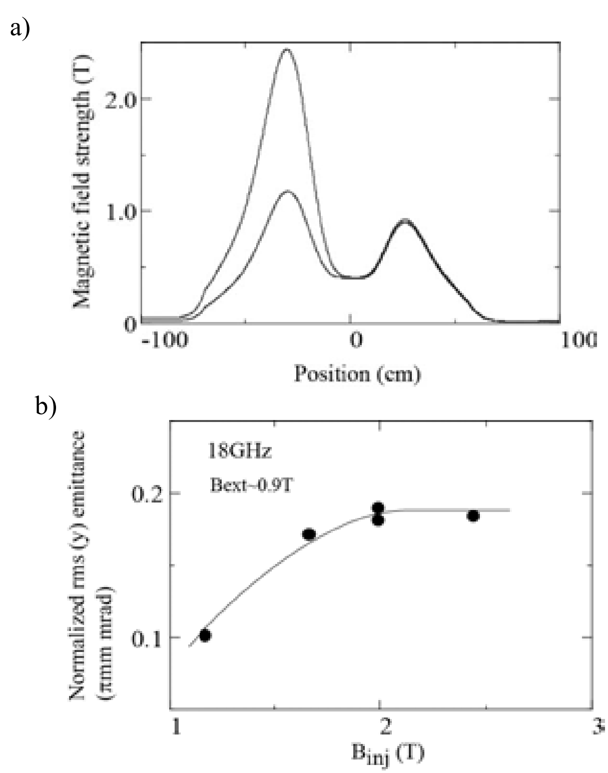

Figure 12: a) Magnetic field distribution for studying the effect of B_{inj}, b) Normalized rms emittance as a function of B_{ext}.

ISBN 978-3-95450-158-8

For the B_{inj} effect, we observed that the emittance increased as B_{inj} increased up to 2 T, and then saturated at ~0.2 π mm mrad. This is an interesting result because the magnetic field strength at the extraction was identical for different values of B_{inj}. In addition, the emittance was not strongly affected by the extraction current. Therefore, the extraction condition should not affect the emittance. This implies that the emittance of U^{35+} ions beam was influenced by the ion dynamics in the plasma modified by the B_{inj}. Further investigation is required to understand this phenomenon.

OTHER ION SPECIES

To study the effect of magnetic field distribution on the emittance for other ion species, we measured the emittance for O, Kr, and Xe ions beams. Figure 13 shows preliminary results of the normalized rms y-emittance for Kr ions as a function of B_{ext}. The B_{inj} and B_{min} were kept at ~3.1 T and ~0.65 T, respectively. The RF power and the extraction voltage were ~1.5 KW (28 GHz) and 22 kV, respectively. It seems that the emittance slightly depended on B_{ext} for higher charge state Kr ions. Figure 14 shows the results for Xe ions. The emittance dependency was nearly the same as that for Kr ions beams. We also measured the emittance for oxygen ions. The emittance of multi-charged oxygen ions did not depend on the magnetic field distributions.

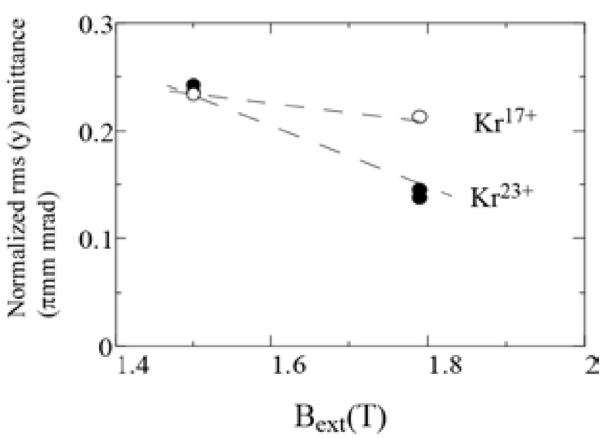

Figure 13: Normalized rms y-emittance for highly charged Kr ions as a function of B_{ext}.

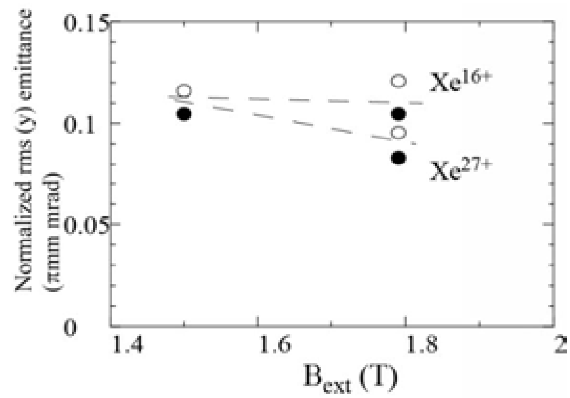

Figure 14: Normalized rms y-emittance for highly charged Xe ions as a function of B_{ext}.

CONCLUSION

We measured the emittance of U^{35+} ions for various ion source conditions. The extent of emittance was independent of the drain current and extraction electrode position. On the other hand, it strongly depended on the magnetic field distributions. The B_{inj} effect may yield some novel information, implying that the emittance of U^{35+} ions is not influenced by the extraction conditions, but rather by the ion dynamics in the plasma modified by B_{inj}. On the other hand, for less heavy ions such as Xe, Kr, and O ions, preliminary experimental results did not show any strong effects of the magnetic field distributions as in U^{35+} ion beams. The magnetic field distribution may affect only highly charged very heavy ions. Additional research is required to understand these phenomena.

REFERENCES

[1] Y. Higurashi et al., Rev. Sci. Instrum. 85 02A953 (2014).

[2] P. Spaedtke et al., *Proc of 18th Int. Workshop on ECR ion sources,* Chicago, USA, 2008, http://www.jacow.org, p 213.

[3] Y. Higurashi et al, *Proc of 19th Int. Workshop on ECR ion sources,* Grenoble, France, 2010, http://www.jacow.org, p 84.

[4] G. Alton and D. Smithe, Rev. Sci. Instrum. 65, 775 (1994).

[5] I. G. Brown, The Physics and Technology of Ion Sources, Wiley, New York, 1989, p. 94.

[6] G. Ciavola and S. Gammino, Rev. Sci. Instrum. 63, 2881 (1992).

FREQUENCY TUNING EFFECT ON THE BREMSSTRAHLUNG SPECTRA, BEAM INTENSITY AND SHAPE IN AN ECR ION SOURCE

G. Rodrigues[#], Narender Kumar, Kedar Mal, Y. Mathur, P. S. Lakshmy, and D. Kanjilal,
Inter University Accelerator Centre, Aruna Asaf Ali Marg, New Delhi 110067, India
A.Roy, Variable Energy Cyclotron Centre, 1/AF Bidhan Nagar, Kolkata, India

Abstract

The effect of the frequency tuning on bremsstrahlung spectra, beam intensity and shape in the 10 GHz, Nanogan ECR ion source have been investigated. The main aim of this work was to study the effect on a lower frequency type of ECR source where the separation between various modes in the cavity is much larger. The warm and cold components of the electrons were observed to be directly correlated with the beam intensity enhancement in the case of Ar^{9+} but not so for O^{5+}. However, the warm electron component was much smaller than the cold component. The beam shapes of O^{5+} measured as a function of frequency showed a strong variation without hollow beam formation. Due to the use of an octupole magnetic structure in the Nanogan ECR source, the quadrupolar structure of the ECR surface is modified with the frequency tuning. In general, we have observed a strong absorption of microwave power at various frequencies whenever the reflection co-efficient showed a minimum value and the effect was seen stronger for the higher charge states. Details of the measurements carried out on the bremsstrahlung spectra, beam intensity and shape are presented together with the results of simulations.

INTRODUCTION

Experiments carried out using various ECR ion sources have shown that even a slight change in the frequency in the order of MHz strongly influences the beam intensities, shape, emittance, brightness and stability. The extracted currents are sensitive to small changes of less than 1 % in the rf frequency. This technique which has been called as the frequency tuning effect [1] was pioneered by the ECR group in Catania. Due to the remarkable change in the beam characteristics, the quality of the beam can be improved further. In the field of ECR ion source development, there is a constant endeavour to improve the beam quality and intensity. Earlier works using the frequency tuning effect have shown the influence on the beam characteristics [2-5] with a clear variation in the beam quality and intensity as a function of frequency. In a few of the experiments performed, the formation of hollow beam was observed just after source extraction before the solenoid focusing element [3]. Understanding of the bremsstrahlung spectrum of cold, warm, and hot electrons, and the electron distribution function are also necessary to study how characteristics of the beam are influenced by the frequency tuning. S. Gammino *et al.* [6] have shown that the number of energetic electrons which populates the spectrum tail slightly changes when passing from one frequency to the other mostly because of variation in the warm population density. The slope of the bremsstrahlung spectra was observed to remain unchanged. But the experimental results shown in Ref. 7 did not show the trend where-in a large number of x-rays seemed to correspond to higher <q> and more intense beam current. For further understanding the frequency tuning effect on the beam characteristics and on the plasma conditions inside the cavity, it was felt necessary to study this effect on a lower frequency type of ECR ion source where the separation between various modes in the cavity is much larger than that of a source operating at a higher frequency. In hybrid modes, due to the superposition of two or more modes, it becomes difficult to explain how the electromagnetic fields can influence the production of beam intensities of highly charged ions. In this case, the measurement of the bremsstrahlung spectrum may give further information on the distribution of cold and warm electrons which can explain the probable ionization processes responsible for producing higher intensities of highly charged ions. At the Inter University Accelerator Centre, a compact, permanent magnet, 10 GHz Nanogan ECR ion source was used [8] to study the frequency tuning effect on the beam intensity, shape, and bremsstrahlung spectrum [9]. In order to further understand the frequency tuning effect on the beam characteristics, 3D simulations of the complete magnetic structure and of the electromagnetic fields for various modes in vacuum of the ECR cavity using CST Microwave Studio have been carried out[10]. To determine the shape of the beam at various tuning frequencies, the CST particle tracking solver was used under the combined influence of the confining magnetic fields and the electromagnetic fields of the cavity for specific modes. These simulations are compared to the beam shapes observed experimentally at various tuning frequencies. Presently, the simulation of one of the dominant modes of the cavity is compared with the observed beam shape at the corresponding frequency.

EXPERIMENTAL SET-UP

A 10 GHz fully permanent magnet, Nanogan ECR ion source was powered by a wide-band (8–18 GHz) travelling wave tube (TWT) amplifier manufactured by Amplifier Research, U.S.A [11]. A Rhode and Schwarz signal generator was used to vary the frequency and in the case of our experimental study, the frequency was chosen

#gerosro@gmail.com

ISBN 978-3-95450-158-8

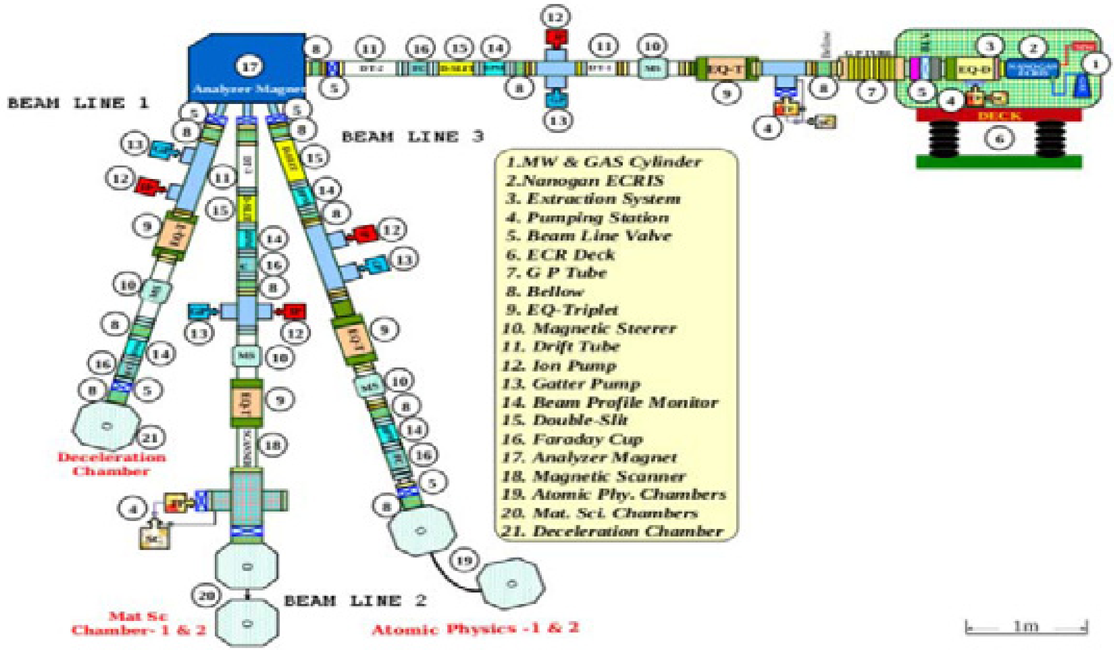

Figure 1: View of the ECR ion source and beam line 2 used for the frequency measurement.

to be varied from ~ 9.5 to 10.5 GHz with a stable mode operation of the plasma over the whole frequency range. A schematic of the ECR ion source and the experimental beam-lines is shown in fig. 1. The plasma chamber has an inner diameter of 26 mm and length 140 mm coupled to an RF cube and a bias tube is positioned inside the plasma chamber for supplying cold electrons to the plasma. The plasma chamber and the bias tube made of copper are air-cooled during normal source operations. The coupling of the electromagnetic waves to the ECR cavity is achieved by using a co-axial transmission line operating in the TEM mode [12] and traditionally used in all Caprice type of ECR ion sources.

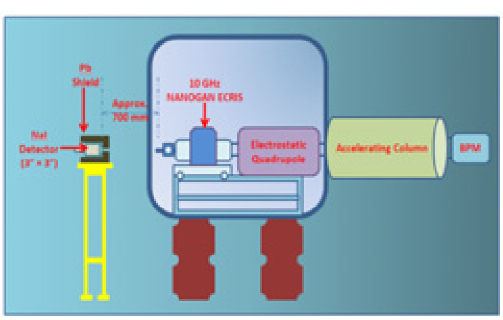

Figure 2: Schematic of the set-up to measure the x-rays from the 10 GHz Nanogan ECR ion source.

The 10 GHz Nanogan ECR ion source is a fully permanent magnet, therefore, the tuning parameters of the source are limited to controlling the gas flow rate and the RF power into the plasma chamber. In all the experiments reported below, the single-stub RF tuner position was fixed at an optimum position for minimizing the reflected power. The bremsstrahlung spectra were measured using a 3 in. × 3 in. NaI detector positioned at the injection side of the 10 GHz Nanogan ECR source placed at a distance of ~ 70 cm with proper collimation to measure only the bremsstrahlung coming from the ECR plasma (see fig. 2). It should be mentioned that the bias tube was used in this measurement to observe its effect on the frequency tuning. Due to the presence of a copper heat sink (for the bias tube) along the line of sight of the emitted bremsstrahlung, the observed count rates were attenuated. Each of the measured spectra at a particular frequency was counted for 3600 seconds. For calculations of the various modes of the ECR cavity and for tracking the electron motion, a model of the magnetic structure and the ECR cavity was built using CST microwave studio and is shown in fig. 3.

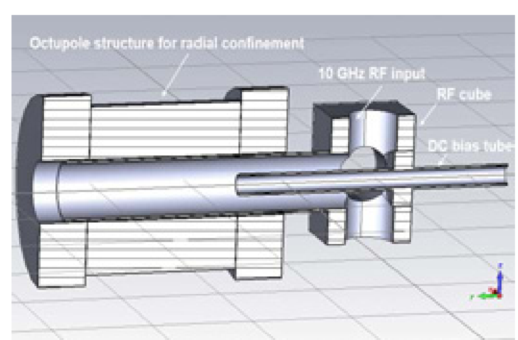

Figure 3: View of the model of the magnetic structure together with the ECR cavity built using CST microwave studio.

Considering the ECR cavity with a radius of 13 mm and length 140 mm, all possible modes in the frequency range of 9 to 11 GHz have been calculated using the standard formula for the TE and TM modes and are

ISBN 978-3-95450-158-8

shown in table 1. The closest mode to the main frequency of operation of the source is the TE_{117} mode with a frequency of 10.0914719844 GHz.

Table 1: Calculated frequencies for various modes for the ECR cavity in vacuum.

Mode type	Calculated frequency (GHz)
TM_{012}	9.0823955987
TE_{116}	9.3238928884
TM_{013}	9.3926442931
TM_{014}	9.8105232596
TE_{117}	10.0914719844
TM_{015}	10.3229699816
TE_{118}	10.9102418779
TM_{016}	10.9166750733

Details of the calculated ECR surface at 10 GHz is shown in fig. 4 and the actual cavity of the ECR ion source including the bias tube coupled to the RF cube is shown on the left side of fig. 5.

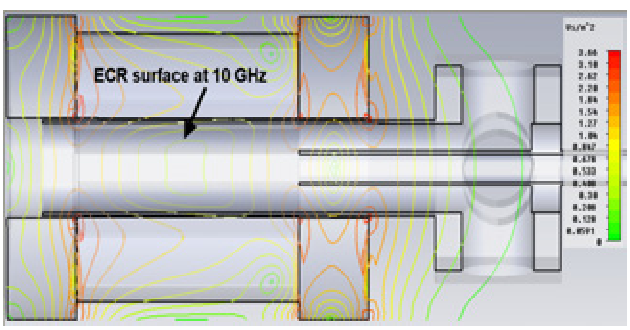

Figure 4: View of the cross section of the ECR surface at the mid-plane of the cavity

The corresponding TE_{117} mode with a calculated frequency of 10.1088 GHz which matches closely to the one calculated by the standard formula and is shown on the right side of fig. 5.

EXPERIMENTAL MEASUREMENTS

The experimental measurements using the frequency tuning effect were performed for two beams, viz., oxygen and argon. In the case of oxygen, the beam tuning was first optimized for O^{5+} (280 enA, RF forward power 27 W, reflected power 5 W, gas pressure 8.4 × 10^{-6} mbar, negative dc bias −88 V, 0.19 mA) at the operational frequency of 10.0 GHz. The frequency was then varied from ~ 9.5 to 10.5 GHz. In fig. 6, the beam currents of oxygen charge states and electron energy distributions were measured as a function of frequency including the reflected co-efficient. In the case of argon, the beam tuning was optimized (70 enA, RF forward power 53 W, reflected power 8 W, gas pressure 5.6 × 10^{-6} mbar, negative dc bias −118 V, 0.25 mA) on Ar^{9+} at the operational frequency of 10.0 GHz. In fig. 7, the beam currents of argon charge states and the electron energy distributions were measured as a function of frequency including the reflection co-efficient. The modes for some particular frequencies where the beam intensities are enhanced have been identified, whereas those frequencies whose modes could not be identified are probably hybrid modes which also contribute to the enhancement of the beam intensities. In the case of oxygen tuning (see fig. 6), the beam current of O^{5+} has been enhanced by a factor of 1.46 at a hybrid frequency of 10.14 GHz with respect to 10.0 GHz. Calculated modes at 10.3229699816 GHz (TM_{015}) and 9.8105232596 GHz (TM_{014}) also show enhancement of beam intensities.

With respect to the warm electron component, no correlation could be observed with the beam intensity enhancement. In fig. 7, the beam current of Ar^{9+} has been enhanced by a factor of 1.05 at a hybrid frequency of 10.26 GHz with respect to 10.0 GHz and a correlation between the warm electron component and the beam intensity enhancement is observed.

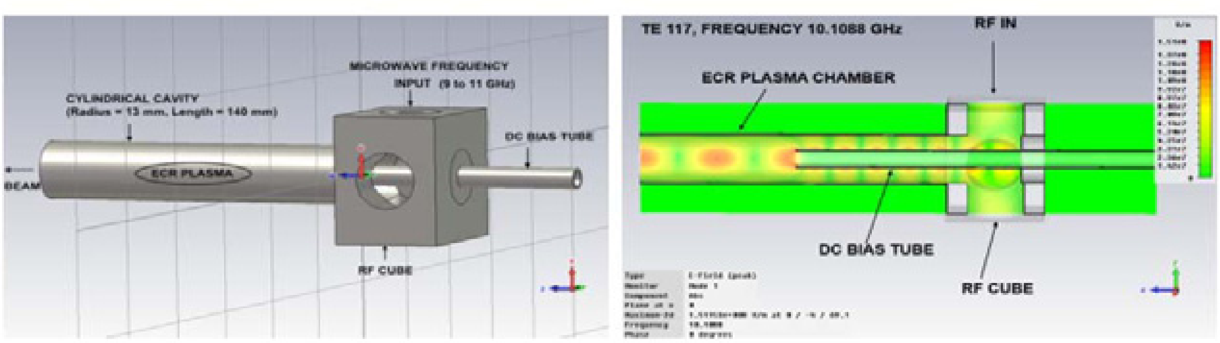

Figure 5: (left) CST model of the ECR cavity coupled to the RF cube (right) one of the simulated dominant modes in vacuum.

ISBN 978-3-95450-158-8

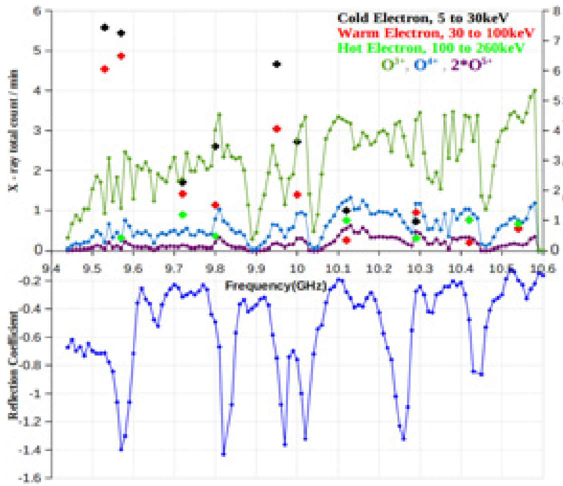

Figure 6: Effect of the various charge states of oxygen, electron energy distributions, and reflection co-efficient as a function of frequency.

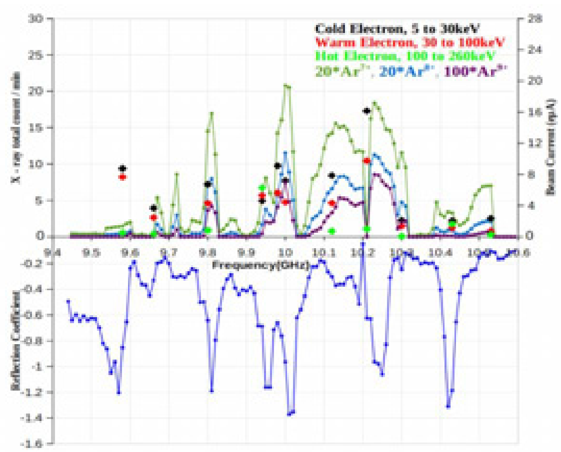

Figure 7: Effect of the various charge states of argon, electron energy distributions, and reflection co-efficient as a function of frequency.

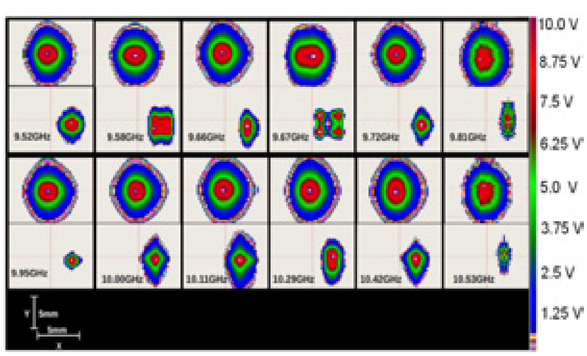

Figure 8: (Top) Measured shape of the beam for oxygen plasma for various frequencies and (bottom) after analysis for O^{5+} with their intensities.

The shapes of the beam as a function of frequency in the case of oxygen plasma were measured at the position of the first beam profile monitor, BPM 1 which had a sensitivity of 10^{-4} A/V, located after the 300 kV accelerating column and another beam profile monitor after A/q analysis (beam profile monitor, BPM 2 with sensitivity of 10^{-6} A/V positioned after the analyzing magnet) for the case of O^{5+}. A clear variation of the beam shape shown in fig. 8 was seen at both the locations of the beam profile monitors (BPM 1 and BPM 2) when the frequency is changed.

PARTICLE TRACKING

In order to further understand the evolution of the beam shapes as a function of frequency, particle tracking under the combined influence of the confining magnetic field and rf electric field was initiated. For this purpose, the CST particle studio program was used. It incorporates a powerful electromagnetic solver for calculating external fields, it has an efficient particle tracking algorithm and sophisticated emission models that can describe the extraction of particles from active surfaces.

The magnetic structure with cavity shown in fig. 3 was used for particle tracking inside the cavity without considering the effect of the plasma. The space charge limited emission model was used which also depends on the strength of the external field at the emitting surface. The particles are pushed through the computational domain by interpolating the field values to their location and calculating the electromagnetic forces. The dominant mode of the ECR cavity was chosen (shown on the right hand side of fig. 5) for tracking the motion of electrons and to further compare it with the measured distribution of the beam shape at that particular frequency (shown in figure 8, at 10.11 GHz). Fig. 9 shows the evolution of the electrons from the DC bias tube at a voltage of 100 V as viewed from the injection side and showing the quadrupole shape of the plasma. The electrons can quickly gain energy of ~ 600 keV in ~ 7.7 ns. In fig. 10, the shape of the plasma on the extraction side is shown. The simulated shape of the ECR plasma matches well with the measured shape of the beam for the dominant mode. Due to memory limitations on a Windows XP platform, the total number of particles was limited to ~ 30,000. Further developments are in progress.

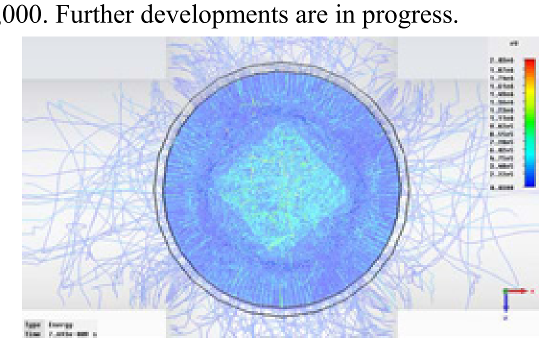

Figure 9: View of the computed electron trajectories at the injection side with initial energy of 100 eV for the dominant mode in vacuum.

ISBN 978-3-95450-158-8

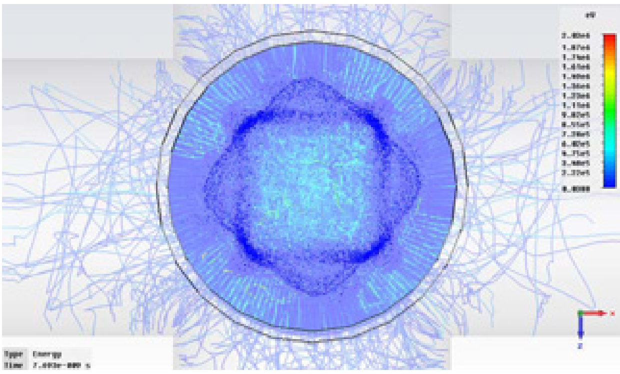

Figure 10: View of the quadrupolar structure of the ECR plasma at the extraction side, computed for the dominant mode in vacuum.

SUMMARY AND CONCLUSION

Considering the measurements for oxygen and argon beams in terms of the beam intensities and the beam shape measurements for oxygen plasma, it is observed that there is a strong absorption of microwave power at various frequencies whenever the reflection co-efficient showed a minimum value and the effect was seen stronger the higher charge states. The shape of the beam as a function of frequency clearly shows a strong variation at BPM 1. The warm and cold components of the electrons were found to be directly correlated with beam intensity enhancement in case of Ar^{9+} but not so for O^{5+}. The warm electron component was, however, much smaller compared to the cold component. The particle tracking in the vacuum mode cavity shows the evolution of the quadrupolar structure of the ECR plasma which is similar to the measurement of the beam shape at the dominant mode with no hollow beam formation. This shows that the electromagnetic field distribution affects the shape of the ECR plasma at a particular mode of operation.

ACKNOWLEDGEMENT

One of the authors (G.R) would like to thank the Department of Science and Technology (DST) for supporting partial financial assistance for travel purposes.

REFERENCES

[1] L. Celona et al., Rev. Sci. Instrum. 79 (2), 023305 (2008).
[2] L. Celona, G. Ciavola, F. Consoli, S. Gammino, F. Maimone, D. Mascali,P. Spadtke, K. Tinschert, R. Lang, J. Mader, J. Robbach, S. Barbarino, and R. S. Catalano, Rev. Sci. Instrum. 79, 023305 (2008).
[3] V. Toivanen, H. Koivisto, O. Steczkiewicz, L. Celona, O. Tarvainen, T.Ropponen, S. Gammino, D. Mascali, and G. Ciavola, Rev. Sci. Instrum.81, 02A319 (2010).
[4] F. Maimone, L. Celona, R. Lang, J. Mader, J. Robbach, P. Spadtke, and K. Tinschert, Rev. Sci. Instrum. 82, 123302 (2011).
[5] F. Maimone, K. Tinschert, L. Celona, R. Lang, J. Mader, J. Robbach and P. Spadtke, Rev. Sci. Instrum. 83, 02A304 (2012).
[6] S. Gammino, L. Celona, D. Mascali, and G. Ciavola, Proceedings of CYCLOTRONS, Lanzhou, China, 2010.
[7] S. Gammino, L. Celona, D. Mascali, R. Miracoli, and G.Ciavola, Proceedings of Linear Accelerator Conference, LINAC, Tsukuba, Japan, 2010.
[8] P. Sortais, M. Bisch, M. P. Bourgarel, P. Bricault, P. Leherissier, R. Leroy, J. Y. Pacquet, and J. P. Rataud, Proceedings of European Particle Accelerator Conference, EPAC (1992), p. 990.
[9] G. Rodrigues, Kedar Mal, Narender Kumar, R.Baskaran, P. S. Lakshmy, Y. Mathur, P. Kumar, D. Kanjilal and A. Roy, Rev. Sci. Instrum. 85, 02A944 (2014).
[10]http://www.cst.com/Content/Products/MWS/Overview.aspx
[11] http://www.arworld.us/index.htm
[12] B. Jacquot, F. Bourg, and R. Geller, Nucl. Instrum. Methods Phys. Res. A 254,13(1987).

ISBN 978-3-95450-158-8

EMISSION SPECTROSCOPY DIAGNOSTIC OF PLASMA INSIDE 2.45 GHZ ECR ION SOURCE AT PKU*

Yuan Xu, Shixiang Peng#, Haitao Ren, Jie Zhao, Jia Chen, Tao Zhang, Jingfeng Zhang, Zhiyu Guo and Jia'er Chen, SKLNPT & IHIP, School of Physics, Peking University, Beijing 100871, China
Ailin Zhang, School of Physics, UCAS, Beijing 100049, China

Abstract

The 2.45 GHz permanent magnet electron cyclotron resonance ion source (PMECR) at Peking University (PKU) can produce high current hydrogen molecular ions H_2^+ and H_3^+ under different conditions, but the physics processes and plasma characteristics within the discharge chamber are not very clear until now. Langmuir probe, laser detachment, absorption spectroscopy and optical emission spectroscopy are common approaches for diagnosing the plasma. Among those methods, optical emission spectroscopy is a simple *in situ* one without disturbing the plasma. To better understand the plasma producing processes, a new ion source with transparent quartz discharge chamber was designed at PKU so that plasma diagnostic can be performed through directly detecting the light generated within ECR zone by fibre optics. A collisional radiative (CR) model is used to calculate plasma parameters like electron density n_e and electron temperature T_e for non-equilibrium plasma in ECR ion source.

INTRODUCTION

High current hydrogen molecular ion source for the generation of both H_2^+ and H_3^+ ions is developing at PKU as they can be potentially applied in high current linac, cyclotron or medical synchrotron[1][2]. The 2.45 GHz ECR ion source at PKU, which can produce more than 100 mA proton, was chosen as the device for obtaining molecular ions. Studies on the inner dimension of source chamber, opreation pressure, microwave power and also pulsed duration indicated some promising results that pure 40 mA H_2^+ and 20 mA H_3^+ ions could be generated with both species fractions approximating 50% by only tuning the operation parameters[3][4]. Besides, a 2.45 GHz microwave driven negative ion source developed at PKU got some promising results that more than 15 mA H^- ions was extracted in pulsed mode recently[5]. These experimental results make us want to know more about the plasma behaviours which are very important in the generation and destruction of H_2^+, H_3^+ and H^- inside the source. Obviously, the pressure inside discharge chamber will influence electron temperature which determines the cross-sections of many interaction processes, and RF-power will also contribute a lot to electron density. It will be better to figure out the relation of these parameters with plasma characteristics, so diagnosis was introduced for getting more information about crucial plasma parameters in ECR ion source such as electron density, electron temperature etc.

*Work supported by NSFC NO. 11175009 and 91126004.
#sxpeng@pku.edu.cn

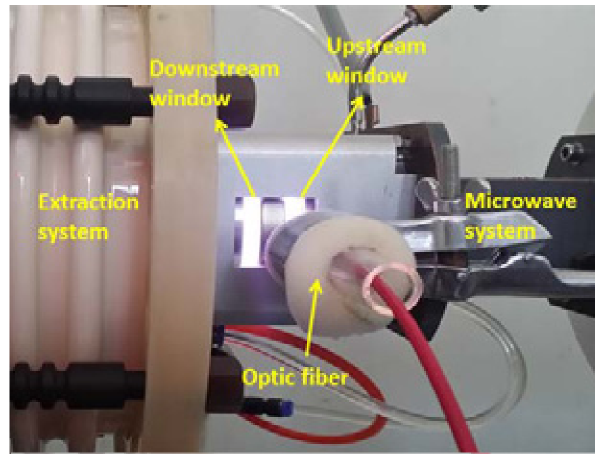

Figure 1: Photo of the ion source with transparent window.

Langmuir probe is a commonly used method to diagnose plasma inside ECR plasma. R. Gobin *et al.*, at CEA/Saclay utilized Langmuir probe to measure electron temperature for the development of H^- ion source, and the measured T_e was 6.7 eV before the microwave-break grid and 3.5~5.3 eV behind the grid[6]. But as they indicated, the Langmuir probe was sometimes hard to interpret under strong RF power and magnetic field environment, and it could only indicate some trends inside ECR plasma[7]. Recently, laser detachment method and absorption spectroscopy method have been developed, but the facilities are complicated and hard to realize with ECR ion source. By comparison, optical emission spectroscopy method is a simple and non-invasive approach to diagnose the plasma by analysing the light emitting from ECR cavity with optic fiber, high revolution spectrometer and auxiliary noble gas[8]. For this reason, a new ion source with transparent quartz chamber was designed and constructed so that the light from plasma could be seen from outside without disturbing the vacuum. The diagnostic method and preliminary results will be presented in this paper.

EXPERIMENTAL SETUP

The ion source is a permanent magnet ECR ion source named PMECR IV (Patent Number: ZL 201110026605.4). For diagnosing the plasma, the discharge chamber is made of quartz which has a high transmissivity for 400 ~800 nm light [9]. The magnetic field is provided by three NdFeB rings which are separated by non-magnetic metal gaskets. Based on above designs, the light from plasma can be detected through gaps between magnetic rings as shown in Fig.1. There are two positions where diagnosis can be carried out. One is located at ECR zone

ISBN 978-3-95450-158-8

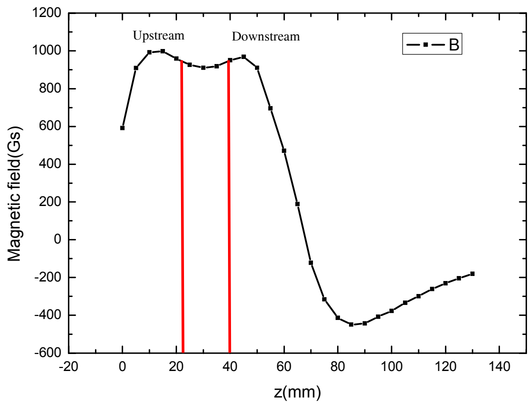

Figure 2: Magnetic field and relative positions of upstream and downstream view points.

and another is downstream closing to extraction hole, and they are located at 18.5 mm (upstream point) and 35.5 mm (downstream point) away from injection point separately as shown in Fig. 2. The ion source can generate nearly 90 mA ion beam with pure hydrogen.

The diagnostic system is composed of fiber, spectrometer (AvaSpec USL3648) and computer etc. It can collect light from 410 nm to 920 nm with a revolution of 0.09 nm~0.18 nm. The light intensity was calibrated by tungsten lamp. As hydrogen needs to mix with noble gases He and Ar at the same time, a three channels gas control system with calibrated flow meters was used to mix gases with specified fractions. The fibre detector was mounted on the test bench vertically to central axis of the source as show in Fig.1.

DIAGNOSTIC METHOD

As the plasma in 2.45 GHz ion source is low-pressure, low-temperature non-equilibrium one, collisional radiative (CR) model which considers both collisional and radiative processes can be used [10]. The method is described in [11], [12] in detail. In hydrogen plasma, the exited state of atomic hydrogen can be generated from atom, molecule and also ions(H^+,H_2^+,H_3^+ etc.), so its density

$$n_H(p) = n_H n_e R_H(p) + n_{H_2} n_e R_{H_2}(p) + n_i n_e R_i(p), \quad (1)$$

where R_H, R_{H_2} and R_i are population coefficients of atom, molecule and ions calculated by CR model. Obviously, the processes for the generation of emission line from hydrogen plasmas are too complicated for calculating T_e and n_e as all involved reactions need to be considered.

For measuring T_e and n_e in H_2 plasma, helium with $E_{thr}\approx 23$ eV and argon with $E_{thr}\approx 13$ eV were introduced into hydrogen plasma as auxiliary diagnostic gases. 10% He and 10% Ar are mixed with H_2 in our experiment and the diagnosis is based on the assumption that specified lines of noble gases are generated from direct excitation of ground state atoms, and Electron energy distribution function (EEDF) is Maxwellian. So, the intensity of emission can be simply written as

$$I_{pk} = n(p)A_{pk} = n_0 n_e R_0(p)\cdot A_{pk} = n_0 n_e X_{pk}^{eff}(T_e, n_e, \ldots) \quad , (2)$$

where n_0 is the density of certain noble atom, p and k are the exited states of the atom. A_{pk} is the spontaneous emission coefficient for the transition, and

$$X_{pk}^{eff}(T_e, n_e, \cdots) = R_0(p)\cdot A_{pk} \quad (3)$$

is effective emission rate coefficient from state p to state k which is available from Atomic Data and Analysis Structure (ADAS) database [13]. The line ratio method can cancel the dependence directly on electron density, solid angle and integral time etc.:

$$\frac{I_{pk}^1 = n_1 X_{pk}^{eff}(T_e, n_e, \ldots)}{I_{mn}^2 = n_2 X_{mn}^{eff}(T_e, n_e, \ldots)}, \quad (4)$$

m, n are different exited states from p , k of same atom or different atom. As line intensity I, particle density n can be measured with calibrated spectrometer and flow meters, the only unknown quantities are T_e *and* n_e. For electron density, the line ratio of He 587.56 nm and He 706.52 nm is recommended as the line ratio which is very sensitive on n_e and less sensitive on T_e with T_e ranging from 1~10 eV [14]. And likewise, the line ratio of He line at 728 nm to the Ar line at 750 nm is suitable for T_e diagnosis which is particularly sensitive on electron temperature. Here, all the results are only line-of-sight averaged parameters.

PRELIMINARY RESULTS

In our experiment, 0.1 sccm Ar and 0.1 sccm He were mixed with 1.0 sccm H_2. Microwave generated by magnetron was coupled into discharge chamber to ignite plasma. The light with pure hydrogen was purple, and it became a little blue with Ar and He (Fig.3). Obviously, the plasma would become weak with mixed gases.

With average RF power 200 W (10% duty factor), we investigated the relation between T_e and the operation pressure measured in the vacuum vessel after extraction system. It is shown in Fig.4 that the electron temperature increases obviously from 2 eV to 14 eV with pressure decreasing from 3×10^{-3} Pa to 6×10^{-4} Pa at both upstream and downstream points. The energy transfer between electron and other particles will decrease with lower pressure which means fewer particles and lower collision frequency, so the energetic electrons will loss less energy

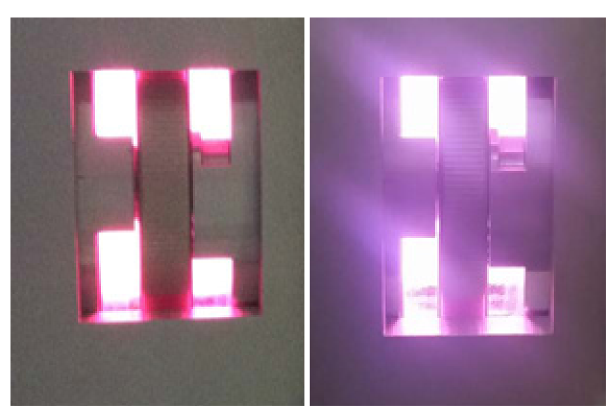

Figure 3: Discharge with pure H_2 (left) and mixed gases (right).

ISBN 978-3-95450-158-8

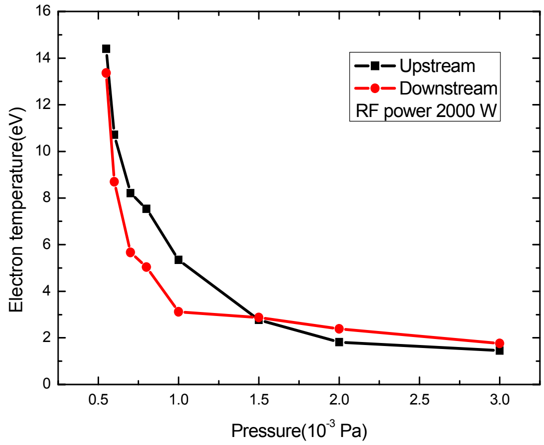

Figure 4: Average electron temperature vs operation pressure at upstream and downstream diagnosis point.

and the electron average temperature will increase. This phenomenon may explain the experimental result in [3] that H_2^+ fraction increases with pressure decreasing as the generation of H_2^+ needs higher temperature. In the other hand, the generation of H_3^+, which is easy to be destructed by energetic electrons, needs lower temperature which is available with high pressure. Fig.4 also shows that the electron temperature measured upstream is higher than the downstream point with lower pressure. But with higher pressure, the T_e measured at downstream and upstream points was close due to more frequent energy transfer in this condition. The T_e was slightly enhanced with more RF power measured upstream (Fig.5). The electron density in the cavity ranged from 5.5×10^{11} cm^{-3} to 9.0×10^{11} cm^{-3} with 100 W average RF power (10% duty factor). The error of spectroscopic method is estimated to be 25% ranging with electron density [10].

CONCLUSION

Plasma characteristics are important in the generation of H_2^+, H_3^+ and also H^-. The physical processes are more complicated than proton generation. Emission

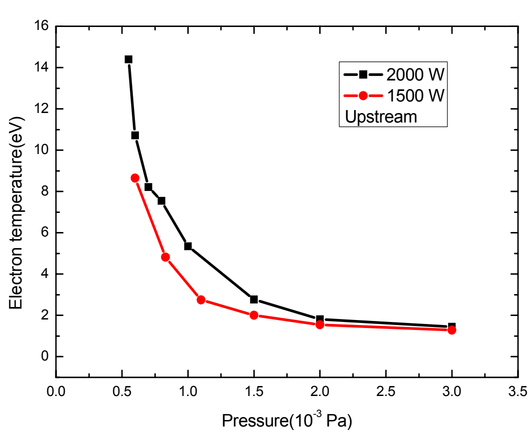

Figure 5: Average electron temperature vs operation pressure with different rf power at upstream diagnosis point.

spectroscopy diagnostic was chosen as a no invasive method to figure out the T_e and n_e in the ECR ion source with a new designed ion source. Preliminary experiment indicated that electron temperature increased with pressure decreasing, and it could be as high as 14 eV which was advantageous for the yield of H_2^+. Electron density diagnosis was also performed, and the measured value was the magnitude of 10^{11} cm^{-3}. There are some factors influencing the accuracy of diagnosis such as opacity of light in the plasma, non-Maxwellian electron energy distribution in ECR plasma, dissociation degrees of mixed gases, instrumental error etc. Detailed analysis of the influence of these factors will be performed in the future to improve the accuracy of the diagnosis.

ACKNOWLEDGMENTS

This work is supported by the National Science Foundation of China (Grant Nos. 11175009 and 91126004).

REFERENCES

[1] Jose R. Alonso, Luciano Calabretta, Daniela Campo, Luigi Celona, Janet Conrad, Ruben Gutierrez Martinez, Richard Johnson, Francis Labrecque, Matthew H. Toups, Daniel Winklehner, and Lindley Winslow, Rev. Sci. Instrum. **85**, 02A742 (2014).

[2]T. Winkelmann, R. Cee, T. Haberer, B. Naas, A. Peters, S. Scheloske, P. Spädtke, and K. Tinschert, Rev. Sci. Instrum. **79**, 02A331 (2008).

[3] Y. Xu, S. Peng, H. Ren, J. Zhao, J. Chen *et al.*, *Proceedings of IPAC2013, Shanghai*, China MOPFI035, p. 363 (2013).

[4] Yuan Xu, Shixiang Peng, Haitao Ren, Jie Zhao, Jia Chen, Ailin Zhang, TaoZhang, Zhiyu Guo and Jia'er Chen, Rev. Sci. Instrum. **85**, 02A943 (2014).

[5] Haitao Ren, Shixiang Peng, Jie Zhao, Yuan Xu, Jia Chen, Ailing Zhang, Tao Zhang, Yuting Luo, Zhiheng Wang, Zhiyu Guo and Jia'er Chen, *Proceedings of IPAC2013, Shanghai*, China MOPFI034, pp. 360–362 (2013).

[6] R. Gobin, P. Auvray, M. Bacal, J. Breton, O. Delferrière, F. Harrault, A. A. Ivanov Jr., P. Svarnas and O. Tuske, 2006 *Nucl. Fusion* **46** S281 (2006).

[7] R. Gobin K. Benmeziane, O. Delferrière, R. Ferdinand, F. Harrault, Atomique and A. Girard, *Proceedings of LINAC 2004*, Lübeck, Germany MOP74, pp. 195 (2004).

[8] U Fantz and D Wünderlich, *New J. Phys.* **8** 301 (2006).

[9] S. X. Peng Z. Z. Song, J. X. Yu, H. T. Ren, M. Zhang, Z. X. Yuan, P. N. Lu, J. Zhao, J. E. Chen, Z. Y. Guo and Y. R. Lu, *Proceedings of ECRIS2010*, Grenoble, France TUCOCK02, pp. 102 (2010).

[10] D. Wünderlich S. Dietrich and U. Fantz, Journal of Quantitative Spectroscopy & Radiative Transfer **110** pp.62–71 (2009).

[11] U Fantz, *Plasma Sources Sci. Technol.* **15** S137–S147 (2006).

[12] U Fantz, H. Falter, P. Franzen, D. Wünderlich, M. Berger, A. Lorenz, W. Kraus, P. McNeely, R. Riedl and E. Speth, *Nuclear Fusion,* Volume **46**, Issue 6, p. S297-S306 (2006).

[13] http://open.adas.ac.uk/.

[14] U. Fantz, *Contrib. Plasma Phys.* **44**, No. 5-6, 508 – 515 (2004).

SIMULATION OF THE CERN GTS-LHC ECR ION SOURCE EXTRACTION SYSTEM WITH LEAD AND ARGON ION BEAMS

V. Toivanen*, G. Bellodi, D. Küchler, A. Lombardi, R. Scrivens, J. Stafford-Haworth,
CERN, Geneva, Switzerland

Abstract

A comprehensive study of beam formation and beam transport has been initiated in order to improve the performance of the CERN heavy ion injector, Linac3. As part of this study, the ion beam extraction system of the CERN GTS-LHC 14.5 GHz Electron Cyclotron Resonance Ion Source (ECRIS) has been modelled with the ion optical code IBSimu. The simulations predict self-consistently the triangular and hollow beam structures which are often observed experimentally with ECRIS ion beams. The model is used to investigate the performance of the current extraction system and provides a basis for possible future improvements. In addition, the extraction simulation provides a more realistic representation of the initial beam properties for the beam transport simulations, which aim to identify the performance bottle necks along the Linac3 low energy beam transport. The results of beam extraction simulations with Pb and Ar ion beams from the GTS-LHC will be presented and compared with experimental observations.

INTRODUCTION

Linac3 delivers the heavy ion beams for the CERN experimental programme and is the first section of the LHC (Large Hadron Collider) heavy ion injector chain. The subsequent accelerator chain utilizing the heavy ions from Linac3 is comprised of LEIR (Low Energy Ion Ring), PS (Proton Synchrotron), SPS (Super Proton Synchrotron) and ultimately the LHC.

The heavy ion beams are produced with the GTS-LHC 14.5 GHz room temperature ECR ion source [1] at an initial energy of 2.5 keV/u. The beams are accelerated with an RFQ to 250 keV/u, followed by an Interdigital-H Drift Tube Linear Accelerator (IH-DTL) to reach the final Linac3 output energy of 4.2 MeV/u. Downstream from the IH-DTL the beam is transported through a carbon foil stripper and a filter line to produce and separate the desired ion species for LEIR injection.

The GTS-LHC is based on the original Grenoble Test Source (GTS) developed at CEA [2, 3]. It has been used predominantly in afterglow mode to produce intense lead ion beams with $^{208}Pb^{29+}$ being the ion of choice since 2007. The normal operation is performed with 10 Hz repetition rate and 50 ms RF heating pulse length. A 200 μs long ion beam pulse is selected from the $\sim$ 1 ms afterglow peak exhibited by the lead beam and accelerated at up to 5 Hz repetition rate through Linac3. Finally, the beam is stripped to $^{208}Pb^{54+}$ for LEIR injection. Following the beam development and testing performed in 2013 [4], the GTS-LHC will deliver $^{40}Ar^{11+}$ beam for fixed target experiments in 2015.

As a part of the LHC luminosity upgrade for ions, a comprehensive study of Linac3 beam formation and transport has been initiated. The first part of this study includes detailed modelling of Linac3 beam dynamics with simulations, starting from beam extraction from the GTS-LHC. The extraction simulations serve two distinct purposes. Firstly, a reliable modelling of the beam transport along Linac3 requires realistic initial beam definitions, which recreate the characteristic properties of ECRIS beams that are observed experimentally. With a realistic model of Linac3 the factors limiting the beam transport performance can then be identified and possibly remedied. Secondly, the optimization of the beam extraction itself has the potential to yield performance improvement.

The current state of beam dynamics studies is presented for Pb and Ar beams. The Ar beam has been chosen due to its availability for measurements in 2014 during the injector chain commissioning and preparation for the 2015 physics experiments.

EXTRACTION SIMULATIONS

Extraction Simulation Settings

The GTS-LHC ion beam extraction has been modelled with the ion optical code IBSimu [5]. The code provides good capabilities to simulate multispecies extraction from plasma in the presence of strong magnetic fields and space charge, conditions which are closely associated with ECR ion sources. Although the nonlinear positive plasma model used by the code [6] considerably simplifies the complex ECRIS plasma conditions, previous studies have shown that IBSimu is a powerful tool in modelling ECRIS extraction systems [7].

The GTS-LHC extraction geometry, presented in Fig. 1, includes a plasma electrode, an intermediate electrode and a grounded electrode, forming a triode extraction system. Downstream from the electrodes the extraction region opens into a vertical cylindrical pumping chamber, followed by a beam pipe section with an inner diameter of 65 mm. The simulations have been performed in 3D with coordinate x denoting the optical axis and z and y the transverse directions. The 3D magnetic field map of the GTS-LHC was calculated with Cobham Opera 3D simulation software [8] and it includes the solenoid and the permanent magnet hexapole fields. In addition, the field of the first beam line solenoid downstream from the extraction region is included in the simulations. The resulting longitudinal magnetic field pro-

* ville.aleksi.toivanen@cern.ch

ISBN 978-3-95450-158-8

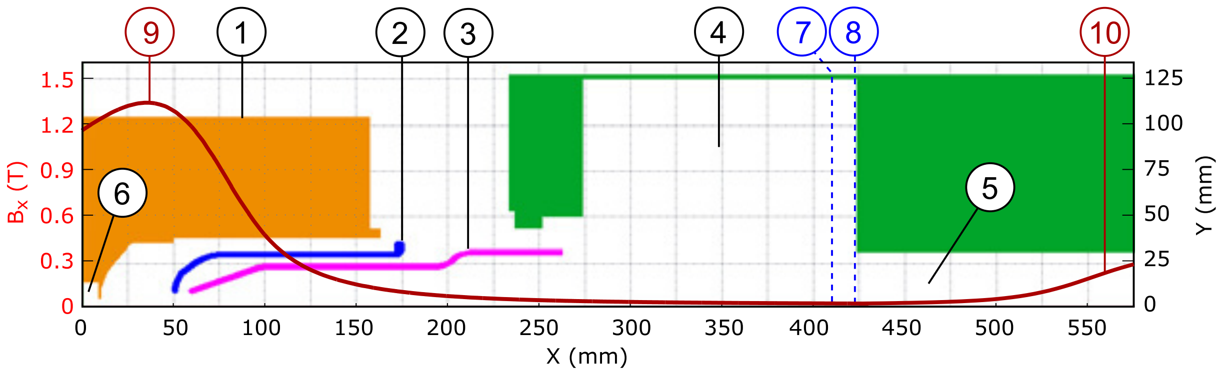

Figure 1: The GTS-LHC extraction geometry used in the simulations and the longitudinal magnetic field (B_x) profile on axis. The extraction system includes the plasma electrode (1), the intermediate electrode (2) and the grounded electrode (3), followed by the pumping chamber (4) and 65 mm diameter beam pipe (5). The plasma is modelled in a reduced volume (6). The locations of transverse beam observations are also indicated (7 and 8). The longitudinal magnetic field includes the ECRIS solenoid field (9) and the field of the first beam line solenoid (10).

file on axis is presented in Fig. 1 superimposed over the simulation geometry.

The afterglow discharge is characterized by the collapse of the electron population due to the loss of confinement by the RF field and the subsequent burst of extracted ions [9]. In the simulation this is modelled by assuming an increased plasma potential of 200 V, about an order of magnitude higher than is usually measured for second generation ECR ion sources in CW mode [10, 11], and a low 10 eV temperature for the cold background electron population. A cold ion population was assumed with longitudinal and transverse temperatures of 1 eV based on the generally accepted order of magnitude in ECR plasmas [12] and discretized into $\sim 1.4 \cdot 10^6$ tracked macro particles. The initial ion species distributions were defined based on the measured charge state distributions (CSD). The ion species dependent losses in the extraction region, caused by the influence of the strong magnetic field, were accounted for by iteratively adjusting the initial distribution to match the simulated CSD of the beam leaving the extraction region to the measured CSD. The simulation assumes full space charge in the extraction region. This is justified by the presence of strong electric fields preventing the accumulation of low energy compensating electrons into the beam potential. In addition, the compensation is mitigated by the low residual gas pressure in the extraction region (low 10^{-8} mbar region) and pulsed operation, which limit the electron production and accumulation time.

Three different cases have been studied with simulations; extraction of a Pb ion beam with the ion source tuned for the production of ^{208}Pb^{27+} and ^{208}Pb^{29+} and extraction of an Ar beam with the ion source tuned for the production of ^{40}Ar^{11+}. The ^{208}Pb^{29+} case corresponds to the current Pb operation settings of the GTS-LHC and is the main case in order to improve the future Pb operation of Linac3. However, the beam is not available for experiments until 2015. In order to compare Pb operation with available experimental data, the earlier operation conditions with ^{208}Pb^{27+} were simulated. The ^{40}Ar^{11+} case corresponds to the Ar operational settings that will be used for the 2015 fixed target physics experiments, and was modelled due to the availability of the Ar beam for experiments during the later half of 2014.

The Pb simulations are based on operational settings of the GTS-LHC at CERN. The Ar simulations are based on tests performed with the GTS-LHC at CERN [4] and the GTS2 at iThemba LABS [13]. The Pb beams are produced with oxygen mixing gas (included in the simulated CSD) whereas the Ar beam is produced with pure argon plasma. The extraction electrode voltages and other details are presented in Fig. 2 showing the simulations results.

Extraction Simulation Results

The simulated particle trajectory densities of the extracted Pb and Ar beams are presented in Fig. 2. In the case of the Pb beams the meniscus forms a convex shape, resulting to extraction of an initially diverging beam. The electric field and the axial magnetic field maximum in the acceleration gap provide strong charge-over-mass dependent focusing effect, yielding a beam waist inside the grounded electrode and separation of the beam envelopes of different ion species. With the argon beam the meniscus has a flat shape, which mitigates these effects and results into initially parallel beam extraction and more uniform particle distribution in the transverse plane (see Fig. 4). Due to the lack of additional focusing elements in the extraction region, in all simulated cases the beams are strongly divergent as they leave the grounded electrode, resulting in significant beam collimation against the walls of the extraction pumping chamber and the following beam pipe walls. With the Pb beams the simulations also show beam collimation at the intermediate electrode face and the inside of the grounded electrode. Visual inspection of the GTS-LHC extraction system shows clear beam induced markings at these locations. As an example, Fig. 3 presents a comparison of the simulated beam profile on the extraction pumping chamber wall (location 8

ISBN 978-3-95450-158-8

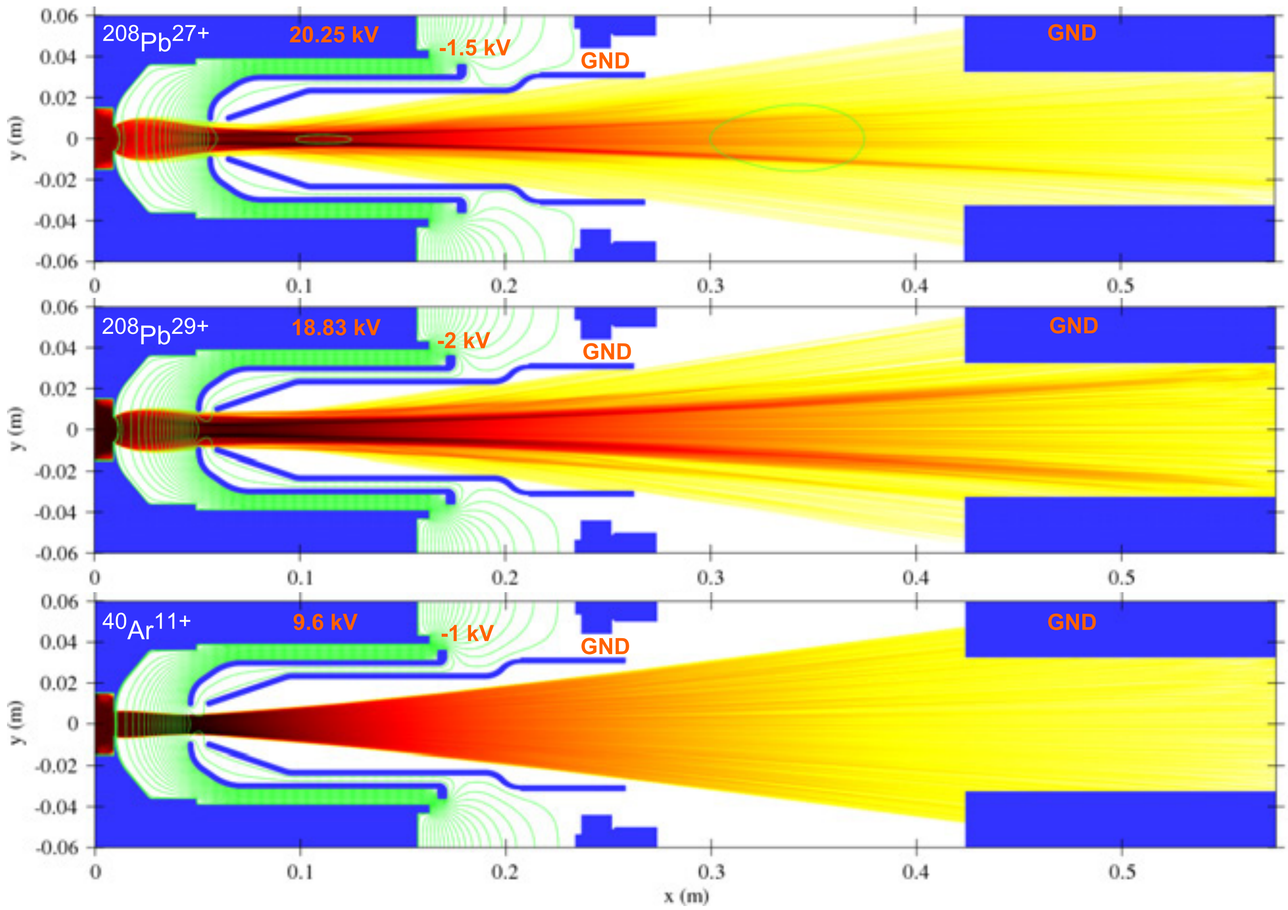

Figure 2: Simulated ion trajectory densities of the three studied cases through the GTS-LHC extraction region. The total extracted ion currents and acceleration gap lengths are: 3.5 mA and 45 mm for the $^{208}Pb^{27+}$ case, 5 mA and 40 mm for the $^{208}Pb^{29+}$ case and 1.6 mA and 35 mm for the $^{40}Ar^{11+}$ case.

in Fig. 1) and the beam induced markings observed at the same location. However, it is noted that the simulation only corresponds to the beam extraction during the afterglow, which constitutes only part of the extracted ion beam pulse. The extracted beam preceding the afterglow burst has different beam properties and can also contribute to the observed markings.

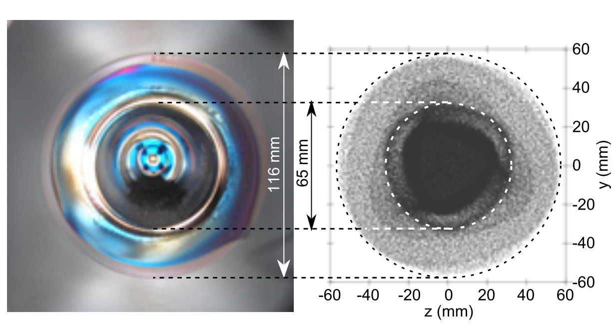

Figure 3: Comparison of the simulated beam particle positions (right) and experimentally observed beam induced markings (left) at the wall of the extraction pumping chamber.

The beam profiles of the total beams (all extracted ion species) and separately the ion species of interest ($^{208}Pb^{27+}$, $^{208}Pb^{29+}$ and $^{40}Ar^{11+}$) are presented in Fig. 4 at axial location x = 414 mm (location 7 in Fig. 1). The beams exhibit triangular shapes, which are the signature influence of the ECRIS magnetic confinement structure combining hexapole and solenoid fields. In addition, the Pb beams exhibit hollow beam structures and the formation of low intensity beam halo and triangular "wings", which are associated with the strong over-focusing inside the grounded electrode (for experimental examples of over-focused beam profiles, see e.g. [14]). These features are often experimentally observed with ion beams produced with ECR ion sources and are produced self-consistently by the simulation model. Due to the different initial extraction conditions avoiding the strong initial (over-) focusing inside the extraction electrodes, the transverse particle distribution of the Ar beam is significantly more uniform and exhibit very little aberrations compared to the Pb beams.

LEBT SIMULATIONS

The extraction simulation results presented in the previous section are used as initial beam definitions for the fol-

ISBN 978-3-95450-158-8

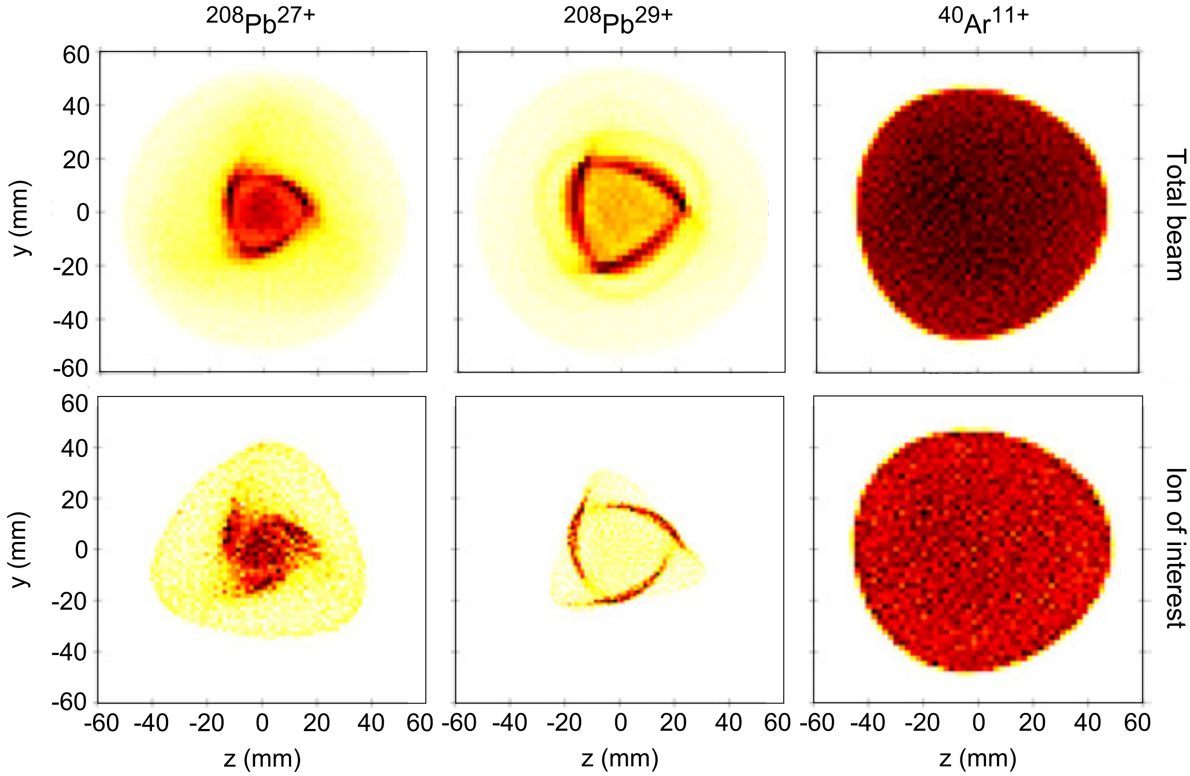

Figure 4: Simulated beam profiles of the three studied cases at the location 7 shown in Fig. 1 (see also Fig. 5). The upper row shows the profile of the full beam (all extracted ion species) and the lower row the profiles of the ion species of interest.

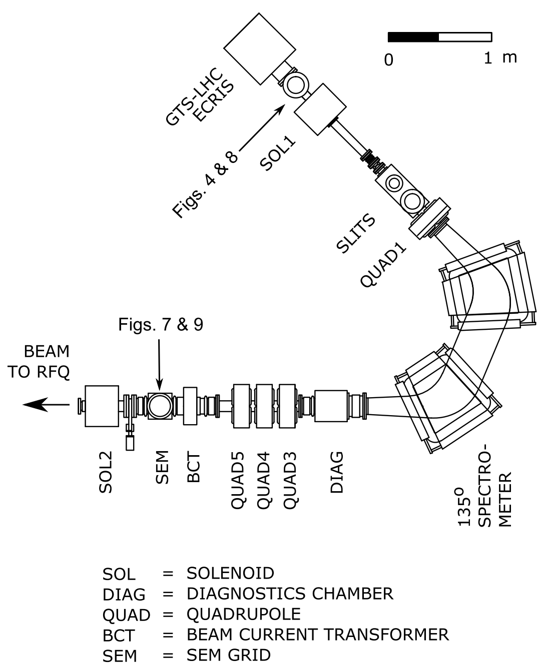

Figure 5: Linac3 LEBT with the main beam line components. The diagnostics chamber houses a horizontal slit, a Faraday cup (FC2) and in future a pepperpot emittance meter. The locations of the transverse beam diagnostics (simulated and measured) presented in the other figures are also indicated.

lowing beam dynamics simulations of the Linac3. This is an on-going study and consequently the discussion here will be limited to the first preliminary results of the low energy beam transport (LEBT) section of Linac3, the schematic of which is presented in Fig. 5. A detailed model of the Linac3 LEBT was constructed with the 3D multiparticle tracking code PATH [15]. To achieve a realistic representation of the beam transport, the machine elements are modelled based on their measured properties with operational settings and beam losses are calculated with a realistic aperture model.

The simulated transmission of $^{208}Pb^{27+}$ ion beam through the LEBT is presented in Fig. 6. As was observed in the extraction simulations, significant amount of the initial extracted beam is collimated at the end of the extraction region before reaching the first beam line solenoid. As a result, Over 60 % of the total extracted beam and about half of the $^{208}Pb^{27+}$ beam is lost during the first 0.3 m of beam transport. Apart from this initial collimation, the $^{208}Pb^{27+}$ does not exhibit further significant beam losses until near the end of the LEBT, yielding ~ 40 % transmission to the RFQ. The other ion species experiencing suboptimal focusing are collimated during beam transport, steadily decreasing the transmission of the total beam, until the last of them are eliminated at the slit downstream from the spectrometer. Similar trends are observed with the other beams from the extraction simulations.

Comparison of simulated and measured beam properties of $^{40}Ar^{11+}$ and $^{208}Pb^{27+}$ beams downstream from the Linac3

ISBN 978-3-95450-158-8

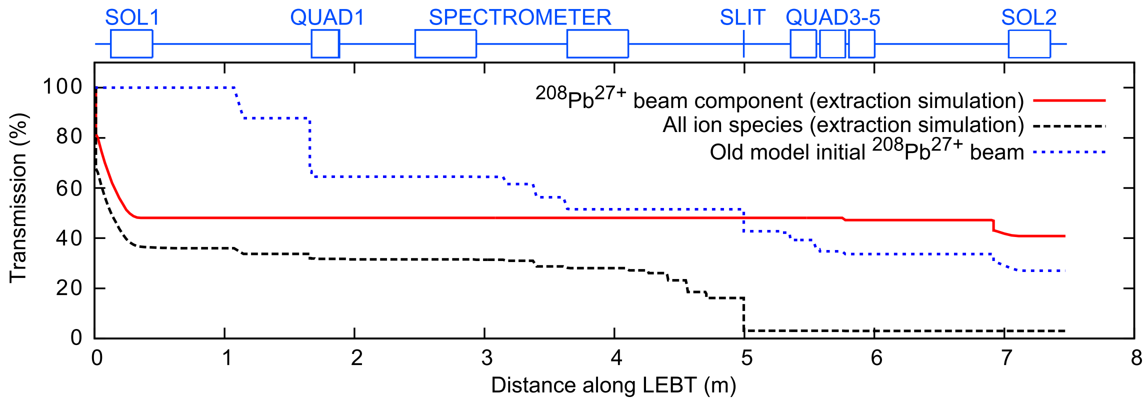

Figure 6: The simulated transmission through the Linac3 LEBT with the $^{208}Pb^{27+}$ initial beam. Location $x = 0$ m corresponds to location 7 in Fig. 1. The main LEBT beam line elements are also shown (see Fig. 5).

Table 1: Comparison of simulated and measured beam properties of $^{40}Ar^{11+}$ and $^{208}Pb^{27+}$ beams downstream from the Linac3 spectrometer. The results with the initial beam used by the old Linac3 model is also presented. $P^{x,y}_{rms}$ denotes the transverse rms beam profile widths and $\epsilon^{x,y}_{rms}$ the rms emittance in the (x,x') and (y,y') phase spaces.

	P^{x}_{rms} (mm)	P^{y}_{rms} (mm)	ϵ^{x}_{rms} (mm mrad)	ϵ^{y}_{rms} (mm mrad)
$^{40}Ar^{11+}$ *simulated*	11	16	38	18
$^{40}Ar^{11+}$ *measured*	14	14	-	-
$^{208}Pb^{27+}$ *simulated*	9	11	30	28
$^{208}Pb^{27+}$ *measured*	7	7	39 ± 4	29.9 ± 0.4
$^{208}Pb^{27+}$ *old model*	25	12	320	118

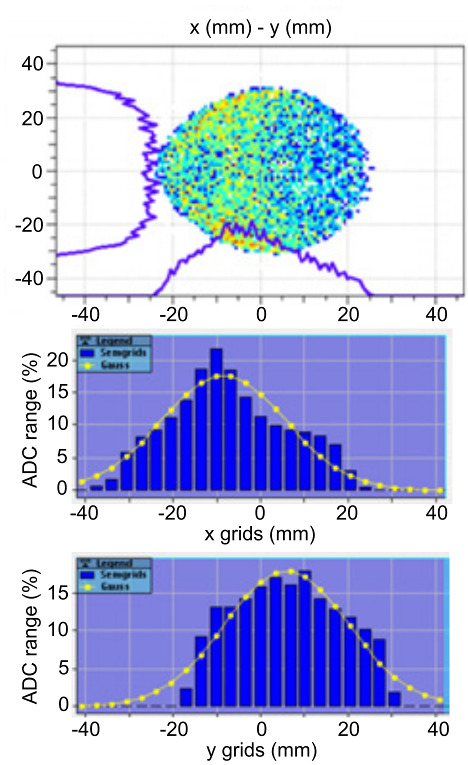

Figure 7: Comparison of simulated and measured $^{40}Ar^{11+}$ beam profiles at the LEBT SEM grid (see Fig. 5).

spectrometer are presented in Table 1. Figure 7 presents the simulated $^{40}Ar^{11+}$ beam profile at the LEBT SEM grid compared with the measured profiles. Although the simulated and measured values are not identical, the simulated beam properties are in reasonable agreement with the measurements. Especially the simulated beam profile shape in Fig. 7 exhibits many of the same features as the measured profile.

The properties of the initial beam description used in the ion optics calculations have high impact on the simulation results. This is demonstrated in Figs. 8 and 9, which show the difference between using an initial beam distribution obtained from the presented extraction simulations ($^{208}Pb^{27+}$ case) and using the idealized initial beam definition for $^{208}Pb^{27+}$ that was originally used to design the Linac3 beam transport. Both cases have been simulated using the operational LEBT settings which experimentally yield the highest performance. It is observed that combining the old initial beam definition with the new 3D multiparticle beam transport model results in strong emittance blow-up during transport. This is caused by mismatch between the beam properties and the ion optical settings of the beam transport leading to cumulative emittance growth in the beam line focusing elements and the spectrometer. The incompatibility is also reflected in the beam losses occurring along the LEBT, as presented in Fig. 6. This underlines the sensitivity of the ion optics to the initial beam properties during the low energy beam transport. The final beam prop-

ISBN 978-3-95450-158-8

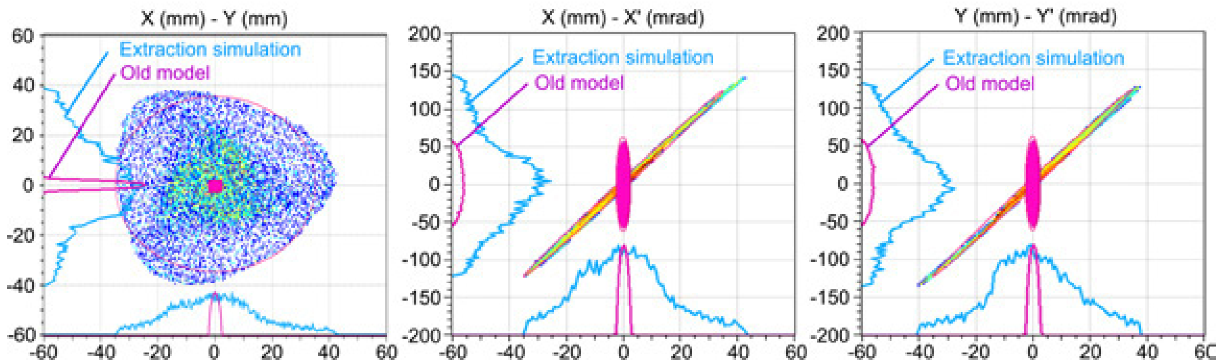

Figure 8: Comparison of the initial $^{208}Pb^{27+}$ beam definition from the extraction simulation and the initial beam used with the old Linac3 beam model. The initial transverse rms emittances are 82 mm mrad (extraction simulation) and 31 mm mrad (old model) in both transverse phase spaces. See Fig. 5 for the location.

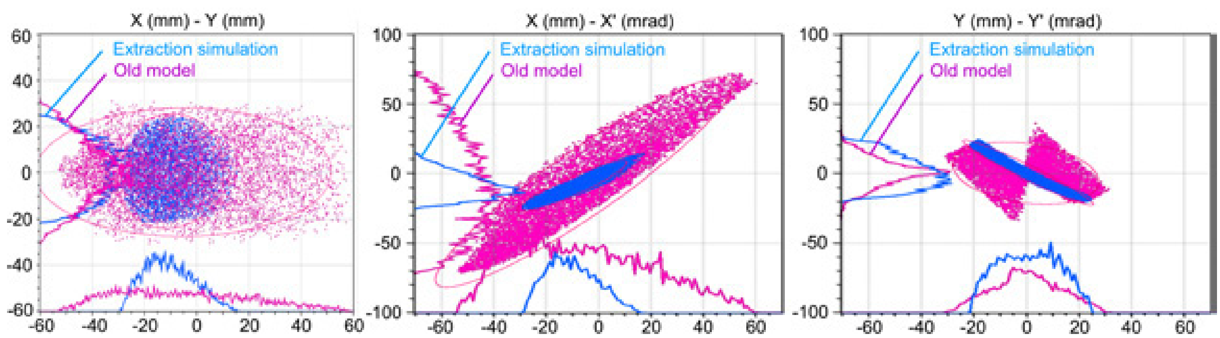

Figure 9: Comparison of the LEBT simulation results with the different initial beam definitions (see Fig. 8) at the location of the SEM grid downstream from the spectrometer (see Fig. 5). The final transverse rms emittances in (x,x') and (y,y') phase spaces are 30 and 28 mm mrad (extraction simulation) and 320 and 118 mm mrad (old model).

erties of the two cases, numerical values of which are presented in Table 1, are significantly different, and the beam properties obtained with the old initial beam definition are in strong contrast with the experimental results.

DISCUSSION

The performed ion extraction simulations provide new insight into the beam conditions and behavior in the GTS-LHC extraction system. The prediction of many signatory features observed experimentally with ECRIS ion beams and the matching of simulated beam losses and observed beam induced markings inside the extraction system increase the confidence in the simulation model. The simulations indicate that the current GTS-LHC extraction system is not fully capable of handling the high beam currents extracted during the afterglow burst. The main reason for this is the insufficient focusing properties provided by the simple extraction electrode configuration combined with the relatively long distance from the extraction to the first focusing element of the beam line. This results into significant beam losses between the extraction and the first beam line solenoid. Mitigation of these losses and consequent increase in usable ion beam current is a good motivation to continue the ion beam extraction study to improve the GTS-LHC, and Linac3, performance. Possible options to study include a redesign of the extraction electrode geometry, implementation of a new focusing lens after the current extraction system and a redesign of the beam line section immediately after the extraction region to allow moving the first beam line solenoid closer to the ion source and reduce beam losses. These would also lead to better beam quality, which would be advantageous for beam transport and matching through the beam line elements and acceleration structures further downstream.

As the preliminary measurements in the Linac3 LEBT section indicate, the model combining the extraction and tracking simulations is promising, but not yet perfect. Further measurements are required to obtain feedback for the simulation model in order to improve it. The installation of the new pepperpot emittance meter (from Pantechnik, based on the KVI design [16, 17]) after the spectrometer, currently under commissioning and coming online in the beginning of autumn 2014, will provide improved diagnostics for this purpose. After further verification, the model will be extended to include the accelerating structures and higher energy sections of Linac3 to gain further insight into its functionality and act as a basis for future performance improvements.

ISBN 978-3-95450-158-8

ACKNOWLEDGMENT

The authors would like to thank Ø. Midttun for providing the original magnetic model of the GTS-LHC.

REFERENCES

[1] L. Dumas et al., "Operation of the GTS-LHC Source for the Hadron Injector at CERN", in Proc. of ECRIS'06, Lanzhou, China, published in HEP & NP, Vol. 31, Suppl. 1, pp. 51-54 (2007). Also available as LHC Project Report 985.

[2] D. Hitz et al., "Grenoble Test Source (GTS): A Multipurpose Room Temperature ECRIS", in Proc. of ECRIS'02, Jyväskylä, Finland, pp. 53-55.

[3] D. Hitz et al., "A New Room Temperature ECR Ion Source for Accelerator Facilities", in Proc. of EPAC'02, Paris, France, pp. 1718-1720.

[4] D. Küchler et al., "Preparation of a Primary Argon Beam for the CERN Fixed Target Physics", Rev. Sci. Instrum. 85, 02A954 (2014).

[5] T. Kalvas et al., "IBSIMU: a Three-Dimensional Simulation Software for Charged Particle Optics", Rev. Sci. Instrum. 81, 02B703 (2010).

[6] J.H. Whealton et al., "Optics of Ion Beams of Arbitrary Perveance Extracted from a Plasma", J. Comput. Phys. 27, pp. 32-41 (1978).

[7] V. Toivanen et al., "Double Einzel Lens Extraction for the JYFL 14 GHz ECR Ion Source Designed with IBSimu", J. Instrum. 9, P05003 (2013).

[8] Cobham Opera Simulation Software Homepage, `http://operafea.com/`.

[9] O. Tarvainen et al., "Diagnostics of Plasma Decay and Afterglow Transient of an Electron Cyclotron Resonance Ion Source", Plasma Sources Sci. Technol. 19, 045027 (13pp) (2010).

[10] O. Tarvainen et al., "Emittance and Plasma Potential Measurements in Double-Frequency Heating Mode with the 14 GHz Electron Cyclotron Resonance Ion Source at the University of Jyväskylä", Rev. Sci. Instrum. 77, 03A309 (2006).

[11] O. Tarvainen et al., "Effect of the Gas Mixing Technique on the Plasma Potential and Emittance of the JYFL 14 GHz Electron Cyclotron Resonance Ion Source", Rev. Sci. Instrum. 76, 093304 (2005).

[12] A. Girard et al., "Electron Cyclotron Resonance Plasmas and Electron Cyclotron Resonance Ion Sources: Physics and Technology", Rev. Sci. Instrum. 75, pp. 1381-1388 (2004).

[13] R.W. Thomae et al., "Beam Experiments with the Grenoble Test Electron Cyclotron Resonance Ion Source at iThemba Labs", in Proc. of ECRIS'12, Sydney, Australia, pp. 68-70.

[14] P. Spädtke et al., "Prospects of Ion Beam Extraction and Transport Simulations", Rev. Sci. Instrum. 79, 02B716 (2008).

[15] A. Perrin and J.F. Amand, Travel User Manual, CERN (2003).

[16] H.R. Kremers et al., "A Versatile Emittance Meter and Profile Monitor", in Proc. of DIPAC'07, Venice, Italy, pp. 195-197.

[17] H.R. Kremers et al., "Comparison Between an Allison Scanner and the KVI-4D Emittance Meter", in Proc. of ECRIS'08, Chicago, USA, pp. 204-207.

ISBN 978-3-95450-158-8

HIGH CURRENT PROTON AND DEUTERON BEAMS FOR ACCELERATORS AND NEUTRON GENERATORS

V. Skalyga, I. Izotov, S. Razin, A. Sidorov, S. Golubev, A. Maslennikova, A. Volovecky,
IAP, RAS, 46 Ul`yanova st., 603950 Nizhny Novgorod, Russia
H. Koivisto, O. Tarvainen, T. Kalvas, University of Jyväskylä, Department of Physics,
P.O. Box 35 (YFL), 40500 Jyväskylä, Finland

Abstract

This paper presents the latest results of high current proton and deuteron beam production at SMIS 37 facility at the Institute of Applied Physics (IAP RAS). In this experimental setup the plasma is created and the electrons are heated by 37.5 GHz gyrotron radiation with power up to 100 kW in a simple mirror trap fulfilling the ECR condition. High microwave power and frequency allow sustaining higher density hydrogen plasma (n_e up to $2 \cdot 10^{13}$ cm^{-3}) in comparison to conventional ECRIS's or microwave sources. The low ion temperature, on the order of a few eV, is beneficial to produce proton beams with low emittance.

Latest experiments at SMIS 37 were performed using a single-aperture two-electrode extraction system. Experiments with hydrogen and deuterium show possibility of beams formation with currents up to 550 mA at high voltages below 45 kV with normalized rms emittance lower than 0.2 π·mm·mrad. Such beams have a high potential for application in future accelerator research.

Also in frames of the present paper it is suggested to use such an ion source in a scheme of D-D neutron generator. High current gas-dynamic ion source can produce deuteron ion beams with current density up to 700-800 mA/cm^2. Generation of the neutron flux with density at the level of $7\text{-}8 \cdot 10^{10}$ s^{-1}cm^{-2} could be obtained in case of TiD_2 target bombardment with deuteron beam accelerated to 100 keV. Estimations show that it is enough for formation of epithermal neutron flux with density higher than 10^9 s^{-1}cm^{-2} suitable for boron neutron capture therapy. Important advantage of described approach is absence of Tritium in the scheme.

EXPERIMENTAL SETUP

The experimental research presented in this work was carried out on the SMIS 37 shown schematically in Fig. 1 [1]. A gyrotron generating a Gaussian beam of linearly polarized radiation at the frequency of 37.5 GHz, with the power up to 100 kW, and pulse duration up to 1.5 ms was used for plasma production and heating. The microwave radiation is launched into the plasma chamber through a quasi-optical system consisting of 2 mirrors, quartz vacuum window and a special μW-to-plasma coupling system shown on the left in Fig. 1. A simple mirror trap was used for plasma confinement. The magnetic field in the trap was produced by means of pulsed solenoids, spaced 15 cm apart. Magnetic field in the mirror was varied from 1.4 to 4 T (ECR for 37.5 GHz is 1.34 T). Ratio of the maximum and minimum magnetic fields of the trap was equal to 5. Hydrogen and deuterium were used as a working gas. Its inlet into the source was realized through an opening incorporated with the microwave coupling system. The delay between gas injection and subsequent microwave pulse (300-3000 μs) as well as the gas pulse duration (about 5 ms) were adjusted for each experimental condition in order to maximize the beam current and optimize the temporal shape of the extracted current pulse.

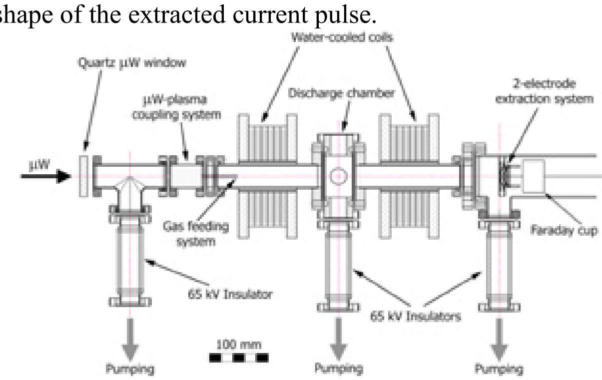

Figure 1: SMIS 37 experimental setup.

The ion extraction and beam formation were realized by two-electrode, i.e. single gap plasma electrode - puller electrode system. Diameters of the holes in plasma electrode and puller were of 10 mm and 22 mm respectively. The plasma electrode was placed 10 cm downstream from the magnetic mirror to limit the extracted ion flux as described in [2], which helps improving the beam transport through the puller.

The maximum available extraction voltage was 45 kV. A Faraday cup was placed immediately behind the puller electrode to measure the total beam current passing through the extractor.

EXPERIMENTAL RESULTS

The use of powerful millimeter wave radiation allows to significantly increase the plasma density in the discharge compared to traditional ECR sources (the density scales with the square of the radiation frequency). In our experiments with 37.5 GHz gyrotron frequency the plasma density could be higher than 10^{13} cm^{-3} [3]. High value of plasma density N_e in combination with quite low ion life-time τ (but still enough for 100% ionization degree) provides high density of ion flux from the trap ~ N_e/τ. In our experiments the total plasma (ion) flux

ISBN 978-3-95450-158-8

density through the plug of the magnetic trap was up to 5 A/cm^2.

A single-aperture extraction system was used for beam formation in presented experiments. The optimization of extraction electrode configuration such as adjusting the gap between the electrodes and the position relative to the magnetic plug of the trap was performed in order to maximize the extracted ion current. The optimal distance between magnetic plug and plasma electrode was found to be 10 cm and the gap between the electrodes 6 mm. Shift of the extraction system closer to the plug was not reasonable because of too high plasma flux density for high voltage range available in experiments. The maximum obtained beam current was 500 mA, corresponding to 640 mA/cm^2 current density through the plasma electrode (see fig.2). To our knowledge, this current density is the record for modern ECR ion sources.

Emittance of the extracted beam was measured with "pepper-pot" method [4], which had been successfully tested earlier at SMIS 37 [2]. "Pepper-pot" plate was placed 1 mm downstream from the puller with another 55 mm gap before a CsI scintillator for beam imaging. Emittance diagram for the 500 mA beam is shown in figure 2. The normalized rms emittance was of 0.07 π mm mrad.

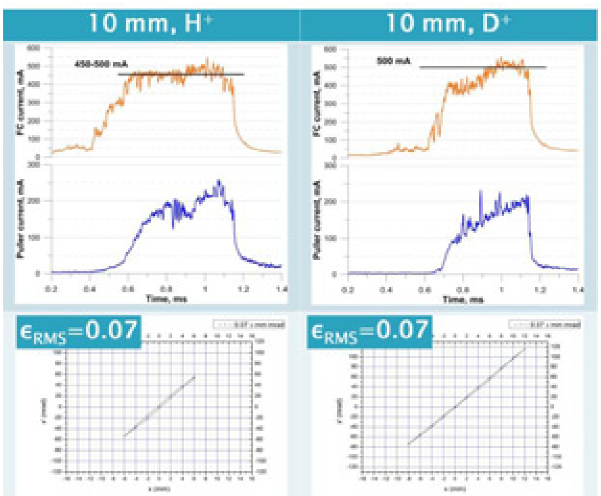

Figure 2: Faraday cup (FC) and puller current oscillograms for H+ and D+ beams and corresponding emittance diagrams obtained with 45 kV extraction voltage.

The spectrum of the extracted ion beam was also measured. The spectrum shown in fig. 3 appeared to be similar to the one demonstrated in [5] for multiaperture extraction. The data is normalized with respect to the total beam current measured with the Faraday cup downstream from the bending magnet. In this case H_2^+-current is less than 6% of the total beam current. Only trace amounts of H_3^+ were observed.

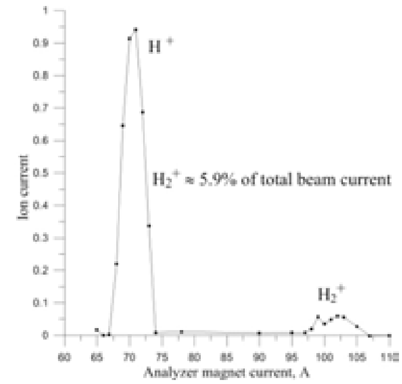

Figure 3: Mass-analyzed ion beam spectrum normalized to the total beam current.

Obtained high current deuteron beams were used for D-D neutron generation: beams were accelerated across high voltage potential (up to 45 kV) to the target containing deuterium (for the most part of experiments it was TiD_2). Due to the D-D reaction 2.5 MeV neutrons were generated. Preliminary thermalized neutron flux was measured by ^{3}He proportional counters.

Neutron yield obtained for different targets presented in the Table 1. The lower yield for titanium targets was due to the target quality (i.e. degree of deuterium implementation). The yield from the "heavy ice" target was close to the theoretical one for 45 kV. It should be noted that it is only the results of preliminary experiments for neutron generation. In these experiments acceleration voltage didn't exceed the value of 45 kV where the cross section of the D-D reaction is quite small.

Table 1: Neutron yields for different targets.

Target type	Neutron yield/mA	Total yield
TiD2(sample 1)	$7{\cdot}10^5$ s^{-1}	$2{\cdot}10^8$ s^{-1}
TiD2(sample 2)	$1{\cdot}10^6$ s^{-1}	$3{\cdot}10^8$ s^{-1}
D2O ("heavy ice")	$4{\cdot}10^6$ s^{-1}	10^9 s^{-1}

CONCLUSION

The experimental results described in the present paper demonstrate the feasibility of high power millimeter wave quasi-gasdynamic ECR ion sources for the production of high brightness proton and deuteron beams with favorable species fraction.

Especially it looks prospectively for neutron production. The performance of commercially available targets is about 10^8 neutrons/second per 1 mA current of the incident deuteron beam accelerated to energy of 100 keV [6]. Thus, bombardment of such target by deuteron beam equivalent to that demonstrated above (and further accelerated to 100 keV) would theoretically yield a neutron flux up to $6{\cdot}10^{10}$ neutrons per second from rather small surface with dimensions of about 1 cm. Neutron

ISBN 978-3-95450-158-8

generator with these parameters seems to be promising for such applications as boron neutron-capture therapy.

As the next step a possibility of D-D neutron generator creation using a source of deuterium ions on the basis of CW ECR discharge supported by powerful microwave technological gyrotron with frequency of 24-28 GHz and a power level of 10 kW should be studied.

ACKNOWLEDGMENT

This work was supported by the Russian Foundation for Basic Research, project № 13-08-00845 and partially by the grant MK-6565.2014.2 of the Russian Federation president (Skalyga V.A. and Sidorov A.V.).

REFERENCES

[1] S.V Golubev, S.V. Razin, A.V. Sidorov, V.A. Skalyga, A.V. Vodopyanov, V.G. Zorin, Review of Scientific Instruments, **75**, 1675-1677 (2004).

[2] A. Sidorov, M. Dorf, A. Bokhanov, I. Izotov, S. Razin, V. Skalyga, V. Zorin, A. Balabaev, P Spädtke, J. Roßbach, Review of Scientific Instruments, **79**, 02A317 (2008).

[3] V. Skalyga, V. Zorin, I. Izotov, S. Razin, A. Sidorov, A. Bohanov, Plasma Sources Science and Technology, **15**, 727-734 (2006).

[4] A. Septier, Applied charge particle optics, Academic Press, New York, p. 214 (1980).

[5] V. Skalyga, I. Izotov, A. Sidorov, S. Razin, V. Zorin, O. Tarvainen, H. Koivisto, T. Kalvas. JINST, v.7, P10010 (2012).

[6] van der Horst, "VIIIc Neutron Generators" Philips Technical Library16. Eindhoven, Netherlands: Philips Technical Library, p. 281-295 (1964).

ISBN 978-3-95450-158-8

OPTIMIZATION OF LOW-ENERGY BEAM TRANSPORT *

H.R. Kremers, J.P.M. Beijers, and S. Brandenburg
KVI-CART, Groningen, The Netherlands

Abstract

Transport of low-energy heavy-ion beams from an Electron Cyclotron Resonance Ion Source to an accelerator often suffers from significant emittance increase caused by aberrations of ion-optical elements in the beam transport line. In this paper we use a combination of four-dimensional phase-space measurements and simulations to study beam transport through an analyzing magnet. It is shown that large second-order aberrations of the magnet lead to a five-fold increase of the beam emittance. Several mitigation strategies are investigated, i.e. adding compensating hexapoles or extra focusing elements between ion source and magnet. The best solution is to use a focusing solenoid between ion source and magnet. Using a compensating hexapole is not recommended, since it introduces significant third and higher-order aberrations.

INTRODUCTION

Low-energy heavy-ion beams extracted from Electron Cyclotron Resonance Ion Sources (ECRIS) have relatively large beam diameters and divergences because the extraction occurs in a decreasing magnetic field. Such beams are therefore very sensitive for ion-optical aberrations in the bending and focusing elements of the beam transport line leading to emittance blowup and beam losses. To give some typical numbers[1], injector ECRIS's have beam emittances in the range of 20-100 mm mrad for low to medium charged ions. The geometrical acceptance of a cyclotron is typically 100-200 mm mrad. However, measured emittances in low-energy beam lines are often in the range of 100-300 mm mrad taking into account the phase space cutoffs by beam limiters. This results in low transport and injection efficiencies [2–4]. There is thus much room for improvement. These issues are particularly relevant for very high-intensity beams where beam losses might lead to damage, or for very low-intensity beams where one cannot afford to loose any ions.

This paper presents methods to determine the beam emittance and ion-optical aberrations quantitatively and discusses possible ways to minimize the emittance blowup caused by these aberrations. The motivation for this work was to better understand beam transport in the low-energy beam transport (LEBT) line of the AGOR facility at KVI-CART [5,6]. The measurements and simulations have been done with a mono-component 25 keV He^+ beam only for the first part of this LEBT line consisting of an ECRIS and a charge-state analyzing magnet, but it is straightforward to include more ion-optical elements. Regarding the simulations to minimize the ion-optical aberrations of the dipole magnet a 21 keV H^+ beam is used. The paper is organized in three sections. The first section describes the experimental and computational methods that have been used. The second section presents and discusses several ways to minimize ion-optical aberrations. The last section finishes with the conclusions.

* Work supported by university of Groningen (RuG).

[1] All quoted beam emittances are understood to be 4-rms emittances according to the definition of Lapostolle [1].

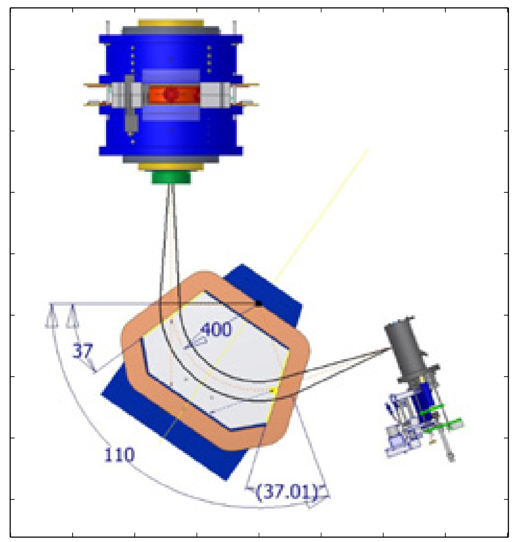

Figure 1: ECR ion source, charge-state analyzing magnet and a pepper-pot emittance meter.

EXPERIMENTAL AND COMPUTATIONAL METHODS

Experimental setup

The first part of the LEBT line includes an ECRIS, charge-state analyzing magnet and a pepper-pot emittance meter (see Fig. 1). The ECRIS is of the AECR-type with two room temperature solenoids and an open NdFeB permanent hexapole magnet. The plasma is heated with 14 GHz microwaves with a maximum power of 2 kW and the source can be biased with respect to ground up to a maximum voltage of 34 kV. Ions are extracted with an accel-decel lens system consisting of a plasma electrode with a 8 mm extraction aperture followed by shielding and ground electrodes. Charge-state selection of the extracted beam is done with an unclamped double-focusing analyzing magnet with a bending radius of 400 mm, bending angle of 110° and pole face

ISBN 978-3-95450-158-8

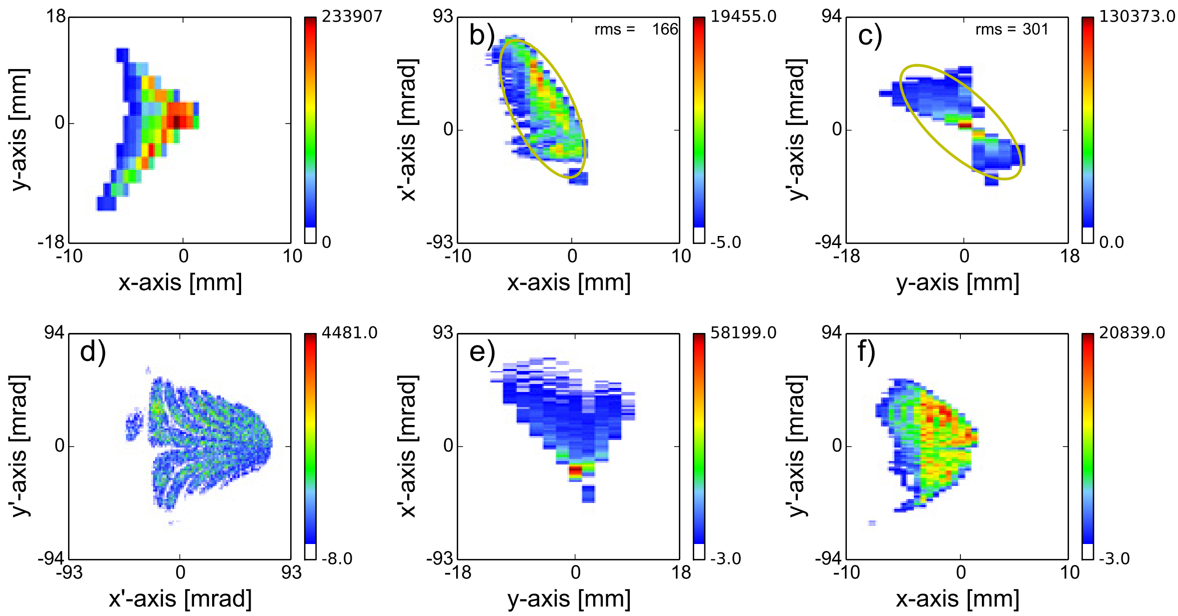

Figure 2: Measured six 2D projections validated by simulations of the 4D phase-space distribution of a 25 keV He$^+$ beam.

rotations of 37°. The geometrical acceptance of the magnet is 60 mm in both horizontal and vertical directions. The distance between the plasma electrode and effective field boundary (EFB) of the magnet is 682 mm.

In order to benchmark the beam transport simulations we have installed a pepper-pot emittance meter close to the image plane of the analyzing magnet [7]. The advantage of a pepper-pot emittance meter compared to a scanning-slit device is that with a pepper-pot meter one can measure the full four-dimensional (4D) transverse phase-space distribution of ion beams including correlations between the horizontal and vertical planes, while a scanning-slit meter only measures the $(x-x')$ and the $(y-y')$ projections of the 4D distribution. Figure 2 shows six 2D projections of the 4D phase-space distribution of a 25 keV He$^+$ beam measured with the pepper-pot emittance meter. Notice the large horizontal and vertical emittances of 116 and 301 mm mrad, respectively, and the higher-order horizontal and vertical correlations in the extracted ion beam. These values would even be a factor of two larger without the beam losses caused by the geometrical acceptance of the system.

Computational methods

We have used several codes to simulate and analyze the extraction and transport of low-energy heavy-ion beams, which are all based on numerically calculating ion trajectories in predefined electromagnetic fields. In previous work we have simulated the ion production in an ECRIS using a Particle-In-Cell, Monte-Carlo-Collision (PIC-MCC) code with which the phase-space distribution of the ions in the extraction aperture of the plasma electrode has been calculated [8]. The ion trajectories through the accel-decel extraction system, drift spaces and analyzing magnet have been calculated with the General Particle Tracer (GPT) code, which is a 3D particle tracking code taking all electric and magnetic fields in the extraction system and analyzing magnet into account as well as the space-charge forces of the ion beam [9]. The LORENTZ-3D code has mainly been used to calculate the 3D magnetic field of the analyzing magnet [10]. These simulations, confirmed by measurements, showed that i) ion beams are fully space-charge neutralized so that the Coulomb forces between ions can be neglected, ii) the ion beam behind the extraction system is strongly divergent, has a triangular spatial profile and 4rms-emittances of 65 mm mrad in both transverse directions determined by the fringe field of the extraction solenoid and iii) large, second-order aberrations of the analyzing magnet cause a five-fold increase of the beam emittances in the magnet's image plane [11].

To further investigate the emittance increase in the analyzing magnet and possible ways to remedy this we use COSY INFINITY [12]. This code applies differential-algebra methods to calculate transfer maps of ion-optical systems up to an arbitrary order. In the present work we have calculated transfer maps of the analyzing magnet and additional focusing elements up to 5th order. An axisymmetric Kapchinsky-Vladimirski (KV) distribution with an emittances of $\epsilon_{4rms} = 65$ mm mrad in both transverse planes is used as an initial phase-space distribution. We use this distribution because previous simulations showed that the emittance of the extracted beams are elliptical and nearly identical in both transversal directions [11]. KV distributions have an uniform intensity and are completely contained in an ellipse with an area of $\epsilon_{4rms}\pi$ mm mrad. The

ISBN 978-3-95450-158-8

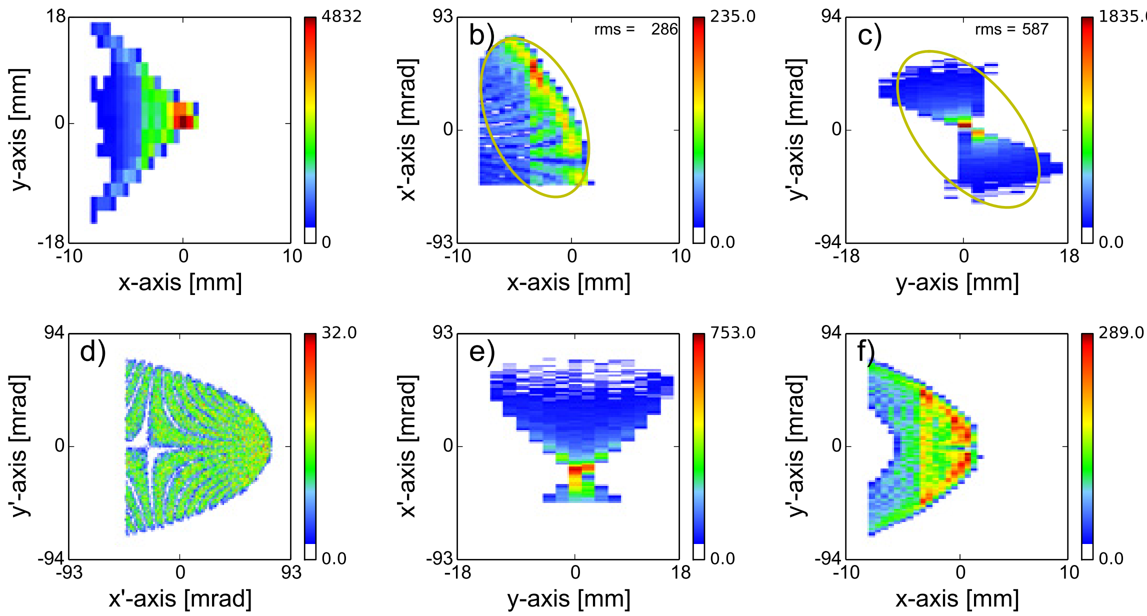

Figure 3: Calculated six 2D projections of the 4D phase-space distribution of a 25 keV He^+ beam. Phase-space cutoffs caused by finite apertures of the magnet have been taken into account.

initial KV distribution $f^0(x, x', y, y')$ is then transformed to a final distribution $f^1(x, x', y, y')$ by randomly sampling f^0 with 10^8 particles, i.e. the transformed phase-space coordinates q_1 in the image plane of the analyzing magnet are related to the initial coordinates q_0 in the object plane by $q_1 = M^{(k)} q_0$ with $M^{(k)}$ the transfer map of the system of order k and $q = x, x', y, y'$. To illustrate, Figure 3 shows six 2D projections of a calculated 4D phase-space distribution of a 25 keV He^+ beam using a second-order transfer map of the analyzing magnet. We used an internal model (FR3) of COSY INFINITY to calculate the fringe fields of the analyzing magnet. Phase-space cutoffs caused by finite apertures of the magnet have been taken into account. The measured and calculated phase-space distributions show good agreement and we conclude that the second order coefficients $(y|x'y')$, $(x|y'y')$ and $(x|x'x')$ are the dominant terms causing a five-fold increase of the beam emittance behind the analyzing magnet.

MINIMIZING ION-OPTICAL ABERRATIONS

Two strategies have been studied to minimize the second order aberrations. The first strategy is to compensate the second order terms with two hexapoles, one before and one behind the analyzing magnet. The second strategy is to use a "field lens" in front of the analyzing magnet to modify the divergent extracted beam into a more parallel beam. In this way the influence of the strong gradients of the fringe field of the dipole is reduced. We consider both a solenoid and an einzel lens.

Hexapole lenses

The hexapoles are positioned at the entrance and exit of the dipole magnet at a distance of 305 and 152 mm of the magnet respectively. The effective length of the hexapoles is 100 mm and the distance between the beam axis and the pole tip is 50 mm. The hexapoles reduce the 2^{nd} order coefficients $(y|x'y')$ and $(x|y'y')$ to nearly zero, but the coefficient $(x|x'x')$ is increased by a factor of 3. That hexapoles are not able to compensate fully for all three coefficients is due to fact that they generates the coefficients: $(y|x'y')$, $(x|x'x')$ and $(x|y'y')$ in a ratio of 1 : +0.5 : -0.5. As the second order coefficients of the magnet aberration do not exhibit these exact ratios the term $(x|x'x')$ remains. Furthermore, third and higher order coefficients become significant in both planes. In Fig. 4 the value of the 4-rms emittance is shown as function of the poletip field of the hexapole. Notice that the minimum value of the horizontal and vertical emittances is reached at different poletip fields.

Field lenses

A thin solenoid with an inner diameter of 200 mm is positioned 305 mm upstream from the dipole magnet. The solenoid reduces the three second order coefficients $(y|x'y')$,$(x|y'y')$ and $(x|x'x')$ to nearly zero. When the solenoid is powered with a current of 320 kA.turn the wide divergent H^+ beam, at the entrance of the dipole magnet, is changed into a smaller more paraxial beam. In this way the beam fits in a more effective way the geometrical acceptance of the magnet and the influence of the strong gradients of the fringe field of the dipole is reduced. This effect is significant as can be seen in Fig. 5. The value of 74 mm mrad

ISBN 978-3-95450-158-8

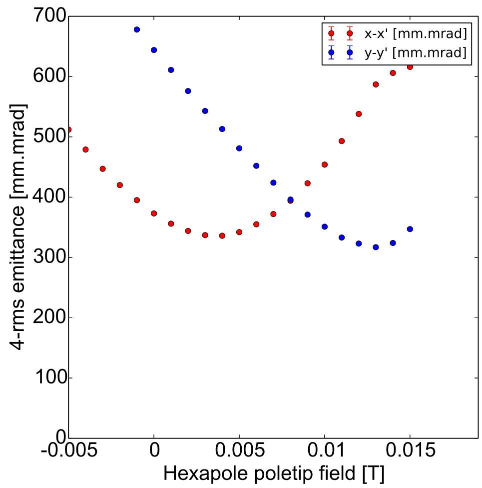

Figure 4: Calculated 4-rms emittance value of a 21 keV H$^+$ beam in the image plane of the dipole magnet as function of the excitation of the hexapoles.

for the 4-rms emittance at 320 kA.turn is of the same order as the 4rms emittance of the initial KV distribution in the object plane. Including a solenoid in the extraction area with this strength is difficult as the magnetic field of the solenoid interferes with the fringe field in the extraction region of the ion source. Therefore, we investigated also a simpler and smaller option i.e an einzel lens.

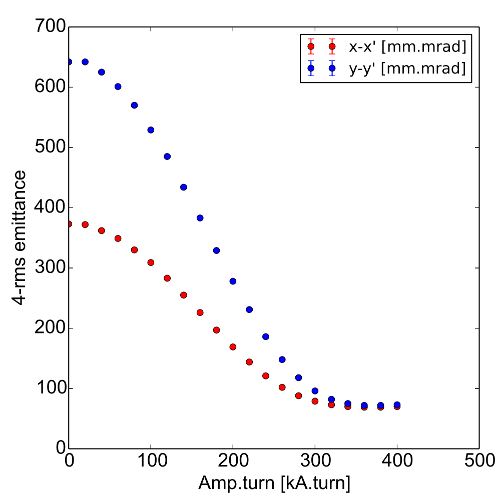

Figure 5: Calculated 4-rms emittance value of a 21 keV H$^+$ beam in the image plane of the dipole magnet as function of the excitation of the solenoid.

An Einzel lens reduces the coefficients $(y|x'y')$,$(x|y'y')$ and $(x|x'x')$ of the second-order transfer map by a factor of 4 by modifying the divergent beam into a more paraxial beam in both transverse directions. Quantitatively, the 4-rms emittance is changed from 375 mm mrad and 650 mm mrad in the horizontal and vertical plane to 120 and 140 mm mrad, respectively. The einzel lens has three identical cylinders, each with an inner diameter of 70 mm and a length of 75 mm. The gap between the cylinders is 10 mm. The distance between the lens and the dipole magnet is 305 mm. As shown in the Fig. 6 a minimum is found for the emittances in both transverse directions at a lens-potential of 9-10 kV. However the initial 4rms-emittance of 65 mm mrad is not regained. A detailed investigation shows that this is caused by the additional aberrations induced by the einzel lens itself. Simulations are in progress for an accel-decel configuration since the aberrations of such a configuration are expected to be smaller with respect to the decel-accel configuration."

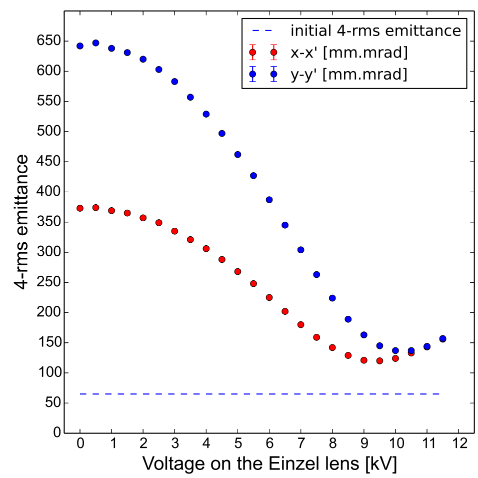

Figure 6: Calculated 4-rms emittance value of a 21 kV H$^+$ beam in the image plane of the dipole magnet as function of the potential on the einzel lens.

CONCLUSIONS

By comparing 4D phase-space measurements and simulations we have identified large second-order aberrations of the analyzing magnet as the main cause of emittance blowup and beam loss in the LEBT line connecting the ECRIS and AGOR cyclotron. The large second-order aberrations are mainly caused by the large divergences that are characteristic of ECRIS beams. Several mitigation strategies have been studied, including compensating hexapoles and a focusing solenoid or einzel lens between ECRIS and analyzing magnet. Our simulations show that adding hexapoles can indeed compensate the second-order aberrations to a large extent, but introduce additional third and higher-order aberrations. Clearly the best solution is a focusing solenoid, with a large inner diameter, between ECRIS and analyzing magnet which, if it has enough focusing power, can recover the initial emittances before the analyzing magnet. When a solenoid cannot be used, e.g. because of space limitations, using an einzel lens is the second best option. However, enough care should be exercised in its design as not to introduce additional aberrations.

ISBN 978-3-95450-158-8

In general, efficient transport of low-energy ECRIS beams with minimal losses can be realized by keeping the beam as paraxial as possible and paying sufficient attention to minimize the fringe fields of the bending and focusing elements. Although this remark may sound superficial it is often overlooked by designers of LEBT lines, who tend to design optical elements which are too short with too small apertures and thus have relatively large fringe fields.

REFERENCES

[1] P.M. Lapostolle, IEEE Trans. Nucl. Sci. **18**, 1101 (1971).

[2] W. Krauss-Vogt, H. Beuscher, H. L. Hagedoorn, J. Reich and P. Wucherer, Nucl. Instrum. Methods A **268**, 5 (1988).

[3] Cao, Y. and Zhao, H. W. and Ma, L. and Zhang, Z. M. and Sun, L. T., Rev. Sci. Instrum. **75**, 1443-1445 (2004), DOI:http://dx.doi.org/10.1063/1.1690482

[4] Harrison, K. A. and Antaya, T. A., Rev. Sci. Instrum., **65**, 1138-1140 (1994), DOI:http://dx.doi.org/10.1063/1.1145039

[5] H.R. Kremers et al., Rev. Sci. Instrum. **77**, 03A311 (2006).

[6] H.R. Kremers, J.P.M. Beijers, S. Brandenburg and J. Mulder, High Energy Physics and Nuclear Physics, Vol 31,supp 1, pg 90, (2007).

[7] H.R. Kremers, J.P.M. Beijers, and S. Brandenburg, Rev. Sci. Instrum. **84**, 025117 (2013).

[8] V. Mironov and J.P.M. Beijers, Phys. Rev. ST Accel. Beams **12**, 073501 (2009).

[9] General Particle Tracer code, see `http://www.pulsar.nl/gpt`

[10] LORENTZ-3D code, see `http://www.integratedsoft.com/products/lorentz`

[11] S. Saminathan et al., Rev. Sci. Instrum. **83**, 073305 (2012).

[12] K. Makino and M. Bertz, Nucl. Instrum. Methods A **558**, 346

ISBN 978-3-95450-158-8

COMBINATION OF TWO ECRIS CALCULATIONS: PLASMA ELECTRONS AND EXTRACTED IONS

S. Biri, R. Rácz, Atomki, Debrecen, Hungary
P. Spädtke, K. Tinschert, R. Lang, J. Mäder, F. Maimone and B.R. Schlei,
GSI, Darmstadt, Germany

Abstract

In strongly magnetized ECRIS plasmas collisions do not influence the path of the charged particle. Electrons and ions can move more freely only along a magnetic field line compared to the transverse direction. Therefore, extraction simulation requires that the trajectories of charged particles have to be traced through the plasma chamber instead of starting at the plasma boundary. In previous simulations the particle density at the beginning of the trajectory deep inside the plasma has been unknown. Now the full 3D electron tracking within the plasma chamber has been combined with the generation of initial ion starting conditions including particle density for ion tracking. The TrapCAD code has been used to determine the electron spatial distribution in a certain energy window. The idea is that at the places where the electron reaches a specific energy, an ion trajectory can be started. The magnetic field has been modeled with OPERA, whereas for solving the electric potential and the particle tracking the computer code KOBRA3-INP has been used. First results will be shown and discussed. The number of affecting parameters on the operating conditions of the ion source may lead to a multi-dimensional optimization space for simulation.

MOTIVATION

Several attempts have been done in the past to simulate the extraction of ions from an Electron Cyclotron Resonance (ECR) Ion Source (ECRIS). Most of these attempts gave only partial results or even failed, because they were not able to reproduce the experimental results. In early simulations the ions started from outside the plasma or just at the plasma boundary. Later models tried to include the effect of the non-cylindrical magnetic field [1]. One of the recent and best models up to now is given by the following procedure: tracing magnetic field lines through the extraction aperture, looking where these field lines are coming from, and using the coordinates of the magnetic field line as starting points for ions to be extracted [2]. This means magnetized ions are considered.

It is also also well-known that energetic plasma electrons are strongly tighten to the magnetic field lines. The question is whether we can use the coordinates of these electrons by simultaneously using the field lines? A simulation study of ECRIS plasma electrons revealed that in certain cases the positions of the electrons inside the plasma chamber may correspond to the positions of the highly charged ions [3]. The study was built on direct experimental results: on visible-light photos and on energy-filtered X-ray photos of argon plasmas.

In this paper we make an attempt to combine the two methods: a plasma electron cloud is simulated in a given ECRIS configuration and the coordinates of these electrons are used to be the starting positions of ions to be extracted. During the extraction procedure the fully 3D magnetic field structure of the ECRIS (inside and outside the plasma) is taken into account.

THE ECRIS CONFIGURATION

For the simulations of plasma electrons and ions to be extracted the CAPRICE-type ECR ion source operating at GSI was selected. The technical details of this ECRIS are described elsewhere [4]. It has a relatively short plasma chamber in a strong magnetic trap (created by two room-temperature coils and by a NdFeB-magnet hexapole) operating on 14.5 GHz microwave frequency (even it is suitable to operate at different frequencies) [4]. The simulation of electron movement requires the knowledge of magnetic field values in a fine 3D mesh. Because ECRISs have certain symmetries, for this pre-calculation a real 3D code was not necessary. Instead, the 2D PoissonSuperfish code (version 6.15) has been used [5]. For the calculation the exact geometry of the GSI-CAPRICE with typical coils currents used for highly charged ion production were applied (see Table 1).

Table 1: Input parameters for Superfish calculations

Parameters for calculation	Value
Plasma chamber length:	187 mm
Plasma chamber diameter:	63 mm
Injection coil current:	1100 A
Extraction coil current:	1100 A
Hexapole materials (VACODYM):	745HR/655HR
Mesh size for the coils system:	0.5 mm
Mesh size for the hexapole system:	0.2 mm

Figure 1 and 2 show the result: the geometries of the axial and radial magnetic traps and the relevant magnetic field distributions. Throughout with Superfish and TrapCAD calculations in this paper the axis of the plasma chamber is marked by z and the radial distance is marked by r. The calculated magnetic curves correspond well (inside the plasma chamber) with measurements carried out by the GSI team earlier. The curves show the minimum and maximum values of the magnetic field

ISBN 978-3-95450-158-8

inside the plasma chamber. These values with different mirror ratios (Bmax/Bmin) effect the production of ions.

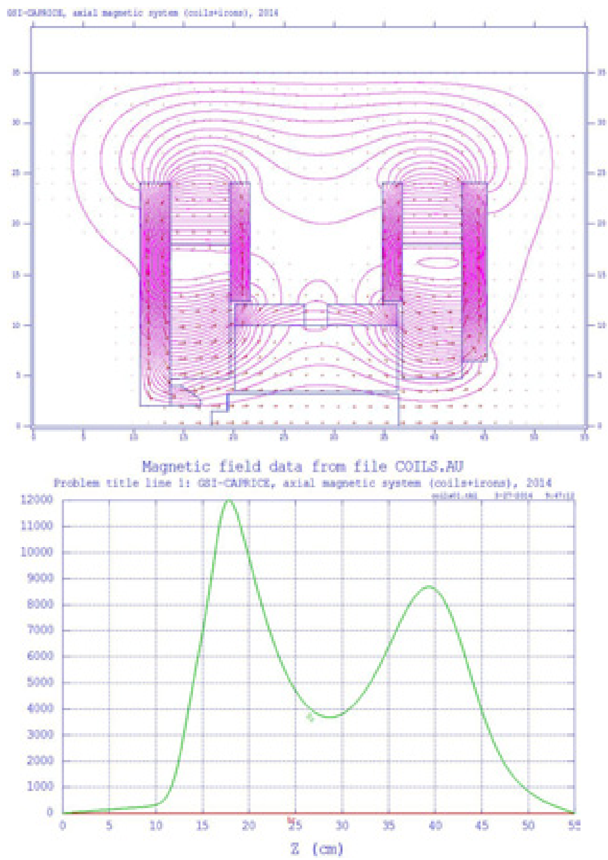

Figure 1: The axial magnetic trap (coils+irons) of GSI-CAPRICE calculated by PoissonSuperfish, injection side left. Down: axial magnetic field curve.

THE TRAPCAD CODE

The superposition of the two components of the GSI-CAPRICE magnetic field was then made including the end-effects of the hexapole magnet in order to get a realistic fine-meshed 3D magnetic array. The special movement and energy-evolution of a high number of electrons were then simulated by the TrapCAD code which was developed and several times upgraded by the Atomki team. Details of the code are fully described in paper [3] and in its references.

TrapCAD was made to visualize the magnetic trap structure of ECR and other ion sources and to follow the energy and spatial evolution of electrons. It is a limited 3D code which means the magnetic system must have some regularities (cylindrical axial field, multipolar radial field), but the resulting motion is calculated in 3D. The magnetic field has to be calculated by other pre-processing codes (usually by the PoissonSuperfish group of codes). A 4-order Runge-Kutta method is applied for the integration of the magnetic field line equation. The Lorentz force integration is processed by a time-centered leapfrog scheme explicitly solving the motion equations. The code is based on the one electron approach with neglecting the particle-particle interactions. The electron heating (the electron–cyclotron-resonance process) is calculated by assuming a simple RF field but realistic magnetic field configuration. The electrons are heated up by stochastic resonance process. As a result, the spatial and energy structure of both the non-lost and lost electrons can be calculated. Non-lost electrons are called those which remain in the plasma chamber by the end of the simulation time. Lost-electrons hit the walls and their energy is given to the wall.

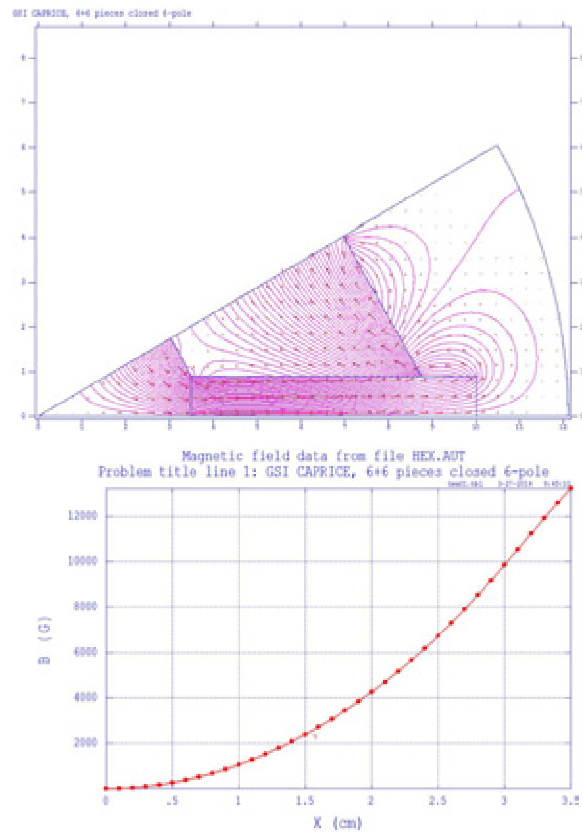

Figure 2: The radial magnetic trap of GSI-CAPRICE calculated by PoissonSuperfish (30 degrees section). Down: the radial magnetic field distribution at a pole.

In a recent work [6] of our team the simulation of the plasma electrons in the Atomki-ECR ion source [7] was carried out in a very detailed way. Graphical front and side views and plasma slices show the spatial structure of the plasma electrons [6].

PLASMA ELECTRONS SIMULATIONS

The spatial and energy distribution of the non-lost (plasma) electrons in the 14.5 GHz GSI-CAPRICE ECRIS were calculated by TrapCAD. Four million electrons were placed with equal density into a thin layer around the closed resonance surface. The simulation time was 200 nanoseconds (a timescale such that the particle–particle interactions can be neglected). In real (CPU) time the calculation lasted for 146 hours in a PC with i7 processor. At the end of the simulation cca 40 % (1.6 million) of the electrons were still remained in the plasma

ISBN 978-3-95450-158-8

and 60 % were lost on the chamber wall. Some important parameters regarding the starting conditions of the simulation and some numerical results are in Table 2.

Table 2: I/O parameters of the TrapCAD calculations

Parameters for calculation	**Value**
Number of electrons:	4000000
Start position (resonant surface)	5200 +/- 200 gauss
Perp. energy components:	1 - 100 eV, random
Parallel energy components:	1 - 100 eV, random
RF frequency:	14.5 GHz
RF power:	1000 W
Simulated time:	200 ns
Number of lost particles:	2396026 (59.9 %)
Number of non-lost particles:	1603974 (40.1 %)
Average energy of lost particles:	118 eV
Av. energy of non-lost particles:	2753 eV

In the subsequent figures (figures 3-6) some direct numerical and graphical results of the TrapCAD simulation are shown.

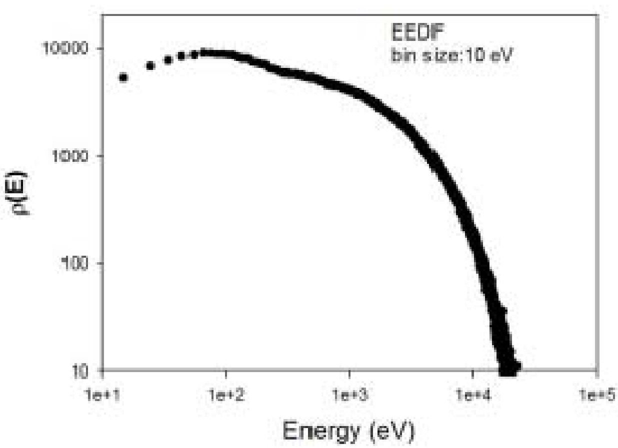

Figure 3: The electron energy distribution function (EEDF) of the non-lost electrons.

The goal and the most important result of the TrapCAD simulation was the creation of the huge non_lost.txt ASCII file containing the starting and ending coordinates (x, y, z) and the starting and ending energy (parallel, perpendicular, total) of all non-lost electrons. This file was used as basic database for the simulation of the ions extraction.

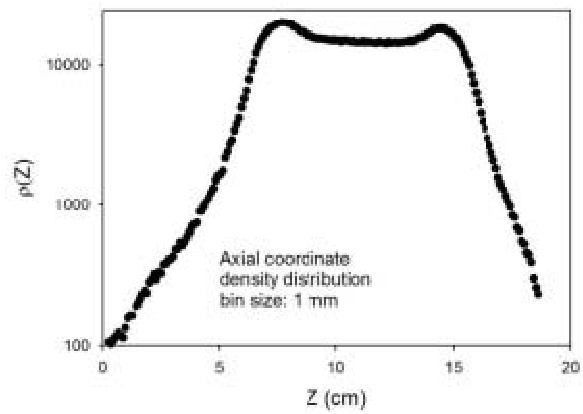

Figure 4: The axial distribution of the non-lost electrons. Left: injection side.

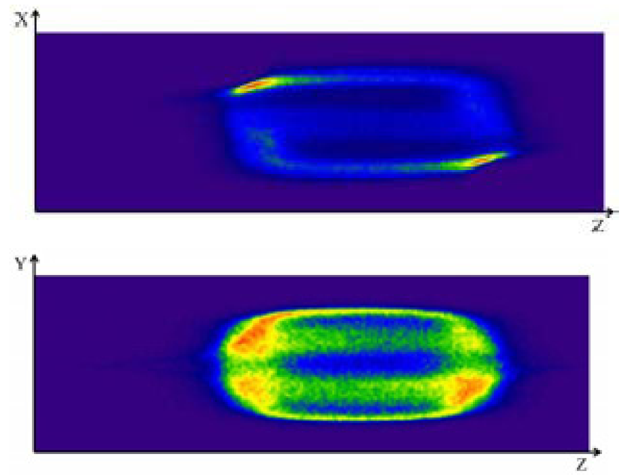

Figure 5: Radial (side-view) projection of the electron cloud from the direction of a magnetic gap (up) and from a magnetic pole (down).

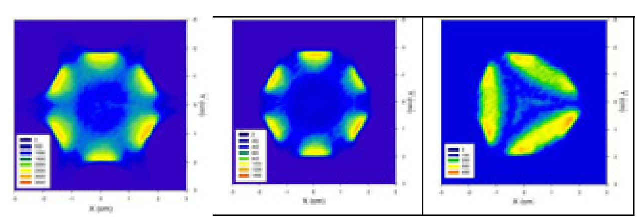

Figure 6: Axial (end-view) projection of the non-lost electrons. Left: all electrons, middle: warm electrons (3 keV <E< 10 keV), right: warm electrons close to the extraction side (Z>13cm).

THE KOBRA3-INP CODE

KOBRA3-INP [8] is a fully 3-dimensional Vlasov solver. It discretizes the geometry to a Cartesian mesh. The Laplacian potential is than determined for each node. Magnetic flux density needs to be defined on each node at that time. Once the starting conditions have been defined, ray tracing can be performed. The space charge of each trajectory will be distributed to the surrounding nodes

ISBN 978-3-95450-158-8

accordingly. This space charge can than be used to calculate Poisson's equation. The space charge is assumed to be neutralized within the plasma, as well as in the extracted ion beam, if an appropriate accel-decel system has been used. As well as in a real experiment, diagnostic tools are essential to present the results. KOBRA-3 can generate (beside other diagnostics) emittance plots. Such an emittance plot is a projection of the 6-dimensional phase space into the 2D drawing plane. As an example, the vertical emittance ε_y is defined as:

$$\varepsilon y = \iiiint f(y,y')\, dx\, dz\, dx'\, dz' \quad (1)$$

where y and z are the transverse directions and x is the longitudinal direction. (Throughout with KOBRA calculations in this paper the axes of the plasma chamber is marked by x.)

Due to the coupling between planes for ECRISs it is not allowed to restrict to 2D subspaces. We do need for a correct presentation of the results at least the 4D transverse phase space (if not the 6D phase space is necessary). Such a possibility is under investigation momentarily at GSI, see the last section. Because of the coupling between planes due to the strong magnetic flux density, other projections than the typical emittances are also used which are important for accelerators:

$$\mathcal{P} y = \iiiint f(y,z')\, dx\, dz\, dx'\, dy' \quad (2)$$

$\mathcal{P}_y$ describes the coupling from the y-plane to the perpendicular one. (In Fig. 12 this coupling will be shown for different charge states.)

TRANSFER FROM TRAPCAD TO KOBRA

It was necessary to build an interface bridge between TrapCAD and KOBRA. The final coordinates of the non-lost electrons were used to start at all of these places an ion. Each ion was started with a very low starting energy. In figure 7 the starting conditions of the ions are drawn in two views.

Altogether 1.6 million trajectories were created by this way for each charge state. From this total number 229635 Ar^+ ions could be extracted (14 %), 185523 Ar^{3+}, (12%), 167193 Ar^{5+} (10%) and 108729 p (7%). All other ions stayed in the plasma chamber. The trajectory calculations required huge disc space, the file size of trajectory coordinates (all coordinates of all trajectories along each path) in total was in the order of 26GB, for singly charged Ar, 34GB for Ar^{3+}, 28GB for Ar^{5+}, and 35GB for p. In figure 8 a typical trajectory plot is shown. The different colors indicate where the ions are coming from (black injection side, yellow and green extraction side). The figure also shows some geometry values which will be important at the emittance figures (see next chapter).

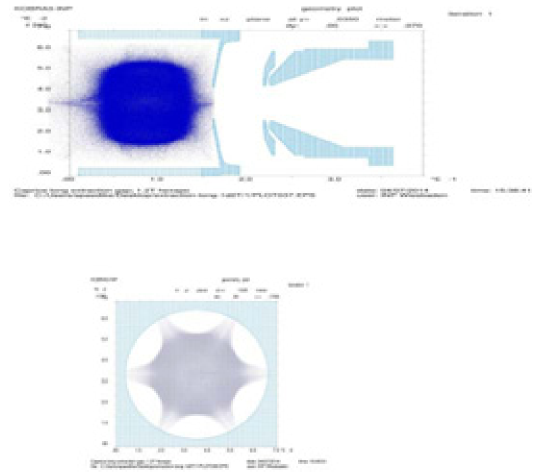

Figure 7: The starting conditions of ions. Up: side view, cut in the mid-plane, down: end view, cut in the plasma chamber. Each dot is one macro particle. Starting conditions are projected into the drawing plane.

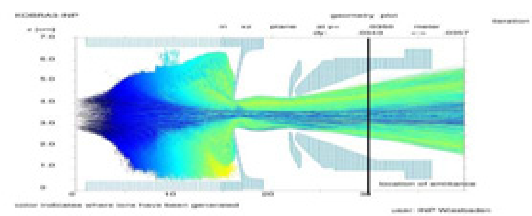

Figure 8: GSI-CAPRICE, typical trajectory plot. The ions are coming from deep inside the plasma. Black are particles coming from the injection side, blue from the middle, green and yellow from the extraction side. The emittance calculations are performed at 30cm.

ION EXTRACTION FROM INSIDE THE PLASMA CHAMBER

The final results of the TrapCAD+KOBRA combined simulation work will appear in emittance figures. In KOBRA each phase space diagram is a projection of the 6D phase space volume into the 2D plane of drawing. As mentioned, in KOBRA x is the longitudinal direction, y and z are perpendicular to it. Because the operation mode is CW, we can forget x,x'. All emittances are given at x=0.3 m, y=0.035 m, and z=0.035m (see Figure 8). y and z are exactly on the middle, x is after extraction.

The following projections can be created: real space, emittance (hor and ver), mixed phase space (hor and ver), and the angle or momentum space. We are using the emittance definition as described in Eq. 1. This definition of emittances is equivalent to the hardware of the Allison scanner. However, this Cartesian interpretation is not suitable for an ECRIS, one should use a pepper pot method instead. In KOBRA we can approximate pepper pot emittances by inserting a slit (hor or ver) just at the

ISBN 978-3-95450-158-8

position x=0.3 m. With that we can differentiate y,y' for different z.

In figures 9-13 different emittance drawings show the beam quality at the z=0.3 m axial position. Ar^{+}, Ar^{3+}, Ar^{5+} and proton particles were calculated and are shown, the color indicates the charge state. Beam current was not included. It is clearly visible, that the typical structure of an ECRIS beam is visible already without space charge effects.

It should be mentioned, that the emittance with the above given definition for each charge state is much larger than the emittance given by the pepper pot definition. If the emittance diagnosis is limited to slices between n*dy and (n+1)*dy it can be seen, that it consists of a serious of emittance figures with much smaller size. However, the single emittance slices do not overlap totally, and the superposition of all slices is the reason for the relatively large emittance. This is shown in Fig. 13.

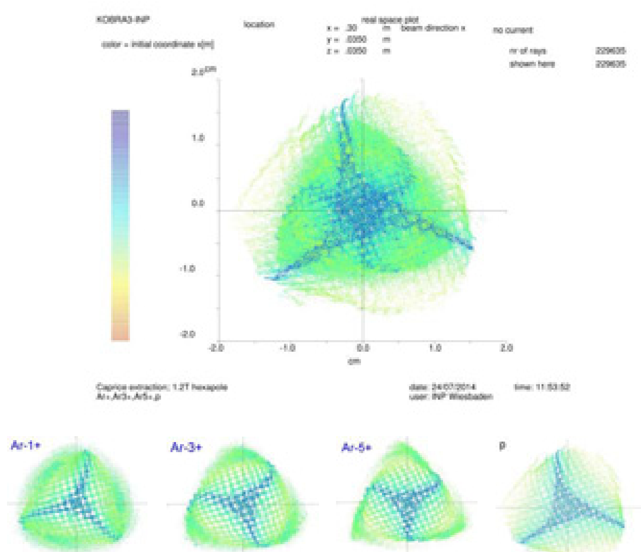

Figure 9: Real space (y-z) emittance plots. Up: all charge states. Down: individual charge states.

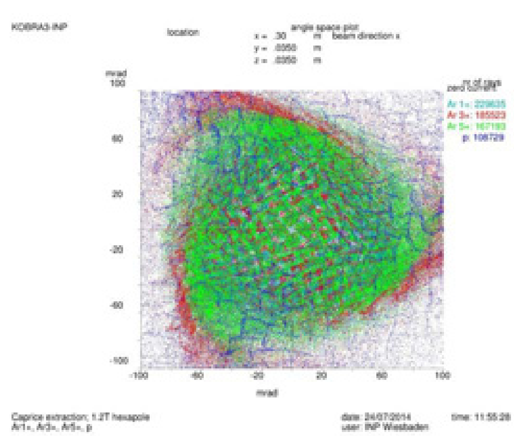

Figure 10: Momentum space (y’-z’) plot.

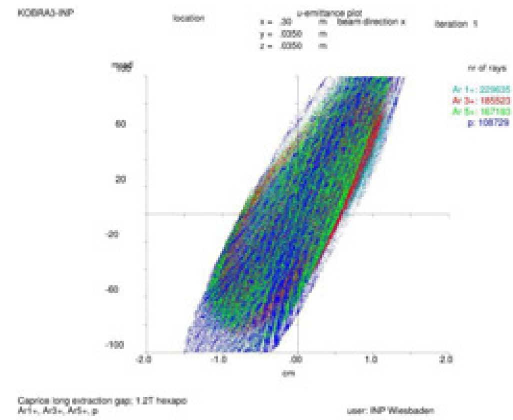

Figure 11: One of the transverse emittances, y-y’. The structure of the beam is clearly visible.

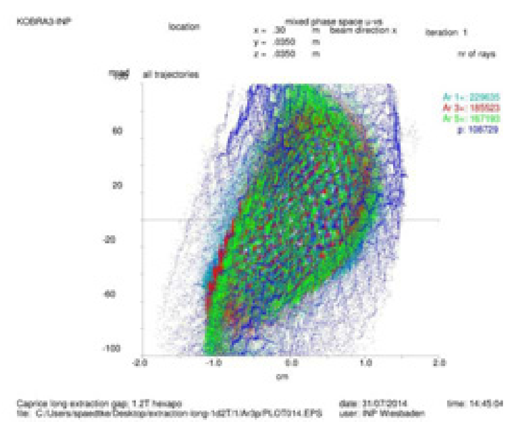

Figure 12: Mixed phase space y-z’. The structure of the beam is clearly visible.

It should be mentioned, that the emittance with the above given definition for each charge state is much larger than the emittance given by the pepper pot definition. If the emittance diagnosis is limited to slices between n*dy and (n+1)*dy it can be seen, that it consists of a serious of emittance figures with much smaller size. However, the single emittance slices do not overlap totally, and the superposition of all slices is the reason for the relatively large emittance. This is shown in Fig. 13, where different parts of the ion beam produce different emittances.

ISBN 978-3-95450-158-8

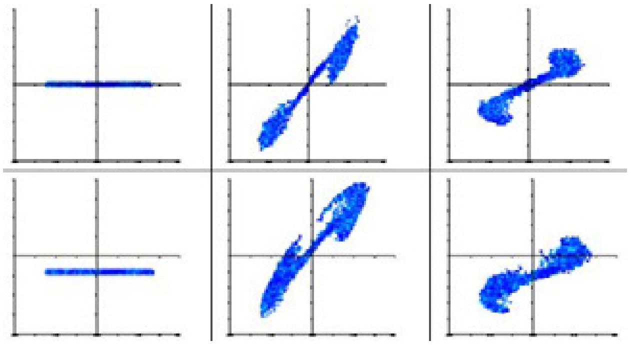

Figure 13: Left real profile (y-z), middle horizontal emittance (y-y'), right: horizontal mixed phase space (y-z'). First row: a slit selects ions only close to the vertical center, second row a slit selects ions from a negative vertical location.

VISUALISATION IN 4 DIMENSIONS

It is possible to extract so-called iso-surfaces from three-dimensional (3D) image data (see [9] and refs. therein). The surfaces usually consist of sets of triangles, which water-tightly enclose regions of the discretized 3D data under consideration. The 3D image data are made up by so-called voxels (i.e., volume pixels). In four dimensions (4D), 4D image data are decomposed into tesseracts (or 4-cubes), and the analogous manifolds of co-dimension 1 are called hyper-surfaces. The STEVE algorithm [10] extracts hyper-hole free iso-hyper-surfaces, which consist of continuous sets of tetrahedrons that are embedded into 4D. Eventually, the hyper-surfaces themselves may be intersected with a 3D subspace, which allows for the rendering of a 3D surface with respect to an initially given iso-value and an associated intersection. The latter is in analogy to intersecting a 3D triangular iso-surface with a single plane, which then yields a curve in the two-dimensional intersecting space. Hence, one can probe the shape dependence of extracted iso-hyper-surface while visualizing (in general volume-enclosing) surfaces that correspond to various intersecting spaces. Such scans provide information about the dimensionality of the object, which is embedded into the 4D image data set and which has been enclosed by the iso-hyper-surface.

Kobra3-INP generates m arrays with rank three. Each array contains the particles having a transverse coordinate between m*dy and (m+1)*dy. Each element of the 3D array having a coordinate between n*dz and (n+1)*dz, an angle between o*dy' and (o+1)*dy', and the other transverse angle between p*dz' and (p+1)*dz'. m, n, o, p are integers. We have chosen m=n=o=p=50. Here, the iso-hyper-surface represents the "machine ellipse" of this transversal 4D phase space, which encloses all generated particles.

One can see clearly in figure 14 that the iso-hyper-surface under consideration (not directly visible here) has true four-dimensional shape features. First, the shapes in each 3D subspace are not flat, but each one of them encloses a 3D volume, and second, the shapes depend on the intersecting cube within the tesseract (i.e., the initial 4D data set).

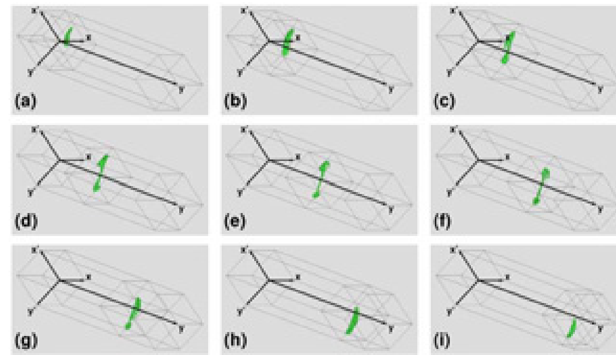

Figure 14: Intersection of the invisible iso-hyper-surface for nine different 3D subspaces (additional, interior cubes within the tesseracts). From left to right then down.

CONCLUSION

Our work showed that to do a realistic ion extraction simulation it is necessary and possible to start the ions from inside the plasma chamber. The starting positions of the ions are developed by positions of the plasma electrons. The first ray-tracing and emittance diagrams are very promising because the known structure of an ECRIS beam could be reproduced. In the next steps the following tasks are planned to be carried out: introducing space charge, energy filtering of the electrons, concentration to specific charge states, improvement of diagnostic properties in the simulation (pepper pot diagnostic), and further comparison with experiments. The diagnostic tools will produce 4D figures, which need to be presented. However, the parameter space to be scanned by simulations is multi-dimensional, mainly because of the magnetic field distribution, gas pressure, rf coupling, charge exchange processes and further more.

ACKNOWLEDGEMENTS

The research leading to these results has received funding from the European Union Seventh Framework Program FP7/2007-2013 under Grant Agreement n° 262010 - ENSAR. The EC is not liable for any use that can be made on the information contained herein.

REFERENCES

[1] Kitagawa A., Muramatsu M., Sekiguchi M., Yamada S., Jincho K., Okada T., Yamamoto M., Biri S., Uno K.: Optimization of the radial magnetic field of an 18 GHz electron cyclotron resonance ion source at the Heavy Ion Medical Accelerator in Chiba. Review of Scientific Instruments 71 (2000)2:981-983

[2] P. Spädtke, R. Lang, J. Mäder, F. Maimone, J. Roßbach, K. Tinschert: Ion Beam Extraction from Magnetized Plasma, 20th International Workshop on ECR Ion Source. ECRIS 12. Sydney, Austalia, 25-28 Sept., 2012. http://accelconf.web.cern.ch/ AccelConf/ECRIS2012/papers/weyo03.pdf

ISBN 978-3-95450-158-8

[3] R. Rácz, S. Biri and J. Pálinkás: ECR plasma photographs as a plasma diagnostic. Plasma Sources Sci. and Tech. 20 (2011) 025002(7)
[4] Maimone, F., Tinschert, K., Celona, L., Lang, R., Maeder, J., Rossbach, J., Spaedtke, P., Operation of the CAPRICE electron cyclotron resonance ion source applying frequency tuning and double frequency heating, Review of Scientific Instruments 83(2) (2012) 02A304
[5] http://laacg.lanl.gov/laacg/services/download_sf.phtml
[6] Biri S., Rácz R., Perduk Z., Vajda I., Pálinkás J.: Recent developments and electron density simulations at the Atomki 14.5 GHz ECRIS. 20th International Workshop on ECR Ion Source. ECRIS 12. Sydney, Austalia, 25-28 Sept., 2012. http://accelconf.web.cern.ch/AccelConf/ECRIS2012/papers/wexo02.pdf
[7] S. Biri, R. Rácz and J. Pálinkás: Status and special features of the Atomki ECR ion source. Review of Scientific Instruments 83 (2012) 02A341
[8] KOBRA-INP, Junkernstr. 99, 65205 Wiesbaden, Germany
[9] B. R. Schlei, Volume-Enclosing Surface Extraction, Computers and Graphics, 36(2), 2012, pp. 111-130, DOI: 10.1016/j.cag.2011.12.008.
[10] B. R. Schlei, STEVE – Space-Time-Enclosing Volume Extraction, (2013) arXiv:1302.5683.

ISBN 978-3-95450-158-8

PRODUCTION OF METALLIC STABLE ION BEAMS FOR GANIL AND SPIRAL2*

F. Lemagnen#, C. Barue, C .Canet, M. Dupuis, J.L. Flambard, L. Maunoury, B. Osmond, J. Piot, P. Jardin, R. Frigot, GANIL, Caen, France
C. Peaucelle, IPNL, Villeurbanne, France
P. Sole, T. Thuillier, T. Lamy, LPSC, Grenoble, France
B. Gall, Z. Asfari, H. Faure, M. Filliger, IPHC, Strasbourg, France

Abstract

GANIL has been producing many stable beams for nearly 30 years. Constant progress has been made in terms of intensity, stability and reliability. The intensity for some stable metallic beams now exceeds or approaches the pμA level at an energy up to 95 MeV/u: 1.14 pμA for ^{36}S (65% enriched) at 77 MeV/u, 0.35 pμA for ^{58}Ni (63%) at 74 MeV/u. The presentation highlights recent results obtained with ^{50}Ti using the MIVOC (Metallic Ions from Volatile Compounds) methods on the ECR4 ion source. The Titanium beam was produced using the organo-metallic compound Titanocene : Cp*TiMe3. The synthesis of this metallocene compound has been successfully performed by the IPHC-Strasbourg from isotopically enriched ^{50}Ti metal. Two tests have been done with the natural Titanocene (^{48}Ti) to validate the new compound, and to qualify the intensity and beam stability. The good results obtained led us to program the Physics experiment in 2013, September and we have produced a very stable $^{50}Ti^{10+}$ beam at an intensity of 20μA for 300 hours. The Spiral 2 facility, currently of installation, will provide gaseous and metallic stable ion beams. The ion source choice for the commissioning of the stable beams Q/A=1/3 is the ECRIS PHOENIX V2. This ECRIS has been designed by LPSC Grenoble and several tests of stable metallic beams have been realized in this laboratory. The results for Nickel ($^{58}Ni^{19+}$) and calcium ($^{40}Ca^{16+}$) are given.

PRODUCTION OF NEW METALLIC BEAM FOR GANIL: ^{50}TI

Introduction

The study of a Titanium beam production started in 2011 with the ion source ECR4 by using the MIVOC method (Metal Ions from VOlatile Compounds).This method was originally introduced at the University of Jyväskylä in Finland [1, 2, 3] and is routinely used at GANIL for the production of Ni and Fe beams, either using natural or isotopically enriched samples.

Thanks to the synthesis of the MIVOC compound Titanocene by B.GALL's team (IPHC-Strasbourg), an isotopicaly enriched $^{50}Ti^{10+}$ beam was successfully delivered for physics experiment (E656-J.PIOT) in October 2013, during 15 days.

Titanocene

The MIVOC method is based on the of the ECR ion source plasma feed by a controlled flow of organo-metallic compound. Such molecules are produced out of enriched material of desired element through dedicated chemistry. Nevertheless, only organo-metallic compounds with high enough vapour pressure can be used for MIVOC beams. It is for example the case for Fe, Ni and Mg where MIVOC method is widely used. Special care has to be taken to handle some of these compounds which are toxic.

With a melting point at 1660 °C for its metal form, titanium is typically a candidate to MIVOC method. Several years of developments were required to fully overcome the problematic of production and handling of this element. Several compounds were synthesized at IPHC Strasbourg and tested at University of Jyväskylä to successfully produce a MIVOC beam of titanium. Finally, first isotopicaly enriched MIVOC beam of titanium was obtained and accelerated in fall 2011 by the K = 130 MeV cyclotron of the University of Jyväskylä. The Compound was produced with a quite high efficiency by a two-step chemistry starting with $TiCl_4$ 92.57 % enriched ^{50}Ti element, then going to $C_5(CH_3)_5Ti(CH_3)_3$ via $C_5(CH_3)_5TiCl_3$. A beam intensity of 19.4 eμA was extracted for titanium-50 at 11^+ charge state from the JYFL 14 GHz ECR2 ion source. This very stable beam – either on short and long time scale - was used for a three week experiment dedicated to the first prompt spectroscopy of a super-heavy element: ^{256}Rf (Z=104) [4].

Following this success, this compound was tested in GANIL Caen in collaboration with IPHC Strasbourg.

Transfer of the Synthesis in the MIVOC Chamber

Like the majority of organo-metallic compounds, the Titanocene is very air and moisture sensitive. The transfer of the synthesis in the MIVOC chamber is thus done under inert atmosphere (Argon). We used a portable glove bag (see Fig.1) for the sample manipulation. A special infra-red light has been used.

*Work partially funded by EU Grant Agreement 283745
lemagnen@ganil.fr

ISBN 978-3-95450-158-8

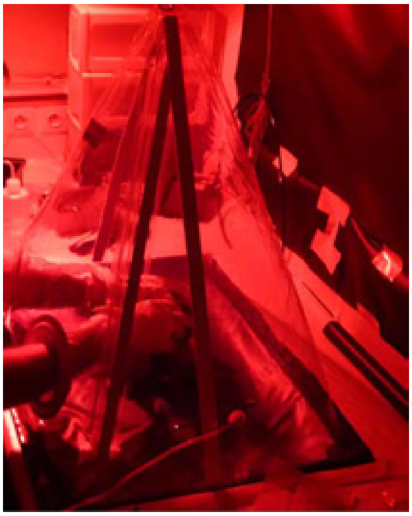

Figure 1: a portable glow bag for the sample manipulation.

Analysis of the Synthesized Compound with the Gas Mass Analyzer

The purity is essential for the beam production with the MIVOC method. The measurement of the partial pressures with a gas mass analyzer allows us to evaluate the relative abundance of the impurities and their time evolution. It is thus a necessary step to qualify the synthesized samples.

We used a “transpector” gas mass analyzer from LEYBOLD to measure the partial pressures of the MIVOC compounds. The first measurement allows us to qualify the level of impurities without compound (valve closed).Once the compound injected into the analyzer chamber, several analyses are made to measure the partial pressures of the compound (see Fig.2).Usually we qualify the compound by determining the ratio of the highest partial pressure representing the metallocene (“XCp2”, “XCp” or “X”) over the highest partial pressure of the main impurity. The compound is considered operational after some hours of pumping when the ratio is higher than 5. For titanocene, we obtained Ti/H_2O =6.2 after 4 hours of pumping.

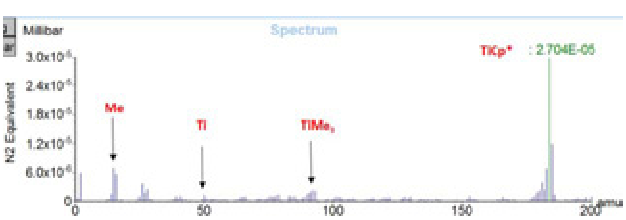

Figure 2: purified TiCp*Me3 spectrum obtained with the gas mass analyzer.

MIVOC Chamber Installed on ECR4 Ion Source

The injection of the compound into the source is controlled by a regulation valve. The fluctuating room temperature can change the flow injected in the ion source through the valve aperture. To get rid of this problem, we have developed a system to control the temperature of the MIVOC chamber. The goal is to regulate the temperature between 20 and 25°C using a Peltier module. We had some problems during the run with a Peltier module: the ambient temperature was around 30°c and the power applied to the Peltier module was too high to obtain a temperature around 20°c (bad optimization of heat sink). To solve this default, a new prototype is being studied with a more powerful Peltier module (100w instead of 50w), a better thermal isolation of the MIVOC chamber and the improvement of the thermal conductivity between the Peltier module and the heat sink.

Production of $^{50}Ti^{10+}$ with ECR4 Ion Source

After two tests (2011-2012) performed with natural material on ECR4 ion source leading to a 25 eµA very stable beam of $^{48}Ti^{10+}$, a beam of $^{50}Ti^{10+}$ was programmed for the physics experiment.

The beam was delivered to the physics experiment for 480 hours. Two samples of Titanocene were used for the run.

The intensity was maintained at the exit of the source between 10 e.µA and 25 e.µA according to the physics requirements, what correspond to 2 and 4.5 e.µA on target at 4.82MeV/u (0.450 p.µA on the target).

<u>Source parameters optimized for $^{50}Ti^{10+}$ =25e.µA:</u>

RF power: 350W, biased tube: floating potential, no gas buffer, extraction: 25 kV / 3.2mA, coils current: 1010A / 1020A, injection pressure: $1{,}3.10^{-6}$mbars, extraction pressure: $3{,}3.10^{-7}$ mbar.

The charge state distribution has been optimized on $^{50}Ti^{9+}$ (see Fig.3).

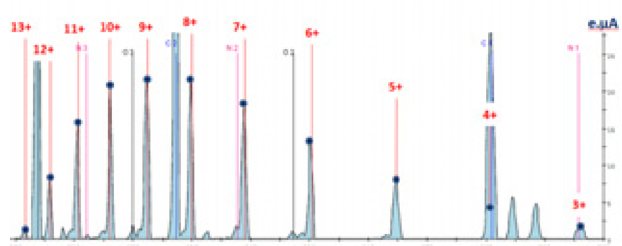

Figure 3: spectrum optimized.

<u>First sample:</u>
Consumption: 2.5 mg/h (0.54mg/h of ^{50}Ti) ~ 190 hours
Intensity: $^{50}Ti^{10+}$=10 to 20 e.µA with fluctuations (failure of PELTIER regulation)

<u>Second sample:</u>
Consumption: 2 mg/h (0.43mg/h of ^{50}Ti) ~ 290 hours
Intensity: $^{50}Ti^{10+}$=15 to 25 e.µA with a very good stability
<u>Total ionization efficiency:</u> 8% (without transport correction)

ISBN 978-3-95450-158-8

Conclusion

The $^{50}Ti^{10+}$ beam was successfully extracted and accelerated with GANIL cyclotron and it was transported on the target of the LISE apparatus for an experiment dedicated to the study of ^{257}Db. The beam stability of the first sample was perturbated by a Peltier module dysfunction but, thanks to the change of Peltier module, the beam stability was better with the second sample. In 2015 a new experiment will be programmed. We will use a new Mivoc chamber with a better control of temperature.

PRODUCTION OF METALLIC BEAMS FOR SPIRAL2

Introduction

The PHOENIX V2 ion source will be used for the Spiral2 linear accelerator commissioning. This source has been designed and built up by LPSC Grenoble and will provide a beam of Q/A=1/3 ions at 60*Q kev of maximum energy. Metal ion beam production (Nickel and Calcium) has been studied for 2 years with the PHOENIX V2 source installed on the SPIRAL2 low energy beam line [5] at LPSC Grenoble.

Production of $^{58}Ni^{19+}$Natural nickel sample (^{58}Ni:68%) and the Large Capacity Oven (LCO) [6] have been used for the tests. Helium buffer gas has been chosen for the first test. Stability and reproducibility have been observed and we obtained, after optimisation, a $^{58}Ni^{19+}$ intensity of 5e.µA. The charge state distribution was peaked on the $^{58}Ni^{15+}$ (22e.µA). In order to increase this intensity, we switched the buffer gas to oxygen. The $^{58}Ni^{19+}$ intensity has been multiplied by 4 and the charge state distribution peaked on the $^{58}Ni^{17+}$ (see Fig.4) [6]. However, we noted an important Getter effect leading to the decrease of the number of oxygen ions in the plasma. This chemical effect can affect the stability after a long time of run. A careful match of the oxygen flux with the oven evaporation rate was necessary to keep the ion beam stable. The consumption of 0.4mg/h has been measured (0.25mg/h for ^{58}Ni) corresponding to a total ionization efficiency of 6% (without beam transport correction).

Source parameters optimized for $^{58}Ni^{19+}$=20e.µA:

RF power: 1.7 kW, oven position: 0 mm, oven electrical power: 71 W (oven temperature 1450°C off line), biased disk:-36 V / 0.5 mA, extraction: 40 kV / 4.7 mA, coils current: 1130 A / 1180 A / 1290 A, extraction: 1.4 10^{-8} mbar.

Production of $^{40}Ca^{16+}$

The optimization of $^{40}Ca^{16+}$ beam was studied to check the possibility to produce $^{48}Ca^{16+}$. Natural calcium sample (^{40}Ca:97%) was evaporated by the LCO and tests were performed with several gas buffer. As a first test, we used Helium as buffer gas, since it is the one used at GANIL to produce $^{40}Ca^{9+}$. The beam stability was correct but the charge state distribution was peaked on the $^{40}Ca^{11+}$ (35e.µA). No significant $^{40}Ca^{16+}$ beam could be produced with the Helium buffer gas, so we decided to replace it by Oxygen.

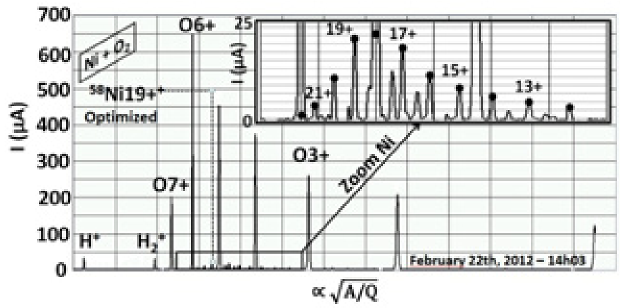

Figure 4: best spectrum optimized.

This time, it was impossible to obtain good beam stability because of strong getter effect. Injecting the buffer gas in the same injection tube as the LCO can increase the chemical effect.

The last test was carried out with nitrogen buffer gas. We observed a good beam stability for several hours and the charge state distribution was better than with helium buffer gas, with a spectrum peaked on the $^{40}Ca^{13+}$ (fig.5) [7]. We obtained a $^{40}Ca^{16+}$ beam stable with an intensity of 16e.µA. On should note that the tuning was limited by the RF induced oven heating: the RF power could not be set above 800W, which is not the optimum for high charge state production, expected above the kW level. A consumption of 1mg/h was measured corresponding to a total ionization efficiency of 4% (without beam transport correction).

Source parameters optimized for $^{40}Ca^{16+}$=16e.µA:

RF power: 800W, oven position: -15 mm, oven electrical power: 0.4 W (oven temperature 50°C off line), biased disk: -9 V / 0.1 mA, extraction: 30 kV / 1.2 mA, coils current: 1170 A / 805 A / 1250 A, extraction: 1.1 10^{-7} mbar.

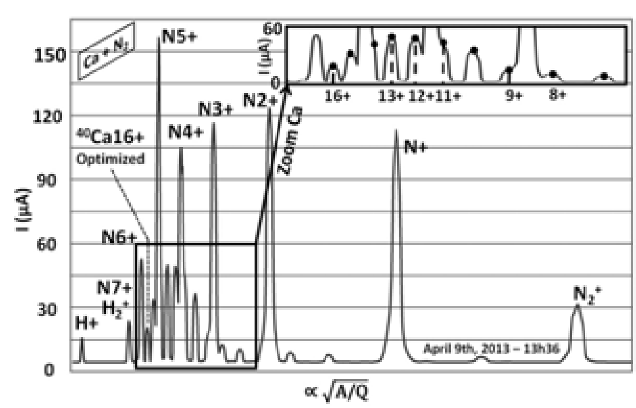

Figure 5: Optimized $^{40}Ca^{16+}$ (16 µA) spectrum.

ISBN 978-3-95450-158-8

Conclusion

Hopeful results were obtained in term of beam stability and intensity for the $^{58}Ni^{19+}$. However these results will have to be confirmed during the commissioning of Spiral2. Concerning the production of $^{40}Ca^{16+}$, it's difficult to optimize the parameters in order to obtain reliable beams. Indeed the Getter effect and the evaporation control of sample due to the RF power were the main difficulties. To increase the performances, a new design of phoenixV2 injection has been studied with a pumping system. The main evolutions are to improve the vacuum level in the injection area and to separate the buffer gas injection from the oven injection. Another possible evolution would be to use a dedicated low temperature oven requiring tens of W heating power to sustain the calcium evaporation rendering any RF induced heating negligible.

REFERENCE

[1] J. Ärje, H. Koivisto and M. Nurmia. « Operation of the JYFL-ECR ion source», Proceedings of the 11th International Workshop on ECR Ion Sources, KVI-Groningen, 1993.

[2] H. Koivisto, J. Ärje and M. Nurmia. « Metal ion beams from an ECR ion source using volatile compounds", Nuclear Instruments and Methods in Physics Research-Section B: Beam Interactions with Material and Atoms, 94, 291-296, 1994.

[3] H. Koivisto, J. Ärje and M. Nurmia. « Metal ions from the volatile compounds-method for the production of metal ions beams", Review of Scientific Instruments, 69, 785-787, 1998.

[4] Greenlees P.T., J. Rubert, J. Piot, B. J. P. Gall, et al., Phys. Rev. Lett. 109 (2012)

[5] C. Peaucelle, J.L. Barriotte, P. Grandemange, T. Lamy, T. Thuillier, and D.Uriot, Proceeding of the 19th International workshop on ECR Ion Sources, Grenoble, 2010; see http://www.jacow.org/

[6] P. Lehérissier, F. Lemagnen, C. Canet, C. Barué, M. Dupuis, J.L. Flambard, M. Dubois, G. Gaubert, P. Jardin, N. Lecesne, R. Leroy, and J.Y. Pacquet, Rev. Sci. Instrum. 77, 03A318 (2006).

[7] C. Barué, C. Canet, M. Dupuis, J.L. Flambard, R. Frigot, P. Jardin, T. Lamy, F. Lemagnen, L. Maunoury, B. Osmond, C. Peaucelle, P. Sole, and T. Thuillier, Rev. Sci. Instrum. 85, 02A946 (2014).

ISBN 978-3-95450-158-8

STATUS REPORT AT THE HEIDELBERG ION-BEAM THERAPY (HIT) ION SOURCES AND THE TESTBENCH

T. Winkelmann, R. Cee, T. Haberer, B. Naas, A. Peters, J. Schreiner,
Heidelberger Ionenstrahl-Therapie Centrum (HIT), D-69120 Heidelberg, Germany
Erik Ritter, DREEBIT GmbH, Großröhrsdorf, Germany

Abstract

Since October 2009 more than 2000 patients were treated at HIT. In a 24/7 operation scheme two 14.5 GHz electron cyclotron resonance ion sources are routinely used to produce protons and carbon ions for more than 8000 hours per year. The integration of a third ion source into the production facility was done in summer 2013 to produce a helium beam. This paper will give a status report of the ion source operating experience and statistics and will summarize the enhancement activities, which were undertaken at an in-house ion source testbench.

INTRODUCTION

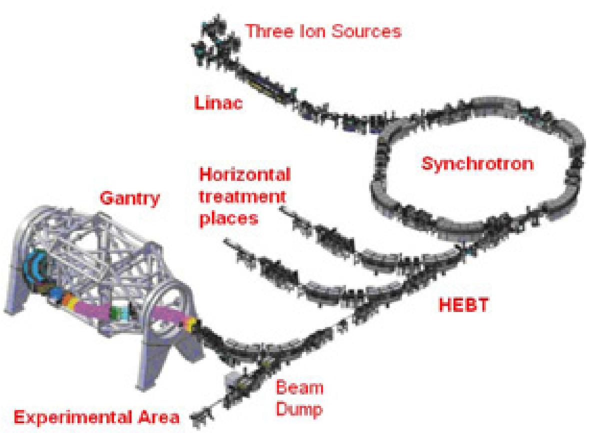

Figure 1: Overview of the HIT facility.

The beam production at HIT consists of two ECR Supernanogan ion sources [1] for the routine operation of proton and carbon beams at 8 keV/u; a third Supernanogan ion source is integrated (see ECR3 in Figure 2) for ion species like helium and oxygen for experiments at the experimental area (see Figure 1) and for the therapy in the future.

The compact 217 MHz linear accelerator (LINAC) consists of a radio frequency quadrupole accelerator (RFQ) and an IH-type drift tube linac (IH-DTL) with the end energy of 7 MeV/u for all ions; a foil stripper directly located behind these cavities produces fully stripped ions (see Figure 2).

A synchrotron of 65 m circumference accelerates protons, helium, carbon and oxygen to predefined end energies e.g. for carbon ions from 89 to 430 MeV/u in 255 steps.

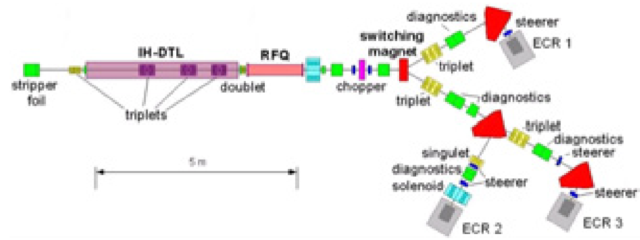

Figure 2: Low energy beam line (LEBT) and the linear accelerator (LINAC).

OPERATION EXPERIENCE

During the last years of operation mainly carbon ions were used by 58 %, followed by hydrogen (39 %), helium (2 %) and oxygen (1 %). The continuous operation runtime of the two sources are about 340 to 360 days per year in a 24h-operation! The operation-statistics since 2008 of the accelerator is shown in Figure 3. The sources in 2013 are in operation for 358 days per year, 7 days for planed maintenance shifts and 4 hours in 2013 are the "off time". The "off time" between 2008 and 2010 is caused by multiple RF amplifiers breakdowns [2].

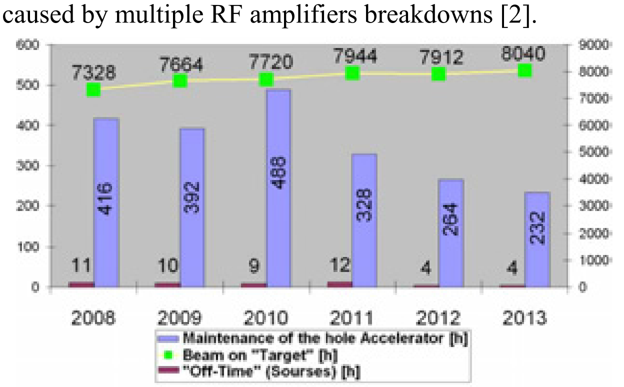

Figure 3: operation-statistic of HIT (2008- 2013).

The peak of the ion source "Off-Time" in 2011 is caused by numerous failures of the extraction system. The pollution of the extraction ceramic led to sparks in that region and generated an isolator ceramic replacement about every 3 weeks. This unfavorable situation could be remedied by the new construction and installation of the extraction system in winter 2011 at the therapy sources.

Since this time we do not have any insulator ceramic contaminations and no "hardware" problems with the sources. These replacements ensure an off time of just 4 hours per year (2012 and 2013). These 4 hours per year of "not usable" and instable therapy beam are used e.g. to find new and stable setting parameters, can be bridged by

ISBN 978-3-95450-158-8

the usage of the second source for the therapy. Additional to this advantageous situation, we finalized in summer 2013 the integration of a third identical ECR ion source in the LEBT to disposal and respond quickly to possible ion source failures. The third source is also used for the production of helium and oxygen ions for experiments at the experimental area (see Figure 1).

All these measures led to smooth operation without ion source induced therapy down time since October 2009.

TESTBENCH

The activities described in this paper on the in-house ion source testbench can be divided into two fractions:

- Investigation of new designed plasma electrode for the therapy used ECR ion source type
- Investigations of the transmission through the RFQ with an EBIS ion source.

Plasma Electrode

The design with a tube is substantially different from the standard plasma electrode, where the electrode thickness is minimal close to the axis. Figure 4 shows the schematic construction and the axial magnetic field of the ECR ion source.

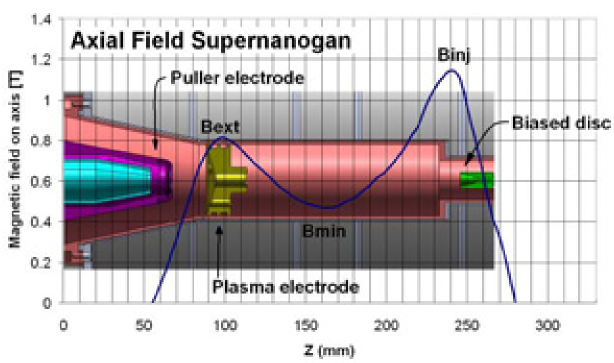

Figure 4: Axial magnetic field of the ECR ion source.

For an improvement of the vacuum in the region between the plasma electrode and extraction puller three additional holes were drilled in the "new" plasma electrode (see Figure 5, left). This creates the opportunity to reduce the distance between plasma electrode and puller electrode, without sparking, originally from 4 cm to 2 cm, leading to an improvement of the beam quality.

Figure 5: Used plasma electrode (left) and ion deposition in the tube after a year's operation in the ECR ion source for C^{4+} (right).

Figure 6 shows a comparison of the different extraction holes (3 and 7 mm) in a "standard" plasma electrode and the new 6 mm extraction "tube" hole with respect to the transmission between the first and the second Faraday cup at the test bench for H_3^+ and C^{4+} beams. The structure of the test bench is comparable to Figure 9, except for the source, for this measurement the EBIS was replaced by the ECR. With the requirement to the active redundancy of the mechanical source set up for all sources, this new design allows up to 220 eμA C^{4+} for carbon operation and up to 1.3 emA H_3^+ for the therapy with protons.

The measurement of the beam profile behind the dipole (Figure 7) shows a smaller beam profile with the new plasma lens at the same ion source settings.

This tube facing the plasma serves as an aperture for magnetic field lines. These field lines are not going through the extraction aperture and shields therefore ions coming from a loss line. Figure 5 (on the right side) shows the deposition of ions [3], in the tube, they are not entering the extraction aperture.

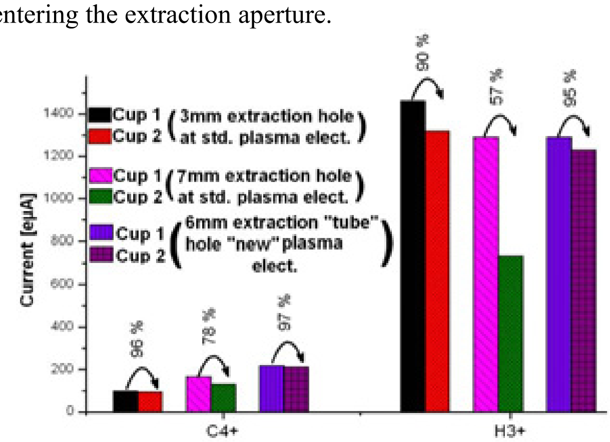

Figure 6: Transmission measurements at the test bench with different plasma electrodes (3 and 7 mm standard and 6 mm new designed electrode).

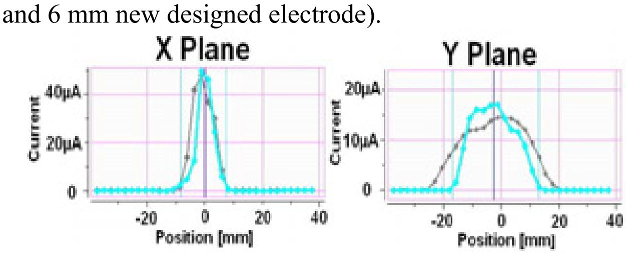

Figure 7: C^{4+} beam profile behind the dipole with different plasma electrodes (7 mm standard (gray) and 6 mm new designed electrode (cyan)).

Investigations of the RFQ Transmission

The objective of the work at the testbench was also determined in recent times by the further investigation of the non-optimal transmission through the RFQ [5]. To the often mentioned beam quality of the ECR source as a cause for the suboptimal transmission through the RFQ, we integrate, together with DREEBIT GmbH [4], a superconducting electron beam ion source (EBIS-SC) into the ion source testbench [6].The EBIS-SC was set on a high voltage platform providing up to 20 kV positive potential additional to the potential of the drift tubes,

ISBN 978-3-95450-158-8

which defines the energy of the extracted ions. The extraction energy of the ions without the platform potential is about 6.9 keV. To reach the injection energy of 8 keV/u for the RFQ the HV-platform was set on 17100 V. The full setup of the testbench with the EBIS ion source is shown in Figure 9. The beam transmission (through the RFQ) of the generated EBIS pulsed beam of 19,8 eμA peak in a 20 μs pulse, $12C^{4+}$ at 8 keV/u showed that the improvement of the beam emittance by a factor 9, in comparison to the beam from the ECR [7], has just minor influences of 10% improvement for the transmission through the RFQ (Figure 8).

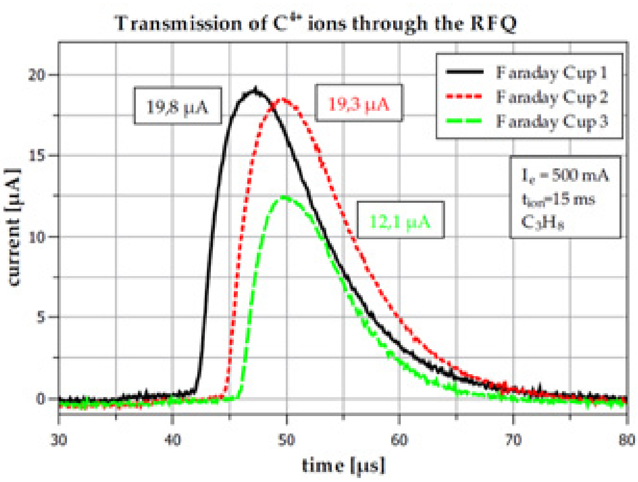

Figure 8: Transmission of a C^{4+} ion pulse from Faraday Cup 1 (black solid line) to Faraday Cup 2 (red dotted line) passing the RFQ to Faraday Cup 3 (green dashed line).

By this low beam quality influence of the transmission through the RFQ it is understandable why we do not see a transmission improvement with the reached emittance (4 x rms) enhancements at the ECR beam [7].

The measurement result implies that a desired time reduction for patient irradiation, by more injected synchrotron beam current, can be achieved only by improving the RFQ structure.

ACKNOWLEDGMENT

We would like to thank Siemens AG for the support of this work by providing beam diagnostic and beam optical equipment for the HIT testbench. We also want to thank G. Zschornack and E. Ritter for the very good cooperation and motivated work at the ion source testbench.

REFERENCES

[1] http://www.pantechnik.com/
[2] T. Winkelmann, et al., “ Experience At The Ion Beam Therapy Center (HIT) With 2 Years Of Continuous ECR Ion Source Operation“, ECRIS08, Chicago, IL USA.MOPO-10
[3] L. Panitzsch et al., “Current density distributions and sputter marks in electron cyclotron resonance ion sources”, Rev. Sci. Instrum. **84** (2013) 013303.
[4] http://www.dreebit.com
[5] S. Yaramyshev et al., „Upgrade of the HIT Injector Linac-Frontend“, HIAT 2009, Venice, Italy, TH-09
[6] E. Ritter, et al., “Implementation of a Superconducting Electron Beam Ion Source into the HIT Ion Source Test Bench” IPAC 2014, Dresden, Germany, WEPRO083
[7] T. Winkelmann, et al.," Integration of a Third Ion Source for Heavy Ion Radiotherapy at HIT", ECRIS, Sydney, Australia(2012); TUPP03.

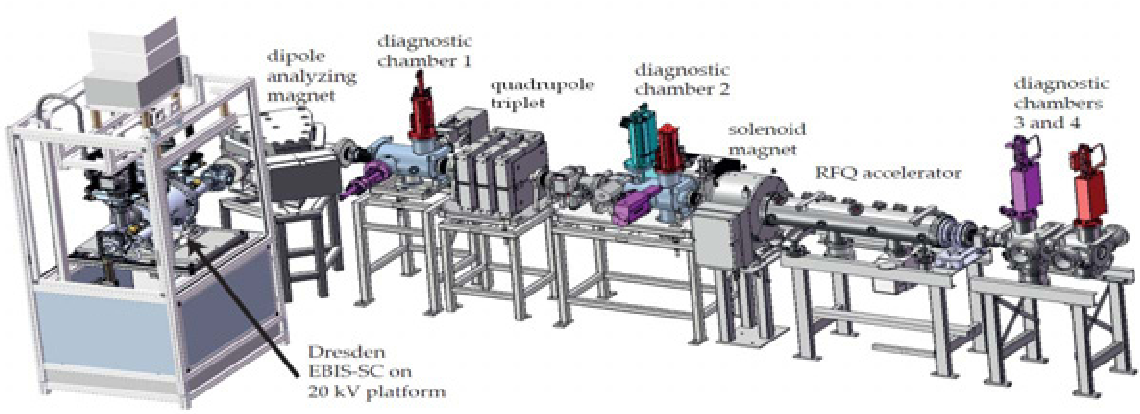

Figure 9: 3D CAD model of the testbench with the EBIS ion source (from left: EBIS-SC with 20 kV-platform, dipole analyzing magnet, diagnostic chamber one with profile grid 1, analyzing slits and Faraday cup 1, quadrupole triplet, diagnostic chamber two with pepper pot, profile grid 2 and Faraday cup 2, solenoid magnet, RFQ accelerator, diagnostic chamber three and four with a set of 3 phase probes, profile grid 3 and Faraday cup 3). The Faraday cups are colored in red, the grids profile monitors are colored in purple and the pepper pot is colored in cyan.

ISBN 978-3-95450-158-8

DIRECT INJECTION OF INTENSE HEAVY ION BEAMS FROM A HIGH FIELD ECR ION SOURCE INTO AN RFQ

G. Rodrigues, Inter University Accelerator Centre, Aruna Asaf Ali Marg, New Delhi, India
R. Becker, Institut fur Angewandte Physik der Universitaet, D-60054 Frankfurt/M, Germany
R.W. Hamm, R&M Technical Enterprises, Inc. 4725 Arlene Pl., Pleasanton, CA 94566, USA
D. Kanjilal, Inter University Accelerator Centre, Aruna Asaf Ali Marg, New Delhi, India

Abstract

Beam intensities achievable from high performance ECR sources for highly charged ions are limited by the high space charge. For high performance ECR sources, the stray magnetic field of the source can provide focusing against the space charge blow-up of the beam when used with the Direct Plasma Injection Scheme (DPIS) developed for laser ion sources. A combined extraction/matching system has been designed for direct injection into a radio frequency quadrupole (RFQ) accelerator, allowing a total beam current of 12 mA for the production of highly charged $^{238}U^{40+}$(0.49 mA) to be injected at an ion source voltage of 60 kV. In this design, the features of IGUN have been used to take into account the rf-focusing of an RFQ channel (without modulation), the electrostatic field between ion source extraction and the RFQ vanes, the magnetic stray field of the ECR superconducting solenoid, and the defocusing space charge of the ion beam. The RFQ has been designed to suppress most of the charge states extracted from the ECR, acting as a filter for the desired $^{238}U^{40+}$. This reduces the transport problem for the beam line as well as reduces the emittance for the transmitted charge states.

INTRODUCTION

High performance superconducting electron cyclotron resonance (ECR) ion sources such as the 28 GHz VENUS [1], the 24 GHz SECRAL [2] and the 28 GHz source at RIKEN [3] operate at higher frequencies than older sources and hence have higher plasma densities and magnetic fields. A new design study of a 56 GHz source by the ECR ion source group at Berkeley shows that the source can have even higher plasma densities, since the density scales as the square root of the operating frequency [4]. A new type of ECR source has been proposed recently by D. Z. Xie [5] for operation at 50 GHz. Considering the frequency scaling from 28 GHz to 56 GHz and without an increased volume of the plasma chamber, the heavy ion beam of U^{40+} produced earlier by the VENUS source [1] at an intensity of 12 μA can be extracted with an intensity of possibly as much as 0.49 mA at the higher 56 GHz operating frequency. The extraction of these intense highly charged heavy ion beams poses several problems. Generally, accel-decel extraction systems coupled to ECR ion sources have shown inherent problems extracting intense beams of highly charged ions due to sparking at the high voltages required and the poor vacuum conditions, which also limits the extraction of intense beams of highly charged ions. Hence, this type of extraction system generally fails due to problems with the high voltage power supplies. This eventually keeps the ion source from functioning smoothly and increases the downtime of the accelerator. In the applications of laser ion sources, with their much higher plasma densities, severe problems of handling intense beams due to sparking and/or beam loading are avoided by using an ingenious technique, the so-called Direct Plasma Injection scheme (DPI) [6]. This technique was utilized for transporting intense beams directly into a radio frequency quadrupole (RFQ) accelerator using the combined focusing of the gap between the ion source and the RFQ vanes (or rods) and the focusing of the rf fields from the RFQ penetrating into this gap. In this scheme, the plasma expands to the entrance of the RFQ, where the electrons are deflected by the fringe field of the RFQ and only the ions get trapped by the RFQ focusing field. Hence, space charge effects are completely controlled, with the great advantage being the ability to transport very intense beams. This technique was experimentally demonstrated for the acceleration of carbon (C^{3+}, C^{4+}, C^{5+}) and aluminum (Al^{9+}) ions with beam intensities greater than 60 mA [7].

In the case of new ECR ion sources, the development of higher operating frequencies in superconducting ECR ion sources will result in higher plasma densities. Therefore, much higher beam intensities will not only be possible by using extraction voltages higher than the 30 kV in use today in most ECR sources, but also by changing the extraction electrode aspect ratio. Operating at these higher extraction voltages will however result in operating the accel-decel systems at relatively higher voltages, increasing the probability of sparking. In order to circumvent this problem in conventional ECR ion source extraction systems, a proposed solution is to couple an RFQ directly to a high performance ECR ion source using the laser ion source DPI scheme. For high performance ECR sources that use superconducting solenoids, the stray magnetic field of the source can be used in the DPI scheme to provide more focusing to overcome the space charge blow-up of the beam [8]. In the present study, the RFQ has been designed to suppress most of the charge states extracted from the ECR, acting as a filter for the desired $^{238}U^{40+}$. This reduces the transport problem for the beam line as well as reduces the emittance for the transmitted charge states.

*gerosro@gmail.com

ISBN 978-3-95450-158-8

COMBINED EXTRACTION/MATCHING SYSTEM

Since the RFQ is very efficient for acceleration in the energy range from 1 keV/u to 1 MeV/u, but space charge effects are dominant at the low energies (10 to 30 kV) and relatively higher beam intensities used for injecting beam into them, our proposal is to energize the ECR ion source to 60 kV to overcome the defocusing forces in the extracted beam due to the beam's space charge. At this extraction voltage a $V^{3/2}$ enhancement factor of 2.8 in the beam intensity is expected as compared to extraction at 30 kV. Since most existing superconducting ECR ion sources operate at ~30 kV with accel-decel extraction systems, the gain in the beam intensities is expected to be even higher at 60 kV using an improved extraction system design.

In the RFQ, the beam Twiss parameters depend on time (or radio frequency phase), but the injected beam from the ion source has constant Twiss parameters that do not vary with time. Although PARMTEQ is generally used for the design of an RFQ, it cannot be used for designing the proposed DPI matching system because it does not simulate the plasma meniscus and the static accelerating field. The full simulation of this problem requires one to match a time independent beam from the ion source to a time dependent beam inside the RFQ, which poses a serious matching problem. However, the design of such a combined extraction/RFQ matching section can easily be performed using the IGUN code [9]. The unique features of IGUN take into account the electrostatic field between the ion source and the RFQ, the stray magnetic field of the ECR source, the defocusing space charge of the intense beam and the rf focusing in the fringe field between the RFQ vanes and the RFQ flange [10]. It allows the user to simulate the beam from the plasma meniscus of the ECR source to the position in the RFQ where the axial acceleration starts with the modulation of the electrodes. An added advantage is that the Kapchinsky-Vladimirsky equations used in IGUN can handle axisymmetric charge density distributions of the input beam.

DETAILS OF THE DIRECT INJECTION DESIGN

The design being proposed implements the matching of the beam from a high performance 56 GHz superconducting ECR source into the matching section of an RFQ (a section without any modulation). The radial matching section of a normal RFQ is typically 4-6 cells in length and has a varying vane tip radius with a constant vane voltage along its length. For this design, a 6 cell matching section with a constant tip radius was used. No focusing element was used between the ECR source and this matching section. The ECR source extraction axial magnetic field of maximum value ~ 4 T (generated by the superconducting solenoid at the extraction side of the ECR source) is selected at the extraction electrode position for optimum extraction conditions, and it defines the beam size at the start of the simulation. The geometry of the problem as simulated in IGUN is shown in Fig. 1. Due to the large axial magnetic field necessary in the ECR ion source, the magnetic field extends significantly into the matching section of the RFQ. The distance between the plasma electrode and the start of the RFQ matching section was chosen to be 25 mm. The source extraction voltage (60 kV) defines the beam injection energy for all extracted charge states. The basic plasma parameters of the electron temperature and ion temperature were chosen to be 5 eV and 0 eV, respectively. Higher values may be more realistic at these higher frequencies as the electron temperature and ion temperature are expected to increase with frequency. However, for a first approximation, these values seem to be justified.

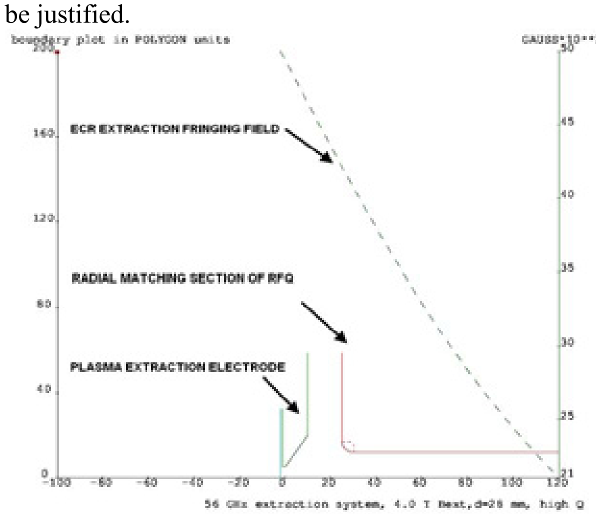

Figure 1: Geometry of the problem simulated with IGUN.

In the first series of simulations for this design, the ECR stray magnetic field was varied from low to high values to determine its effect on the focusing at the entrance of the RFQ matching section. For a matched beam at the entrance of the RFQ-channel, the variation of the axial magnetic field gives the smallest radius for different q/m at different magnetic fields, and the radius and the divergence decrease with increasing magnetic fields. Therefore, there is an optimal magnetic field for each charge state of U. A total beam intensity of 12 mA consisting of 0.49 mA of $^{238}U^{40+}$ ions, other charge states of U ions and ions of the mixing gas were used, with all the beam intensities scaled from Ref. 1. While keeping the beam intensity constant in the simulation (i.e., the ion current is 12 mA), IGUN adjusts the plasma density over a number of iteration/convergence cycles until the loss to the aperture is compensated. The calculated results are shown in Fig. 2. The rf focusing parameter (%) for the RFQ is plotted with the values given on the vertical axes in the middle of the plot, and the stray magnetic field from the ECR source are labelled on the right vertical axes. In Fig. 3, the current densities and RMS emittances of the U^{40+}ions, other U^{+} charge states, and oxygen mixing gas components are shown inside the RFQ matching section (units for 1 micron = 1 mm.mrad).

ISBN 978-3-95450-158-8

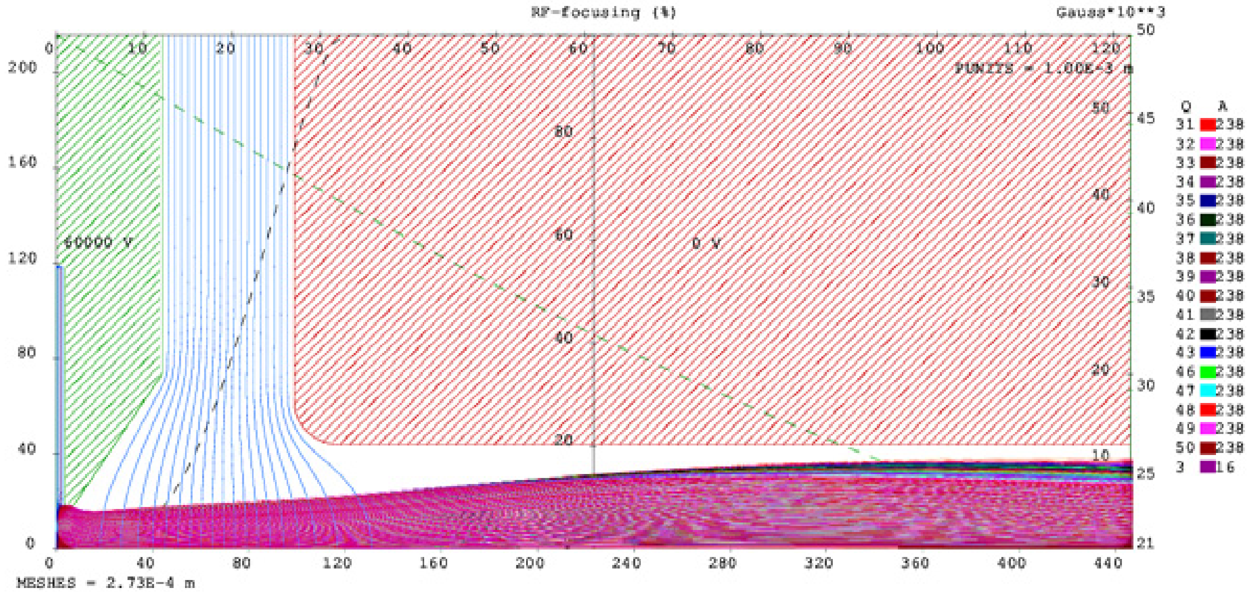

Figure 2: Optimized design for transporting a total current of 12 mA (from 56 GHz ECR source), consisting of U^{40+}, other U^{+} charge states, and oxygen mixing gas ions directly into an RFQ.

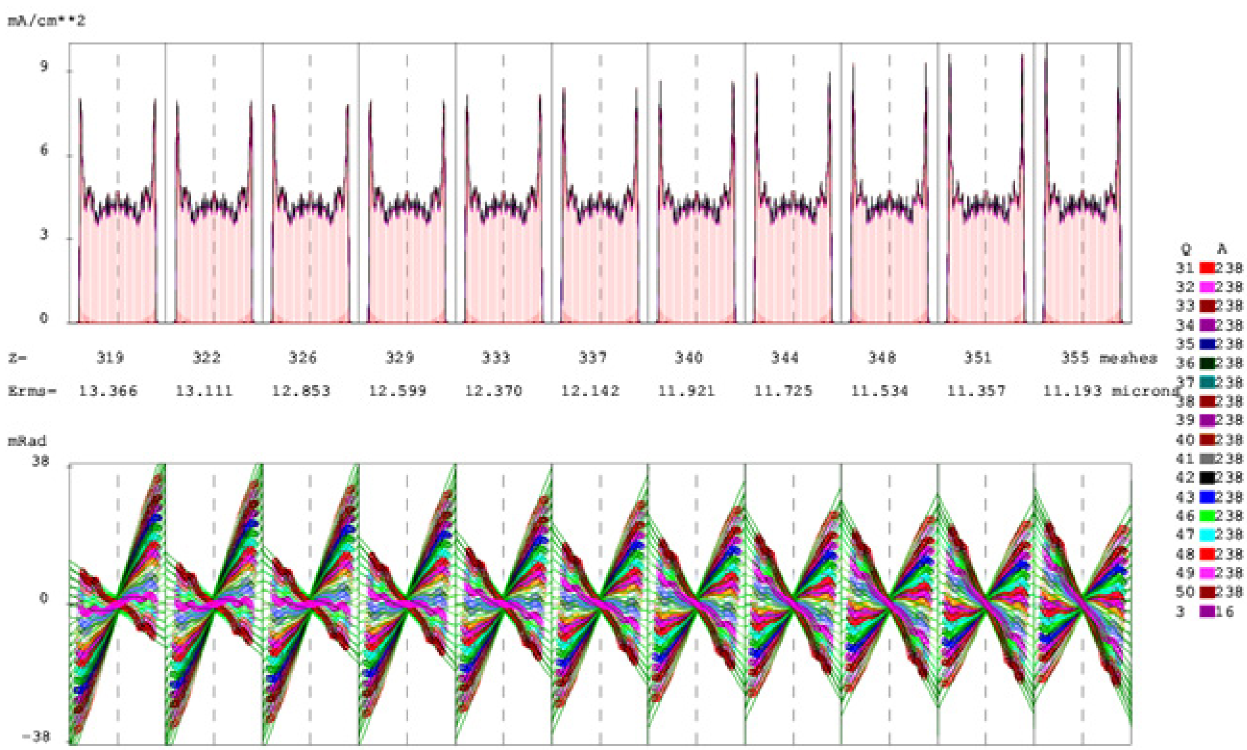

Figure 3: Current densities and RMS emittances of the U^{40+}ions, other U^{+} charge states, and oxygen mixing gas components inside the RFQ matching section.

PERFORMANCE OF THE RFQ DESIGN

The RFQ design being proposed for the 56 GHz superconducting ECR source with its extraction and direct injection uses the constant radius matching section designed above as the first section of the RFQ. The RFQ vanes then have a short modulated section with no acceleration followed by an unmodulated section, and then a gentle bunching section is used to accelerate the beam to the final output energy. The slight bunching caused by the first modulation enhances the loss of the unwanted charge states in the main acceleration, while preserving the emittance of the transmitted charge states.

ISBN 978-3-95450-158-8

A realistic 48.5 MHz RFQ with a total length of 2.98 m and average aperture radius of 12 mm was calculated by PARMTEQ [11] assuming an injection beam energy of 10.084 keV/u for a beam of $^{238}U^{40+}$ (A/q =5.95). The results showed that > 89% transmission could be achieved for this beam and a total beam current of 12 mA can be accelerated to a final energy of 60 keV/u. Shorter RFQ cells are advantageous since the stable phase and accelerating field change very slowly over the length, resulting in the dc beam from the ion source being bunched by the RFQ with minimum emittance growth. Since the characteristic impedance of the structure depends on its type, design parameters and operating frequency, a lower operating frequency of 48.5 MHz and shorter length were chosen to minimize the RF power requirements. This 4-rod RFQ requires an rf power of only 9.2 kW. The concept of a variable energy RFQ can be easily adopted especially in the case of the 4-rod RFQ as compared to the 4-vane RFQ where the electrodes and the driving inductances are practically separable [12].

The performance of the final RFQ is shown in Fig. 4, which shows the scaled charge state distribution from the 56 GHz superconducting ECR source and the calculated final charge state distribution from the RFQ at 60 keV/u. For this calculation, the emittance parameters calculated in IGUN at the end of the fourth cell in the matching section were injected directly into the rest of the RFQ. The RFQ output has a much narrower charge state distribution than the beam extracted from the ECR ion source and does not transmit any of the O^{3+} ions extracted from the ion source carrier gas. The output phase space of the $^{238}U^{40+}$ions in the x and y planes are respectively shown in Fig. 5 and 6. The normalized RMS emittance is only 0.52 microns (mm.mrad) in the X-plane and 0.71 microns in the Y-plane.

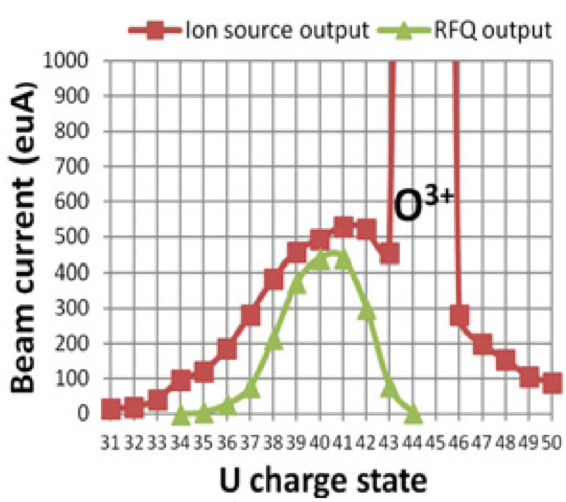

Figure 4: The scaled U^{+} charge states extracted from the 56 GHz ECR and the calculated charge states transmitted through the RFQ.

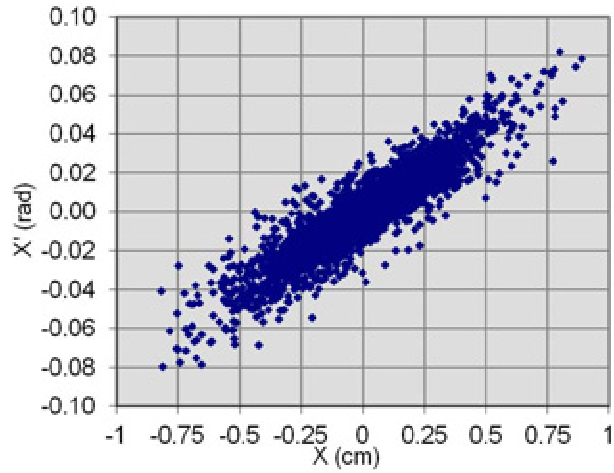

Figure 5: The calculated output phase space in the x plane of the U^{+40} charge state extracted from the 56 GHz ECR and transmitted through the RFQ.

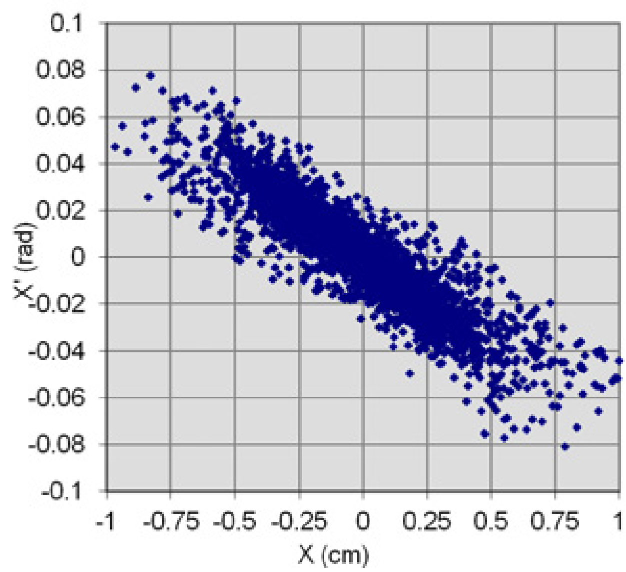

Figure 6: The calculated output phase space in the y plane of the U^{+40} charge state extracted from the 56 GHz ECR and transmitted through the RFQ.

CONCLUSION

It has been shown that a high performance ECR ion source can be coupled to an RFQ to transport intense beams of highly charged heavy ions without the problems of space charge beam blow-up and/or sparking in the extraction region. It was shown that the stray magnetic field of the ECR source is critical for a matched beam. The rf focusing in IGUN shows its versatility and simplicity to directly match the beam from the ECR source to the matching section of the RFQ.

The added advantage is that axisymmetric forms of charge density distributions can be properly matched. It is evident that such an rfq-channel might be very effective and less q/m sensitive for the extraction system of all high

ISBN 978-3-95450-158-8

performing ECR ion sources. This technique has promising applications for injecting and transporting very intense beams into RFQ accelerators for research, ADSS and more efficient, compact neutron generators [13]. The accelerator driven sub-critical system (ADSS) being developed at various laboratories around the world to create nuclear energy may also benefit from this technique, both in terms of transporting intense beams of protons and making the low energy segment more compact. This RFQ is essentially a buncher configured as a charge filter, so RIB facilities can take advantage of this technique. The charge breeding concept can be utilised with a powerful ECR ion source directly coupled to this RFQ charge filter and then injected into an another higher frequency RFQ for additional acceleration

ACKNOWLEDGEMENT

One of the authors (G.R) would like to thank the Department of Science and Technology (DST) for supporting partial financial assistance for travel purposes.

REFERENCES

[1] C. Lyneis, D. Leitner,M. Leitner,C. Taylor and S. Abbott, Rev. Sci. Instrum., 81, 02A201 (2010).
[2] H. W. Zhao, W. Lu, X. Z. Zhang, Y. C. Feng, J. W. Guo, Y. Cao, J. Y. Li, X. H. Guo, S. Sha, L. T. Sun and D. Z. Xie, Rev. Sci. Instrum., 83, 02A320 (2012).
[3] Y. Higurashi, J. Ohnishi, T. Nakagawa, H. Haba, M. Tamura, T. Aihara, M. Fujimaki, M. Komiyama, A. Uchiyama and O. Kamigaito, Rev. Sci. Instrum., 83, 02A308 (2012).
[4] C. Lyneis, P. Ferracin, S. Caspi, A. Hodgkinson and G. L. Sabbi, Rev. Sci. Instrum., 83, 02A301 (2012).
[5] D. Z. Xie, Rev. Sci. Instrum., 83, 02A302 (2012).
[6] M. Okamura, T. Katayama, R. A. Jameson, T. Takeuchi, T. Hattori, Rev. Sci. Instrum., 73, 761 (2002).
[7] M. Okamura, T. Takeuchi, R. A. Jameson, S. Kondrashev, H. Kashiwagi, K. Sakakibara, T. Kanesue, J. Tamura, T. Hattori, Rev. Sci. Instrum., 79, 02B314 (2008).
[8] G. Rodrigues, R. Becker, R.W. Hamm, R. Baskaran, D. Kanjilal and A. Roy, Rev. Sci. Instrum., 85, 02A740 (2014).
[9] R. Becker, W. B. Herrmannsfeldt, Rev. Sci. Instrum.63, 2756 (1992).
[10] R. Becker, R. A. Jameson, Nucl. Instrum. Methods A558, 20 (2006).
[11] PARMTEQ, Los Alamos National Laboratory, http://laacg1.lanl.gov/laacg/services/serv_ann.phtml #parmteq
[12] A. Schempp, Nucl. Instrum. Methods, B40/41, 937 (1989).
[13] R. W. Hamm and R. Becker, Int. J. Modern Phys. Conf. Series, Vol. 27, 1460126 (2014).

CURRENT DEVELOPMENTS FOR INCREASING THE BEAM INTENSITIES OF THE RIKEN 18-GHz SUPERCONDUCTING ECR ION SOURCE

T. Nagatomo*, Y. Kotaka†, V. Tzoganis‡, M. Kase, T. Nakagawa, O. Kamigaito
RIKEN Nishina Center, Saitama 351-0198, Japan
Y. Ohshiro, Center for Nuclear Stady, Univ. of Tokyo, Saitama 351-0198, Japan

Abstract

The RIKEN 18-GHz superconducting ECR ion source (18-GHz SC-ECRIS) and the RIKEN AVF cyclotron function as the light-ion injector at the RI Beam Factory (RIBF) as well as being used for low-energy nuclear physics experiments and additional RI production. We are currently trying to measure and improve the beam quality of the 18-GHz SC-ECRIS because the beam intensities are lower than those obtained from the other injector using the RIKEN Linear Accelerator (RILAC). In order to improve our understanding and to increase the beam intensities, we are developing the simulation of the low energy beam transportation and an online emittance meter based on the pepper-pot method. We have tested a prototype emittance meter and confirmed an analysis procedure to deduce the emittance from the measured data.

INTRODUCTION

Since the RIKEN AVF cyclotron was constructed in 1989, it has been used as an injector for the RIKEN ring cyclotron (RRC). It has been used as stand-alone experiments related to low-energy nuclear physics and RI production. Since April 2009, the AVF injection mode started in the RIKEN RI Beam Factory (RIBF), where the cascaded chain of AVF, RRC, and Superconducting Ring Cyclotron (SRC) has provided light ion beams such as D, ^{14}N, and ^{18}O ions. The RIKEN 18-GHz superconducting ECR ion source (18 GHz SC-ECRIS) is one of three ion sources used for the AVF cyclotron as shown in Fig. 1. One of the current problems in the AVF injection mode is that the beam intensities are significantly lower than those obtained with the RIKEN Linear Accelerator as the injector (the RINAC injection mode), as show in Table 1. In order to increase the beam current of the AVF injection mode, a comprehensive understanding of the behavior of the ion beam not only around the extraction area of the ion source but also for the low energy beam transport (LEBT) to the AVF cyclotron is necessary. To this end, we have started developing simulations to elucidate the ion trajectory through the LEBT and an online emittance monitoring system based on the pepper-pot method [1]. The current status of the 18-GHz SC-ECRIS is also discussed.

Table 1: Beam intensities achieved from SRC.

Beam	Energy / A (MeV)	Intensity (pnA)	Injector
^{18}O	230	400	AVF
^{18}O	250	200	AVF
^{18}O	345	1000	RILAC

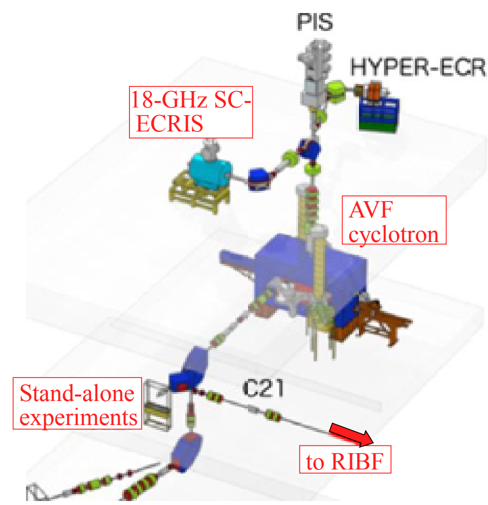

Figure 1: Schematic view of the RIBF injector apparatus with the 18-GHz SC-ECRIS.

APPARATUS

The 18-GHz SC-ECRIS is one of the ion source for the AVF cyclotron. At present, the 18-GHz SC-ECRIS mainly provides light-ion beams generated from gaseous elements,e.g. D^{+}, ^{12}C^{4+}, ^{18}O^{6+}, ^{40}Ar^{11+} ions and so on. The dimensions of the SC-ECRIS and LEBT are shown in Fig. 2. The specifications of the 18-GHz SC-ECRIS are given in Table 2. The length and diameter of the plasma chamber are 70 mm and 378 mm, respectively. The plasma chamber is encapsulated by a hexapole permanent magnet of which the magnetic field is ~1.1 T at the surface. A set of superconducting solenoids is used to achieve the minimum-B condition. A moveable biased disc with a dimeter of 30 mm is installed, to which a negative voltage of a few hundred volts with respect to the plasma chamber can be applied to increase the multi-charged ion flux. A 750-W TWTA (XTRT-750DBS, Comtech Xicom Technology, Inc) is installed to generate the 18-GHz microwaves that induce the ECR heating. The multi-charged ions are extracted and accelerated towards a grounded extraction electrode by applying a high voltage,

* nagatomo@riken.jp
† SHI Accelerator Service Ltd., Tokyo, Japan
‡ The University of Liverpool, Liverpool, United Kingdom

ISBN 978-3-95450-158-8

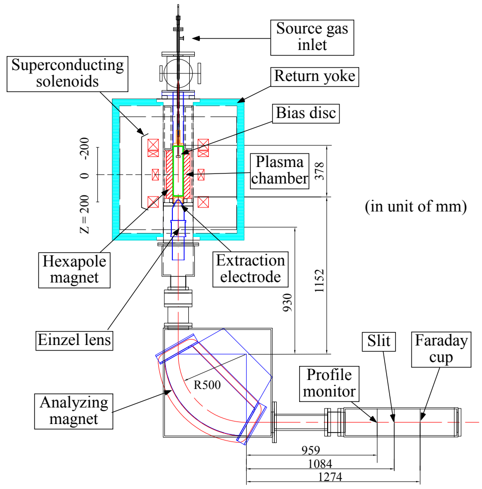

Figure 2: Schematic of the 18-GHz SC-ECRIS and LEBT leading to the AVF cyclotron.

typically 10 kV, to the plasma chamber. The extracted ion beam is passed through an Einzel lens installed just behind the extraction electrode, analyzed by the analyzing magnet of the LEBT and fed into the AVF cyclotron. The LEBT consists of an analyzing magnet and a diagnosis chamber in which a profile monitor, a set of horizontal and vertical slits and a Faraday cup are installed. At present, there is no device for measuring the beam emittance in the LEBT.

Table 2: Specifications of the 18-GHz SC-ECRIS. $B_{||}$ is the longitudinal magnetic field along the axis of the ion source at the designed maximum current density of 100 A/mm^2 .

18-GHz SC-ECRIS	
Superconducting material	Nb-Ti
Bore (room temperature)	220 mm
Radius of plasma chamber	70 mm
Length of plasma chamber	378 mm
Length of hexapole magnet	380 mm
$B_{||}$ (z = −200 mm)	3.0 T
$B_{||}$ (z = 0 mm)	0.6 T
$B_{||}$ (z = 200 mm)	2.0 T
Frequency of the ECR microwave	18 GHz
Typical power of the ECR microwaves	500 W
Typical extraction voltage	10 kV
Analyzing magnet in LEBT	
Pole gap	80 mm
Radius of curvature ρ	500 mm
Bending angle	90 degrees
B_{max}	0.15 T
Edge angle	29.6 degrees

DEVELOPMENTS

Beam Transport simulation in LEBT

Simulating the beam transportation is an effective method of estimating the quality of the extracted beam from the ion source. An important point in the simulation is to use accurate electromagnetic field maps calculated with three-dimensional models to reduce errors. We employed OPERA-3D [2], an approach based on the finite element method, to calculate the mirror field generated by the superconducting solenoids and the hexapole magnet, the electric field generated by the extraction electrode and the Einzel lens, and the magnetic field produced by the analyzing magnet.

The strength of the mirror field around the end of the plasma chamber is related to the density of the plasma, which influences the envelope of the extracted beam. The estimated field map for the transverse magnetic field $B_\perp$ at the end of the plasma chamber is shown in Fig. 3. In the future, we are planning to simulate a realistic beam transport with a initial condition in which the beam density is determined by the strength of the mirror field and evaluate the beam profile obtained using the emittance meter. On the other hand, the absolute value of the mirror field on the ion source axis is shown in Fig. 4. Fig. 4 shows that the Einzel lens is not placed at the optimum position because the mirror field is over 0.3 T at the lens center (z = 385 mm).

The beam transportation is simulated through a Monte Carlo approach using the geant4 tool kit [3], taking the actual geometries of the beam line and the electromagnetic field maps into account. The space-charge effect is currently not included in the simulation. The simulation estimates the momentum dispersion at the slit position to be −22.05 mm/%. Two setups for the transportation of $^{12}C^{5+}$ ions of 50 keV are shown in Fig. 5; the first is for parallel beams having the horizontal size of ±10 mm and the second is for beams emitted from a point source with an angular spread of ±40 mrad. In both cases, no voltage was applied to the Einzel lens. Comparing the figures shows that it is important to control the emission angle of the beam because the focus

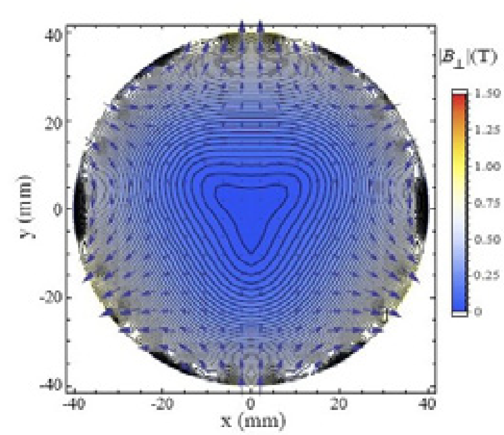

Figure 3: Estimated map of the transverse component of the mirror field at the end of the plasma chamber.

ISBN 978-3-95450-158-8

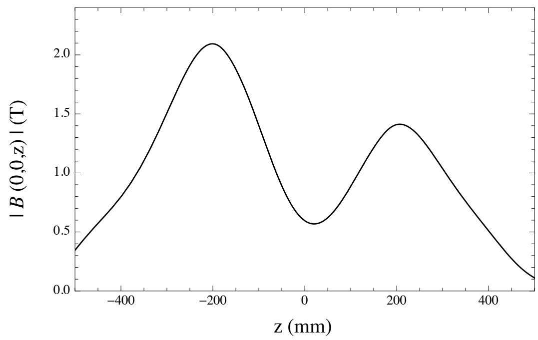

Figure 4: Absolute value of a typical mirror field along the ion source axis.

point of the tilted beam is shifted behind the focus of the parallel beam. With the simulation at this stage, we can now attempt to incorporate the space-charge effect. However, treating such collective effects consistently in event-by-event Monte Carlo simulations remains an open problem.

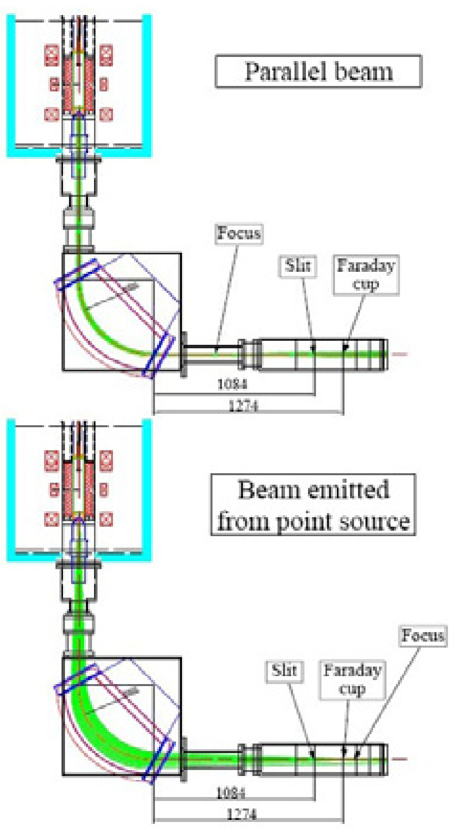

Figure 5: Setups for $^{12}C^{5+}$ transportation. Top: parallel beam with the initial x position spread across ±10 mm. Bottom: beam emitted from a point source over ±40 mrad. The ion beam trajectories are shown as green lines.

Emittance Meter

A prototype of a pepper-pot emittance meter [1] has been developed through a collaborative project between RIKEN and Center for Nuclear Study, the University of Tokyo (CNS) [4]. On the pepper-pot plate, there are 480 holes with the diameter of 0.357 mm at intervals of 2 mm aligned in a lattice structure. In the downstream (65 mm) of the pepper-pot plate, a fluorescent screen (a copper plate covered with KBr) is placed tilted at an angle of 45 degrees with respect to the beam direction. Its role is to produce images that are captured using a digital camera that is set perpendicular to the beam direction. On the fluorescence screen, crossed lines of 11 holes are drilled at a certain pitch to calibrate the length of the obtained image and to account for distortion of the image due to the tilt of the screen. In addition, the hole at the center of the pepper-pot plate was masked to indicate the center of the fluorescence image on the screen. As shown in Fig. 6, a fluorescence image induced by the 10-keV proton beam passing through the pepper-pot holes was successfully obtained. The proton beam was provided by another ECR ion source, Hyper-ECR in Fig. 1, which belongs to CNS. The beam intensity was 95 μ A.

In order to estimate the beam emittance, it is necessary to determine the correspondence between the beam spots on the screen and the holes on the popper-pot plate. From the difference in transverse position between the beam spot and the corresponding pepper-pot hole, angles with respect to the beam direction were obtained as a function of the beam position. In addition, the brightness of the beam spot is proportional to the beamlet intensity in principle, meaning the beam emittance can be determined from only a single shot of the image. After the calibration and correction discussed above were applied to the obtained image, the image was transformed to fit the transverse coordinates of the beam frame, x, y and z, which correspond to the horizontal, vertical and beam axes, respectively. From the transformation, the beam image in the x-y plane is shown in Fig. 7. The beam image is separated into segments using the troughs in

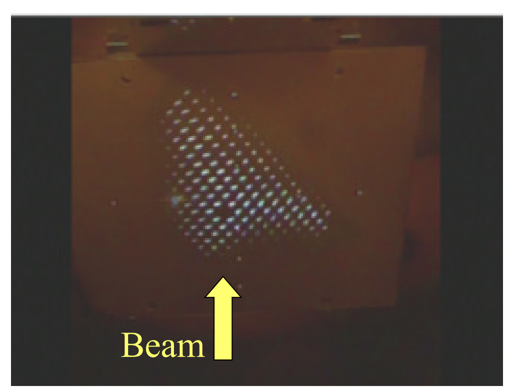

Figure 6: Image of the beam spots induced by the 10-keV protons passing through the pepper-pot plate, together with an image of the fluorescence screen with several holes used for calibration and correction.

ISBN 978-3-95450-158-8

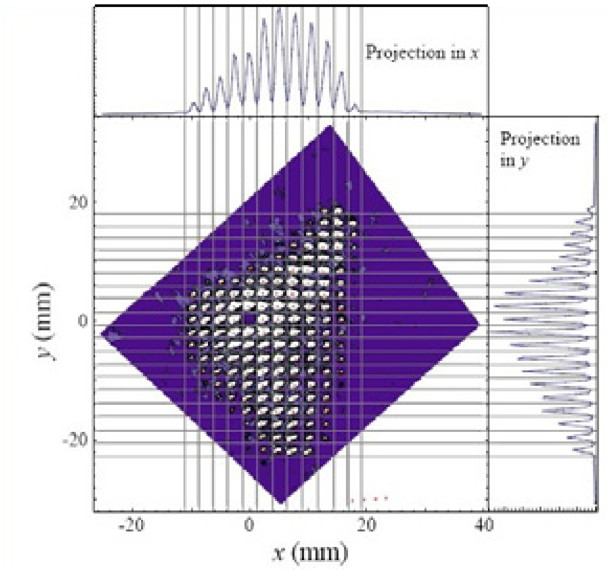

Figure 7: Contour plot showing the beam intensity, which is extracted from the pepper-pot image, transformed to transverse coordinates. The projections in the x (horizontal) and y (vertical) axes are also shown.

the x and y projections. By searching for a segment with smaller intensity that is surrounded by segments with higher intensities, the segment corresponding to the masked pepper-pot hole is identified on the fluorescent screen. Taking the masked position as a reference, we identified the correspondence between the pepper-pot holes and the beam spots. From the transverse position difference between these corresponding holes and spots, the beam emittance was obtained as shown in Fig. 8.

Although this is an offline analysis, the procedure described here was quickly and automatically executed; thus, we have confirmed that the algorithm works well. Further developments to incorporate the algorithm into the image acquisition system using LabView (National Instruments Co.) are in progress to establish an online emittance monitor.

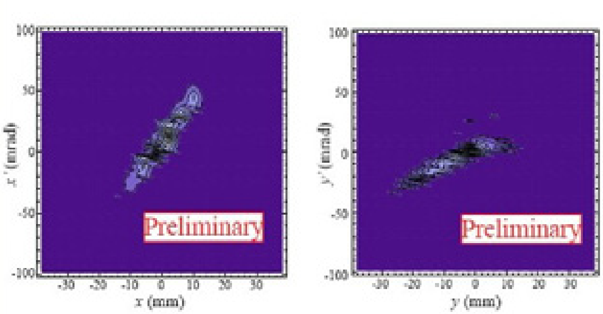

Figure 8: Beam emittance obtained from the pepper-pot image in Fig. 6. The left figure shows the emittance in horizontal phase space and the right in vertical phase space.

SUMMARY AND FUTURE PROSPECTS

A combination of the RIKEN 18-GHz SC-ECRIS and AVF cyclotron is used as the injector for the RIKEN RIBF, providing light-ion beams such as D, ^{14}N and ^{18}O ions. However, at present, the beam intensity is lower than that provided with the RILAC injection mode. In order to increase the beam intensity, a comprehensive understanding of the properties of the 18-GHz SC-ECRIS and the subsequent LEBT is required. Using geant4, Monte Carlo simulations of the LEBT were performed. We employed OPERA-3D, which is based on the finite element method, to calculate an electromagnetic field map using an accurate 3D model of the magnets and electrodes. The current transport simulation does not account for the space-charge effect. In order to investigate the properties of the beam from the 18-GHz SC-ECRIS, development of a pepper-pot emittance meter is in progress. Using a prototype device, we obtained an image of the beam spots with a 10-keV proton beam with an intensity of 90 μA. An algorithm to automatically determine the correspondence between the pepper-pot holes and the beam spots on the fluorescent screen was confirmed and the beam emittance was obtained. The incorporation of this algorithm into the data acquisition system is also in progress in order to create an online emittance meter.

As the intensity of a highly charged ion beam increases just after extraction from the ion source, the space-charge effect considerably degrades the beam quality due to its low energy and high charge density. In the future, we are planning to investigate the relationship between the beam quality and the beam intensity with the online emittance meter and simulations in order to improve the beam quality.

REFERENCES

[1] C.C. Cutler and J.A. Salom, Proc. IRE 43, 299 (1955), C.C. Cutler and M.E. Hins, Proc. IRE 43, 307 (1995).

[2] "OPERA-3D" is a code suite for electromagnetic field calculations developed by Cobham PLC `http://operafea.com`

[3] S. Agostinelli et al., Nucl. Inst. and Meth. A 506, 250 (2003), J. Allison et al., IEEE Trans. on Nucl. Sci. 53, No. 1, 270 (2006)

[4] Y. Kotaka et al., to be published in the Proceedings of the 11th Annual Meeting of the Particle Accelerator Society of Japan (2014).

ISBN 978-3-95450-158-8

DEVELOPMENT OF AN INTERFACE AND DIAGNOSTIC SYSTEM FOR THE ECR ION SOURCE AT KBSI

Jungbae Bahng, Eun-San Kim, Kyungpook National University, Daegu 702-701, Korea
Byoung Seob Lee*, Jung-Woo Ok , Seyong Choi, Jonggi Hong, Seong Jun Kim, Jin Yong Park, Chang Seouk Shin, Jang-Hee Yoon, Mi-Sook Won, Korea Basic Science Institute, Busan, 609-735, Korea

Abstract

A 28 GHz superconducting ECR (electron cyclotron resonance) ion source was recently developed at KBSI (Korea Basic Science Institute) to produce a high current and high charge state ions [1]. The condition of the ion beam extracted from the ion source should be analyzed by a diagnosis tool after accelerating and focusing process. For this, we developed an ion beam diagnostic system composed of a slit, a wire scanner, a view screen and a faraday cup. The interface of the diagnostic system was designed so as to achieve stable operation of the ECR ion source. The information obtained from the diagnostic system can be used as a reference in studies of the optimum beam conditions needed to adjust the extraction parameters. The details of the diagnostic system and initial test results will be reported.

INTRODUCTION

A heavy ion accelerator using fast neutrons was developed for the radiography facility at KBSI. A 28 GHz superconducting ECR (electron cyclotron resonance) ion source was employed for a high current ion beam to meet the requirements needed for generating fast neutrons. The key part of heavy ion accelerator system is comprised of the 28 GHz ECR ion source, an LEBT (low energy beam transport) system with a series of electromagnets (a dipole, two quadrupoles and three solenoids), RFQ (radio frequency quadrupole) for ion beam acceleration from 12 keV/u to 500 keV/u and DTL (Drift Tube linear accelerator) for acceleration up to 2.7 MeV/u. The layout is shown in figure 1. Neutron imaging is planned to be generated by the reaction of an accelerated lithium beam and a hydrogen target.

The figure 2 shows the components of the LEBT system, which are a dipole magnet, three solenoids, two quadrupoles and the diagnostic system. Ion beams extracted from the ECR ion source are transported to the RFQ entrance via the LEBT system. After analysing the process at the dipole magnet, we prepared a diagnostic chamber to obtain the beam profile, the transverse emittance and the intensity of the beam current at this location. Inside of the diagnostic chamber, we installed horizontal and vertical slits, a wire scanner, the screen monitor and the faraday-cup. The slits and wire scanner permit us to select the desired beam and to measure the transverse emittance. The screen monitor and wire scanner are utilized to identify the horizontal and vertical profiles of the ion beam. The faraday-cup provides information regarding the beam intensity as an electrical current.

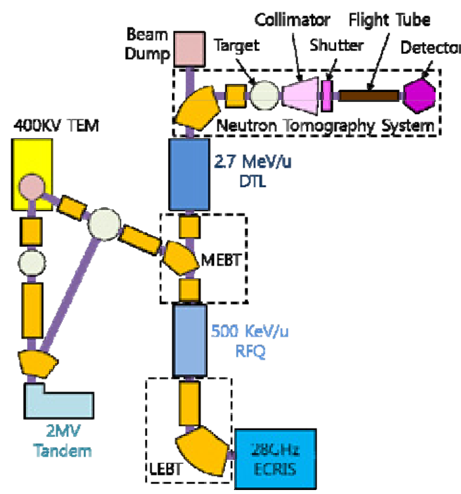

Figure 1: The layout of the KBSI accelerator.

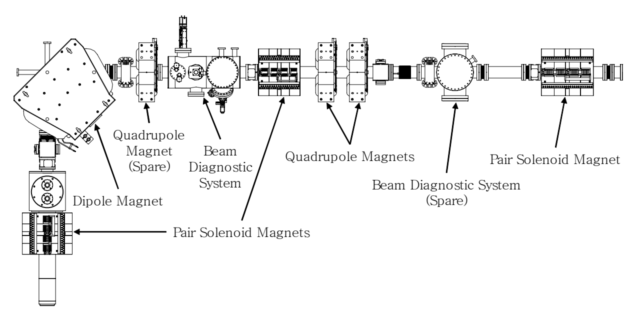

Figure 2: Schematic diagram of the LEBT system.

Simulations of the ion beam optics were carried out using the TRANSPORT code. The basic parameters used in this simulation are listed in Table 1.

---
* bslee@kbsi.re.kr

ISBN 978-3-95450-158-8

Table 1: The beam parameters used in the simulation of the beam optics.

Beam	Lithium
Mass	7
Charge	3+
Energy	12 keV/u
Beam emittance$_{(n,r)}$	0.2 π mm mrad
Current	1.0 emA

Figure 3 depicts the results for the beam optics in the overall LEBT apparatus. The size of the beam pipe and the location of the LEBT components were determined based on the simulation results. According to the results shown in figure 3, the maximum beam envelope is within 4 cm and the entire length of the LEBT system was around 7 meters [2, 3].

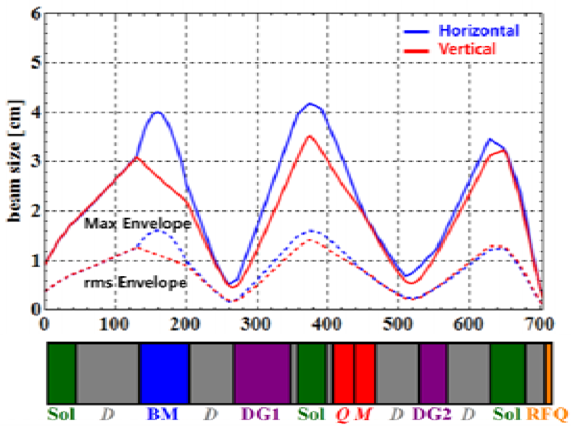

Figure 3: The results of the beam optics simulation.

DESIGN

For the specific design of the diagnostic system, we enlarged the DG1 (purple color) in figure 4 from the simulation results in figure 3. As in figure 4, the beam radii at the diagnostic chamber were changed from 1 to 3.2 cm. For achieving an effective beam separation, the size of the beam needs to be as small as possible. Several of the instruments in the diagnostic chamber were used to determine this, according to the results of beam optics simulation. Each component of the diagnostic system is described in the following chapter.

Slit

A slit is used as collimator to select the desired beam after passing through the analyzing magnet. Another reason for the existence of a slit in the diagnosis chamber is to remove ineffective particles around beam halo, which cause an increase in emittance. The slit also could be applied to the emittance measurement with a profile monitor (wire scanner and screen monitor). Transverse beam emittance can be calculated with a high resolution using information on beam divergence and the slit position.

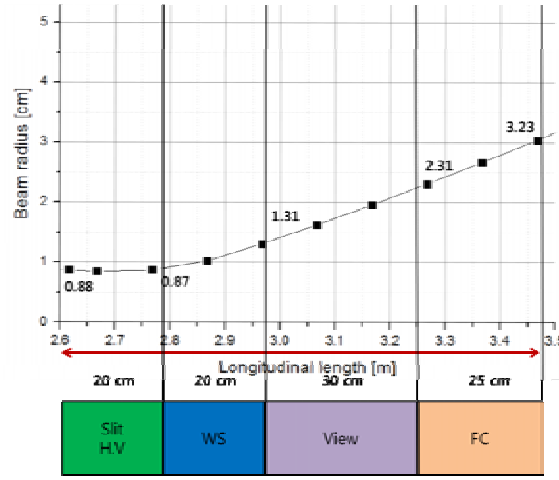

Figure 4: The beam radii in the diagnostic chamber

The designed slit system consists of two tungsten plates and step motors for precise movement. We used a tungsten material at the slit because it has the highest melting point, low electrical resistivity and is remarkably robust compared to other candidate materials.

To confirm the effectiveness of beam separation and selection in our slits, we used the TRACK code for multi-charge simulation. Figure 5 shows the results for the beam distribution using a uranium beam at the slit. It is well known that it is the most difficult species to separate and select at the slit. As shown in the figure, the beam is well seprated and selected.

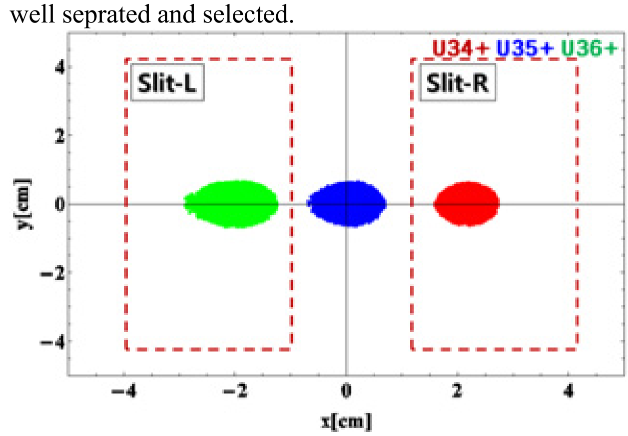

Figure 5: The distributions of beam at the slit.

Wire scanner

In the diagnostic chamber, it is necessary to measure the beam profile to verify the magnitude of beam focuing in the transverse direction and matching the lattice along with the beam transport line. Wire scanners are commonly used for beam profile measurements in many accelerators due to its high resolution and simple structure. The wire scanner system was made of thin tunsten wire, a step motor and bellows. It should be moved forward and backward keeping the high vacuum level in the chamber. The minimum step of the motor is 0.1 mm and the wire thickness is 0.1 mm. A finer step and thinner wire usually can provide a high resulution profile measurement. We

ISBN 978-3-95450-158-8

adopted three wires in wire scanner. The advantage of a three wire scanner is that not only can the projection signal be obtained as in a conventional two wires scanner but additional information such as the correlation, the twiss alpha can be obtained in a single measurement.

Screen monitor

The screens, which are made of stainless steel, are thought to be a kind of popular profile monitor due to its simplicity and convenience of use. The screen monitor system consists of a stainless steel screen, a CCD camera and an air cylinder for achieving movement. The screen was tilted at a 45° angle so as to permit the beam to be viewed through a viewport. The thickness of the screen was 10 mm with several pin holes to calibrate the physical position. We coated the the surface layer of the screen with Y_2O_2S. Such a doping material provides the optimized conditions for achieving a short decay time and a high luminance, even at low energy.

Faraday Cup

A Faraday Cup is typically used to measure the intensity of the beam current. Furthermore the faraday cup is also used as a dump to consume the beam energy. During the dumping process, heat is generated in the device. We therefore added a cooling water channel to control the temperature in the structure. The interaction of the beam and faraday cup produces a secondary electron emission (SEE) effect. To avoid secondary particles outflowing to another device, we adopted a high voltage plate to suppress the SEE effect.

The Faraday cup consists of a copper body, an electrode for high voltage, a water cooling channel and an air cylinder for the movement in the chamber. Figure 6 shows the structure of the faraday cup. The copper body is 55 mm in diameter and 220 mm in length. The faraday cup will be operated at an electrical potential at -200 V at the electrode to suppress outflowing SEE. The faraday cup was designed to be cooled with the cooling water with a flow rate of 0.5 m/s, which enables to to operate the equipment at room tempeature.

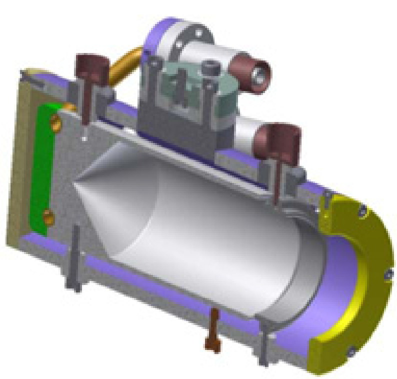

Figure 6: The structure of faraday cup.

CONCLUSIONS

The size and position of a diagnostic system was determined by a simulation of the beam optics of teh equipment. The components of the diagnostic system include a slit, a screen monitor, a wire scanner and a faraday cup. They were successfully installed inside the diagnostic chamber, as shown in figure 7. The diagnostic system is used to obtain information regarding the ion beam, such as beam profile, beam intensity and beam emittance. An initial test of most of the components in the diagnostic system was performed to check the movement and the communication between devices and controller. Beam extraction from a 28 GHz superconducting ECR ion source is scheduled the autumn in 2014. We expect that the developed diagnostic system will be ready to use at the time of the KBSI ion beam commissioning.

Figure 7: The installed diagnostic system.

REFERENCES

[1] M. Won, et. al., International Nuclear Information System Vol.44 IS.09 44026105, 2012.

[2] J. Bahng, et. al., “Design study of LEBT beam line in KBSI at Busan”, Journal of Korea Physics Society, 2011.

[3] J. Bahng, et. al., “Design study of LEBT beam line and Diagnostics for ECR-IS in KBSI”, Journal of Korea Physics Society, 2012.

ISBN 978-3-95450-158-8

PRODUCTION AND ACCELERATION OF TITANIUM-50 ION BEAM AT THE U-400 CYCLOTRON*

S. Bogomolov, A. Bondarchenko, I. Kalagin, K. Kuzmenkov, A. Lebedev, V. Lebedev, V. Loginov, R. Vaganov, JINR, Dubna, Moscow Region, Russia
Z. Asfari, B.JP. Gall, H. Faure, M. Filliger, IPHC, Strasbourg Cedex 2, France

Abstract

The production of Ti-50 ion beam with ECR ion source using MIVOC method is described. The experiments were performed at the test bench with the natural and enriched compounds of titanium $(CH_3)_5C_5Ti(CH_3)_3$. The compounds were synthesized in collaboration with IPHC (Strasbourg) group. In the experiments at the test bench the beam currents of Ti^{5+} - 80 μA and Ti^{11+} - 70 μA were achieved at different settings of the source. After successful tests two 3 weeks runs with Ti-50 beam were performed at the U-400 cyclotron for the experiments on spectroscopy of super heavy elements. The intensity of the injected beam of $^{50}Ti^{5+}$ was about of 50÷60 μA, during experiment the source have shown stable operation. The compound consumption rate was determined to be about of 2.4 mg/h, corresponding to ^{50}Ti consumption of 0.52 mg/h.

INTRODUCTION

In recent years, the reactions ^{48}Ca with ^{238}U, ^{242,244}Pu, ^{243}Am, ^{245}Cm and ^{249}Cf were used to synthesize new super heavy elements with Z = 114-116 and 118. In the frame of these experiments a technique for producing of metallic ^{48}Ca was developed, optimization of operation mode of ECR ion source was performed in such a way that the necessary intensity of $^{48}Ca^{5+}$ ions was achieved with maximum efficiency ionization [1]. The methods of collection and recovery of expensive isotope also were developed. The complex of these studies made it possible to conduct long-term experiments on the synthesis of super heavy elements with high efficiency using of the working substance.

The most heavy target, with which it is possible to carry out experiments on the synthesis of super heavy elements in heavy-ion reactions is ^{249}Cf, so further progress in the area of the elements with Z > 118 requires the production of intense beams of accelerated neutron-enriched isotopes such as ^{50}Ti, ^{58}Fe, ^{64}Ni and others. The use of each new isotope for production of the accelerated beam requires investigations directed on optimization of the ECR source operation mode and development of technique for material feed into the source.

Several methods for production of ions of solids from ECR sources have been developed. Solid material can be evaporated by resistor or inductive oven, which is inserted into source chamber [2,3].

Refractory metals can be sputtered by plasma ions [4] or inserted into the plasma and heated by energetic plasma electrons (“insertion technique”) [5,6].

The other possibility for production of ions of solids is the feeding of the plasma with an organometallic compound through the Metal Ions from VOlatile Compounds (MIVOC) method [7].

PRODUCTION OF TITANIUM ION BEAM

The experiments on production of Ti ion beams were carried out at many laboratories with the use of different methods.

The production of Ti ion beams by evaporation from the resistor oven was studied at GSI [8]. The evaporation of pure titanium requires the temperature between 1750 °C and 1800 °C. During the experiments with HTO more than 50 eμA of $^{50}Ti^{8+}$ were produced with high level of beam stability. The oven life time of 6 days was obtained.

The experiments on production of Ti ion beams by evaporation from the induction oven were carried out at ANL [9]. The beam of $^{50}Ti^{12+}$ with the intensity of 5.5 eμA was produced during seven days.

The MIVOC method was first adopted for production of Ti ion beam by JYFL group [10]. Commercially available $(CH_3)_5C_5Ti(CH_3)_3$ compound was used as a working substance. In the case of $^{48}Ti^{11+}$ion beam the intensity of 45 eμA was produced.

The consumption of the compound was measured to be 47 mg giving the value of 0.22 mg/h for the consumption of titanium. The ion beam was very stable during the period of 282 h. So, from the point of view beam intensity, stability, reliability and material consumption the MIVOC method seems very promising for providing ^{50}Ti ion beam for long term (several months of non-stop operation) experiments on synthesis of super heavy elements.

The compound is sensitive to air, moisture, temperature and light that needs cautious handling when loading the material for use. The synthesis of this compound is rather complicated especially with the use of enriched titanium which is available in a small, about 1 g, quantity.

Test Experiments

First time the ^{50}Ti ion beam was accelerated at the U-400 cyclotron in 2005. The task was to provide about of 30 enA of ^{50}Ti beam at the target for experiments on the fission physics. Due to the moderate requirements for the intensity it was decided to use $TiCl_4$ which has a vapor pressure of about 10 torr at room temperature that is sufficient for feeding of the ECR source with working substance. The natural $TiCl_4$ (5.2 % of ^{50}Ti) was used. The glass ampule with $TiCl_4$ was connected to the standard

*Work supported by Russian Foundation for Basic Research under grant number 13-02-12011

piezoelectric leak valve, which is used when the source is operating with gases. The intensity of ^{50}Ti ion beam, extracted from the cyclotron constitutes about 200 enA, the source was running stable during two weeks.

But the use of $TiCl_4$ do not provide the intensity required for the experiments on the synthesis of super heavy elements.

Taking into account the problems with synthesis and handling of $(CH_3)_5C_5Ti(CH_3)_3$ we decided to try to find the other compounds, suitable for MIVOC method. The titanium isopropoxide $(Ti\{OCH(CH_3)_2\}_4)$ and cyclopentadienyl cycloheptatrienyl titanium $(C_5H_5TiC_7H_7)$ were tested, but no noticeable titanium current were observed, just a few microamperes of Ti^{5+}. The $(C_5H_5TiC_7H_7)$ compound was later used at IMP [11] with LAPECR2 source for production of titanium ions by oven method. During the test, 24 eμA of Ti^{11+} has been achieved with 250 W 14.5 GHz microwave power.

After that the experiments on production of titanium beam with oven method at the DECRIS-2 [12] source were performed. The titanium tetrafluoride (TiF_4) was used as working substance. TiF_4 is colorless crystals with melting point of 426° C, and the temperature about of 50÷80° C is required to provide the vapor pressure sufficient for the source operation. In this temperature range it is difficult to control the oven temperature due to the additional heating of the oven by u.h.f. and plasma [13]. To decrease the material flux into the source chamber the oven with a thin long channel, 15 mm in length and 1 mm in diameter, was used. The oven was inserted into the source axially and its position was adjusted remotely. More or less stable mode of the source operation was possible to achieve at the intensity level of $^{48}Ti^{6+}$ about of 10÷20 eμA, with the increase of the material feed the discharge became unstable.

The next step was the production of titanium ions by insertion method. The experiments were also performed with the DECRIS-2 ion source. The titanium rod with diameter of 3 mm was axially inserted into the source chamber through the bias tube. The position of the rod can be adjusted remotely. Helium was used as a support gas. The evaporation rate is dependent on microwave power, helium pressure and position of the rod.

Figure 1 shows typical spectrum of titanium ions produced at the microwave power of about 140 W with the source tuning on Ti^{5+}. The intensity is quite suitable, but the long term stability of the beam was not achieved. Without source tuning during one hour the beam intensity was varied in the range of 30% and then discharge became uncontrollable or the beam intensity droped to zero.

Our further activity in the production of titanium ion beam was related with MIVOC method and (trimethyl)pentamethyl-cyclopentadienyltitanium compound.

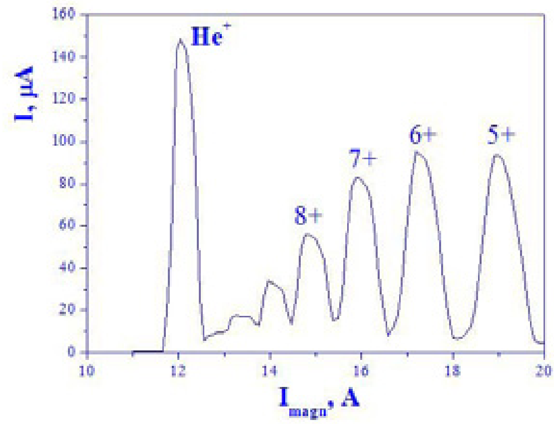

Figure 1: Ti ion spectrum produced by rod insertion from the DECRIS-2 ion source.

The commercially available compound produced by Sigma-Aldrich company [14] was tested with DECRIS-4 [15] and DECRIS-2 sources. The sources were optimized for production of Ti^{5+}, similar results were produced with both sources and figure 2 shows the spectrum of Ti ions, produced from DECRIS-4 source at the microwave power of 34 W.

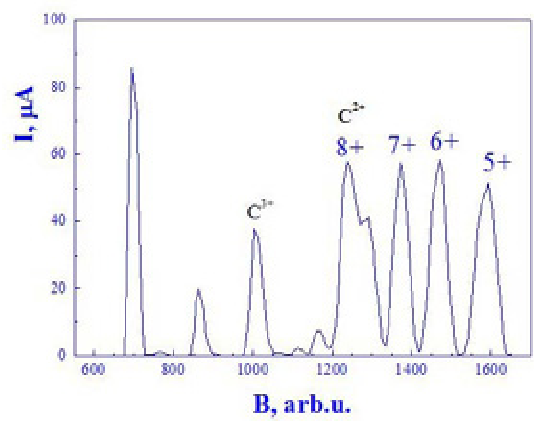

Figure 2: Ti ion spectrum produced by MIVOC method from the DECRIS-4 ion source.

Next step was the test of compound, produced by DALCHEM company [16]. The main feature is that the compound is provided in a welded glass ampules, that makes the handling of the compound much more easier - it is not necessary to use the argon filled glove box, the ampule can be destroyed under the vacuum in a specially designed MIVOC chamber. The tests were performed with the modified ECR4M [17] source at the test bench. Figure 3 shows the spectrum of titanium ions with the source tuning on Ti^{5+}. In all experiments no support gas and no control of MIVOC chamber temperature were used. The operation of the sources was stable and reproducible.

ISBN 978-3-95450-158-8

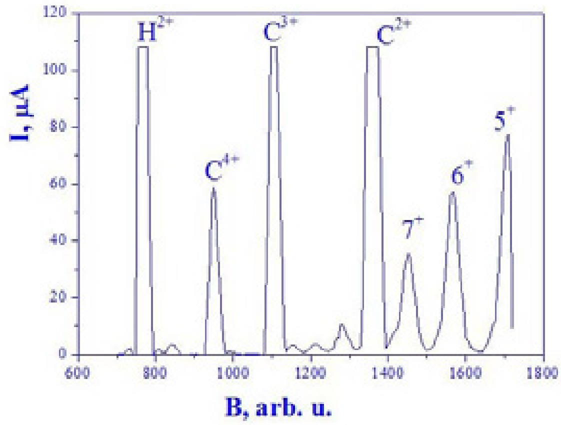

Figure 3: Ti ion spectrum, produced by MIVOC method from the ECR4M source at microwave power of 20 W.

Production of Titanium-50 Ion Beams

The development of titanium-50 beam production was performed in the frame of collaboration between IPHC (Strasbourg, France) and JINR.

After several years of chemistry developments at IPHC the $C_5(CH_3)_5Ti(CH_3)_3$ compound was synthesized using 92.57 % enriched ^{50}Ti. A two step chemistry was done starting from $TiCl_4$ going to $C_5(CH_3)_5Ti(CH_3)_3$ through an intermediate $C_5(CH_3)_5TiCl_3$ organic compound with quite high efficiency.

First MIVOC isotopicaly enriched beam was developed and tested in 2011 at the University of Jyväskylä. After optimization, up to 19.4 eμA of titanium-50 in charge state 11^+ could be extracted from the JYFL 14 GHz ECRIS2 ion source [18,19].

The compound from natural titanium, synthesized at IPHC, was also tested at GANIL [20]. An intensity of 20 eμA for $^{48}Ti^{10+}$ was maintained for 4 days, with regulation the temperature of the MIVOC chamber. The consumption of 1.5 mg/h for the MIVOC compound has been deduced, i.e. 0.23 mg/h for ^{48}Ti.

During 2012÷2013 years several samples of $(CH_3)_5C_5Ti(CH_3)_3$ compound synthesized at IPHC were tested at the FLNR test bench. The main problem was the long time transportation of the samples from IPHC to JINR that leads to destroying of the compound, and very pure currents of titanium were produced. After that it was decided to perform the final step of synthesis at FLNR chemistry laboratory.

First natural material synthesized at FLNR by IPHC group was tested in October 2013 with ECR4M ion source at test bench. After optimization, very stable ^{48}Ti beams were produced with intensities up to 70 eμA for the 11^+ charge state (6.2 pμA) and 75 eμA for the 5^+ charge state (15.0 pμA). Figure 4 shows the charge state distribution of ^{48}Ti ion beam with source settings for optimum production of $^{48}Ti^{11+}$.

Following these very promising results, a 92.57 % enriched compound was synthesized and tested with ECR4M test bench. Under similar conditions up to 80 eμA of $^{50}Ti^{5+}$ beam was extracted, corresponding to 16.0 pμA. Figure 5 shows the charge state distribution of ^{50}Ti ion beam with source settings for optimum production of $^{50}Ti^{5+}$.

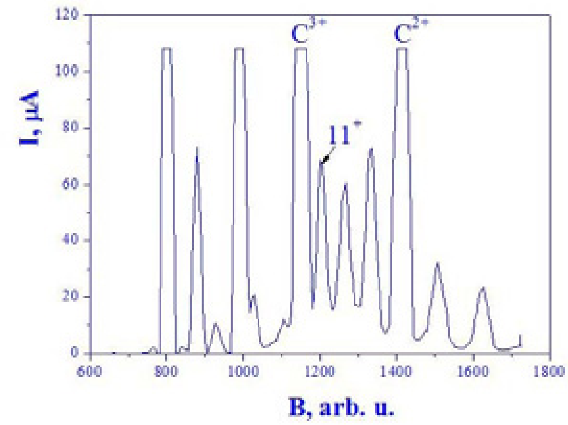

Figure 4 : Ti ion spectrum, produced by MIVOC method from the ECR4M source at microwave power of 300 W.

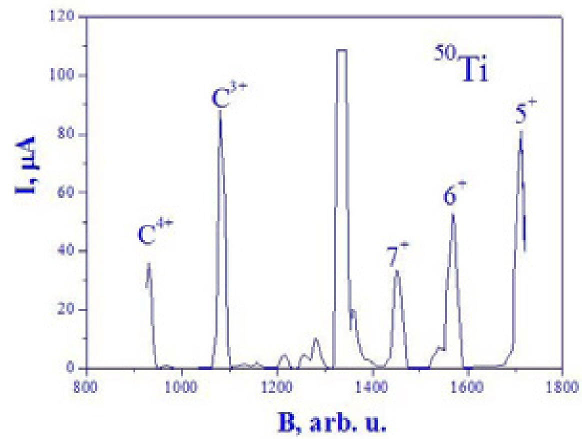

Figure 5 : ^{50}Ti ion spectrum, produced by MIVOC method from the ECR4M source at microwave power of 30 W.

This beam was then produced with the DECRIS-2m [21] source and accelerated at the U400 cyclotron. A very stable and intense 55 eμA beam was injected at 5^+ charge state (11.0 pμA) in the cyclotron. Chopped after extraction, transport to the targed a 0,490 pμA was used on target for several weeks in October-November 2013. This beam was very stable with wery low, about of 0.6 mge/h titanium consumption.

Next run with titanium-50 ion beam was performed at the U-400 cyclotron during April-May 2014. By then the DECRIS-2m source at the U-400 cyclotron was replaced by ECR4M source. During three weeks the intensity of $^{50}Ti^{5+}$ beam was maintained at the level of 55÷62 eμA. The material consumption was similar to the previous run with DECRIS-2m ion source.

ISBN 978-3-95450-158-8

CONCLUSION

During last years significant progress was achieved in production of intanse multiply charged ion beams of titanium from ECR ion sources. Table 1 summarise the results of titanium ion beam production at different Laboratories by MIVOC (JYFL, GANIL, FLNR) and oven (GSI, ANL, IMP) methods.

Table 1: Intensity (eμA) of Titanium Ion Beams Produced at Different Laboratories by MIVOC and Oven Methods

	JYFL	GANIL	FLNR	GSI	ANL	IMP
$^{48}Ti^{5+}$			79			
$^{48}Ti^{10+}$		20				
$^{48}Ti^{11+}$	45		68			24
$^{50}Ti^{5+}$			82			
$^{50}Ti^{8+}$				50		
$^{50}Ti^{11+}$	20					
$^{50}Ti^{12+}$					5.5	

The MIVOC method was successfully used for production and acceleration of titanium-50 ion beam at the U-400 cyclotron. This method provides intense beams with long term stability, and is quite promising for experiments on synthesis of super heavy elements.

ACKNOWLEDGMENT

This work was supported by Russian Foundation for Basic Research under Grant number 13-02-12011.

REFERENCES

[1] V. B. Kutner, S. L. Bogomolov, A. A. Efremov et al., Rev. Sci. Instrum. V. 71, N2, 2000 p. 860.

[2] D. J. Clark, C. M. Lyneis, J. Phys. (Paris) Colloq. 50 (1989), C1–759.

[3] R. Harkewicz, Rev. Sci. Instrum., 67, (1996), p. 2176.

[4] R. Harkewicz, P. J. Billquist, J. P. Greene et al., Rev. Sci. Instrum., 66, (1995), p. 2883.

[5] R. Geller, P. Ludwig, G. Melin, Rev. Sci. Instrum. 63 (1992) 2795–2800.

[6] T. Nakagawa, T. Kageyama, E. Ikezawa et al., Proceedings of the 10th International Workshop on ECR ion sources, Oak Ridge, USA, 1990, p. 163.

[7] H. Koivisto, J. Дrentje, M. Nurmia, Rev. Sci. Instrum., 69, (2). 1998, p. 785.

[8] K. Tinschert, R. Lang, J. Mäder et al., WEPP15, Proceedings of ECRIS2012, Sydney, Australia.

[9] R.Vondrasek, R.Scott, R.Pardo High energy physics and nuclear physics (HEP & NP) A Series Journal of the Chinese Physical Society (C) vol.31, Supp.I, July, 2007, p. 101.

[10] H. Koivisto et al., NIM B, 187 (2002), p.111.

[11] W. Lu, J. Y. Li, L. Kang et al., Rev. Sci. Instrum. **85**, 02A947 (2014).

[12] A. Efremov, V. Bekhterev, S.L. Bogomolov et al., Rev. Sci. Instrum., 1998, v.69, N2. p. 662.

[13] S.L. Bogomolov, A.A. Efremov, A.N. Lebedev et al., Proc. of the 16th Int. Conf. on Cyclotrons and their Applications. East Lansing, Michigan. 13-17 May 2001 p. 271. Ed. F.Marti, Michigan State University, East Lansing, Michigan Melville, New York, 2001. AIP Conference proceedings. Volume 600.

[14] http://www.sigmaaldrich.com

[15] M. Leporis, V. Bekhterev, S. Bogomolov et al., Rev. Sci. Insrum., **77**, 03A301, 2006.

[16] http://www.dalchem.com/

[17] S. Bogomolov, V. Bekhterev, A. Efremov et al., FRYOR01, Proceedings of RUPAC2012.

[18] J. Rubert, J. Piot, Z. Asfari et al., NIM B 276 (2012), p. 33.

[19] H. Koivisto, O. Tarvainen, V. Toivanen et al., FRYA03, Proceedings of ECRIS2012, Sydney, Australia.

[20] P. Jardin, O. Bajeat, C. Barué et al., FRYA01, Proceedings of ECRIS2012, Sydney, Australia.

[21] V.N. Loginov, V.V. Bekhterev, S.L. Bogomolov et al., Nukleonika 2003, Volume 48(Supplement 2), p. S89.

ISBN 978-3-95450-158-8

MODERNIZATION OF THE MVINIS ION SOURCE

V. Bekhterev, S. Bogomolov, A. Efremov, Yu. Kostyukhov, A. Lebedev, FLNR, JINR, Dubna, Russia

A. Dobrosavljević, V. Vujović, N. Nešković, I. Trajić, Lj. Vukosavljević, D. Ćirić, Laboratory of Physics, Vinča Institute of Nuclear Sciences, University of Belgrade, P. O. Box 522, 11001 Belgrade, Serbia

Abstract

The mVINIS Ion Source was designed and constructed jointly by the team of specialists from the Flerov Laboratory of Nuclear Reactions, Joint Institute for Nuclear Research (JINR), Dubna, and the Laboratory of Physics, Vinča Institute of Nuclear Sciences, Belgrade. It was commissioned in 1998. From that time, it has been widely used in the field of modification of materials with different kinds of multiply charged ions. Recently, we decided to modernize this electron cyclotron resonance (ECR) ion source in order to improve its operation capability. Our main goal was to enhance the basic construction of the source in order to improve the production of multiply charged ion beams from gaseous and solid elements. We changed the shape of the plasma chamber and consequently reconstructed the magnetic structure. Also, we improved the construction of the injection chamber. Besides, we decided to refurbish its major components that have been in operation for quite a long time (the vacuum pumps, microwave generator, control system etc.). These improvements have resulted in a substantial increasing of the ion beam intensities, especially in the case of high charge state ions.

INTRODUCTION

The mVINIS Ion Source was designed and constructed jointly by the team of specialists from JINR, Dubna, and the Vinča Institute, Belgrade. This is a CAPRICE type ECR ion source [1], where the axial confinement of plasma is obtained by two solenoid coils with an iron yoke. The cone-shaped rings around the plasma chamber are used to increase the axial magnetic field peaks and fix their positions. The radial confinement of plasma is performed by a NdFeB permanent hexapole magnet with the Halbach type structure. The operating frequency of the source is 14.5 GHz. A detailed description of the components and performances of mVINIS have been published elsewhere [2, 3]. It was commissioned in 1998. From that time, it has been widely used in the field of modification of materials with different kinds of multiply charged ions4. During the 15 years of operation, we have noticed some disadvantages, which are listed below.

- The use of the microwave coupling system having the standard waveguide connected with a coaxial line through a non-regular element (the injection cube) causes big losses of the microwave power. As a result, we have a strong heating on the injection side of the source and an uncontrolled outgasing. A special tuning mechanism for the coupling system is also required.
- The manufacturing of the water cooled plasma chamber is complicated and expensive (the variable diameter double-wall chamber requires the welding of parts made of copper and stainless steel).
- There is no room to install some additional elements inside the chamber because the injection part of the chamber is used as a coaxial waveguide.
- The only place to introduce a micro-oven to evaporate solid substance is the internal conductor of the coaxial line. It is also used as a bias electrode and has to be insulated from the plasma chamber. As a result, the oven power supply should be also insulated. The size of the oven is strongly restricted by the diameter of the internal conductor of the coaxial line.
- The position of the micro-oven is exactly on the axis of the ion source. The interaction of the oven with plasma causes an additional oven heating. As a result, the oven temperature depends on the source regime. In order to minimize this effect, the fine tuning mechanism is required to define the optimal position of the oven.

MODERNIZATION OF THE ECR ION SOURCE

We decided to enhance the basic construction of the ECR ion source in order to solve the above mentioned disadvantages and improve the production of multiply charged ion beams from gaseous and solid elements. We changed the shape of the plasma chamber and consequently reconstructed the magnetic structure. Also, we improved the construction of the injection chamber.

First of all, we made a decision to increase the internal diameter of the plasma chamber from 64 mm to 74 mm to provide enough room for the installation of all the required elements. As a consequence, this should also increase the plasma volume and ion lifetime, which will enable one to obtain higher charge state ion beams and higher beam intensities. Such a reconstruction required some changes in the magnetic structure and introduction of a completely new injection chamber.

ISBN 978-3-95450-158-8

The new water cooled double-wall plasma chamber has a constant diameter and has been completely made from stainless steel. We had to increase the internal diameter of the injection soft iron plug to 80 mm to allow the installation of the new chamber into the source (see Fig. 1). In order to compensate the magnetic field losses at the injection side, the additional soft iron plug was installed directly into the plasma chamber. The extraction soft iron plug was also adapted to the new chamber.

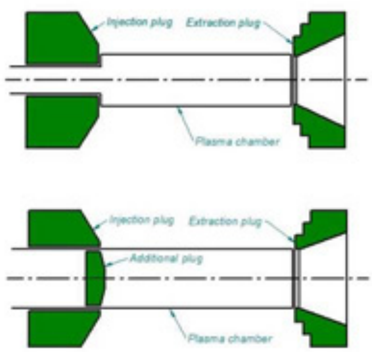

Figure 1: Schematic presentation of the old axial magnetic system (top) and the new axial magnetic system (bottom).

The comparison of the axial magnetic field distributions for the old and new versions of the axial magnetic system is shown in Fig. 2. The small magnetic field drop at the extraction side can be easily compensated by increasing the extraction coil current, Iextr, over 1000 A (the power supply can provide the current up to 1300 A).

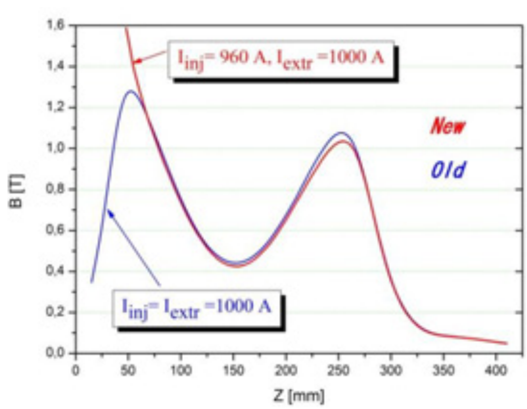

Figure 2: Axial magnetic field distributions for the old and new versions of the magnetic system.

The old hexapole magnet for radial confinement of plasma was replaced with a new one, allowing installation of the new plasma chamber with a bigger external diameter. The new hexapole with a Halbach type structure consisted of 24 identical trapezoidal sectors made of permanent magnet material (NdFeB) with the appropriate easy axis direction. In order to obtain a smooth magnetic field distribution along the pole, each sector was made from a single piece of magnetic material. This technology eliminated some imperfections in the magnetic field near the permanent magnet junctions. The inner diameter, outer diameter, and length of the hexapole were 80 mm, 170 mm, and 200 mm, respectively. The comparison of the radial magnetic field distributions for the old and new hexapoles is shown in Fig. 3. The measurements were performed on the plasma chamber wall in front of the pole. It is obvious that the application of the modern magnetic material and new construction technology provided a higher level of magnetic field, despite the fact that the new hexapole inner diameter was bigger and the outer diameter was smaller than the corresponding dimensions of the old one.

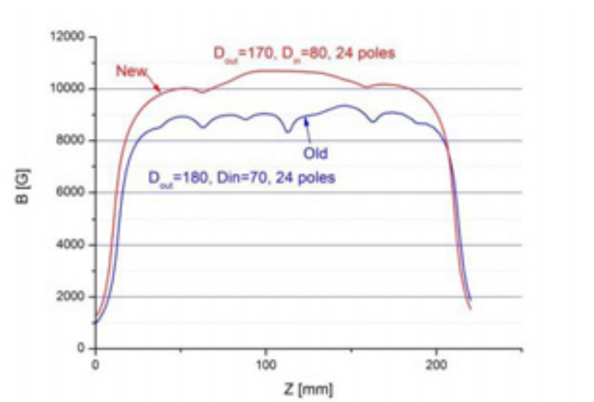

Figure 3: Radial magnetic field distributions for the old and new hexapoles.

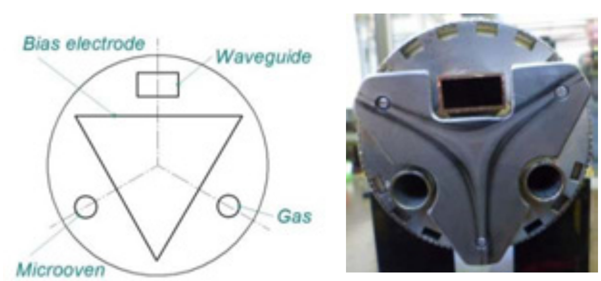

Figure 4: Injection side of the plasma chamber.

The microwave power is introduced directly into the plasma chamber through a standard waveguide. Two identical stainless steel tubes situated out of the axis are used for gas feeding and insertion of a miniature oven for evaporation of solid materials. A biased electrode made of tantalum is mounted on the soft iron plug. The shape and size of the bias electrode are chosen to protect the iron plug from direct interaction with plasma. The disposition of these elements is shown in Fig. 4.

The cross-sectional view of the new version of the mVINIS Ion Source is shown in Fig. 5. The maximal current of the injection and extraction coils is 1300 A. The additional iron plug installed directly inside the discharge chamber significantly increases the injection magnetic

ISBN 978-3-95450-158-8

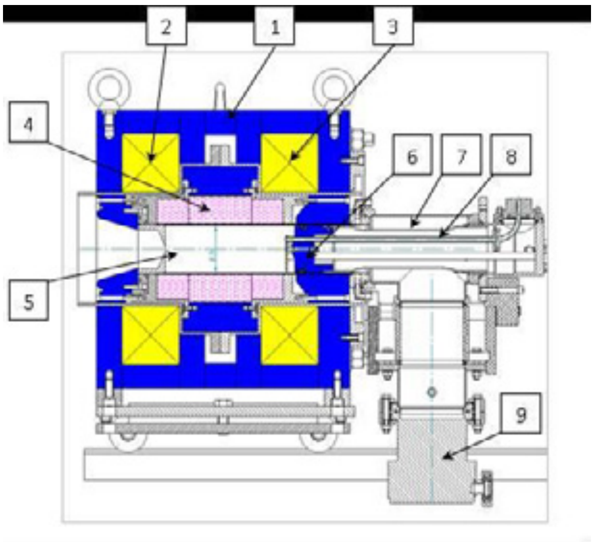

Figure 5: Cross sectional view of the mVinis Ion Source: 1 – the yoke, 2 – the extraction stage coil, 3 – the injection stage coil, 4 – the hexapole magnet, 5 – the plasma chamber, 6 – the additional iron plag, 7 – the injection chamber, 8 – the waveguide, and 9 – the turbomolecular pump.

field. At the full excitation of the injection solenoid, the magnetic field at the injection side can reach 1.8 T. This strong field significantly reduces the ion diffusion at the injection side and consequently increases the extracted beam intensity. The injection flange supports the soft iron plug, standard waveguide, gas feeding tubes and bias electrode. The working gases (e.g., Ar, Kr and Xe) and the supporting gas (He or O2) are introduced into the chamber with two fine gas dosing valves.

RESULTS AND CONCLUSION

The modernized ECR ion source was tested with a new 14.5 GHz UHF klystron power amplifier and the completely refurbished vacuum system (the new turbomolecular and cryogenic pumps), the gas inlet system, the solid substance inlet system, and the control system. The source was tested for production of Ar, Xe and Pb ion beams. During these tests, the operation of the source was very stable and reproducible. The obtained results have shown a substantial increase of the ion beam intensities, especially in the case of high charge state ions.

A comparison of the obtained results with the best results obtained with the old mVINIS Ion Source has shown that the increase of the intensities are mostly in the range from 50 to over 100 %. As an example, one of the obtained spectra of xenon ions is shown in Fig. 6. We used enriched isotope 129Xe with oxygen as a support gas and the source was tuned to maximize the Xe20+ production. The extraction voltage was 20 kV.

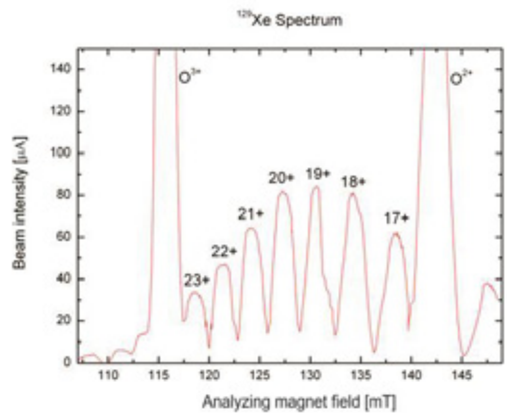

Figure 6: A spectrum of xenon ions optimized for maximal Xe20+ production.

REFERENCES

[1] B. Jacquot and M. Pontonnier, The new 10 GHz CAPRICE source – magnetic structures and performances, Proc. of the 10th International Workshop on ECR Ion Sources, Oak Ridge, USA, 1990, pp. 133-156.

[2] A. Efremov, S. L. Bogomolov, V. B. Kutner, A. N. Lebedev, V. N. Loginov, N. Yu. Yazvitsky, A. Dobrosavljević, I. Draganić, S. Djekić and T.Stalevski, Rev. Sci. Instrum., Vol. 69, No. 2, Part II, February 1998, pp. 679-681.

[3] A. Dobrosavljević, I. Draganić, S. Djekić, T. Stalevski, A. Efremov, V. Kutner and N. Yazvitsky, Commissioning of the mVINIS Ion Source, Proc. of the 15th Int. Conf. On Cyclotron and their Application, Caen, France, 14-19 June 1998, Institute of Physics Publishing, Bristol, 1999, pp. 443-446.

[4] A. Dobrosavljević, M. Milosavljević and N. Bibić, Rev. Sci. Instrum., Vol. 71, No. 2, 2000, pp. 786-788.

ISBN 978-3-95450-158-8

LEGIS FACILITY FOR STUDY OF REACTOR STEELS RADIATION RESISTANCE

A.Galatà, M.Comunian, INFN/LNL, Legnaro (PD), 35020, Italy
T.Kulevoy, A.Aleev, S.Rogozhkin, ITEP, Russia, and NRNU MEPhI, Moscow, Russia
S.Andrianov, B.Chalykh, R.Kuibeda, A.Nikitin, ITEP, Russia

Abstract

Considerable efforts have been drawn to adapt heavy ion beams imitation experiments for investigation of radiation stability of materials in nuclear industry, mainly structural materials - steels. Formation of defect structure in the steel using the neutron flow from the nuclear reactors is fraught with many difficulties such as a long-term session of exposure and induced radioactivity in the irradiated samples. Heavy ions instead could provide a versatile tool to induce a precise damage in material under controlled condition. The LEGnaro ECR Ion Source (LEGIS) installed on a high voltage platform (up to 300 kV) allows for the unique possibility of a program for reactor steels investigation by several heavy ion beams. The sample irradiation up to hundreds of dpa (displacement-per-atom) in less than an operation day can be provided by beams of different ions ranging from hydrogen to the iron with different energies. The investigation program and details of experimental facility are presented and discussed in the following.

INTRODUCTION

Nowaday, due to the active development of nuclear power engineering, an actual issue is the investigation of new structural materials for the active zone of nuclear reactors. The exploitation properties degradation of reactor materials is mainly initiated by local structure faults that appear under the influence of high energy particles. Microstructure alterations in materials can be observed both at the grain scale and at the atomic level. Examples of negative macroscopic consequences of these processes are irradiation swelling, embrittlement, irradiation induced growth, and a number of other changes in material properties (see, for instance, [1, 2]).

To characterize structural materials and evaluate their residual operation period, accumulation of corresponding damaging doses under conditions close to real ones is required. It takes too much time and it is not always justified. For example, the accumulation of a dose of ~100 dpa (displacement-per-atom) upon neutron irradiation is achieved for several years even in fast fission reactors. An accelerator-based neutron source is under developing in framework of IFMIF project. It aims at constructing quite an intense (about 10^{17} s^{-1}) 14 MeV neutron source facility, in order to test materials which are foreseen to be employed, as critical components in the future fusion reactors. But even after the IFMIF facility starts operation the test procedure will take significant amount of time and, besides, neutron irradiation leads to a high induced radiation activity of materials, which significantly complicates further investigations.

In structural materials for nuclear reactors, radiation defects are formed, first of all, due to elastic collisions with neutrons. They are generated non uniformly, in cascades of atom–atom collisions.. A neutron with energy of 1 MeV transfers about 70 keV to a primary knocked on atom (PKA) of iron, which is the main chemical element of steels. It is assumed that a PKA with an energy more than 50 keV creates subcascades with an average energy of about 20–30 keV. Low energy ions can simulate PKAs similar to those formed upon neutron reactor irradiation and, correspondently, can simulate cascades that are typical of neutron irradiation. Therefore, over a long period of time, there have been developed methods of express analysis of materials (imitation experiments) with the use of ion beams [3–10].

The LEGnaro ECR Ion Source (LEGIS) installed on a 300 kV High Voltage Platform (HVP) enables the allows for the possibility of a program for reactor steels investigation by several heavy ion beams. The sample irradiation up to hundreds of dpa in less than an operation day can be provided by beams of different ions ranging from hydrogen to the iron with different energies. The continuous beam generated by an ECR source provides many advantages for the imitation experiments. First of all it allows controlling the heating of the samples. Therefore the temperature dependence for irradiation swelling and embrittlement can be investigated in temperature range typical for fusion and fission reactors. Since beams from an ECR can be widely varied in intensities, in addition to investigation of defect generation dependence on the dose, the investigation of the dose accumulation velocity that influence on the defect generation can be carried out as well. Even if it is impossible now to provide at the existing lay-out the simultaneous irradiation of samples by two beams (iron and hydrogen or helium), it is possible to provide mix irradiation by those beams just by selecting the different ion by means of a bending dipole without stopping the ECR operation.

Therefore the developing of imitation experiments with the LEGIS source at LNL provides the good experimental base for material radiation resistance investigation. Those investigations, which are under developing in collaboration with ITEP and MEPhI (Moscow) will be the first step (so called express-analysis) for materials developed for future reactors before their tests at the IFMIF-EVEDA facility.

The experimental lay-out including the target assembly as well as the beam dynamics simulation throughout of

ISBN 978-3-95450-158-8

LEGIS High Voltage Platform (HVP) to the irradiated samples are presented and discussed.

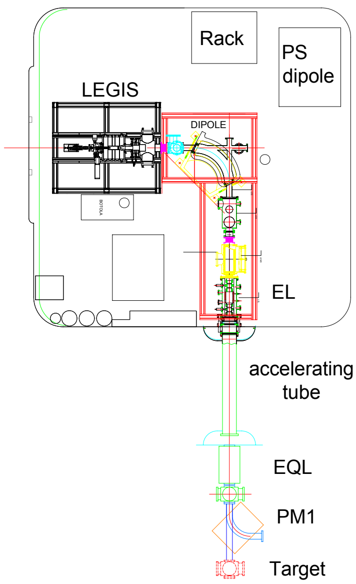

Figure 1: Experimental lay-out.

EXPERIMENTAL LAY-OUT

The experimental lay-out is shown in **Figure 1**. It is an injector for PIAVE superconducting RFQ in LNL-INFN. It is based on the ECR ion source LEGIS (LEGnaro Ion Source - Figure 2) installed at the 300 kV High Voltage Platform (HVP - Figure 3).

LEGIS, High Voltage Platform, Transport Channel

LEGIS is a SUPERNANOGAN type ECR ion source built by Pantechnik for LNL. It provides beams of different materials to be injected in the following SC RFQ PIAVE working as injector for the SC linac ALPI [13].. It is expected that it will provide the beam of Fe^{10+} with an intensityof at least 1 μA. Such beam, accelerated by 200 – 300 kV in accelerating tube, will induce on the target the integral dose of 10^{15} particles/cm^2 in less than half of hour, corresponding to few dpa. The beam with current 10 μA will provide the dose of 10^{18} particles/cm^2 during two days of ion source operation. That dose overcome maximum requested dpa generation. Now Fe ion beam generation by the MIVOC technique is under preparation. We plan to use Ferrocene. Additional advantage of the Ferrocene is the high part of hydrogen ions in the same beam. Therefore the hydrogen beam can be delivered to the target by simply tuning the bending dipole as well as the energy to provide the same depth of implantation for both hydrogen and iron ions.

Figure 2: LEGnaro ECR Ion Source LEGIS.

Figure 3: 400 kV high voltage platform, accelerating tube, electrostatic quadrupoles and PM1.

Focusing elements are located at the input and output of accelerating tube. to ensure beam matching. The line ends with a diagnostic box called PM1 and a bending dipole. The 0° port of this dipole will be used to install the target. The electrostatic triplet at the AT output enables the beam matching with target assembly as it will be shown below.

Target

Target assembly is under developing now. It has to provide the following experimental condition –

i) the vacuum should be better then 10^{-7} mB. It is necessary both to minimize the residual gas atoms insertion into the samples under ion beam bombardment

Figure 4: Samples holder.

ISBN 978-3-95450-158-8

and to keep high vacuum in PIAVE transport channel

ii) the samples heating system has to provide the stable samples temperature during the irradiation. The temperature range is from room temperature to 700°C. Temperature stability during irradiation should be better than ±2°C The target holder will be similar to the one developed for experiments in ITEP and shown in **Figure 4**. Seven samples with diameter of 3 mm can be irradiated during one beam session. They are mounted inside the removable sandwich installed at the cooper holder. Cooper holder has axial hole for heating element and several holes for thermocouple detectors. As it was shoun during experiments in ITEP, using the PID regulator such holder construction provides the samples smooth heating to the required temperature as well as the stability of that temperature within ±1°C. To avoid the heating of target assembly vacuum tank, the tank is designed with water cooling channel. Required heat gradient between sample holder and vacuum tank is provided by the two stainless stars shown in the figure. The dimensions of all elements both for holder and stars and tank were defined by the simulation with COMSOL code [11].

Beam Simulation

The beam dynamics simulation after beam selection to the target assembly was carried out by the TraceWin code [12]. Both transversal emittances and the Twiss parameters for initial beam are shown in **Figure 5** Transport line includes several drift gaps, two electrostatic lenses, accelerating tube and electrostatic quadrupole triplet. The channel parameters were optimized to form the beam spot at the point of samples location with rather uniform distribution inside the diameter of 10 mm. The simulation was carried out with "ideal" fields into all focussing elements. As one can see in figure the beam can be transported along all channel without losses and provide the required spot at the samples surfaces. Moreover the beam is convergent in both planes. Therefore it is possible to change the beam density at the samples by the last triplet tuning only keeping all other parameters of beam line stable.

CONCLUSION

The LEGnaro ECR Ion Source (LEGIS) installed on the 300 kV High Voltage Platform (HVP) allows for the unique possibility of a program for reactor steels investigation by several heavy ion beams. The imitation experiments for material irradiation resistance investigation in collaboration with ITEP and MEPhI (Moscow) are now under preparation. The beam dynamics simulation demonstrated the possibility of Fe10+ ion beam transportation with necessary parameters to the target without losses.

REFERENCES

[1] L. I. Ivanov and Yu. M. Platov, *Radiation Physics of Metals and Its Applications* (Interkontakt Nauka, Moscow, 2002) [in Russian].

[2] V. N. Voevodin and I. M. Neklyudov, *Evolution of Structural Phase State and Radiation Strength of Structural Materials* (Naukova Dumka, Kiev, 2006) [in Russian].

[3] R. S. Nelson, D. J. Mazey, and J. A. Hudson, "The Use of Ion Accelerators to Simulate Fast Neutron_Induced Voidage in Metals," J. Nucl. Mater. 37, 1–12 (1970).

[4] A. D. Marwick, "The Primary Recoil Spectrum in the

Emittance_RMS=0.0686
alfa=0.311
beta=0.422
Emittance XXp - 0.0686 P.mm.mrad
Emittance YYp - 0.0686 P.mm.mrad
alfa=0.311
beta=0.422

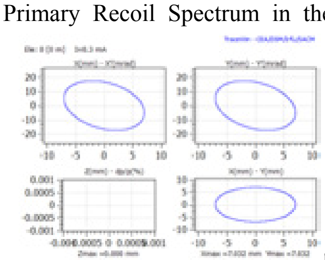

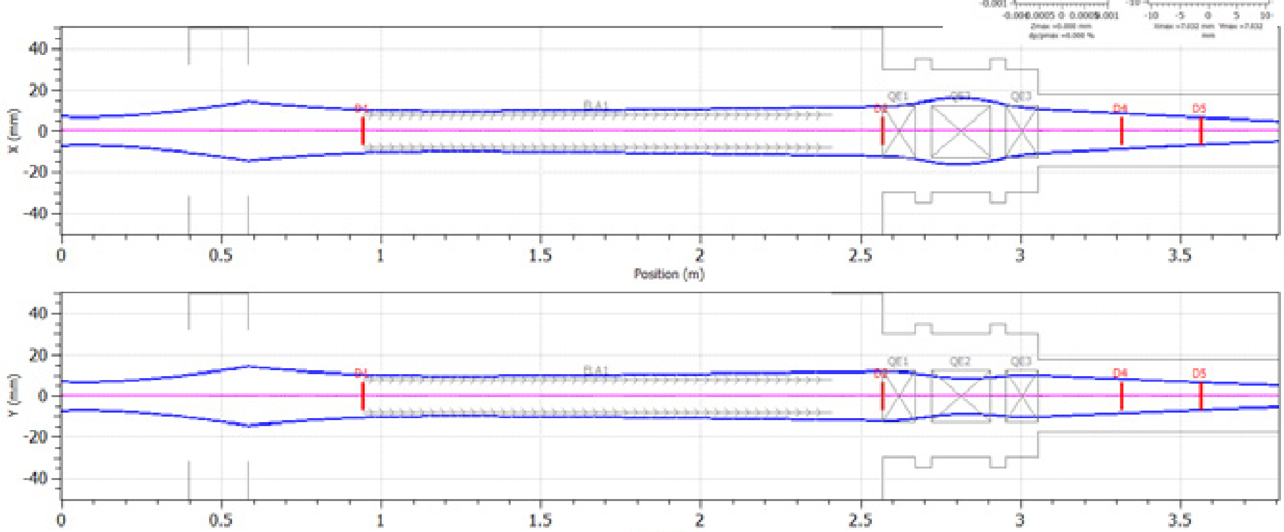

Figure 5: Fe10+ ion beam dynamic simulation. Initial beam parameters and the beam envelope evolution along transport channel.

ISBN 978-3-95450-158-8

Simulation of Fast_Reactor Radiation Damage by Charged_Particle Bombardment,” J. Nucl. Mater. 55, 259–266 (1975).
[5] Ishino Shiori, “A Review of in Situ Observation of Defect Production Heavy Ions,” J. Nucl. Mater. 251, 225–236 (1997).
[6] V. Voyevodin, I. Neklyudov, G. Tolstolutskaya, V. Bryk, J. Fomenko, and R. Vasilenlo, “Modern Status of Accelerators in R&D of Structural Materials for Nuclear Reactors,” http://www_pub.iaea.org/MTCD/publications/PDF/P1433_CD/darasets/papers/ap_int_02.pdf
[7] S. Pellegrino, P. Trocellier, S. Miro, Y. Serruys, Bordas , H. Martin, N. Chaвbane, S. Vaubaillon, J.P. Gallien, L. Beck, "The JANNUS Saclay facility: A new platform for materials irradiation, implantation and ion beam analysis", NIM, 273 (2012) pp.213–217
[8] G.N. Kropachev et al.,“ITEP HEAVY ION RFQ OUTPUT LINE UPGRADE FOR EXPERIMENTS OF REACTOR MATERIAL INVESTIGATION UNDER IRRADIATION”, http://www.lnl.infn.it/~HIAT09/papers/poster/A6T.pdf
[9] T. Kulevoy et al.,“ITEP MEVVA ion beam for reactor material investigation”, and S. Rogozhkin, REVIEW OF SCIENTIFIC INSTRUMENTS 81, 02B906 (2010)
[10] N. Orlov et al., "Tomographic atome probe investigation of chemistry alteration in oxide dispersion steel ODS Eurofer under heavy ion irradiation", Junior Euromat July 2012, pp. 23-27, http://webdb.dgm.de/dgm_lit/prg/FMPro?-db=w_review&-recID=33862&-format=prog_kurzfassung.htm&-lay=Standard&-find
[11] http://www.comsol.com/
[12] http://irfu.cea.fr/Sacm/logiciels/index.php
[13] A. Galatà, T. Kulevoy et al "FIRST BEAMS FROM THE NEW ELECTRON CYCLOTRON RESONANCE SOURCE LEGIS (LEGnaro ecrIS) AT INFN-LNL" RSI 81, 02A315 (2010)

A MICROWAVE ION SOURCE FOR PULSED PROTON BEAM PRODUCTION AT ESS-BILBAO

R. Miracoli*, I. Arredondo, D. Belver, I. Bustinduy, J. Corres, P. Echevarria, M. Eguiraun, Z. Izaola, N. Garmendia, P. Gonzalez, L. Muguira, I. Rueda, ESS-Bilbao, Spain

Abstract

Ion Source Hydrogen Positive (ISHP) is a microwave discharge installed at ESS Bilbao in Spain. This source will be employed in future application of high proton current in the field of research projects and for industrial processes. ISHP produces over 30 mA of pulsed proton beam by operating at 2.7 GHz. The magnetic field is produced by two independently movable coil pair and the extraction system is composed of a plasma electrode at high voltage platform potential, two ground electrodes and a negatively biased screening electrode inserted between the ground electrodes. The last three electrodes are contained in the extraction column, and can be moved as a group by stepper motors, to change the distance between the plasma electrode and first ground electrode. Measurements with different extraction system setups will be described to show the improvement of the beam intensity and beam emittance.

INTRODUCTION

The microwave discharge ion sources for proton production are widely employed in many areas of the research and for a growing number of industrial application, because they have many advantages in terms of compactness, high reliability, reproducibility, and low maintenance. These sources are used to work at low frequency and they require only an axial magnetic field distribution in order to dissociate the H_2 molecules and to produce high proton beams. At ESS Bilbao there is a very versatile proton source, ISHP that is able to support a wide variety of experiment. In fact the source can work for different values of duty cycle and for each configuration it's possible to optimize the magnetic confinement by changing the solenoid position and coils current. Moreover it's possible to change the distance between the plasma electrode and the puller electrode, adapting the beam dynamics with the extraction voltage and plasma conditions.

PROTON SOURCE

ISHP is composed by a water-cooled, cylindrical plasma chamber, made of copper 97 mm in length and 80 mm in diameter. A RF generator produces continuous or pulsed signal at the resonant frequency of 2.7 GHz, the microwaves, then, are amplified by a 2 kW, S-band satellite communications Klystron. The RF chain is, also, composed of a circulator with a water load to protect the klystron from excessive reflected power, a triple stub tuner placed between two directional couplers, is used to match plasma impedance with that of the waveguide. The tuner is composed of three rods that can penetrate inside the waveguide allowing to match the plasma load to impedance of the power transmitter system to transfer the maximum power [1, 2]. The microwave line also comprises a quartz RF window acting as a vacuum seal, a E-plane bend and a coupler, that is a double ridge stepped waveguide transition. The last one is a matching transformer which couples the rectangular waveguide to the plasma chamber and concentrates the electromagnetic field increasing plasma density [3].

The extraction system is composed of a plasma electrode at high voltage platform potential, two ground electrodes, and a negatively biased screening electrode (repeller) inserted between the ground electrodes. The last three electrodes are contained in the extraction column, and can be moved as a group by stepper motors, to change the distance between the plasma electrode and first ground electrode. In this way it can be possible to optimize the beam focusing for different experimental set-ups in terms of extraction voltage, plasma parameters, and beam current. The plasma electrode has 7.5 mm diameter aperture, and is made of copper plated pure iron. The ion source, the microwave line, and their complementary components are installed on a 75 kV high voltage platform.

Figure 1: Layout of ISHP source: the klystron, the RF chain and components, and the plasma chamber are installed on a high voltage platform.

Magnetic System

At 2.7 GHz the resonant field (B_{ECR}) is 0.964 T. The B_{ECR} is provided by two movable solenoids, shown in fig-

* rmiracoli@essbilbao.org

ISBN 978-3-95450-158-8

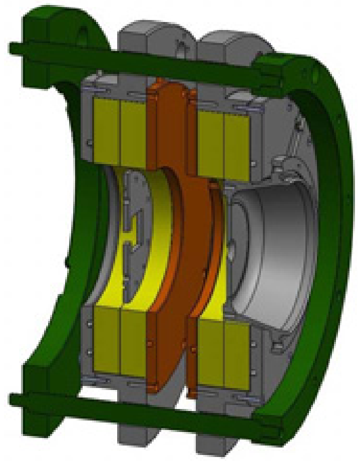

Figure 2: A scheme of the Magnetic System: in yellow the 4 coils, in grey the pure iron part, in green the stainless steel component and in orange the water cooling system.

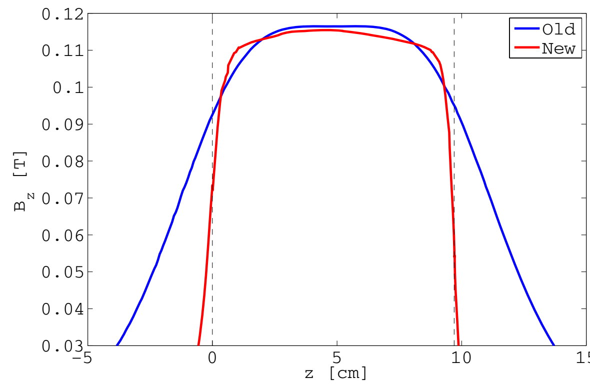

Figure 3: Comparison between the old and the new magnetic system.

ure 2, each solenoid can be moved independently by two stepping motors. Moreover each solenoid is divided in two coils, independently powered and enclosed by a ferromagnetic yoke. In figure 3 the blue line is the simulation of the axial magnetic field along chamber axis, obtained with the original magnetic system: B_z was too high in the extraction region where is necessary to limit the risks of breakdown. In order to limit the risks of Penning discharge in region of large electric field and cross magnetic induction it has been chosen to replace the orignal copper plasma electrode with a new one made in soft iron, in such a way the magnetic components can close the magnetic return path, and decreases the magnetic field in the extraction region. Moreover the firsts plasmas weren't stable and high values of reflected powers have been measured, since the microwaves could be absorbed inside the coupler at cyclotron harmonics. We have thought to put a soft iron plate between the coupler and plasma chamber, shown in figure 2. 3D finite-element simulation Comsol were, also, used to verify that the new magnetic system was able to produce a magnetic field higher than B_{ECR} inside the plasma chamber, in figure 3 there is a comparison between the two magnetic systems [4]. To test the accuracy of the simulations, the axial magnetic field B_z was measured with a Hall probe along the centerline of the chamber. The experimental results show a good agreement between the measured and simulated fields; there are deviations of only tenths of mT [4].

LEBT

The Low Energy Beam Transport (LEBT), following the extraction system, is nowadays composed of two vacuum vessel, as shown in figure 4. In each diagnostic chamber there is an ACCT to determine the beam losses in LEBT section, and a wire scanner in order to measure the beam profile produce by the source by changing the extraction gap and other plasma parameters. Between the vacuum vessel there is a solenoid, that have two steerers located inside it.

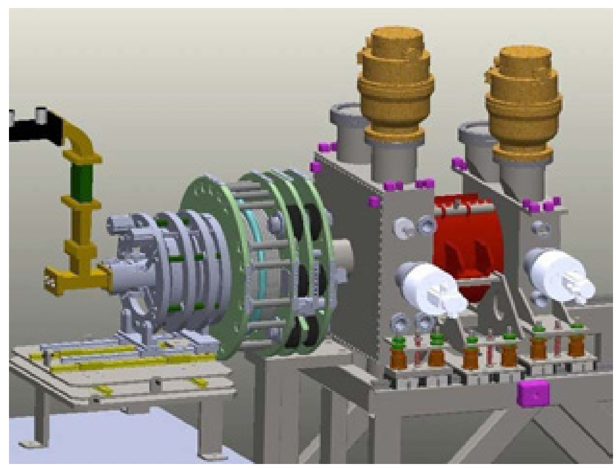

Figure 4: Layout of ISHP LEBT.

EXPERIMENTAL RESULTS

One of the peculiarities of our source is the possibility to move the electrodes of the extraction system. By changing the distance between the plasma electrode and the puller one changes the beam focusing, so it effects the beam density that reach the two ACCT, the beam shape and beam divergence. In order to find the optimal extraction gap the measurements were performed through several days with differently tunned plasmas. To get the profile of the beam, two wire scanners have been used. The wire scanners consist of two 0.2 mm tungsten wires mounted on the same support, we can chose the start and the stop of the measurements, the distance between the acquisition point and for each position we can chose the number of the pulse to be averaged. While the device sweeps the wires cross the beam, carried out a signal proportional with the number of the particles interacting with the wire, so the beam profile is acquired pulse by pulse.

ISBN 978-3-95450-158-8

The distance between the plasma electrode and the puller (the extraction gap) has been moved from 8.5 mm to 14 mm. In these measurements we fixed the extraction voltage at 45 kV and the microwave power at 600 W; the beam pulse was 1.5 ms and the repetition rate was 10 Hz. For each position the source parameters have been set in order to extract stable and intense beams, after that two wire scanners have been used to acquire the beam profile. Typical profiles measurements are shown in figure 5, where the signals are carried out by means of the wire scanner located in the first vacuum vessel and by putting a beam collimator in front of the wire scanner (to avoid unwanted particles that cause to increase beam size). The advantage to have a vacuum vessel next to the extraction system is to have the opportunity to investigate how the plasma parameters can affect the beam without the use of magnetic lens.

Figure 5 shows beam profiles for three values of the extraction gap: 8.5 , 10 and 11 mm, and for each curve the signals intensity, the peak position and sigma have been calculated, see table 1. The wire scanner signals are higher in correspondence of smaller extraction gap (8.5 mm), and if we compare the distance between the two peaks of the beam profiles, it is evident that at 8.5 mm increase the beam dimension, in correspondence of higher currents. Moreover the transmission of the beam trough the LEBT has been measured, by comparing the current of the two ACCT and by using the solenoid. The beam transmission is about 74 % at 8.5 mm, then it starts to increase and reaches 78 % only for extraction gaps included between 9.5 and 10.5 mm, at higher distances the transmission decrease until 76 %. Additional measurements will be done in order to verify the optimal extraction gap at different values of the platform voltage. At the same time the measures of beam emittance will be carried out in the next month by means of a pepper pot, that will be located in the second vacuum vessel and will yield more information about beam divergence

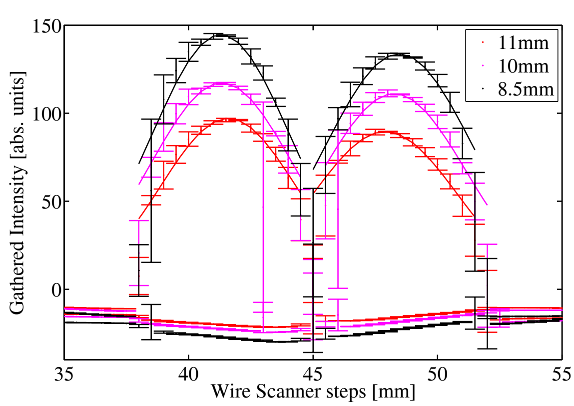

Figure 5: Typical profile measurements, obtained for three different extraction gap: 8.5 mm (black), 10 mm (pink) and 11 mm (red).

Other measurements has been done by changing the duty cycle (pulse width and repetition rate). The typical wave form of the pulse detected in two ACCT is shown in figure 6,

Table 1: Characterization of beam profile.

	Intensity [a. u.]	Peak position[mm]	σ [mm]
8.5 mm			
$Wire_1$	144.68	41.3	2.77
$Wire_2$	133.83	48.46	2.97
10 mm			
$Wire_1$	117.26	41.33	2.86
$Wire_2$	111.16	48.26	2.88
11 mm			
$Wire_1$	97.14	41.6	2.7
$Wire_2$	89.57	47.89	2.89

the operating parameters were: RF power 600 W, platform voltage 45 kV, and repeller −1.25 kV, pulse width 3 ms and repetition rate 20 Hz. The rise time is about 100 µs.

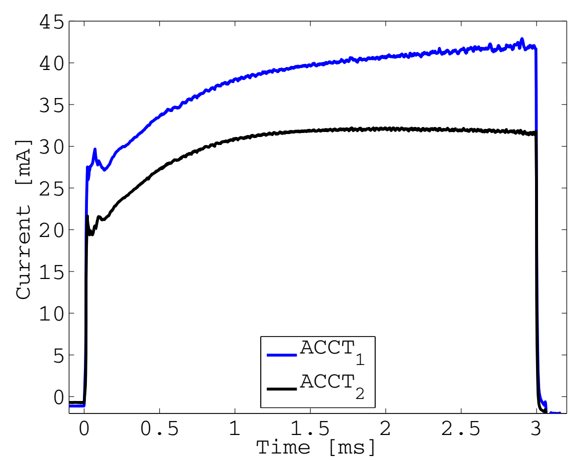

Figure 6: 45 KeV extracted beam current measured with two ACCT located in the first and the second vacuum vessel respectively.

CONCLUSION

IHSP is a versatile proton source that is able to produce pulsed current higher than 45 mA and to work in pulsed mode for different pulse length (from 0.6 ms to a few ms) and repetition rate (from 1 to 40 Hz), by adapting in each configuration the magnetic confinement. Moreover by working at several values of platform voltage it can always optimize the beam focusing, adapting the extraction gap.

Furthermore in the future it will be necessary optimize the production of H^+, and in this respect the magnetic profile plays an important role not only in the heating processes but also affects the ion lifetime, so the current coils should be set to maximize the proton fraction. And the same time by working in pulsed mode it has been noticed in previous works [5] that the production of protons is affected by the pulse width and microwave power.

ISBN 978-3-95450-158-8

ACKNOWLEDGMENTS

The authors would like to thank the other team members for their contribution to this work especially J. Bilbao, X. Gonzalez, G. Harper, G. Mugika and A. Zugazaga.

REFERENCES

[1] L. Muguira et al., "Automatic tuner unit operation for the microwave system of the ESS-Bilbao h+ ion source", WEPPD070, *Proceedings of* IPAC'12, New Orleans, USA (2012).

[2] L. Muguira et al., Nuclear Instruments and Methods in Physics Research A 741, 95-103 (2014).

[3] L. Celona et al., "Design issues of the proton source for the ESS facility ", THPB076, *Proceedings of* Linac'12, Tel-Aviv, Israel, 1008-1010 (2012).

[4] R. Miracoli et al., Rev. Sci. Instrum. 83, 026117 (2014).

[5] R. Xu, et al., Rev. Sci. Instrum. 79, 02B713 (2008).

ISBN 978-3-95450-158-8

METALLIC BEAM DEVELOPMENT WITH AN ECR ION SOURCE AT MICHIGAN STATE UNIVERSITY (MSU)*

Derek Neben†, Dallas Cole, Daniela Leitner, Guillaume Machicoane, and Larry Tobos,
NSCL, East Lansing, MI 48824, USA

Abstract

Electron Cyclotron Resonance (ECR) ion sources have been used at MSU to provide metal ion beams to the coupled cyclotron facility (CCF), and in the future, for The Facility for Rare Isotope Beams (FRIB). The challenges of metallic beam production with ECR are in production, efficiency, stability and contamination. Future facilities such as FRIB will add the challenge of intensity. We report development of two rare earth metals and the conversion from the oxidized state into metal.The enriched isotopes of ^{144}Sm, and ^{176}Yb are commonly available in the sesquioxide form which is unsuitable for use in our standard ovens. We report here results from the off-line chemical reduction of samarium, and ytterbium oxides into metal. We were able to demonstrate efficiencies of up to 90% throughout the conversion process. The samples were then run on our ECR ion sources to confirm the products of the reduction. In addition we report the development of cadmium metal by passing vapor though over 3/4 m of heated stainless steel tubing and observed 4.3 eμA of Cd^{20+} with an average consumption of 1 mg/hr.

INTRODUCTION

The Coupled Cyclotron Facility(CCF) at Michigan State University provides the nuclear science community with beams of rare isotopes produced by fast fragmentation. All rare isotopes produced through CCF operation have been obtained from about 30 primary beams (from Oxygen to Uranium) accelerated to an energy range of 80 to 160 MeV/u. To enhance the yield of rare isotopes, the primary beam is generally a separated isotope with either the largest or the smallest neutron excess available. So far the primary beam list has never included rare earth elements. Specifically of interest for the nuclear science community are ^{144}Sm, and ^{176}Yb, for good production of proton rich and neutron rich elements respectively. Initial production of the ion beam is done using an ECR ion source. Normal operation of an ECR relies on feeding the plasma with the vapor of the element to be ionized. A practical problem with rare earth elements is that they are naturally found in an oxidized form that would require extremely high temperature to reach a decent vapor pressure (range of 10^{-2} to 10^{-3} mbar) for operation with an ECR. Therefore, we need to efficiently convert the available rare earth oxide into metal before using them with an ECR ion source.

* This work was supported by Michigan State University and the National Science Foundation: NSF Award Number PHY-1102511.

† neben@nscl.msu.edu

Also of interest are primary beams of ^{82}Se, ^{106}Cd, and ^{204}Hg. Due to the relatively high volatility of these metals [1]. it may be possible to control the flow of vapor into our plasma chamber with a simple setup that positions the sample outside the ion source and uses a variable leak valve and a heated transfer line to transmit the vapor to the plasma chamber. This was demonstrated recently in the case of mercury [2] where transfer of the vapor to the chamber and ionization by the ECR plasma lasted for about 150 hours.

CHEMICAL REDUCTION OF RARE EARTH SESQUIOXIDES

The chemical separation of metal oxides were investigated for the purpose of reducing calcium carbonate and calcium oxide (quicklime) into metal, and our procedure for the chemical conversion of the rare earth oxides is largely based on techniques developed for the benefit of the experimental program at NSCL. The rare earth metals (including scandium and yttrium) will readily oxidize into the sesquioxide, R_2O_3 [3], wherein R represents a rare earth element. The process to convert from the sesquioxide of samarium and ytterbium is known [4], and is reversible.

$$R_2O_3 + 2B \Leftrightarrow B_2O_3 + 2R \tag{1}$$

Metal B is the reagent to the reaction, and R is a rare earth metal. The chemical conversion will proceed in both directions if the temperature is sustained and the supply of materials allows. Extraction of a metal from the mixture occurs by diffusion with one metal leaving the mixture at a larger rate than the other. The reagent B is chosen to have a negligible vapor pressure in both elemental and oxide forms at the reaction temperature, to ensure minimal evaporation. According to [4] the oxides of ytterbium and samarium will undergo reactions with lanthanum reagent at 1350 °C and 1200 °C respectively. In the case of ytterbium sesquioxide the reduction-distillation will proceed at a temperature far below the oxide melting point. Furthermore, samarium and ytterbium metals are relatively stable in atmosphere unless heated in excess of 200 °C [5] and allowed for handling of pure metal samples in atmospheric conditions.

Procedure

Our experimental set-up is constructed of two basic parts, the oven which heats the oxide-reagent mixture and collector plates which captures metal vapor diffusing from the oven. The chemical conversions were performed in a vacuum chamber that could reach pressures of about 10^{-7} mbar.

ISBN 978-3-95450-158-8

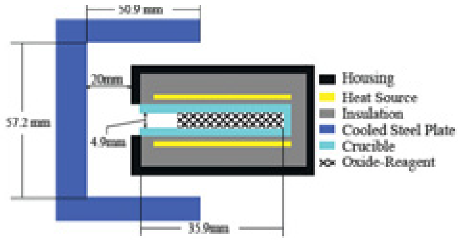

Figure 1: Schematic of reduction-distillation apparatus (not to scale) with a resistive oven, the oxide-reagent mixture may in general be heated by a resistive or inductive vaporization oven, and the more volatile rare earth metals distill out of the crucible and deposit on the steel plate.

Figure 2: Ytterbium metal deposited on the collector plates.

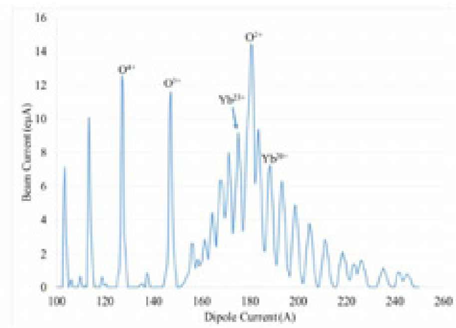

Figure 3: Natural ytterbium metal, reduced from the sesquioxide, as observed in ARTEMIS.

In order to maximize the reduction efficiency an excess of lanthanum was added to samarium and ytterbium sesquioxides. We used a molar ratio of lanthanum to rare earth metal between 8:7 and 3:2 and for comparison R. E. Reed and W. B. Grisham used an 11:10 ratio [6]. The lanthanum was stored in an anaerobic environment and was exposed to atmospheric conditions only when mixing and weighing. The oxide and reagent were then mixed and placed into a cylinder open at one end and is used as a crucible. The oxide-reagent mixture was pressed by hand to the rear of the crucible with a metal rod and then loaded into our oven. Compression of the mixture ensures good contact between rare earth oxide and lanthanum reagent, producing the largest yield [4]. The setup is summarized in Figure 1.

Although, typically conversions are performed with a resistive oven, sometimes an inductively heated oven capable of reaching a higher temperature was also used. The temperature of our oxide-reagent mixture was calculated from calibration curves taken with a thermocouple placed inside the crucible, and are listed in table 1. Reductions were typically maintained at temperature 12-24 hrs to ensure a complete distillation of the metal sample onto the water cooled plates.

Results and Discussion

The distilled rare earth vapor was deposited onto 5 stainless steel plates (3 are shown in Fig. 1). The collection plates are screwed into water cooled blocks to prevent heating of the plates and subsequent evaporation of the rare earth sample. By using separate plates the deposited metal is easier to remove from the surface. The rare earth sample was scraped from the stainless steel plate with a razor. Table 1 exhibits efficiencies of rare earth sample collection by weight as a percent of the ideal yield. Both of our ytterbium runs were performed with the resistive oven and the oxide-reagent mixture was compressed by hand. An image of ytterbium metal as deposited on our plate assembly is shown in Fig. 2.

Our lowest efficiency, at 39 % for the element Sm, was performed on our inductive oven and is probably due to poor compression of the oxide-reagent mixture and incomplete reduction of the samarium sesquioxide. In this case the geometry of our inductive oven did not allow for effective manual compression of the oxide-reagent mixture. Reduction efficiencies up to 90 % were achieved in the case of samarium using the resistive oven with good compression of the oxide-reagent mixture. Collected samples were placed into the ARTEMIS plasma chamber and heated.

ARTEMIS is a 14 GHz Electron Cyclotron Resonance (ECR) ion source based on the Advanced ECR-Upgrade (AECR-U) at Berkley [7]. The plasma chamber has radial openings allowing for access ports and vacuum pumping. Microwave powers of up to 2 kW are attainable however, a maximum of about 800 W was employed to produce highly charged ions of samarium and ytterbium. For these measurements the axial magnetic field in ARTEMIS was about 1.8 T at injection and 0.8 T at extraction. A charge state distribution for Yb and Sm metal samples are shown in Fig. 3 and Fig. 4 respectively.

Contamination due to evaporation of lanthanum reagent with the rare earth metal could not be evaluated because our resistive ovens do not reach high enough temperatures on-line to vaporize lanthanum. However, deposition of the lanthanum reagent onto the collector plate is likely a small effect due to the fact 1760 °C is required to reach a vapor pressure of about 10^{-2} mbar [1] and the reduction of both Sm and Yb was maintained below 1500 °C as shown in Table 1. Trace analysis of a reduced sample by a technique such as mass spectroscopy in an inductively coupled plasma is an avenue of further investigation.

Oxidation of the rare earth metals while exposed to atmospheric levels of oxygen for approximately 1-5 hr while

ISBN 978-3-95450-158-8

Table 1: Table of chemical conversions by weight.

Element	$R_2O_3(m\ )$	La (mg)	R (mg)	Residues (mg)	Temperature (°C)	Efficiency %
Yb	353	353	208	433	1200	66
Yb	251	252	196	302	1300	87
Sm	214	270	167	290	1500	90
Sm	203	277	68	260	1340	39

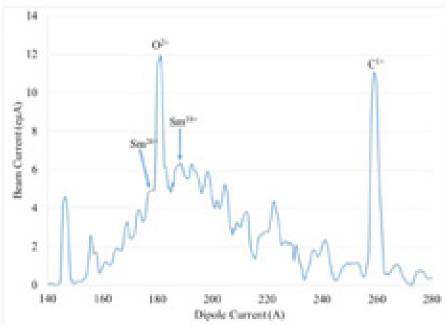

Figure 4: Natural samarium metal as obtained from reduction of the sesquioxdie, as observed in ARTEMIS. The ragged peaks are from the mass spread of 10 amu in the natural abundance of samarium metal, with the most abundant isotope is ^{152}Sm at 26.75 % [8].

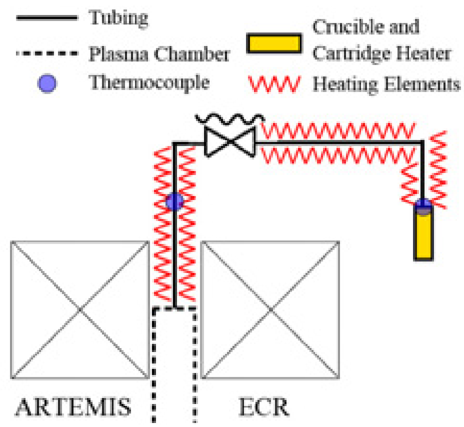

Figure 5: A schematic of the apparatus to produce cadmium vapor in reference to our ECR ion source. The cadmium sample is heated by a cartridge heater (yellow rectangle).

fabricating the alumina crucible for use in ARTEMIS is unclear. It is assumed some oxidation took place when exposing the samples to atmosphere and the photograph in Fig. 2 is representative of rare earth metal immediately after removal from vacuum. The rainbow of colors may be indicative of a thin oxide layer as is the case with bismuth [9].

Our experience in chemical reduction may be summarized in that larger temperatures and good compression of the oxide-reagent mixture produce the largest efficiencies. Furthermore, our results from ytterbium and samarium reduction are consistent with R. Reed and W. Girsham who reduced samarium oxide to metal over 6 hr with an efficiency of 94.9 % [6].

CADMIUM DEVELOPMENT

A technique was developed for the production of mercury ion beams on ARTEMIS. Mercury metal vapor was introduced into the plasma chamber, like a gas, though a variable leak valve and a heated transfer line. The ion source was operated using this setup for over 150 hours and we were able to achieve 4 eμA of Q=30+ with heating of about 60 °C. In addition the charge state distribution of mercury could be easily shifted toward higher of lower charge states by adjustment of the leak valve set-point [2]. With the aim to expand this technique, we sought to produce cadmium ions. A new heating scheme was developed to reach a temperature of up to 260 °C corresponding to a vapor pressure of 10^{-2} mbar in cadmium.

Oven Design

A schematic of the experimental set-up is shown in Fig. 5 in relation to our ion source.The vapor diffuses from the oven crucible to the plasma chamber though heated tubing and a bellows valve. The transfer line allows for vapor to enter the plasma chamber though the injection assembly on ARTEMIS. Connected to the transfer line is the sample reservoir which contains and heats the metal sample. The cadmium is loaded into a small stainless steel cylinder that is then sealed using a compression fitting onto the sample reservoir. The cadmium crucible and sample reservoir are visible in Fig. 6 without the cartridge heater installed.

The sample crucible was heated with a carbon cartridge filament and steel sheath screwed onto the bottom of the crucible. A K type thermocouple was wrapped around the cartridge heater sheath to provide an approximate sample temperature. The sample reservoir was wrapped in two heater tapes, as shown in Fig. 6, and then was wrapped in aluminum foil. The transfer line was heated with sections of threaded alumina tubing wrapped in filament wire. A second K type thermocouple was placed midway between two heaters to measure temperature as highlighted in Fig. 7. The transfer line is 79 cm in length and has an inner diameter of 4.8 mm.

Results and Discussion

Power to the transfer line heaters, heating tapes, and crucible cartridge heater could be independently controlled, and we maintained transfer line heaters and heater tapes

ISBN 978-3-95450-158-8

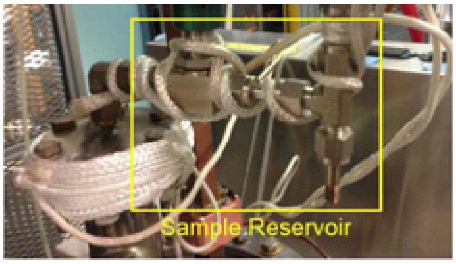

Figure 6: The sample reservoir as seen, without aluminum foil, exhibiting the heating tapes. In addition the bellows valves (green) and the sample crucible (on bottom) are shown. The crucible cartridge heater was removed for this photograph.

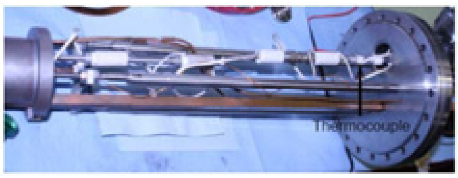

Figure 7: A photograph of the transfer line to transmit cadmium vapor through the ARTEMIS injection assembly with minimal losses. Heating elements are visible (white boxes) and an arrow points to our thermocouple (on right).

at a fixed setting while adjusting Cd vapor production by increasing the temperature of the crucible cartridge heater The bellows valve isolating the transfer line and sample reservoir was fully opened for operation, and we used the ion source vacuum system to evacuate the sample reservoir

A sample of natural cadmium was developed for the Q=20+ charge state. The most abundant isotope of cadmium, at 28.73 % [8], is atomic weight 114 and this isotope dominated our spectrum and was used to identify charge states. Cadmium was developed for 13 hrs with an average consumption of 1 mg/hr. The charge state distribution in Fig. 8 was obtained with a transfer line thermocouple reading of 140 °C and a sample temperature of 260 °C at a power consumption of 336 watts across all heating elements, with 65 % drawn by the heater tapes. Microwave power from the klystron was 500 W with a drain current of 1.2 mA at 23kV.

Initally an attempt was made to develop elemental cadmium using a variable leak valve similar to the one used

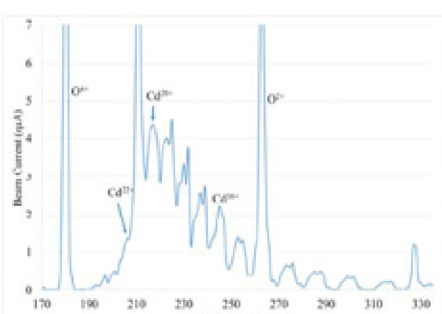

Figure 8: Cadmium as observed in ARTEMIS using the exterior oven technique.

previously with mercury. However, with cadmium we were unable to pass vapor though the leak valve, possibly due to cadmium vapor depositing inside the valve. A similar situation occurred when we tried to develop a selenium beam with the same setup using a variable leak valve, we observed excellent volatility of the selenium metal and residues were present throughout the sample reservoir but no metal was transmitted into the plasma. It is possible selenium vapor was stopped at the sapphire-copper interface inside the variable leak valve due to selenium-copper reactivity [5]. The variable leak valve was then replaced with a bellows valve as described above.

CONCLUSION

We demonstrated the efficient chemical conversion of ytterbium and samarium from the sesquioxide into elemental form with efficiencies up to 90 % without modification to our standard resistive oven. We were able to positively identify Yb and Sm samples by vaporizing these metals into ARTEMIS and observing the species distribution of the plasma. In addition we proved the concept of an exterior oven design previously used to provide mercury vapor is applicable to a metal such as cadmium. A beam current of 4.3 eμA of Cd^{20+} was measured for a sample temperature of 260 °C and, the exterior oven may be useful for developing selenium beams from the metal or dioxide.

ACKNOWLEDGMENT

The author would like to thank Alain Lapierre at the NSCL for his help in editing, and to Trevor Riedemann at AMES laboratory for guidance through literature on the reduction-distillation process.

REFERENCES

[1] K. J. Ross and B. Sonntag, *Rev. Sci. Instrum.* 66, 4409 (1995); doi: 10.1063/1.1145337

[2] Guillaume Machicoane, Dallas Cole, Daniela Leitner, et al. *Review of Scientific Instruments* 85, 02A957 (2014); doi: 10.1063/1.4858095.

[3] Jean-Claude G. Bünzli, Kirk-Othmer Encyclopedia of Chemical Technology, "Lanthanides" (John Wiley & Sons, Inc., Online, (2013)); doi: 10.1002/0471238961.1201142019010215.a01.pub3.

[4] E. H. Kobisk and W. B. Grisham, *Mat. Res. Bull.* 4, 651 (1969)

[5] P. Patnaik, The Handbook of Inorganic Chemistry, edited by K. McCombs, D. Penikas, S. Souffrance, et al. (McGraw-Hill, New York, 2003).

[6] R. E. Reed and W. B. Girsham, *Nuc. Instrum. Meth.* IO2 513 (1972).

[7] Z. Q. Xie and C. M. Lyneis, Proceedings of the 13th International Workshop on ECR Ion Sources, College Station, Texas, Feb 1997, p. 16.

[8] N. E. Holden, "Table of the Isotopes", in Haynes, W. M., Ed. CRC Handbook of Chemistry and Physics, 95th Ed., CRC Press, Boca Raton, FL, 2014.

[9] L. Msing and L. Youn, *Canadian J. Chem.*, 40, 903 (1962).

ISBN 978-3-95450-158-8

IMPROVEMENT OF BEAM INTENSITIES FOR ION BEAMS WITH CHARGE-TO-MASS RATIO OF 1/3 WITH THE TWO-FREQUENCY HEATING TECHNIQUE

A. Kitagawa#, T. Fujita, M. Muramatsu, NIRS, Chiba, Japan
Y. Kato, Osaka Univ., Osaka, Japan
K. Fukushima, N. Sasaki, K. Takahashi, W. Takasugi, AEC, Chiba, Japan

Abstract

In order to increase the beam intensities of ions with a charge-to-mass ratio of about 1/3 like Ar^{13+} and Fe^{18+} from an electron cyclotron resonance ion source (ECRIS), a technique was tested to feed multiple microwaves with different frequencies, the so-called two-frequency heating technique. Our group studied the improvements when the two frequencies are close together each with a power of more than 1kW using an 18GHz ECRIS installed in the Heavy Ion Medical Accelerator in Chiba (HIMAC) at the National Institute of Radiological Sciences (NIRS). The intensities of highly charged ions of C, Ar, Fe and Ni were increased successfully.

INTRODUCTION

Although the best ion species for heavy ion radiotherapy principally depends on the type and location of a tumor, a carbon ion beam was finally chosen at the Heavy Ion Medical Accelerator in Chiba (HIMAC) due to its better biological dose distributions than helium or neon for the typical depth and thickness of a tumor. Presently, seven carbon-ion radiotherapy dedicated facilities are operated worldwide. Four of the seven facilities are located in Japan. For the production of the carbon ions, ECRISs have been developed and utilized because its lifetime is longer than other types of ion sources. The ion sources satisfy medical requirements at each facility[1].

The Gunma University Heavy-ion Medical Centre (GHMC)[2], the Saga Heavy Ion Medical Accelerator in Tosu (SAGA-HIMAT), and the Ion-beam Radiation Oncology Centre in Kanagawa (i-ROCK, under construction), are facilities specific for carbon-ion radiotherapy exclusively. One ECRIS was installed in each facility. Compact ECRISs, named Kei-series, were developed[3] to reduce the size, initial construction cost, and electric power consumption. 'KeiGM', and 'KeiSA', were manufactured with minor modifications of the magnetic configuration and the high voltage insulation. Typically, the ECRIS has to deliver C^{4+} ions at 30 kV extraction voltage with current of at least 200 eμA[4]. KeiGM and KeiSA satisfy the requirements. At GHMC were during 20130 hours of operating time three serious failures which interrupted the patient treatment and Saga-HIMAT had no failures during 7200 hours.

Recently, several countries made plans to construct such a carbon-ion radiotherapy facility. However, in order to carry out biological experiments to encourage basic research in these countries, there are occasionally requirements to produce various other ion species. Since the injector design is fixed for the acceleration of ions with a charge-to-mass ratio of about 1/3, the performance of the Kei-series does not satisfy such requirements. We developed a new compact ECRIS, named Kei3, for ion species between He^{+} and Si^{9+}[5]. Kei3 is now under commissioning. However, production of highly charged ions like Ar^{13+} or Fe^{18+} will not be possible with that source. So we tested the ion production with charge-to-mass ratio of 1/3 by an 18GHz room-temperature ECRIS, named NIRS-HEC. In order to improve the intensity, we fed RF power into an ECRIS at two frequencies, the so-called two-frequency heating technique.

#kitagawa@nirs.go.jp

TECHNICAL METHOD

18GHz NIRS-HEC ECRIS

In order to extend the range of available ion species for HIMAC, NIRS-HEC was designed to reach a high extraction voltage and a high magnetic field with normal conducting magnets. For the production of intermediate charge-state ions, optimization of the extraction configuration is most effective. The extraction electrode is electrically isolated from the ground and a high voltage power supply on the source potential safely applies the extraction voltage between the plasma electrode and the extraction electrode independent of the source potential. The position of electrode can easily be changed. With these two parameters extraction configuration can be optimised. The maximum voltage between plasma and extraction electrode is 60 kV. The maximum mirror fields at the injection and at the extraction side are 1.3 and 1.2 T, respectively. NIRS-HEC supplied various ion species since 1996[6].

For a carbon-ion radiotherapy facility, NIRS-HEC has some drawbacks. Its initial construction cost is two or three times higher than Kei-series. Electric power consumption is huge. However, due to its vertical beam extraction, the footprint including an analyzing magnet system is not so different from Kei-series shown in Figure 1. In addition, NIRS-HEC has a long lifetime even for 'dirty conditions' like carbon depositions. NIRS-HEC is usually operated over a half year without ~~a~~ maintenance during which the vacuum chamber is not exposed to atmosphere. All operation parameters are set by a remote control system and are able to restore by a software. The failure rate is also low. These performances are suitable for a medical facility.

ISBN 978-3-95450-158-8

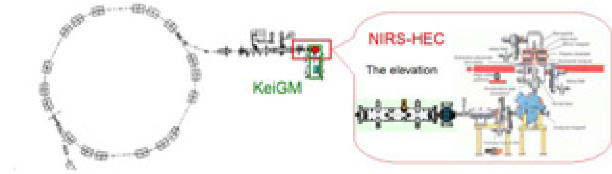

Figure 1: Footprints of NIRS-HEC and KeiGM with a carbon specified accelerator.

Two-Frequency Heating Technique

The two-frequency heating technique was initiated by ECR pioneers Jongen and Lyneis in Berkeley, and some years later more successfully by Xie and Lyneis again in Berkeley[7]. Since then many ECR laboratories have tested this technique. The two-frequency heating technique has advantages; it is effective for any kind of ion species, it is coexistent with almost other techniques, and no modification of existing structure is necessary. Between 1998 and 2013 numerous experiments were carried out in NIRS; in each experiment a positive effect of the second microwave was demonstrated[8]. The mechanism is still not completely clear. Our basic observation is that when the primary microwave power increases, the plasma shows instability and it is difficult to keep. When an additional microwave is added in the above situation, the plasma stability is improved at larger microwave power obtained by the mixture of two different frequency microwaves. The important points to obtain the highest effectiveness with this technique are as follows.

- To supply enough power for both microwaves.
- To precisely adjust the additional frequency. The best frequency depends on operation parameters; magnetic configuration, vacuum pressure, and so on.

The primary microwave source is an 18 GHz fixed frequency Klystron (KLY) amplifier system with a maximum power of 1500 W. The additional source is a travelling wave tube (TWT) amplifier system with the frequency range from 17.10 to 18.55 GHz and with maximum power of 1200 W. Of course, power stability is important for the reproducibility. Therefore, both microwave systems have installed a power feedback. The block diagram is shown in Figure 2.

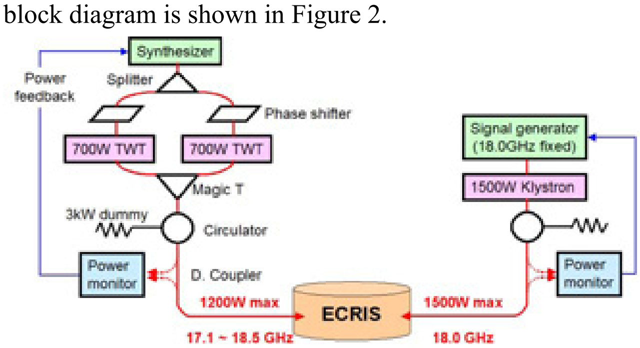

Figure 2: A block diagram of two-frequency heating system at NIRS-HEC.

MIVOC Method

Metallic ion species like Fe are especially interesting in biomedical researches, for example, to study the risks of space exploration due to galactic cosmic rays. The MIVOC is a method[9] to apply metallic vapors from volatile metallic compounds including the requested elements. MIVOC was adapted for the productions of Fe, and Ni ions. The biggest advantage of MIVOC is to be able to use a solid sample *as if it is a gas*. It is easy to operate and maintain and the equipment is small. The ion species can be changed without exposing the vacuum chamber to atmosphere. These features are also suitable for a medical facility.

The two-frequency heating technique is very sensitive to a gas pressure. For the precise and stable tuning of pressure, we used the thermal control system at a MIVOC compound container[10]. In the cases of Fe^{18+} and Ni^{19+}, the Peltier cooling system was utilized for ferrrocene and nickelocene. It works between 0 C° and room temperature.

EXPERIMENTAL RESULTS

Productions of Ar, Fe, and Ni

Figure 3 shows a typical mass spectrum of Ni from nickelocene. All operation parameters were optimised for Ni^{17+}. Peaks of oxygen appeared due to residual gas from the previous measurement. The intensity of Ni^{17+} was 26 eμA. In this case, the after-glow technique was effective[11]. The microwave powers of 18.0 GHz and 17.87 GHz were 630 W and 1100 W, respectively, while both generators were set with microwave width of 30 ms. The injection and extraction side mirror magnetic fields are 1.21 T and 0.74 T, respectively. The extraction voltage and distance between the plasma electrode and the extraction electrode are 31 kV and 20 mm, respectively. The gas flow of O_2 is 0.024 atom cc/min. The temperature of the MIVOC container is 23 C°. The vacuum pressure at the injection-side chamber was 3.3×10^{-5} Pa. Since the peak of $^{58}Ni^{18+}$ was covered by the peak of O^{5+}, the intensity was estimated at about 12 eμA from the peak of $^{60}Ni^{18+}$. Although the peak of $^{58}Ni^{19+}$ and $^{60}Ni^{19+}$ were covered, we expected an output current for $^{58}Ni^{19+}$ of a few or at least one eμA from the charge state distribution.

ISBN 978-3-95450-158-8

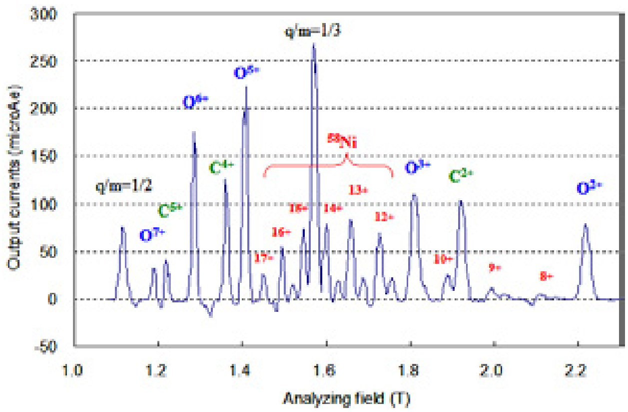

Figure 3: A typical mass spectrum of nickel ions produced with nickelocene. Oxygen gas was used as a support gas.

Production of C

Carbon production is the most important requirement for a carbon-ion radiotherapy facility. Although the two-frequency heating technique is not necessary for this purpose, we tested the effectiveness of highly-charged carbon ions. Figure 4 shows a typical mass spectrum of C from CH_4. All operation parameters were optimised for C^{5+}. The intensity of C^{5+} was 550 eμA under unsuitable conditions due to residual oxygen from previous productions. In this case, the after-glow technique was utilized. As a result, the technique was effective for C^{5+}, but not so much for C^{4+}.

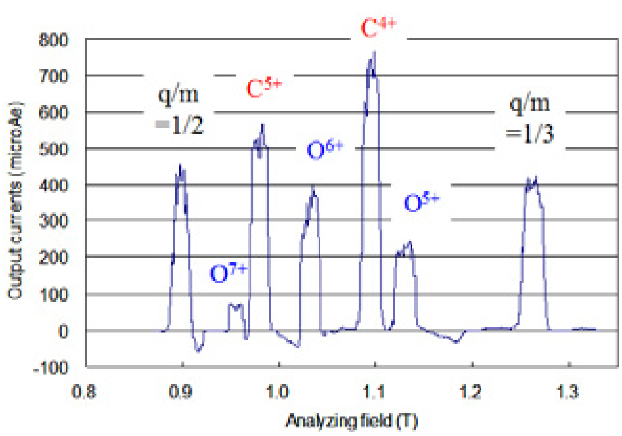

Figure 4: A typical mass spectrum of carbon ions produced with CH_4 gas. Oxygen impurities came from the previous residuals.

CONCLUSSION

Table 1 shows the highest intensity of Ar,, Fe, and Ni with the two frequency heating technique. The output currents for Fe^{18+} were 2 eμA. With this current the HIMAC facility can deliver a dose rate of several Gy/min in a diameter of 20mm at the biology experiment room shown in Figure 5, which is sufficient for cell experiments. However, it's better to obtain more intensities for animal experiments.

Table 1: Output currents of C, Ar, Fe, and Ni

Ion	5+	12+	13+	14+	15+	16+	17+	18+
C	**550**							
Ar		116	**42**	**15**				
Fe		130	120		70	41	12	**2**
Ni		110	83	78	75	56	26	12

Bold: available for acceleration by a carbon ion radiotherapy specified facility.
Ni^{19+} was estimated a few or at least one eμA from the other charge state.

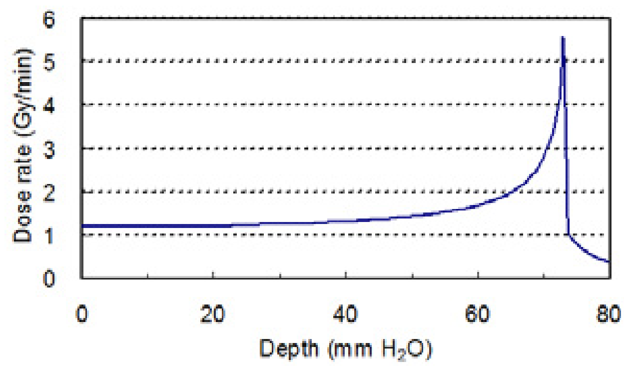

Figure 5: Estimated physical dose rate of Fe beam in a diameter of 2cm at the biology experiment room.

In order to consider the realistic possibility to use NIRS-HEC in a hospital, we must point out an important reality; an ion-source specialist is not expected in a hospital. The installation of gas bottles or MIVOC containers must be simple; complicated operation is not acceptable. All operation parameters must be stored for the software control system. How to check the reproducibility by non specialists? We must solve all of such problems.

Another problem is an interval to exchange ion species. The hysteresis appears in the routine operations to produce different ion species cyclically. It caused the delay to reproduce an expected operation condition. The reason of the hysteresis is mainly caused by the varying surface condition of the plasma chamber. So the interval time strongly depends on the ion species. It is typically a few or several hours. If the facility does not allow the interval between the treatment and the experiment, we must have two sources for exchange ion species quickly.

The importance of fine tuning of the second microwave frequency was observed in early stages of our development[12]. We guessed the additional frequency controls anisotropy of electrons' velocity distribution and it may affect the plasma instability. Some recent observations of the additional frequency dependence suggested that an electron orbit effect might play some role[8]. One approach to verify or to reject this assumption is a computer simulation. The calculation by the TrapCAD code[13] has continued by our collaborators. The result will be published soon.

ISBN 978-3-95450-158-8

ACKNOWLEDGMENT

The authors would like to express our special thanks to Dr. Arne Drentje for the discussion on understanding of the phenomena. The authors also thank the collaborators, Dr. Sandor Biri and Dr. Richard Racz, for their supports of simulation calculations in this study. It is only a reason of their absence in co-authors that the simulation results are not included in this paper.

REFERENCES

[1] A. Kitagawa et al., Rev.Sci.Instrum. **81**, 02B909 (2010).
[2] T. Ohno, et al., Cancers **3**, 4046 (2011).
[3] M. Muramatsu, et al., Rev. Sci. Instrum. **76**, 113304 (2005).
[4] Y. Iwata et al., Nucl. Instrum. Meth. **A572**, 1007 (2007).
[5] M. Muramatsu, et al., "Design of a compact ECR ion source for various ion production", ECRIS2012, Sydney, September 2012, p.49 (2012); http://www.JACoW.org
[6] A. Kitagawa et al., Rev.Sci.Instrum. **71**, 981 (2000).
[7] Z. Q. Xie and C.M. Lyneis, "Improvements on the LBL AECR source", ECRIS1995, RIKEN, April 1995, INS-J-182 p. 24 (1995).
[8] S. Biri et al., Rev.Sci.Instrum. **85**, 02A931 (2014).
[9] J. Arje, H. Koivisto, and M. Nurmia, "Status report of the JYFL-ECR ion source", ECRIS1995, RIKEN, April 1995, INS-J-182 p. 136 (1995).
[10] W. Takasugi, et al., Rev. Sci. Instrum. **81**, 02A329 (2010).
[11] P. Sortais et al., Rev. Sci. Instrum. **63(4)**, 2801 (1992).
[12] A. Kitagawa et al., "Recent developments on ECR ion sources at the medical accelerator HIMAC" EPAC'00, Wien, June 2000, p.1607 (2000); http://www.JACoW.org
[13] S. Biri, et al., IEEE Trans. Plasma Sci. **39**, 2474 (2011).

ISBN 978-3-95450-158-8

ECR ION SOURCE DEVELOPMENTS AT INFN-LNS

L. Celona#, G. Castro, M. Castro, F. Chines, S. Gammino, O. Leonardi, S. Marletta, D. Mascali, L Neri, D. Nicolosi, F. Noto, G. Torrisi, S. Vinciguerra, INFN-LNS, Catania, Italy
G. Ciavola, INFN-LNS, Catania, Italy and CNAO, Pavia, Italy
A. Galatà, INFN-LNL, Legnaro, Italy

Abstract

At INFN-LNS, ECRIS development during the '90s permitted to optimize the K-800 Cyclotron performances: SERSE and CAESAR have well supported Nuclear Physics research, since then. For the new needs of the facility, further improvements are required and they are here described. Activities recently started, aimed to the production of multicharged ion beams and to the production of intense light ion beams with different schemes of plasma generation.

Technological developments led the AISHa source design, in order to adapt a high performance ECR ion source to hospital facilities needing multiply charged ion production with high reliability and brightness, easy operations and maintenance. The realization of a proton source, called PS-ESS, and of its LEBT line for the Linac of the European Spallation Source in Sweden is one of the major activities at INFN-LNS. Other developments are ongoing on high charge state and high intensity beam production: a major update is going to be finalized on SERSE cryogenic system and on CAESAR injection side; at Vancouver, the VIS source is used for producing multi-mA beams of H_2^+ for a high-current cyclotron; a new flexible plasma trap is under test for fundamental research about innovative plasma heating methods.

INTRODUCTION

During the '90s different ion sources have been built at INFN-LNS, two for the production of highly charged heavy ions to be accelerated by the K-800 Superconducting Cyclotron [1,2] and one for the high intensity proton beam injector for the TRASCO/ADS projects [3]. The SERSE source have been working for about 15 years, but during the last three years a shortage in the availability of LHe from the main liquefier has blocked its operation for many months per year. The performances of the second source, CAESAR, have been acceptable for the Cyclotron needs, but the fact that it was the only source has made impossible to proceed to further optimization, after that the injection part has been totally redesigned.

In the recent past, the requests have been more and more relevant either in terms of beam current and in terms of highly charged ion beams from metallic samples, so the decision to update the existing hardware to fulfil the new needs and to improve the two sources has been taken and the first steps have been done; the update operations of the SERSE and CAESAR sources will be completed in 2015. The major changes to the SERSE design will concern the cryostat, that will be operated in stand-alone mode. After this major improvement, a new commissioning phase is to be started, in order to increase the beam current out of the K800 Superconducting Cyclotron. This phase will involve the LEBT revision with the increase of on-line beam diagnostics.

The changes to the CAESAR source are of four types: i) increase of maximum frequency to 18 GHz, ii) update of the control system to decrease the EMI and the related electronics failures, iii) implementation of a compact oven and iv) increase of the injected microwave power.

All these improvements will be even more remarkable if the proposal of the refurbishment of the 20-years-old cyclotron will be funded: in that case the demand of high brightness heavy ion beams will further increase of a factor 10 to 100, in order to support the future studies on double beta decay.

In the meantime, new projects have been started: the AISHA source for hadrontherapy facilities is designed for high brightness multiply charged ion beams with high reliability, easy operations and maintenance.

AISHa has been designed to meet the above cited requirements by means of high field He-free superconducting magnets, while the radial confinement will be provided by a Halbach-type permanent magnet hexapole structure. The source will take profit of all the know-how acquired in the years by the INFN-LNS ion source team. After the prototype, now under construction at INFN-LNS in the frame of a partnership with three Italian SME, a second copy will be built for CNAO and discussion for a third one started.

Another project is going to start as an advanced design study, in the frame of an European collaboration aimed to the construction of a high intensity heavy ion beams accelerator in Huelva, Spain [4]. For this project the design study will be focused on an updated version of AISHA, named ASIA.

On the side of high current proton beams source, following the successful experience of TRIPS and VIS sources, the high intensity proton source named PS-ESS is under construction for the European Spallation Source; it is designed to meet the request of an accelerator chain deemed to produce 2 GeV - 62.5 mA beams, 4% duty cycle. Another activity in this field is the one under way at Best Cyclotron Company, Vancouver, where the VIS source is in use to produce multi-mA beams of H_2^+ for the injection in a high-current cyclotron. Though it is a proof-of-principle experiment, a new customized microwave injection system and plasma chamber for enhanced H_2^+ production has been studied and constructed. The new setup after some off-line tests at INFN-LNS has been moved to Vancouver and in the next month will be tested.

ISBN 978-3-95450-158-8

ECRIS FOR HIGHLY CHARGED IONS

After the experience with SERSE operation at 28 GHz, for many years there were no constructions at INFN-LNS concerning ECRIS for highly charged ion beams, though the team was involved in construction of ECRIS elsewhere, e.g. at CNAO, Pavia or within the EU Framework Programmes (MS-ECRIS source). As the SERSE and CAESAR sources were serving the Cyclotron without troubles, the activity was concentrated onto modelling, diagnostics, study of microwave coupling to plasma, etc. Now that a new season of ECRIS construction has started, the accumulated know-how has been used as a basis for innovative design of the next sources. But it does not mean that the already developed ECRIS, SERSE and CAESAR, will be left out; in fact the revamping of the two sources will play a major role in the upgrade strategy of the INFN-LNS accelerators facility.

SERSE Cryostat Refurbishment

The SERSE source was designed in 1994-1996 and installed at LNS in 1998, with the best technology available at that time for such a complex B-minimum trap; the magnets' design was considered safe only in presence of a LHe bath, with conventional current leads. The cryostat designed in collaboration with CEA- SBT, Grenoble has been indeed very reliable and only few problems have been met for about 15 years. The only limitation was coming from the main liquefier plant, which is serving the K-800 Superconducting Cyclotron as a primary duty, with decreasing additional power in the last few years until the major failure occurred in 2013. The decision to restore the SERSE reliability was taken in 2013 and the order for two cryocoolers Cryomech PT415 was placed recently, while the procedure for the reconstruction of the turret is going to start. The conventional current leads will be replaced by High Temperature Current Leads and the liquefiers will be assembled in such a way to minimize the maintenance time (less than one time per year, safely). As the coil mass is larger than 800 kg, the thermal budget was carefully studied and the choice of the two cryocoolers was taken for the sake of additional margins in case of malfunctioning and of X-ray absorption in the cold mass.

The same safety level in case of quench is guaranteed by the new design, while the cooldown time may be slightly increased after a quench. These drawbacks are not relevant, while the gain in terms of manpower savings and of beam availability will be remarkable.

During the preparation of the proposal, a series of tests was carried out and it was observed that the cryostat performance did not change since 1997, while the current leads present some degradation because of the thermal cycles. So their maintenance would be anyway necessary, which makes reasonable this investment.

The choice of pulse tube cryocooler was carried out in the sense of a larger reliability of the system: this type of cryocooler has very low vibrations and the parts subject to degradation are the compressor and a 5-fold valve which follows a scheduled maintenance (one per 2 years). The operation scheme chosen for SERSE will not permit to exploit the full cryocoolers' power, but only 1.35 W per each, which anyway is much more than the expected thermal budget (1.68 W at 4.5 K). It means that even if the pulse tubes may lose 10% of power at the end of their cycle, there is still 0.7-0.8 W for recovering the X-ray losses into the cold mass.

The Cyclotron schedule will define the time schedule for the SERSE turret refurbishment and the cryocooler installation, but it may be possible to complete the work by the end of summer 2015.

Finally, an important advantage for operation will be the removal of the 500 liters dewar close to the source, which may make easier any intervention on the source hardware, including microwaves supplies.

CAESAR upgrade

The CAESAR upgrading had an impact on different parts of the setup; the goal was not only to increase the energy content of the plasma by increasing the magnetic field at the injection side but also the injected microwave frequency and power used, shifting the maximum operating frequency to 18 GHz. The update of the control system allows to decrease the impact of the electromagnetic interferences and the related electronics failures. A compact oven has been also designed and realized to increase the beam variety.

Therefore the injection side has been totally redesigned as shown in fig. 1, removing the "magic cube" with a new setup which permits to house: two WR62 inputs, an oven, two gas inputs and the biased disk. The increase of the magnetic field at injection has been achieved by inserting an iron plug which boosted the maximum value from 1.5 to more than 1.8 T at the chamber entrance (fig. 1 and 2).

The source commissioning in these new operating conditions is in progress and during the preliminary tests in July the operational range was extended up to 18 GHz; the tuning of frequency is important to achieve the best performances especially for highly charged ions. Another remarkable improvement is the lower beam ripple, even below ± 0.5% for highly charged ion species.

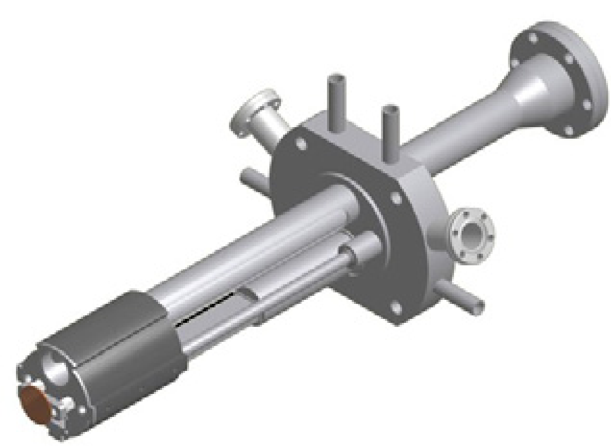

Figure 1: CAESAR new injection system assembly.

ISBN 978-3-95450-158-8

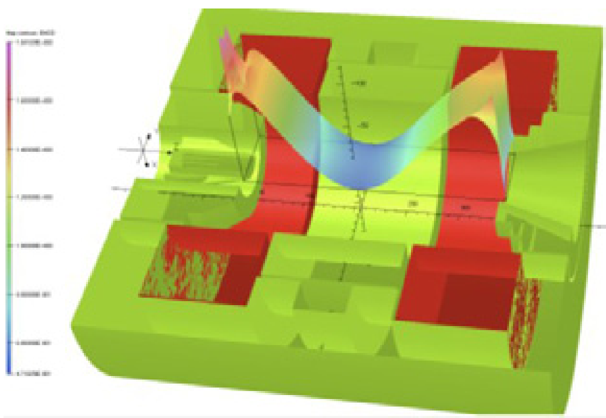

Figure 2: OPERA simulation of the CAESAR axial magnetic field enhancement due to the iron plug insertion.

The AISHa ion source

In order to answer to specific requests of the hadron therapy facilities, the AISHA source was designed in 2012 with the aim to provide highly charged ion beams with low ripple, high stability and high reproducibility; key features were also the low maintenance time and the minimization of electrical consumption. In 2013 the proposal of AISHA construction was approved by the Regional Government of Sicily and the funding was allocated to a private-public partnership including INFN.

The AISHa ion source is a hybrid ion source whose magnetic system is based on a permanent magnet hexapole able to reach up to 1.3 T radial field on plasma chamber walls (ϕ=92mm) and four superconducting coils for the axial plasma confinement. The main characteristics of the source are summarized in table 1.

Table 1: Main AISHa source parameters

AISHa source parameters	
Radial field (max)	1.3 T
Axial field (INJ/MID/EXTR)	2.6 T / 0.4 T / 1.7 T
Operating frequencies	18 GHz (TFH)
Operating power (max)	1.5 kW + 1.5 kW
Extraction voltage (max)	40 kV
Chamber diameter	ϕ=92mm
LHe	Free

The axial magnetic field confinement has been designed on the basis of the previous experiences, in particular to minimize the hot electron component and to optimize the ECR heating process by controlling the field gradient at injection and extraction and the resonance length. For the AISHa source it has been decided to adopt a solution employing four coils which permits to have a good control on the above cited parameters and that will also permit to shift the position of the minimum B field within the ± 15 mm range. Figure 3 shows the magnetic field on source axis, while a 3D view of the magnetic system is shown in fig. 4.

The hexapole has been deeply studied and designed with the OPERA 3D code. The Halbach type hexapole structure is characterized by magnetic elements with nine different directions of magnetization and it is able to reach a radial field close to 1.3 T at 46 mm radius along the whole plasma chamber length, as shown in fig. 5.

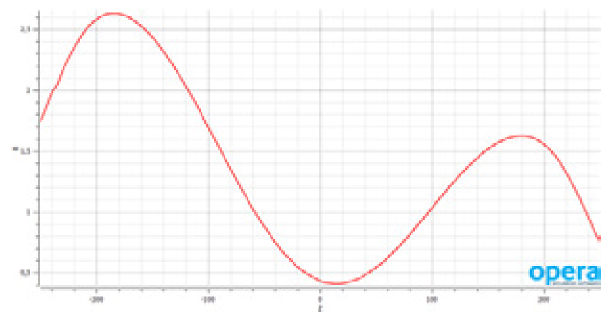

Figure 3: The AISHa magnetic field along plasma chamber axis.

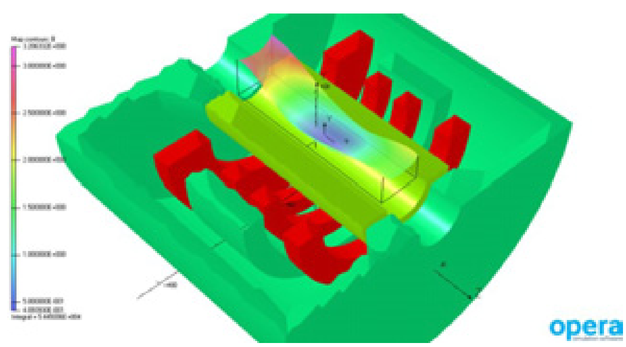

Figure 4: A 3D view of the entire magnetic system.

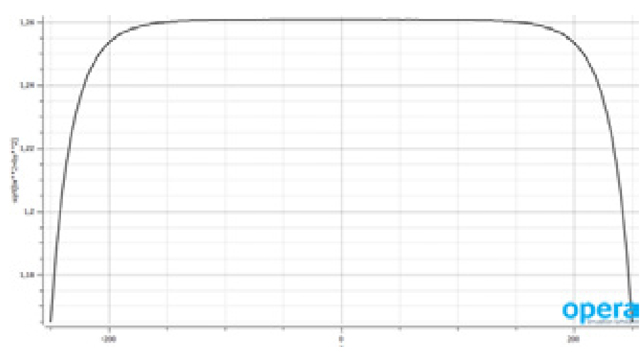

Figure 5: Radial component along z at the inner wall of the AISHa plasma chamber (radius=46 mm).

During the design the efforts have been focused to analyze and minimize the permanent magnet demagnetization. In fact, due to the presence of high values of H_x and H_y generated by the SC coils a local demagnetization of part of the hexapole assembly may happen.

Since only the radial field component may be cause of demagnetization in an already fabricated sector with a given radial direction of magnetization, the z component

ISBN 978-3-95450-158-8

can be neglected, while the x and y components play the key role in the hexapole performance.

A solution to the problem of demagnetization consists in the selection of the sectors where the phenomenon takes place by calculating for each sector the resultant, along the direction of magnetization, of the H_x and H_y vectors. Demagnetization takes place in the sectors where such resultant has an opposite direction with respect to the magnetization itself and a value higher than the coercitivity of the used material. To avoid that the radial confinement magnetic field be decreased, the sector must be replaced with one having higher coercitivity.

In fig. 6 only the region where the resultant magnetic field H is above than 1.1×10^3 kA/m is shown (a 15% safety factor has been taken into account with respect to the minimum coercitivity value).

Since, in such zones, the resultant of H_x and H_y along the direction of magnetization of the sector considered is greater than the coercitivity, another material with higher H_{cJ} must be adopted to avoid demagnetization. Therefore to optimize the structure it is necessary to divide the hexapole in two shells as shown in fig. 7.

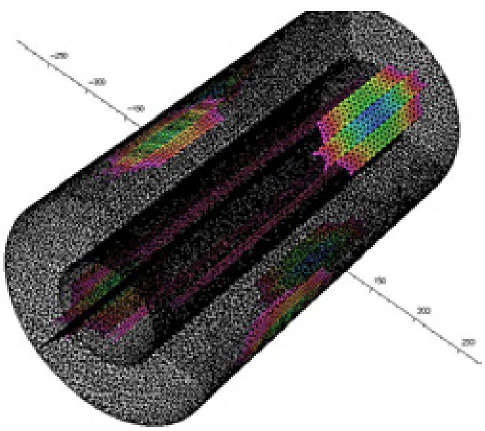

Figure 6: AISHa's hexapole sectors where the field is higher than the coercitivity value are shown.

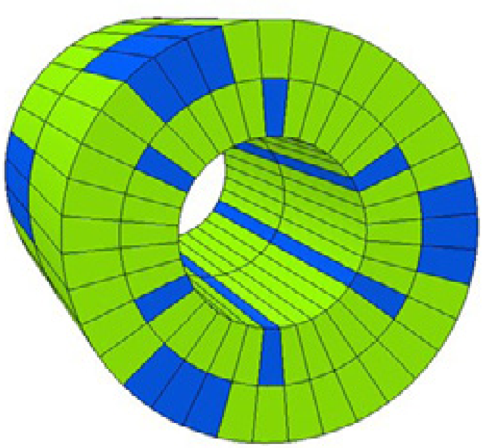

Figure 7: Double shell hexapole geometry (blue sectors have higher coercitivity).

Moreover, on the outer side the maximum radial field values are located in different sectors depending if we are considering the forward half of the structure or the rear half. Therefore, to have the maximum flexibility in the choice of the material, trying to keep material with high value of B_r, the outer shell has been divided in two parts.

The magnetic system has been ordered and it is actually under construction, the delivery is expected for mid-2015.

ION SOURCES FOR HIGH CURRENT OF MONOCHARGED LIGHT BEAMS

Different ion sources have been constructed at INFN-LNS for this purpose. The TRIPS source for the TRASCO/ADS accelerator study paved the way at the end of the 90s. TRIPS met all the requirements [3] and then was moved to INFN-LNL in November 2005 to be coupled to the RFQ. Since then a parallel work on the realization of test-bench called "plasma reactor" and of the optimized source named VIS started. The Versatile Ion Source (VIS) is an off-resonance Microwave Discharge Ion Source (MDIS) which produces a slightly overdense plasma at 2.45 GHz. It is able to produce more than 50 mA of proton beams and He^+ beams at 65 kV, while for H_2^+ a current slightly below 20 mA was obtained. The entire source has been designed in order to present many advantages in terms of compactness, high reliability, capability to operate in cw mode or in pulsed mode, reproducibility and low maintenance. The know-how obtained with the VIS source has been useful for the design of the proton source for the European Spallation Source which is nowadays one of the major engagement for the INFN-LNS.

PS-ESS

The European Spallation Source facility will be one of the fundamental instruments for science and engineering of the future. A 2 GeV proton accelerator is to be built for the neutron production. INFN-LNS is responsible of the design of the proton source and Low Energy Beam Transport (LEBT) line. It is required to produce at RFQ entrance a low emittance 75 keV - 74 mA proton beam pulse, 2.86 ms long, with a repetition rate of 14 Hz. Microwave Discharge Ion Sources (MDIS) enable us to produce such high intensity proton beams with an rms normalized emittance around 0.2 π.mm.mrad. The source design is based on a flexible magnetic system which can be even adapted to electrostatic Bernstein waves heating mechanism; that will permit to explore a new heating method, already tested at INFN-LNS, with an expected increase in the electron density and in the output current with respect to the classical flat magnetic field profiles.

The typical shape of the magnetic field for MDIS machines is the one labeled by (Standard) in Fig. 8, i.e. a quasi-flat profile everywhere above the resonance value of 875 Gauss. This ensures electron densities around the cutoff at 2.45 GHz or slightly larger ($n_e\approx10^{17}$ m^{-3}), temperatures sufficient for hydrogen ionization (T_e=15-20 eV) and H_2 molecule lifetimes long enough for complete

ISBN 978-3-95450-158-8

ionization and proton generation. Such plasma parameters require RF power values close to 1 kW and background pressures down to 10^{-5} mbar. The PS-ESS source and its extraction system are shown in fig. 9.

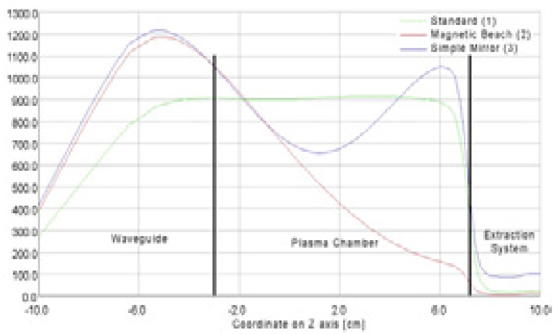

Figure 8: PS-ESS magnetic field profiles.

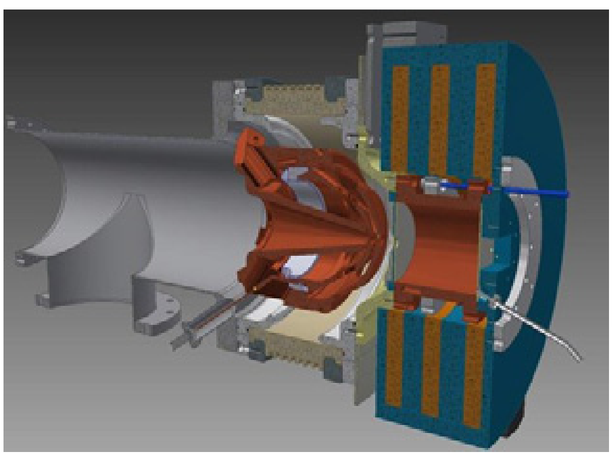

Figure 9: The PS-ESS body source layout.

Recently, the possibility to overcome the cutoff density by converting the incoming electromagnetic wave into a plasma wave has been investigated [5]. This study goes in parallel with similar investigations in fusion science, where large plasma densities are needed to fulfil Lawson criterion [6]. At INFN-LNS the evidence about the occurred conversion mechanism has been observed with the VIS source equipped with a movable permanent magnets and operating at variable frequency [7]. The process is based on the conversion of an oblique (with respect to the applied magnetic field) electromagnetic wave (called extraordinary mode, or X mode) into an electron oscillation (longitudinal wave) propagating across the magnetic lines and called Bernstein Waves (BWs). Plasma waves travel in plasmas of whatever densities and are absorbed at cyclotron harmonics. Since they are sustained by the electron motion, BWs cannot be externally excited, but it originates from an X mode interacting with gyro-rotating electrons at the Upper Hybrid Resonance (UHR) [8]. The first experiments have put in evidence the formation of a two times overdense plasma when operating in second harmonic mode [5]. To be converted into a BWs, the X mode requires a rapidly dropping magnetic field which makes possible either UHR and second harmonic absorption. This configuration is labeled as (Magnetic Beach) in Fig. 8. We expect this second way of RF-plasma energy coupling will significantly enhance the output currents, but it can be employed in a second phase, after a careful study of its implications on ion dynamics (possible ion heating as ancillary mechanism) and then on beam emittance.

Finally, another way to operate the PS-ESS source will be the simple-mirror trap, like the one labeled by (Simple Mirror) in Fig. 8. Studies about balance equations of the different plasma species (H_2, H_2^+, H^+) revealed that their reciprocal abundance is regulated by the relative lifetimes. In a quasi-flat magnetic field, under normal operational pressure conditions, ions lifetime is only governed by collisional diffusion across the magnetic field, which is a rather fast process. The prolongation of H_2^+ molecule lifetime, obtained when using the simple-mirror configuration, may increase the ionization efficiency thus boosting the proton fraction already at moderate RF power and improving also the reliability of the source. Reliability has been sought for in the design of any source component; e.g. in the case of the extraction system, the four electrodes are all directly or indirectly cooled: the plasma electrode is placed on the HV platform at a voltage of 75 kV and the set of the remaining three electrodes is attached to the grounded flange, with the repeller electrode placed between two grounded electrodes to preserve the space charge compensation of the LEBT.

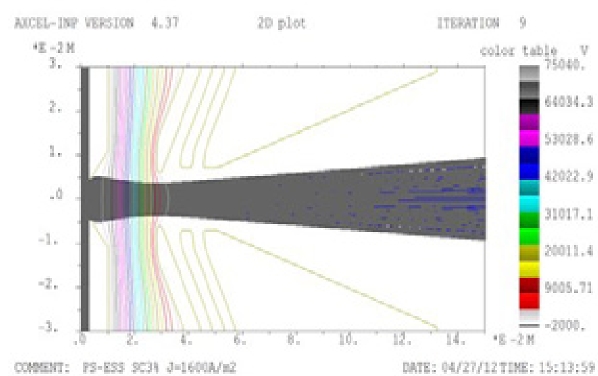

Figure 10: PS-ESS four electrode extraction system.

A multi-parametric optimization of the geometry was done using AXCEL for a 2D axial symmetric simulations (Fig. 10) and converted in a 3D distribution by an on-purpose developed code to be used as input for the TraceWin code to optimize the LEBT lattice. The total beam current used in the simulation is 74 mA : the proton fraction considered is 80%, while 20% is H_2^+.

A two solenoid LEBT will match the beam into the first acceleration stage, the Radio-Frequency Quadrupole (RFQ), and the requested Twiss parameters are obtained. The correct strength of the two solenoids' field was evaluated by using the optimization features of TraceWin code that take also in consideration the space charge of the beam.

ISBN 978-3-95450-158-8

The ESS requirements update of June 2013 defined that the injector must be able to provide current from 10% to 100% of the nominal value with step of 10% and precision of 2% without change of the proton source parameters. This was satisfied by inserting in the LEBT an iris that will cut the beam with high precision. With TraceWin we estimated that the beam must be cut in the range from 5 mm to 30 mm of radius, and we also evaluated for each desired current value the optimum magnetic field strength of the two solenoids to keep the nominal Twiss parameters. As expected, when reducing the current by eliminating peripheral beam the emittance was reduced as well. The LEBT will be equipped with an electrostatic chopper in order to remove the unwanted part of the beam pulse during the beam rise and fall times.

In the low energy beam transport of high intensity beams the self-generated repulsion between charged particles can generate a large and irreversible emittance growth, while the optimum matching with the RFQ require high focusing and low emittance. To reduce this effect the space charge neutralization of the beam can be obtained by ionizing the residual gas. The generated electrons are captured by the beam potential, while the generated ions are repelled by the beam and lost on the surface of the vacuum chamber. In order to preserve the space charge compensation (SCC) from the high electric field located in the extraction system and inside the RFQ, a repelling electrode was inserted both in the extraction system and in the RFQ collimator. Such SCC regime has many similarity to a plasma but the electric field produced by the chopper and the change of the trajectory of the beam inside the LEBT introduces many significant variations in the two transitions: from chopper ON to OFF (beam pulse rise time), and from chopper OFF to ON (beam pulse fall time). We have studied these transitions by performing PIC simulation and by experimental measurements done at CEA, Saclay; the simulations properly represented the measured few hundred nanosecond rise time (Fig. 11) and less than 100 nanosecond fall time.

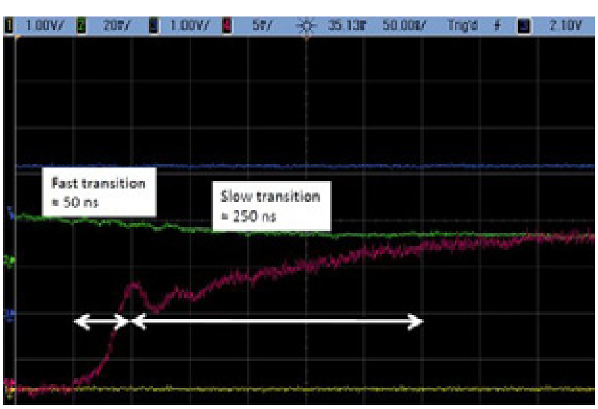

Figure 11: Beam pulse rise time measured.

THEORETICAL ADVANCES

A better comprehension of electron heating, ionization and diffusion processes, ion confinement and ion beam formation is mandatory in order to further increase ECRIS performances. Investigation of plasma dynamics in ECRIS still remains a challenge. At INFN-LNS we have developed a series of releases of a numerical code able to simulate electron heating inside a resonant cavity (i.e. including cavity electromagnetic modes) [9]. Now we are working on an advanced version which attempts three-dimensional (3D) full-wave simulations (including the effects of the cylindrical metallic walls) coupled to a kinetic code to self-consistently retrieve a solution of Vlasov equation via PIC – Particle-In-Cell strategy.

The Vlasov equation:

$$\frac{\partial f_\alpha}{\partial t} + \boldsymbol{v} \cdot \frac{\partial f_\alpha}{\partial \boldsymbol{r}} + \frac{q_\alpha}{m_\alpha}(\boldsymbol{E} + \boldsymbol{v} \times \boldsymbol{B}) \cdot \frac{\partial f_\alpha}{\partial \boldsymbol{v}} = 0$$

is solved starting from Klimontovich sampling of the phase-space electron distribution, where the mean fields $\boldsymbol{E}$ and $\boldsymbol{B}$ are calculated via FEM solvers including the cold plasma approximation, which allows calculating the three dimensional dielectric tensor assuming the following form:

$$\bar{\bar{\varepsilon}} = \varepsilon_0 \bar{\bar{\varepsilon}}_r = \varepsilon_0 \left(\bar{\bar{I}} - \frac{i\sigma}{\omega \varepsilon_0} \right)$$

$$= \begin{bmatrix} 1 + i\frac{\omega_p^2}{\omega}\frac{a_x}{\Delta} & i\frac{\omega_p^2}{\omega}\frac{c_z + d_{xy}}{\Delta} & i\frac{\omega_p^2}{\omega}\frac{-c_y + d_{xz}}{\Delta} \\ i\frac{\omega_p^2}{\omega}\frac{-c_z + d_{xy}}{\Delta} & 1 + i\frac{\omega_p^2}{\omega}\frac{a_y}{\Delta} & i\frac{\omega_p^2}{\omega}\frac{c_x + d_{yz}}{\Delta} \\ i\frac{\omega_p^2}{\omega}\frac{c_y + d_{xz}}{\Delta} & i\frac{\omega_p^2}{\omega}\frac{-c_x + d_{zy}}{\Delta} & 1 + i\frac{\omega_p^2}{\omega}\frac{a_z}{\Delta} \end{bmatrix}$$

with: $a_m = \left(-i\omega + \omega_{eff}\right)^2 + B_{0m}^2 \left(\frac{e}{m_e}\right)^2$,

$c_m = B_{0m} \left(\frac{e}{m_e}\right) \left(-i\omega + \omega_{eff}\right)$,

$d_{mn} = B_{0m} B_{0n} \left(\frac{e}{m_e}\right)^2$.

Where: $m = x, y, z,\ n = x, y, z$ and $\Delta =$ $\left(-i\omega + \omega_{eff}\right) a_x + \left(\frac{e}{m_e}\right) \left[B_{0z}\left(c_z - d_{xy}\right) + B_{0y}\left(c_y + d_{xz}\right)\right]$

ω the angular frequency of the microwave, $\omega_p = \sqrt{\frac{n_e e^2}{n_e \varepsilon_0}}$ the plasma oscillation angular frequency, n_e the electron density, m_e the electron mass, e the electron charge, i the imaginary unit and ω_{eff} the collision frequency; the latter accounts for the collisional friction.

Figure 12 depicts the full-wave solution of the field inside an ECRIS cavity (SERSE is the test case). In order to cope with time-consuming computational procedure, the operational frequency was decreased to 8 GHz (by scaling the magnetostatic field as well). In this way the FEM solver retrieves a solution via a direct solver and the self-consistent loop runs for a couple of days; 8 GHz is the upper level of frequency currently producing significant results. In particular, figure 12-up shows the 1D plot – along the plasma chamber axis – of the current density

ISBN 978-3-95450-158-8

$j = \bar{\sigma}E$, where $\bar{\sigma}$ is the tensorial conductivity. This plot is particularly significant since illustrates the plasma response on the electromagnetic field propagation: the current is in fact enhanced in proximity of the resonance zones, where the conductivity and the electric field tend to increase (or even diverge without collisional friction). This demonstrates the model is able to "catch" the wave absorption mechanism in a correct way. Fig. 12-down shows the electromagnetic field structure in case of plasma filled cavity. Localized areas of high field intensity demonstrate that even in a full-wave view the resonant nature of the cavity is not completely destroyed, thus supporting the theoretical explanation of the frequency tuning effect (and its impact on output current and beam shape) given elsewhere [10,11]. Results about full-wave simulations and the entire self-consistent loop have been largely discussed in [12] and [13].

In order to carry out more advanced studies on these subjects, we have designed a new test-bench machine named "Flexible Plasma Trap" with flexible magnetic system and a injection system permitting both axial and radial injection of microwaves [14].

CONCLUSION

The overview of the activities concerning ECR ion sources and related equipment, described in this paper, is not exhaustive, as the major development in the field of plasma diagnostics have not yet been completed and they will reported in future workshops.

Additionally we expect that the R&D to be done with the Flexible Plasma Trap will permit to trigger the construction of a new third generation ECRIS to be coupled to the K-800 Superconducting Cyclotron, after its upgrade. The same expertise is also going to find an application in the construction of ad-hoc traps for the Nuclear Physics, which conversely will make easier to find the support for the construction of new devices focused to the ion beam production.

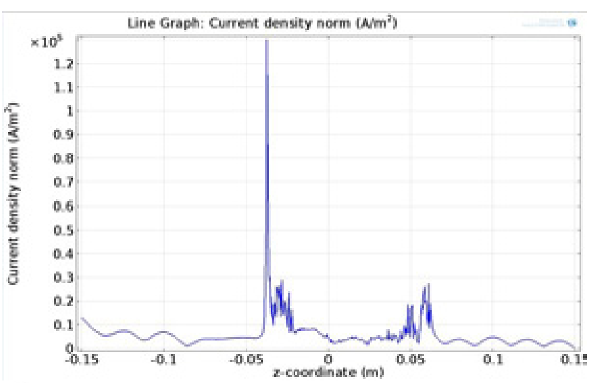

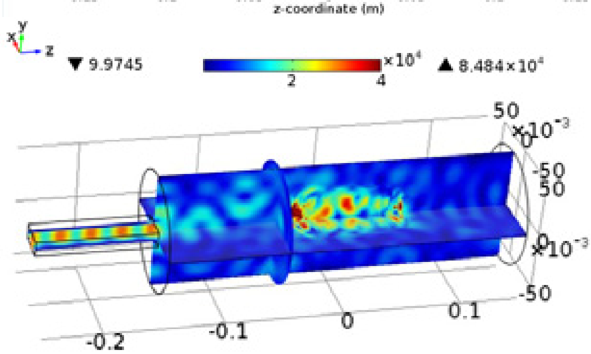

Figure 12: *up* – simulated current density $j = \bar{\sigma}E$ trend along the plasma chamber axis; *down* – simulated electromagnetic field distribution inside a plasma filled cavity at 8 GHz.

ACKNOWLEDGMENT

The authors acknowledge the support given by all the LNS divisions to the above reported activities. The work here reported got benefit of the contributions of M. Cafici (Cryogenics group), G. Gallo, L. Allegra, S. Passarello and E. Zappalà (Mechanical Design group), M. Piscopo and G. Schillaci (Technical Division) and A. Caruso and A. Longhitano (RF group).

The AISHa project is supported by the incentives in favour of Research Development and Innovation Art.5 Regional law 16/12/2008 - Intervention line 4.1.1.1 POR FERS Sicilia 2007-13 devoted to small and medium companies integrated with Research Institutions (Partners: INFN-LNS, HITEC2000 srl, UNICO srl, C3SL). The cooperation of the personnel of the three companies is to be underlined.

Finally we wish to thank the colleagues of CEA-IRFU, Saclay for their support during the tests of the PS-ESS chopper, particularly R. Gobin and O. Tuske.

REFERENCES

[1] S. Gammino et al., Rev. Sci. Instrum. 70, 9 (1999), 3577
[2] S. Gammino, G. Ciavola, Rev. Sci. Instrum. 71, 2 (2000), 631
[3] L. Celona et al., Rev. Sci. Instrum. 75, 5 (2004),1423.
[4] I. Martel et al., "ECOS-LINCE: a high intensity multi-ion superconducting LINAC for nuclear structure and reactions", THPME036, IPAC'14, Germany (2014).
[5] G. Castro et al., Rev. Sci. Instrum. 83, 02B501.
[6] H.P. Laqua, "Plasma Physics and Controlled Fusion" 49 (2007) R1
[7] D. Mascali et al., Nucl. Instr. & Meth. A, 653-1, 11-16 (2011).
[8] F. F. Chen, "Introduction to the Plasma Physics and Controlled Fusion", U.K., London Press, London, 1986.
[9] L. Neri et al., Rev. Sci. Instrum. 83, 02A330 (2012);
[10] D. Mascali et al., Rev. Sci. Instrum. 83, 02A336 (2012).
[11] L. Celona et al., Rev. Sci. Instrum. 79, 023305 (2008).
[12] G. Torrisi et al Journal of Electromagnetic Waves and Applications, 28(9), 1085-1099 (2014)
[13] D. Mascali et al., accepted for publication on European Physical Journal – D.
[14] D. Mascali et al., "ECR Ion Sources Developments at INFN-LNS for the production of high brightness highly charged ion beams", MOPP066, LINAC'14, Switzerland, (2014).

ISBN 978-3-95450-158-8

STATUS REPORT OF SECRAL II ION SOURCE DEVELOPMENT *

L. Sun#, W. Lu, W. Wu, T. J. Yang, Y. Yang, B. M. Wu, E. M. Mei, S. J. Zheng, D. S. Ni, B. Zhao, L. Zhu, Q. Hu, M. Z. Guan, W. H. Zhang, J. W. Guo, X. Fang, X. Z. Zhang, H. W. Zhao, L. Z. Ma, IMP/CAS, Lanzhou, 730000, China

Abstract

For a new injector linac project launched at IMP, a superconducting ECR ion source SECRAL II is now under construction. This ion source is a duplicated one of SECRAL I which is operated routinely for HIRFL facility at the frequency of 18-24 GHz. SECRAL II is designed to be operated at the frequency of 28 GHz, which needs slightly higher radial field at the plasma chamber wall. The fabrication of the cold mass was started at early 2013, and it has been completed in May 2014. The engineering design of the whole superconducting magnet has also been finished and ready for fabrication. After a brief introduction of the recent results obtained with SECRAL I ion source, this paper will present the cold mass test results and the cryogenic system design of SECRAL II magnet. The test bench design will be also discussed.

INTRODUCTION

As an indispensable machine to provide intense highly charged ion beams, ECR ion sources have been used as the ion beam injectors at IMP for over 20 years. At IMP, the national laboratory accelerator facility is HIRFL (Heavy Ion Research Facility in Lanzhou) as shown in Fig. 1, which is mainly composed of one K69 cyclotron SFC, one K450 cyclotron SSC, RIBLL1 for radioactive beam production, cooler storage rings CSRm and CSRe, and the radioactive beam line RIBLL2 to connect the two rings [1, 2]. The HIRFL facility can work with several schemes for experimental researches. The 50 years old K69 cyclotron can work standalone for nuclear, atomic physics and material research purposes with the beam species from H to U. When the K69 and K450 cyclotron work with a coupling scheme, the HIRFL facility can deliver tens of MeV/u CW heavy ion beams. For the operation of HIRFL-CSR, two injection schemes are now available: one is the direct injection of high Q/M heavy ion beam from SFC with the energy of several MeV/u, and the other one is the injection of the beam delivered by SFC + SSC working with a coupling mode. When utilizing the standalone injection scheme with SFC, it is very hard to deliver sufficiently high current with the necessary beam energy, especially in terms of high Z ion beams. By utilizing the coupling scheme of SFC + SSC to do beam injection for CSRm, beam energy is guaranteed, but as a cause of very low coupling efficiency between the cyclotrons, the output beam intensity is far below the injection needs of CSRm, especially for the very heavy ion beams such as Bi, U, and etc. The HIRFL-CSRm is designed to be able to accumulate and accelerate very heavy ion beam such as U with the beam intensity of several 10^9 ppp, which is about 2 orders higher than the present performance. The barrier is the non-optimal injection scheme. A project proposal has been recently issued to build a dedicated injection linac injector for CSRm so as to boost the performance by ~2 orders for heavy ion beams. For this injector linac (called CSR-Linac), a high performance state of the art ECR ion source is needed to provide the needed intense high Q/M heavy ion beams. SECRAL II project is therefore initiated.

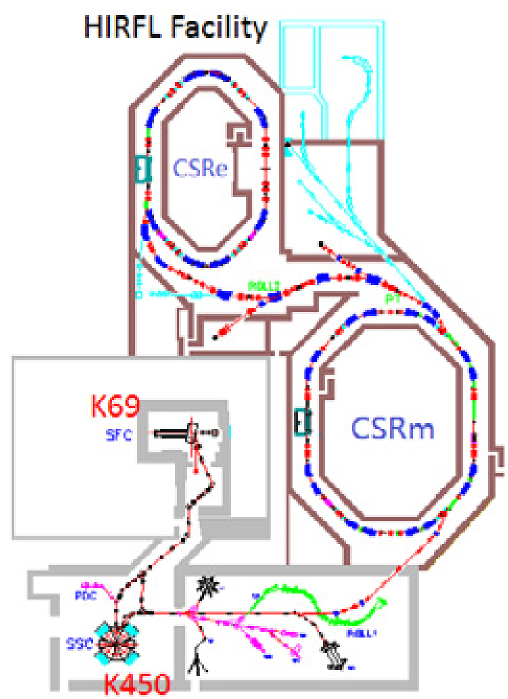

Figure 1: Layout of HIRFL facility.

SECRAL I was connected to the injection line of HIRFL complex in 2007 and had been in service for more than 17,000 hours for routine operation. It has been the main working horse for the facility, especially in terms of very heavy ion beams operation. In case of any severe problem with the ion source, HIRFL facility would lose most of its performance and capacity. As a contingency plan, SECRAL II project was proposed. Combined with the CSR-Linac project, SECRAL II project serves a dual purpose.

*Work supported by the 100 Talents Program of the CAS (No. Y214160BR0), NSF (contract No. 11221064) and MOST (contract No. 2014CB845500).
#sunlt@impcas.ac.cn

ISBN 978-3-95450-158-8

INTENSE BISMUTH BEAM PRODUCTION WITH SECRAL I

SECRAL I ion source was successfully built and tested at IMP in 2005, and promising performance was obtained in the following years at either 18 GHz or 24 GHz [3, 4]. The research work with such a high performance tool to study advanced ECR ion source has never been stopped, and the highest priority in the research activity list is to explore the ultimate capacity of such a machine in production of highly charged heavy ion beams, especially of those heavier than Xe, such as Bi and U. For the production of uranium ion beams, the oven technique is very challengeable. While for bismuth ion beam production, the oven solution is more straightforward.

Oven Design

3 types of micro-ovens have been designed and tested at IMP, i.e. resistor oven with the highest operating temperature of 1600ºC but moderate material loading capacity, low temperature oven with the highest operating temperature of 650ºC and much larger material loading capacity, and high temperature oven that could reach the temperature of 2000ºC mainly designed for refractory material ion beam production. For the production of intense Bi ion beams, low temperature oven is adopted. The low temperature oven is a design incorporated with a commercial Watt-Flex Cartridge Heater and a large capacity crucible for long term uninterrupted routine operation of intense low melting point metallic ion beams, such as bismuth, calcium, lead beams, and etc. The design concept of this oven was borrowed from LBNL cartridge oven. In 2013, with the help of this oven, 422 eμA Bi^{30+} and 396 eμA Bi^{31+} had been obtained with SECRAL I at 24 GHz [5]. During the test, the oven was found still not powerful enough to yield sufficient Bi vapour for more intense beam production. Several modifications has been made to improve the oven capacity. The cartridge heater power is raised from 150 W to 180 W. Mo replaced the oven furnace material instead of copper, so as to make the oven be more durable under high temperature operation conditions.

Intense Bi Beam Production

In 2013, with a 3.5 kW 24 GHz microwave power heating of the plasma, 422 eμA Bi^{30+} and 396 eμA Bi^{31+} had been obtained on the faraday cup. Since the 24 GHz gyrotron amplifier has the maximum output capacity of 7 kW, there is still big improvement margin of SECRA I to produce more intense Bi ion beams. The major improvement in the 2014 test is the incorporation of a modified cartridge oven with higher power and Mo furnace design, while the loading capacity is conserved. At the highest working temperature of 650 ℃, a nominal vapour pressure of 10^{-2} Torr can be achieved. Actually, heated by the strong plasma radiation, the oven temperature could be higher than the off-line measured values.

During the test of high intensity Bi beam production, 24 GHz microwave is the main power source to heat the plasma, and 18 GHz microwave power is an auxiliary tool to enhance the performance. With 4.74 kW@24 GHz + 1.4 kW@18 GHz, 710 eμA Bi^{30+} and 680 eμA Bi^{31+} have been obtained at the faraday cup. Fig. 2 gives the spectrum when 710 eμA Bi^{30+} produced. The source output of high intensity Bi ion beams is increasing linearly with the microwave power level and oven temperature. Even at the level of 710 eμA Bi^{30+}, there was no indication of beam intensity saturation. The present results seem to be still limited by oven output of Bi vapour and ion source conditioning at high power. A later analysis of the material consumption rate according to the source operation log shows that an average value of 10.91 mg/hr@400 eμA Bi^{31+} and 8.18 mg/hr@300 eμA Bi^{31+} could be expected, which is very close to the value obtained in the 2013 test.

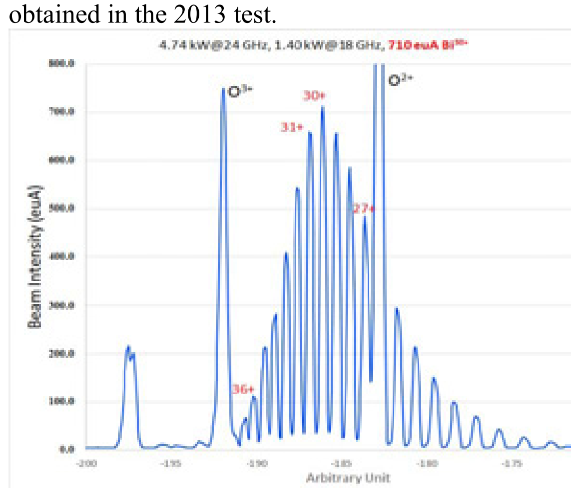

Figure 2: Spectrum optimized for 710 eμA Bi^{30+}.

As the plasma condition was well conditioned for the production of bismuth ion beams, highly charged Bi beams were also tested with lower oven power settings. Different from the production of high intensity Bi ion beams, highly charged ion beams need better plasma stability and less plasma contaminations. At the 24 GHz power level of ~4.0 kW, 100 eμA Bi^{41+} and 10.7 eμA Bi^{50+} have been produced. ~0.05 eμA Bi^{57+} can also be well distinguished from the beam spectrum. Fig. 3 is the spectrum when Bi^{41+} production is optimized.

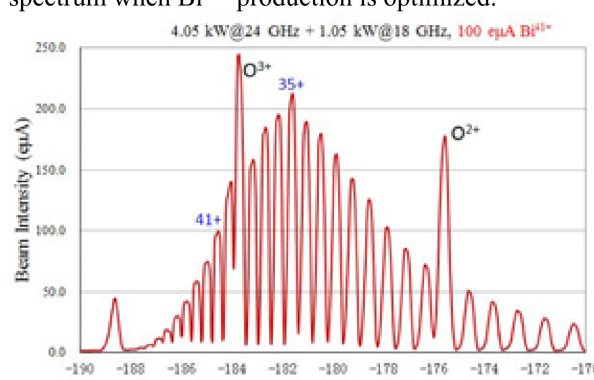

Figure 3: Spectrum obtained when 100 eμA Bi^{41+} produced.

ISBN 978-3-95450-158-8

Beam Emittance

In general, two issues are essential for ion beams injected to an accelerator, i.e. beam intensity and beam brightness. High power accelerators need very intense ion beams, while optimal brightness can guarantee the transmission of ion beam with less losses. With the increase of ion beam extracted from an ECR ion source, beam quality will deteriorate as a cause of more severe space charge effect. It is worth checking the beam emittance evolution with the increase of beam intensity. With SECRAL I source, the beam emittance was measured with Alison type scanners. Fig. 4 shows the horizontal and vertical normalized rms emittances measured for Bi^{31+} intensity from 100 eμA to 600 eμA. Error bars are not given here, which should be in the range of ±10% [6]. According to the study, the emittances do not deteriorate dramatically with the beam intensity increase. For high charge state ion beams, provided with the same beam optics, two dominant factors have big impact on beam emittances from an ECR ion source, i.e. plasma conditions and extracted beam intensity. Beam emittances could be optimized through plasma condition manipulation.

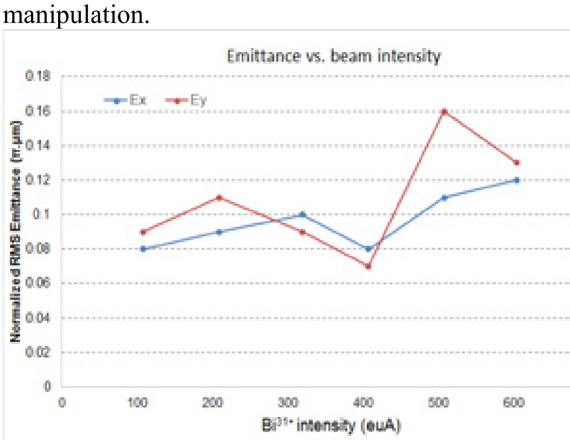

Figure 4: Bi^{31+} beam emittance variation with the increase of beam intensity.

SECRAL II MAGNET

SECRAL I ion source has the unique feature of a reversed configuration magnet structure over traditional ECR ion sources. This makes the source magnet body very compact, typically in the magnet length. The success of SECRAL I reveals that The ECR plasma is not affected by the magnet configuration as long as the magnetic confinement is sufficient. SECRAL II ion source will also adopt the unique magnet configuration already demonstrated. SECRAL II magnet is a close copy of the fully superconducting ECR ion source SECRAL I. The main difference is in the cryogenic system design.

SECRAL II is designed to be operated at 28 GHz. Table 1 summarizes the typical parameters. To have sufficiently high radial field at the plasma chamber wall, and also have the 1.5 mm thickness Ta shielding tube incorporated, the warm bore size is slightly increased by optimizing the vacuum and 70 K shield gaps.

Table 1: Main design parameters of SECRAL II

ω_{ecr}	28 GHz
B_{inj}	3.7 T
B_{ext}	2.2 T
Mirror Length	420 mm
Radial field at inner chamber wall	2.0 T
Warmbore ID	Ø142 mm
Coldmass length	810 mm
Plasma volume	> 5 L

Cold Mass Fabrication

Cold mass is the critical part of the magnet, and it is also the most technically challengeable part of the project. SECRAL II magnet cold mass is mainly composed of three axial solenoids wound on a stainless steel bobbin, six sextupole coils rested on the axial coils bound with 0.3 mm×3.3 mm stainless steel strip, cold iron blocks to boost the radial field and also to minimize the stray field, two iron flanges to connect and fix the position of the sextupole coils and axial coils, and the outer most aluminium rings to clamp the sextupole coils. Fig. 5 gives the Solidworks sketch of the cold mass. Both the sexupole coils and axial solenoids are using the same type of NbTi wire from WST (Western Superconducting Technologies Co., Ltd). The typical features of the adopted wire are given in Table 2. The guaranteed superconducting performance is 668.7 A@7 T (4.2 K). Calculation with TOSCA 3D shows that the highest superimposed field on the superconductor is situated on the sextupole coils of 7.8 T@191.0 A which corresponds to the loading factor of ~86%. The highest field on the injection solenoid is 7.3 T@308.7 A which also corresponds to a loading factor of ~86%.

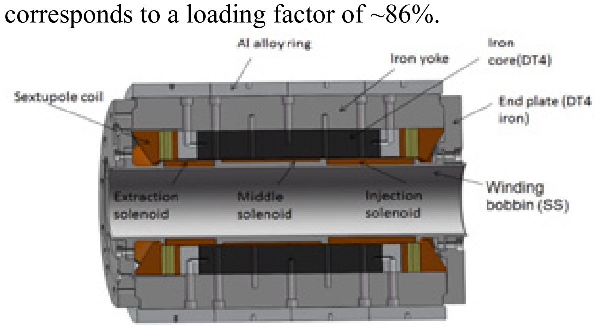

Figure 5: Sketch plot of SECRAL II cold mass.

Table 2: typical features of the rectangular wire from WST used for SECRAL II fabrication

Item	Specs.
Type	Monolith
Insulation	Formvar
Bare size (mm^2)	1.20 × 0.75
Insulated size (mm^2)	1.28× 0.83
Cu/Sc ratio	1.3:1
RRR	>100
No. of Filaments	630
Filament size (μm)	27.6
Pitch size (mm)	15

ISBN 978-3-95450-158-8

All the coils are wound through wet winding with Stycast 2850FT black epoxy. After the solenoids were finished, stainless steel strip is used to do the coil binding. Fiberglass cloth is adopted for insulation purpose. Sextupole coil winding is more complicated and difficult because of the special cross-section configuration and the racetrack layout. Each coil was wound around a 5-piece core, the central portion being an iron pole to enhance the radial field, two aluminium ends to compensate for thermal contraction and two G10 fillers to avoid the localized highest field region. The picture of one of the sextupole coils is given in Fig. 6. After curing, the sextupole coils were also formed to have even external shape for assembly by vacuum impregnation. The finished sextupole coils were bolted to cold iron segments separately, and thus 6 completed sextupole blocks were ready for assembly. The sextupole blocks were positioned around the solenoid bobbin through two end iron plates to fix the position and do pre-clamping. One of the very obvious virtues of SECRAL type configuration is that the Lorentz forces at the sextupole coils ends are all pointing outwards radially instead of being inwards and outwards periodically with traditional configuration magnet, therefore no radial support of the sextupole coil ends were needed provided that the coils are robust enough after curing. Very efficient pre-clamping of the sextupole coils were made by tight fitting installation of the aluminium rings. The negative tolerance designed aluminium rings were installed externally to the cold iron cylinder through hot shrinkage fit at about 150℃. Fig. 7 is the picture of the completed cold mass at the assembly site.

Figure 6: Picture of one of the sextupole coils.

Figure 7: Completed cold mass at the assembly site.

Cold Mass Test

The solenoids were tested in test Dewar separately when they were ready in 2013. Limited by the current power supply, all the three solenoids were only energized to 115% of the design currents without any quenches. 18 months after the fabrication contact being signed, the cold mass was ready for test Dewar training. The magnet system was supported vertically from the top of the magnet test Dewar. A set of quench protection system was installed, which is identical to the final one to be utilized in the real Dewar. The voltage on each coils were monitored to diagnose the quench triggering. Cold mass temperature and LHe depth were also monitored during the training. Since the stored energy of SECRAL is about 0.7 MJ at the designed currents, most of the LHe filled in the test Dewar (~220 liters) were evaporated when a quench happed at ~90% of the designed currents.

Energized separately, the sextupole coils reached 85% of the designed currents with 6 quenches. Then they were energized together with the axial coils. During the whole system training, all the elements were energized evenly together, which was realized by matching the ramping rate of each superconducting coil controllers and going in steps. 8 quenches were detected before the cold mass trained to 90% of the designed currents. It seems that more quenches are predicted if the magnet needs to be further trained to the designed values.

Cryogenics

The cold mass will be housed in a Ø817 mm ID 821 mm long LHe tank. Cold mass, LHe and the helium tank all together weighs about 1.54 tons, which will be supported by 8 support rods. To minimize the heat load to 4.2 K region, G10 material is utilized. 6 auxiliary SUS304 rods are also considered in the design to have redundant supports to ensure transportation safety. External to the 4.2 K reservoir, generally two thermal installation stages are designed. The first one is the 60 K copper shield, and the second one is the vacuum buffer between 60 K and room temperature. MLI solution is also considered in the design. The MLI are used between LHe tank and the 60 K shield, and inside the vacuum vessel. A typical layer density of 25 layers/cm is adopted. Evaporated helium gas will be recondensed to LHe by 5 condensers bolted to the 2nd stages of five 1.5 W GM coolers individually. To realize quick maintenance of the GM coolers without warming up the whole system, cryocooler sleeves are introduced in the design with the sacrifice of about 0.13 W extra heat load induced by each of the sleeves. 5 HTS leads are used to minimize the ohmic and conduction heat load between 60 K and 4.2 K stages. 5 Sumitomo RDK-415 D coolers can provide about 200 W cooling capacity at 60 K that is sufficient for the 60 K thermal shield cooling. The estimated total static heat load to 4.2 K is about 1.86 W, which allows a maximum dynamic heat load of 5.64 W. According to the operation experience with VENUS [7] and SECRAL I [3], this will be equivalent to the bremsstrahlung radiation heat load to 4.2

ISBN 978-3-95450-158-8

K induced by ~3.5 kW 28 GHz microwave heated ECR plasma. But in actual operation condition and for technical reasons, the practical dynamic heat load capacity will be much lower than the nominal value 5.64 W. Fig. 8 is the sectional plot of SECRAL II magnet with most of the subsystems integrated.

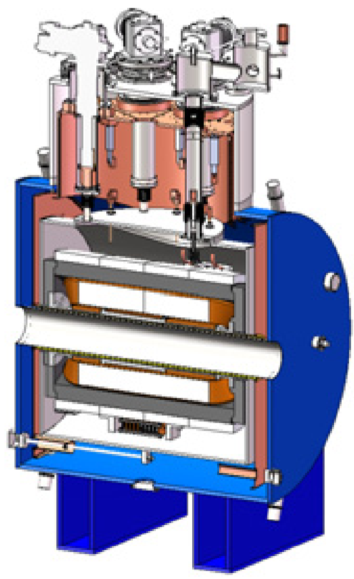

Figure 8: Side view of the magnet sectional plot.

SECRAL II TEST BENCH DESIGN

SECRAL II plasma will be heated by the microwave power from a CPI 10 kW/28 GHz gyrotron amplifier. The plasma chamber will be floated to 25 kV high voltage so as to have efficient beam extraction. A triode extraction system will be adopted to have flexibility on beam extraction optics optimization and suppression of secondary electrons entering the acceleration region. Ion source vacuum is pumped by oil free pumps. A 700 L/s turbo pump is to be installed at source injection tank and a 2000 L/s pump is going to be mounted on the source extraction box. Extracted beam will be focused by a solenoid with aberration correction design. Extracted ion beams will be analysed by a 180 mm gap, 510 mm bending radius, 90 ° double focusing bending magnet. Knowledge from beam line design of VENUS [8] and experimental results from SECRAL [9] indicates that large vertical gap can maximize the beam transmission efficiency through the M/Q analyzer and minimize the high order aberration pickup at the meantime. A set of triplet quadrupole magnets are designed to be mounted after the bending magnet so as to have optimal tuning of the analysed beam twiss parameters and also to improve the beam optical resolution. One 10 cm long solenoid is designed to be installed between the beam slits and the faraday cup or emittance scanner to do beam coupling de-correction compensation, so as to improve the beam quality. The layout of beam line design is given in Fig. 9.

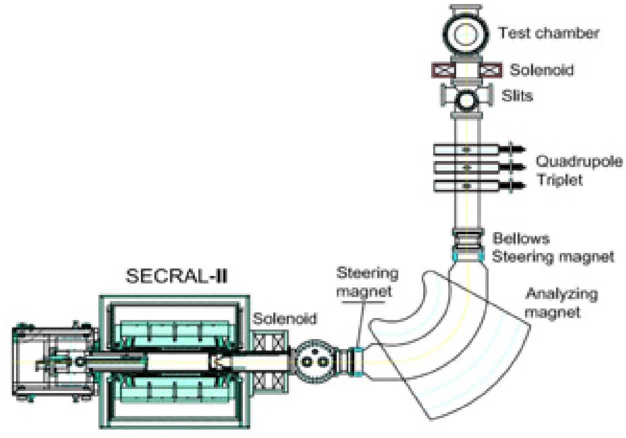

Figure 9: Layout of the SECRAL II test bench.

CONCLUSION

By technical improvement of the cartridge oven technique at IMP, SECRAL I ion source have almost doubled its production performance of intense highly charged bismuth ion beams i.e. 710 eμA Bi^{30+} and 680 eμA Bi^{31+}. Thanks to the fine plasma confinement and efficient ECR heating at 24 GHz + 18 GHz, intense ion beams of very high charge state were also obtained, such as 100 eμA Bi^{41+} and 0.05μA Bi^{57+}. Based on the same conceptual design, a close copy of SECRAL I ion source, SECRAL II is now under construction at IMP. The cold mass was tested in June 2014. The magnet had been successfully trained to 90% of its design currents in the test Dewar. Provided more quenches, the excited currents could be much closer to the designed ones.

ACKNOWLEDGMENT

Dr. Daniel Xie is well acknowledged for the discussion on cartridge oven technique. Dr. Detlef Krischel is well acknowledged for his fruitful suggestions on SECRAL II fabrication. The authors would also like to thank the team in XSMT (Xi'an Superconducting Magnet Technique) company for their great work on SECRAL II magnet fabrication.

REFERENCES

[1] J. W. Xia et al., "HIRFL Status and HIRFL-CSR Project in Lanzhou", APAC'98, Tsukuba, Japan, March 1998, p.342 (1999); http://www.JACoW.org
[2] Y. J. Yuan et al., Nucl. Instr. Meth. B 317, 217 (2013).
[3] H. W. Zhao et al., Rev. Sci. Instrum. 81, 02A202 (2010).
[4] L. T. Sun et al., Rev. Sci. Instrum. 81, 02A318 (2010).
[5] L. Sun et al., Rev. Sci. Instrum. 85, 02A942 (2014).
[6] Y. Cao et al., Rev. Sci. Instrum. 77, 03A346 (2006).
[7] D. Leitner et al., Rev. Sci. Instrum. 77, 03A302 (2006).
[8] M. Leitner, S. R. Abbott, D. Leitner, C. Lyneis, "A High Transmission Analyzing Magnet for Intense High Charge State Beams", ECRIS'02, Jyvaskyla, Finland, June 2002, p. 32 (2002).
[9] Y. Yang, L. T. Sun, Q. Hu, Y Cao, W. Lu, Y. C. Feng, X. Fang, H. W. Zhao, and D. Z. Xie, Rev. Sci. Instrum. 75, 02A719 (2014).

ISBN 978-3-95450-158-8

HIISI, NEW 18 GHZ ECRIS FOR THE JYFL ACCELERATOR LABORATORY*

H. Koivisto#, O. Tarvainen, T. Kalvas, K. Ranttila, P. Heikkinen, JYFL, Jyväskylä, Finland
D. Xie, LBNL, Berkeley, USA
G. Machicoane, NSCL, East Lansing, USA
T. Thuillier, LPSC, Grenoble, France
V. Skalyga, I. Izotov, IAP RAS, Nizhny Novgorod, Russia

Abstract

At the end of 2013 the Academy of Finland granted an infrastructure funding for the JYFL Accelerator Laboratory in order to increase beam intensities for the international user community. The primary objective is to construct a new high performance ECR ion source, HIISI (Heavy Ion Ion Source Injector), for the K130 cyclotron. Using room temperature magnets the HIISI has been designed to produce about the same magnetic field configuration as the superconducting ECRIS SUSI at NSCL/MSU for 18 GHz operation. An innovative structure will be used to maximize the radial confinement and demagnetization safety margin of the permanent magnets. The sextupole magnet is separated and insulated from the plasma chamber providing two advantages: 1) the permanent magnet can be cooled down to -10°C to increase its coercivity and 2) at the same time to reach slightly higher radial field on the inner surface of the plasma chamber. Comprehensive simulations were performed with the radial heat load to analyse and address all the heat loads and temperature distribution on the permanent magnet. This information is crucial to define the maximum plasma heating power and the grade of the permanent magnets. In this article the magnetic field design of HIISI and detailed innovative scheme for sextupole magnet will be presented.

INTRODUCTION

Figure 1 shows the xenon ion beam intensities produced by high performance ECR ion sources. GTS [1], operating at 18 GHz frequency, is the best performing ECR ion source using room temperature magnets (resistive coils and permanent magnet sextupole), while VENUS [2] and SUSI [3] are fully superconducting ECR ion sources. The same performance level has also been achieved by fully superconducting SECRAL [4]. Although the great performance of superconducting ion sources meets and exceeds our goals, their construction costs greatly exceeds the available funding for the new JYFL ECR ion source leading to the choice of a room-temperature magnet ECRIS.

From the ion source performance point of view the most challenging requirement for HIISI is the production of highly charged heavy ion beams. For example, an intensity of about 10 nA for Xe^{44+} ion beam is needed to guarantee the requested beam energy and particle flux after the K130 cyclotron. This requirement is shown in Figure 1 by a red circle, which is beyond the performance of any present room-temperature magnet ECR ion source. The development of this new ECR ion source HIISI will enhance the high quality nuclear physics research at JYFL and potential for exciting discoveries in the future.

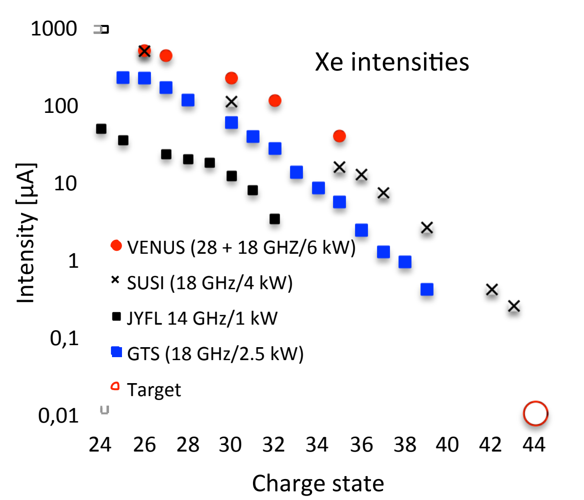

Figure 1: Intensities of Xe ion beams produced by different ECR ion sources. The red circle indicates the beam intensity of Xe^{44+} ion beam to be produced with the new ECRIS operated at 18 GHz.

MAGNETIC FIELD STRUCTURE

As Figure 1 shows, the performance of SUSI exceeds the desired intensity of Xe^{44+} ion beam when operated at 18 GHz with the microwave power of 4 kW. The magnetic field configuration of SUSI for the production of Ar^{12+} and Xe^{35+} ion beams are listed in Table 1 indicating that the intensive highly-charged ion beams can be produced with the magnetic field strengths in the range of: 2.5 – 2.8 T (B_{inj}), 1.2 – 1.5 T (B_{ext}), 1.1 – 1.35 T (B_{rad}) and about 0.45 T (B_{min}). All these field strengths agree well with the empirical source design criteria [5]. The

* This work has been supported by the EU 7th frame- work programme Integrating Activities - Transnational Access, project number: 262010 (ENSAR), the Academy of Finland under the Finnish Centre of Excellence Programme 2012- 2017 (Nuclear and Accelerator Based Physics Research at JYFL) and under the Finnish Research Infrastructure (FIRI) Programme of the Academy of Finland.
#hannu.koivisto@phys.jyu.fi

ISBN 978-3-95450-158-8

plasma chamber of SUSI is 100 mm in diameter with axial resonance surface length (cold electrons) varying between 110 – 145 mm. Although somewhat challenging these field configurations could be achieved with room temperature magnets and are the design basics for HIISI.

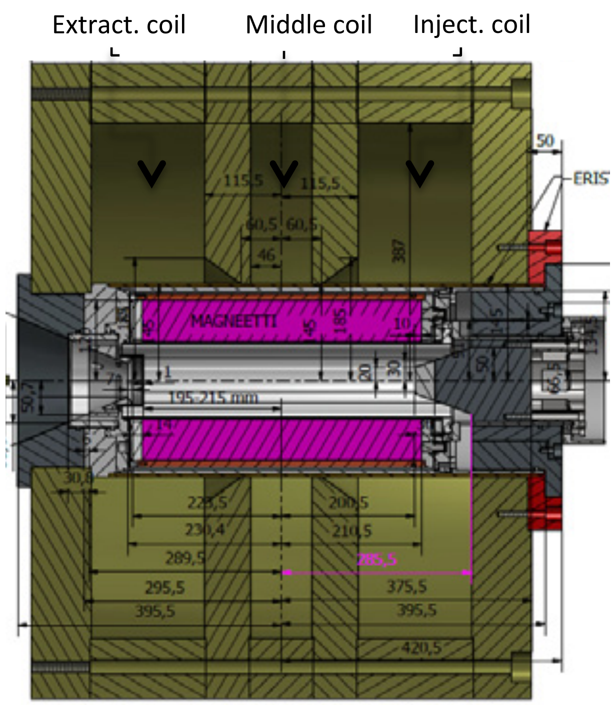

Figure 2: Layout of the JYFL 18 GHz ECRIS, HIISI.

Figure 2 shows the cross-sectional view of the new 18 GHz ECRIS HIISI. Each of the injection and extraction coils has 7 double pancakes with 20 radial turns. A middle coil of 3 similar double pancakes will be used for fine-tuning of the minimum-B (B_{min}). Table 2 shows the magnetic field configurations with different coil excitations, that are very close to the SUSI operation parameters at 18 GHz as shown in Table 1. The power consumption for generating these field configurations ranges between 137 kW – 216 kW. The axial magnetic field profile is shown in ref. [6].

Both tables show also the gradients of magnetic field (gradB) on the axial resonance points (for cold electrons). Several groups have observed the link between the magnetic field gradient and plasma instabilities: for more details see for example [7, 8]. For example, the operation experience with SUSI has shown that the ion beam becomes unstable when the gradient of magnetic field goes below 5 T/m but this threshold can be different for different ion source geometries. HIISI can be operated in single-frequency mode of either 18 GHz or 14 GH waves and also in multiple-frequency mode of 14 GHz and 18 GHz waves together with TWTA. In 14 GHz operation mode the power consumption of coils can be kept below 100 kW.

REFRIGERATED AND INSULATED SEXTUPOLE CHAMBER

Both the injection coil and the permanent magnet sextupole generate high demagnetizing fields on the permanent magnet blocks. To minimize the demagnetization, permanent magnet grade of N40UH, having B_{rem} and coercivity of 1.29 T and 1990 kA/m at 20˚C, respectively, has been chosen for constructing the sextupole magnet for HIISI. A comprehensive demagnetization analysis will be presented elsewhere in this proceeding [6]. According to the analysis a negligible permanent magnet volume exposes to demagnetizing field exceeding 1800 kA/m. Therefore safe operation is guaranteed as long as the magnet temperature will not exceed 20˚C.

The high coercivity of selected magnet material limits the remanence (B_{rem}) to 1.29 T. As a result, the radial field of 1.36 T (B_{rad}) shown in Table 1 is very difficult to reach. Two techniques have been studied in order to maximize B_{rad}: 1) new cooling scheme to minimize the gap between the plasma and inner surface of permanent magnet sextupole and 2) cooling of the permanent magnets to 0˚C or less.

Table 1: Intensities of Ar^{12+} and Xe^{35+} ion beams produced by SUSI at 18 GHz heating frequency with the shown magnetic field configurations.

Element	q	I [uA]	$P_{\mu w}$ [kW]	B_{rad} [T]	B_{inj} [T]	B_{min} [T]	B_{ext} [T]	gradB Inj [T/m]	gradB Ext [T/m]	Plasma Length
^{129}Xe	35+	16	3.2	1.36	2.8	0.46	1.56	6.6	5.9	115 mm
^{40}Ar	12+	730	3.8	1.06	2.5	0.43	1.19	6.8	5.6	142 mm

Table 2: Magnetic field configurations of HIISI designed for 18 GHz operation.

Pcoils [kW]	I_{inj}	I_{mid}	I_{ext}	B_{inj} [T]	B_{min} [T]	B_{ext} [T]	gradB Inj [T/m]	gradB Ext [T/m]	Plasma Length
216	1050	600	1050	2.51	0.43	1.52	6.3	6.3	132 mm
158	1000	300	820	2.48	0.42	1.33	6.1	6.1	143 mm
137	1000	210	680	2.48	0.41	1.18	6.2	5.5	157 mm

ISBN 978-3-95450-158-8

Plasma Chamber Cooling Scheme

The new cooling scheme of plasma chamber is presented in Figure 3. The plasma chamber and permanent magnets are fully separated by a vacuum insulated gap (about 1.5 mm). The water-cooling channel is located by the side of the plasma flux, i.e both sides of radial magnetic pole. This makes it possible to decrease the wall thickness of plasma chamber on the magnetic pole to about 2.5 mm. Such a design leads to a total distance of 4 mm between the plasma chamber inner wall and permanent magnet inner surface. The plasma chamber is placed inside a refrigerated sextupole chamber, which is shown in Figure 7.

The plasma chamber is not physically in direct contact with the permanent magnet blocks and consequently its temperature does not play a critical role regarding the demagnetization of the permanent magnet blocks. In this design the total heat load on the permanent magnet blocks comes from the heat radiation, heat transfer by the residual molecules inside the vacuum gap and by the heat conduction from the support structure of the sextupole chamber. Although the heat load is small it will increase the temperature of the magnets and these effects have to be taken into account in the design of the cooling of the sextupole magnet. These studies are presented elsewhere in these proceedings by T. Kalvas [6].

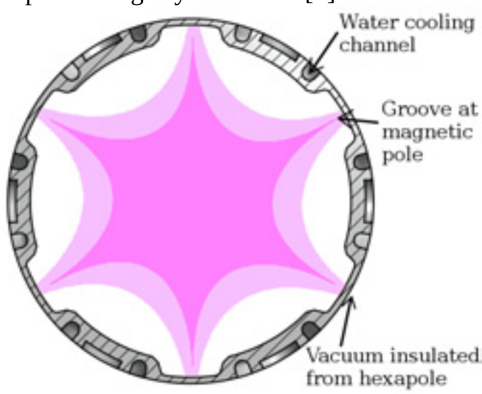

Figure 3: Plasma chamber structure for maximizing radial field strength.

Temperature Distribution and Maximum Microwave Power

The temperature distribution of the plasma chamber is needed for two reasons: 1) to define the heat load and temperature distribution of permanent magnets and 2) to define the maximum temperature of the aluminium chamber. The first information is needed in order to design the cooling of the permanent magnets and to choose the magnet grade, while the latter one to define the maximum operating microwave power. Based on the magnetic symmetry the chamber has been divided to 3 symmetric sectors to minimize time needed for the simulations. Figure 4 shows the temperature distribution (1/12 sector) on the surface of the plasma chamber wall when an electron flux carrying a total power of 6 kW is lost radially. According to our plasma flux simulations about 80 % of the microwave power will be directed to radial loss cones (see [6]). As Figure 4 shows the total radial heat load of 6 kW for the given geometry will result in a maximum temperature of around 410 K on the plasma chamber wall. In the simulations the cooling water temperature of 300 K was used. The total wall thickness and width of the groove was 2.5 mm and 16 mm, respectively. In order to avoid the aging of aluminium (deterioration of strength properties) the maximum temperature should be kept below 370 K (100 ˚C). Consequently, the total microwave power fed into the plasma chamber has to be kept below 5 kW. Here it is assumed that 80 % of the power is directed toward the radial poles corresponding to the radial power load of 4 kW. This value is not exceeded by using simultaneously two Klystrons and TWTA having the power of 2.4 kW and 500 W, respectively. Here it is assumed that the transmission losses are 10 % or more.

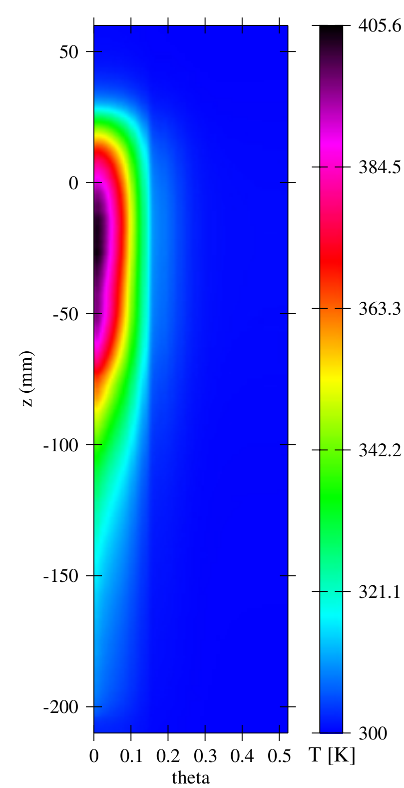

Figure 4: Temperature distribution on surface of the plasma chamber. Total radial power flux of 6 kW was used in the simulations.

Refrigerated Permanent Magnets

It is a well-known fact that the coercivity and the remanence magnetic field B_{rem} of permanent magnets decrease with increasing temperature. This effect was studied at JYFL [9] by cooling of the magnets and by defining the value of B_{rem} as a function of temperature.

ISBN 978-3-95450-158-8

The experimental behaviour of remanence field is shown in Figure 5. The experiments were performed using the permanent magnet grade of N48 having the values of 1.42 T and 1353 kA/m for B_{rem} and coercive force, respectively. This magnet grade is used for the sextupole of the JYFL 14 GHz ECRIS. The field increased from 1.4 T (at room temperature) up to 1.57 T by using liquid N2 cooling. A cryogenic sextupole scheme has been studied also by LSPC ion source group by simulations [10]. This property of permanent magnets will be studied and tested with HIISI.

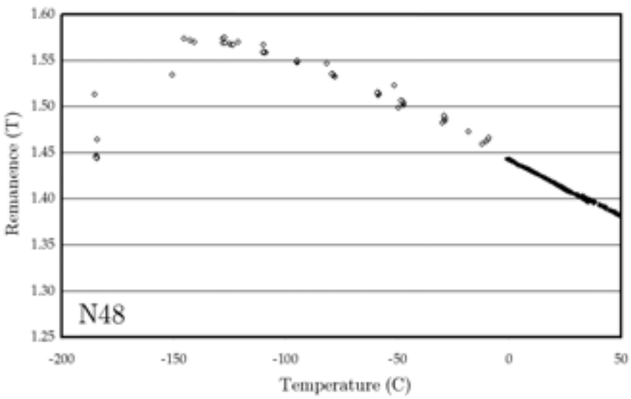

Figure 5: Remanence magnetic field B_{rem} of grade N48 permanent magnet experimentally defined as a function of temperature [9].

Figure 6 shows the demagnetization curves and coercive force for selected magnet grade (N40UH) at different temperature. As mentioned above the demagnetization analysis has shown a negligible volume of the permanent magnets experiences demagnetizing stress exceeding 1800 kA/m. Consequently, the magnets are in safe operation point as long as their temperature is kept at around 20˚C (or below). The extra cooling will increase B_{rad} and especially the coercive force of the magnets. A mechanical stress analysis indicated that the sextupole magnet configuration can be cooled down to -10˚C without any irreversible damages or reaching the yield point of sextupole chamber made of aluminum (see Figure 7).

As a consequence of mechanical stress analysis the design goal is to cool the permanent magnet down to -10˚C. This would strongly improve the coercive force making it possible to use other grade of permanent magnet material – for example N48. The effect of cooling and use of other magnet grade is shown in Table 3. The configuration numbers 1-7 are related to 24-segment Halbach and configuration number 8 to 36-segment Halbach. The first sextupole configuration will be realized by using a 24 -segment offset [11] Halbach structure having the gap of 4 mm and magnet grade of N40UH (configuration number 4 in Table 3). This will result in B_{rad} of 1.24 T/1.28 T depending on the temperature of the permanent magnets (20˚C/-10˚C). The latter value, which is reached at -10˚C, fulfils the scaling rule for sextupole field. However, it does not fully reach the B_{rad} value, shown in Table 1, needed for the production of high intensity Xe^{35+} ion beam.

Table 3: Value of B_{rad} with different configurations.

Config. No	Gap [mm]	T [˚C]	B_{rem} (at 20˚C) [T]	B_{rad} [T]
1	3	20	1.29	1.29
2	4	20	1.29	1.24
3	5	20	1.29	1.19
4	**4**	**-10**	**1.29**	**1.28**
5	4	-30	1.29	1.31
6	4	-30	1.32	1.34
7	4	-30	1.42	1.44
8	4	-30	1.42	1.51

As a next step, when the operation with the refrigerated sextupole structure at -10˚C is fully developed and found reliable, the sextupole structure will be realised by using other grade of magnet material (N48 grade shown in Table 1, Config. No 7-8). In addition to this and further development of cooling (for example down to -30˚C) the sextupole field up to 1.5 T could be reached.

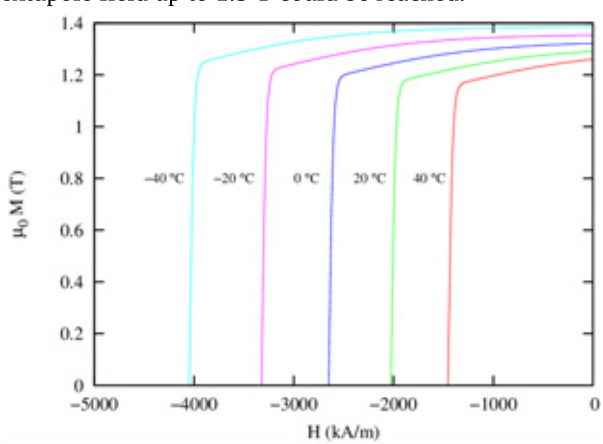

Figure 6: Demagnetization behaviour of N40UH permanent magnet as a function of temperature.

Figure 7 shows the configuration designed for the cooled and vacuum insulated permanent sextupole magnet. The plasma chamber is situated inside the sextupole chamber, which is nested in a pumping chamber. Using this arrangement the permanent sextupole magnet is in rough vacuum and exposed to following heat loads: 1) heat radiation from surrounding structures, 2) power flux caused by the residual gas and 3) heat conduction via support structure. Although the microwave power will not exceed 5 kW the temperature distribution shown in Figure 4 has been used for the afore-mentioned simulations for some extra safety margin. The comprehensive heat load and temperature distribution simulations are presented in [6] confirming that this scheme for the cooling of sextupole magnet is feasible.

ISBN 978-3-95450-158-8

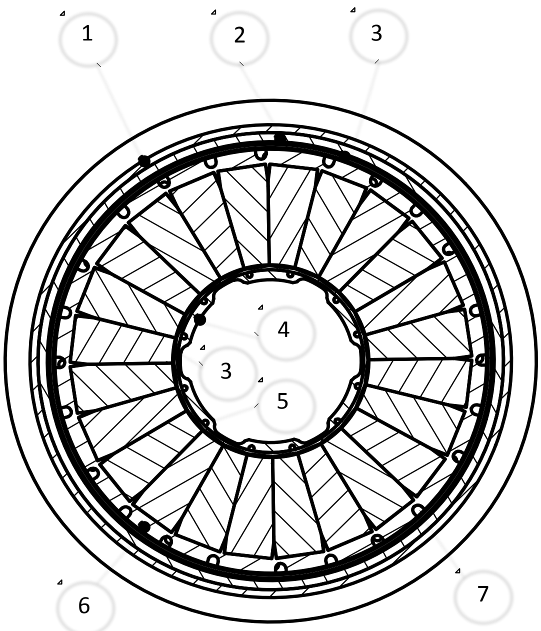

Figure 7: Plasma chamber inside the sextupole chamber and sextupole pumping chamber: 1) Insulator, 2) Sextupole pumping chamber, 3) Rough vacuum, 4) Plasma chamber, 5) Plasma chamber cooling line, 6) Sextupole chamber, 7) Sextupole chamber cooling line.

The design project was started in the beginning of 2014. In fall 2014 we are now ready to start the work for the detailed drawings. The first components will be ordered by the end of 2014 while the main components for the production of magnetic field will be ordered by summer 2015. Site construction will be started during the fall of 2015 and source commissioning is expected by summer 2016.

REFERENCES

[1] D. Hitz, A. Girard, K. Serebrennikov, G. Melin, D. Cormier, J. M. Mathonnet, and J. Chartier, Rev. Sci. Instrum, Vol 75 (5), (2004), p. 1403.
[2] C. M. Lyneis, D. Leitner, S. R. Abbott, R. D. Dwinell, M. Leitner, C. S. Silver, and C. Taylor, Rev. Sci. Instrum., Vol. 75 (5), (2004), p. 1389.
[3] P. A. Zavodszky et. al., Rev. Sci. Instrum., Vol. 79, (2008), p. 02A302.
[4] H.W. Zhao, et al., Rev. Sci. Instrum., Vol. 77, (2006), p. 03A333.
[5] D. Hitz, A. Girard, G. Melin, S. Gammino, G. Ciavola, and L. Celona, Rev. Sci. Instrum. **73**, (2002), p. 509.
[6] T. Kalvas et al., this proceeding.
[7] O. Tarvainen et al., Plasma Sources Sci. Technol. 23 (2014), p. 025020.
[8] G. Machicoane, private discussion.
[9] P. Frondelius, Master thesis, Department of Physics, University of Jyväskylä, 2005.
[10] T. Thuillier, T. Lamy, C. Peaucelle and P. Sortais, Rev. Sci. Instrum., Vol. 81, (2010), p. 02A316.
[11] P. Suominen, O. Tarvainen, H. Koivisto and D. Hitz, Rev. Sci. Instrum., Vol. 75 (1), (2003), p. 59.

ISBN 978-3-95450-158-8

THE INSTALLATION OF THE 28GHZ SUPERCONDUCTING ECR ION SOURCE AT KBSI

Jin Yong Park, Byoung-Seob Lee, Seyong Choi, Jung-Woo Ok, Seong Jun Kim, Jonggi Hong, Chang Seouk Shin, JungBae Bahng, Jang-Hee Yoon, Mi-Sook Won#, Busan Center, Korea Basic Science Institute, Busan 609-735,South KOREA

Abstract

In 2009, a 28 GHz superconducting electron cyclotron resonance (ECR) ion source was developed to produce high currents, diverse heavy ion charge state for the compact heavy ion linear accelerator at KBSI (Korea Basic Science Institute). The aim of this study was to generate a high current, and fast neutrons for interacting a heavy ion with the proton target. The fabrication of the key parts, which are the superconducting magnet system with the liquid helium re-condensed cryostat, the 10 kW high-power microwave considering for optimum operation at the 28 GHz ECR Ion Source, were completed in 2013. The waveguide components were connected with a plasma chamber including a gas supply system. The plasma chamber and ion beam extraction were inserted into the warm bore of superconducting magnet. In this paper, we present the current status of the installation of an ECR ion source and report on the test results for ECR plasma ignition.

INTRODUCTION

The compact linear accelerator employing the 28 GHz ECR ion source was developed at KBSI [1]. The practical purpose of the KBSI accelerator is to produce fast neurons for the high-resolution radiography technology. We have been fabricating a 28 GHz superconducting ECR ion source to deliver high intensity beams of highly charged heavy ions into the radio frequency quadrupole (RFQ) and the drift tube linear accelerator (DTL). To fulfill this target, accelerated ^{7}Li ions need to interact with a hydrogen gas jet at an energy of a few MeV/u, which then generate high-intensity fast neutrons at forward angles. The 28 GHz superconducting ECR ion source was developed in 2009. The design of each component of the ECR ion source was completed in 2010. The individual components were assembled in 2011. Very recently, a 28 GHz superconducting ECR ion source has been installed, as shown in Figure 1. In this article, we present information regarding the components required for the ion source in details, and the experimental setup for the first plasma ignition.

THE SUPERCONDUCTING MAGNETS

The superconducting magnet system is comprised of 3 mirror solenoid coils and a hexapole magnet [2, 3]. The inside diameters of the hexapole magnet and solenoid coils are 207 mm and 442 mm, respectively. Two kinds NbTi superconducting wire was used for the magnet system. A higher current density NbTi wire was selected for the winding of hexapole magnet, respectively. The copper/NbTi ratios were 4.9 for the solenoid coils and 2.32 for the heaxpole magnet. The superconducting magnets have an operating margin of about 30% away from the critical current, according to the design values. Figure 2 shows a schematic drawing of the superconducting magnet system.

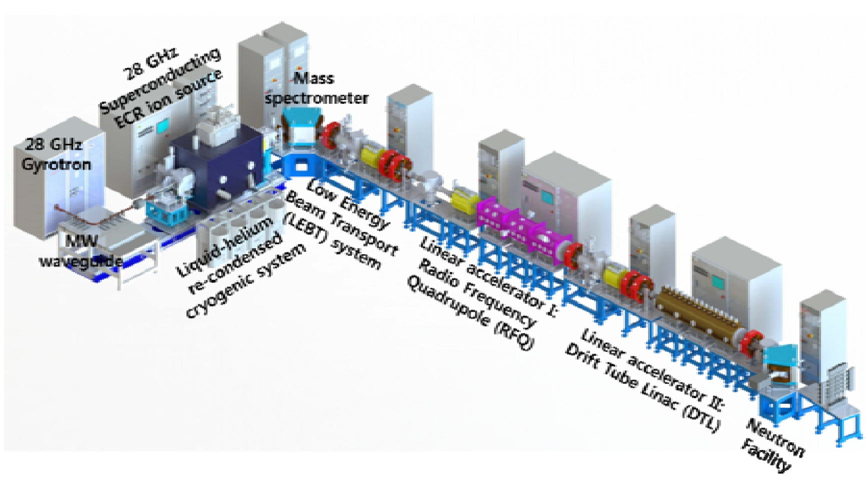

Figure 1: Schematic view of the heavy ion accelerator with the 28 GHz superconducting ECR ion source.

#mswon@kbsi.re.kr

ISBN 978-3-95450-158-8

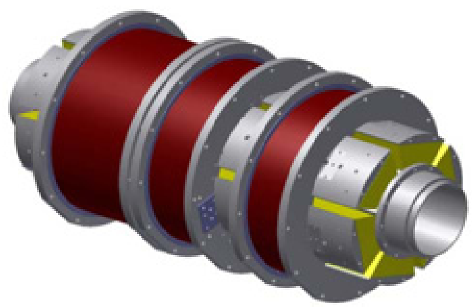

Figure 2: Layout of the superconducting magnet system.

The three solenoid magnets were assembled with stainless steel pipe. Step-type racetrack coils were placed around the aluminum bore tube. We inserted titanium wedges at the interfaces of each coil, to provide azimuthal compression. The ends of the hexapole magnet are fixed with a stainless steel metal clamp, in order to support the large radial electromagnetic force.

Figure 3 shows the layout of the cryogenic system. The cryogenic system for superconducting magnet operates at 4.2 K with liquid helium, and was designed to operate in a closed loop mode Additional liquid helium is not needed to be transferred during operation because a helium recondenser is used to maintain a constant liquid level. The four recondenser units are installed at the top of the liquid helium vessel and linked with the cryocoolers. They liquefy the helium gas and it then drops by gravity. The helium recondenser controller monitors (HRC-100) control the pressure in the vessel to maintain the level of the liquid helium inside of the cryostat within a target value. It was demonstrated that the cryogenic system is capable of achieving appropriate recondensing performance through long time experiments[4]. Even when the superconducting magnet is in full operation, there is no changes in the liquid helium level. Based on the experimental results for the superconducting magnet and cryogenic system, we concluded that the superconducting magnet system is now ready for the plasma ignition.

PLASMA CHAMBER

The plasma chamber is also shown in Figure 3. The chamber length and its diameter are 500 mm and 150 mm respectively and is made of a stainless steel (SUS316L) material. The cooling water channel (>5 L/min) is located at each end side of the plasma chamber wall. The electrode and chamber for ion beam extraction was designed so as to be retractable in the case when maintenance work is needed. The two turbo molecular pumps are installed under the injection and extraction boxes. The chamber is pumped by the capacity of 1100 L/sec for the realization of ultra-high vacuum level (~ 10^{-8} Torr). If plasma ignition occurs in the chamber, the generation of a large amount of X-rays would be predicted. It is generally reported that the X-rays would be as a heat load for a cryogenic system. Such an unexpected heat load would affect cryogenic performance. Therefore, a simulation with regard to the generation of X-rays was carried out and considering the likely effect of X-rays on shield thickness[5]. We plan to wrap the plasma chamber with a 2 mm thick tantalum sheet to reduce the effect of X-rays and to also employ a Kapton sheet for electrical insulation.

MICROWAVE SYSTEM

The microwave are initially delivered from a gyrotron with 28 GHz, 10 kW at a TE02 mode through a circular waveguide (WC128). In order to avoid damage arising from reflected power, the security and detection system are located in front of the gyrotron. For safety reasons, it is necessary to protect the devices and personnel. One 90-degree corrugated bend and three linear waveguides are connected to deliver the microwave power from the gyrotron to the plasma chamber.

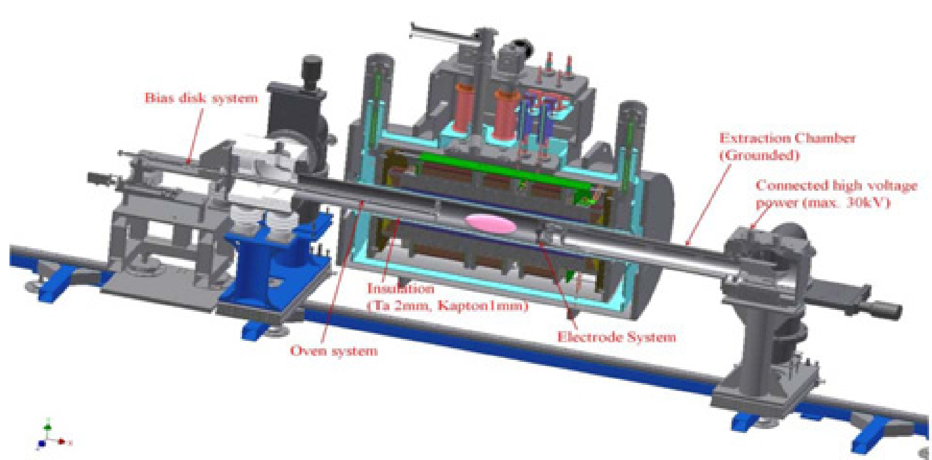

Figure 3: Layout of the cryogenic system and plasma chamber.

ISBN 978-3-95450-158-8

Figure 4: The 28 GHz microwave transmission line from gyrotron to ECR ion source.

The waveguide system is connected in series with the following components as shown in Figure 4 and 5. We measured the values of microwave power at each component using a self-developed dummy load. 2 kW of microwave power was generated and delivered to the waveguide components. The results are listed in Table 1. As shown in the table, most of the microwave power was measured at several location. Compared to out power from the gyrotron, most of power was delivered and consumed at the dummy load. This also means that the output of gyrotorn (2 kW) was not forwarded completely to the waveguides but the deviation (reflected power) appeared to be negligible. It was observed that the output frequency variation at 28 GHz was from 27.9740 GHz to 27.9893 GHz and the frequency fluctuation was found to be below 0.1 %.

Table 1: Forward microwave power at each

Location	Component	Measured Power[kW]
Default	Gyrotron + Directional coupler: (A)	1.9
1	(A) + Mode Converter : (B)	1.88598
2	(B) + Mode Filter : (C)	1.89102
3	(C) + 90° bend: (D)	1.88598
4	(D) + DC Break	1.87658

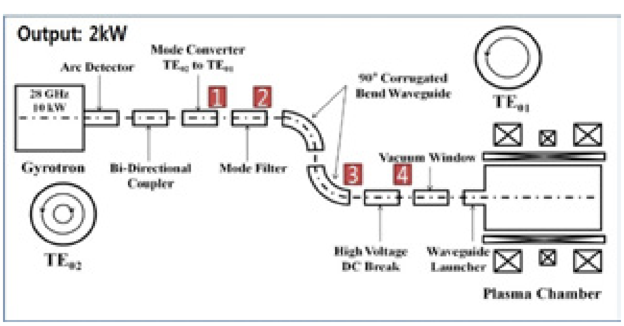

Figure 5: The 28 GHz microwave transmission line from gyrotron to ECR ion source.

PLASMA IGNITION

As we reported above, the majority of the parts(superconducting magnet with liquid helium cryostat, plasma chamber, microwave system and so on) were ready for plasma ignition. For the initial ignition, Ar gas was prepared for the experiment. After injecting Ar gas into the plasma chamber, the vacuum changed from a few of 10^{-8} Torr to 10^{-6} Torr. We carried out the experiment under normal condition for the superconducting magnet because the training of the entire magnet has not finished yet. The axial magnetic field is about 2.3 T at the injection area, and 2.1 T at the extraction region. A radial magnetic field of 1.3 T on the plasma chamber wall was used for the initial plasma ignition. According to the magnetic field distribution, we limited the microwave power to less than 1 kW. Figure 5 shows the Ar gas plasma after applying the gyrotron operation power. It can be seen that the typical ECR plasma was shaped like a star, which was mainly caused by the hexapole magnet field.

We already installed the extraction part for producing the ion beam. In the next step, we plan to extract and transport the ion beams through the LEBT beam line during this year. Ion beam current and intensity will be measured at the diagnosis chamber with various tools (slits, wire scanner faraday cup and so on).

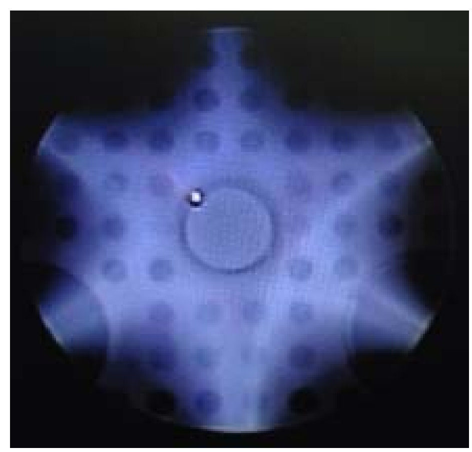

Figure 6: Picture of Argon plasma ignition.

ACKNOWLEDGMENT

This work was supported by the Korea Basic Science Institute under Grant No. D34300.

REFERENCES

[1] J. -H. Yoon et al., Rev. Sci. Instrum., 83 (2012), 02A315.
[2] B. S. Lee et al., Rev. Sci. Instrum., 83 (2012), 02A347.
[3] J. Y. Park et al., Rev. Sci. Instrum., 85 (2014), 02A928.
[4] S. Y. Choi et al., Rev. Sci. Instrum., 85 (2012), 02A315.
[5] J. Y. Park et al., Rev. Sci. Instrum., 85 (2014), 02A948.

ISBN 978-3-95450-158-8

FIRST COMMISSIONING RESULTS OF AN EVAPORATIVE COOLING MAGNET ECRIS-LECR4*

W. Lu, L.T. Sun, X.Z. Zhang,C. Qian, B.H. Ma and H.W. Zhao, IMP, Lanzhou 730000, China
B. Xiong, S. Q. Guo and L. Ruan, IEE, Beijing 100190, China
D. Z. Xie, LBNL, USA

Abstract

LECR4 (Lanzhou ECR ion source No.4) is a room temperature ECR ion source, designed to produce high current, multiple charge state ion beams for SSC-LINAC project at IMP. The ion source has been optimized to be operated at 18 GHz. A unique feature of LECR4 is that all of its axial solenoid coils are fully immersed in a special coolant and cooled by evaporative cooling technology when excited. At design currents, the coils can produce peak mirror fields on axis 2.5Tesla at injection, 1.3 Tesla at extraction and 0.5 Tesla at minimum-B. The nominal radial magnetic field is 1.0-1.1 Tesla at plasma chamber wall, which is produced by a Halbach structure 36-segmental hexapole magnet. Recently, the project has made significant progress. In January 2014, the first plasma at 18 GHz was ignited. During the ongoing commissioning phase with a stainless steel chamber, tests with ion beams: Oxygen, Argon,Xenon and Bismuth have been conducted. Some intense ion beams have been produced with microwave power less than 1.6 kW, such as 1.97 emA of O^{6+}, 1.7 emA of Ar^{8+}, 1.07 emA of Ar^{9+}, 290 euA of Xe^{20+} and so on.

INTRODUCTION

A room temperature ECR ion source named LECR4 (Lanzhou ECR ion source no.4) was designed and built at Institute of Modern Physics (IMP) to meet the demand of intense multiple charge state ion beams for SSC-LINAC project [1]. The other purpose of the LECR4 project is to test an evaporative cooling technology for its application to accelerator magnet. SSC-LINAC is a new CW heavy ion LINAC used as the injector for the Separated Sector Cyclotron (SSC) at IMP. The SSC-LINAC consists of an ECR ion source, low energy beam transport (LEBT), a 4-rod RFQ, medium energy beam transport (MEBT) and IH-DTL, as shown in Figure 1. The required ion species are from Carbon to Uranium. According to the demand, traditional room temperature ECR ion sources with operation microwave frequency 14- 18 GHz were considered. According to Prof. Geller's famous scaling laws, we know that higher magnetic fields and higher frequencies will increase the performance of ECR ion source. Following these guidelines, many high performance room temperature ECR ion sources like AECR-U [2], RIKEN 18 GHz [3], IMP-LECR3 [4] and GTS [5] have been built. All these ECR ion sources need high pressure de-ionized water system to cool the high current axial mirror field magnet coils. Recently, with advances in evaporative cooling technology at Institute of Electrical Engineering of Chinese Academy of Science (IEE, CAS) [6], a de-ionized water free room temperature ECR ion source with new cooling technology is possible. IEE institute has been researching the evaporative cooling technology since 1958. Up to now, this technology has been applied in many high-power, high current density devices, such as Three Gorges Power Station. According to careful simulation and prototype experiments [7], the final design of ECR ion source (named LECR4) was completed in 2012. About one year later, the source body assembly was fabricated at IMP. In October 2013 the axial magnet reached 100% of the design fields. The first beam of LECR4 was extracted and analyzed in February 2014. The ion source commissioning of intense multiple charge state ion beams was performed from February 2014 to July 2014.The first test with RFQ was performed on 4th April 2014. The preliminary results will be presented in this paper.

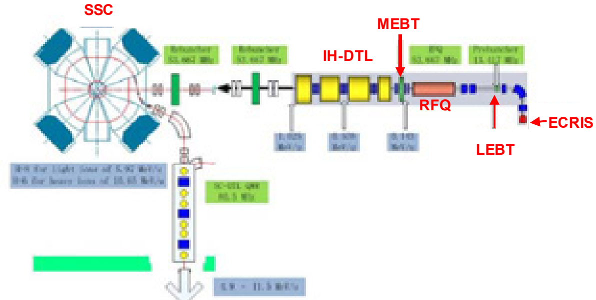

Figure 1: General view of the SSC_Linac.

LECR4 ION SOURCE

Figure 2 shows the layout of LECR4 and its beam transport line. There is no vacuum pump at the injection side for simplicity. The detail design of LECR4 ECR ion source can be found in the reference paper [8].The features of LECR4 are following:

- LECR4 is the first ECR ion source using evaporative cooling technology in the world. All the coils are fully immersed in a special coolant, named ZXB-21. Its boiling temperature is 47.7 degree in a standard atmospheric pressure. Solid square copper wires (3.32 mm×5.77 mm with insulation) are used to wind the solenoid coils. The maximum exciting current is 300 A, that means an average current density about 12 A/mm², slightly higher than using

*This collaboration project was supported by the Research Foundation of Chinese Academy of Sciences.

ISBN 978-3-95450-158-8

normal hollow copper conductor with pressurized water cooling at IMP.

- LECR4 is the first high performance ECR ion source with only one pump for vacuum evacuation, which greatly simplifies the ion source injection components and reduces the cost. The typical vacuum without plasma is 7×10^{-8}mbar at extraction side and 3.0×10^{-8}mbar at the beam line.
- The optimization of magnetic field distribution and effective application of other advanced technologies: such as double 18 GHz heating, biased disk, insert iron, result in an excellent performance for intense multiple charge state ion beam production. The axial magnetic field of LECR4 is similar to SECRAL (Superconducting Electron Cyclotron Resonance ion source with Advanced design in Lanzhou) ECR ion source operating at 18 GHz. At full excitation, the measured peak mirror field on axis are 2.5 T at injection (slightly higher than calculation), 1.3 T at extraction and 0.5 T at minimum-B position, as shown in Figure 3. The measured field distribution agrees well with the calculated result.

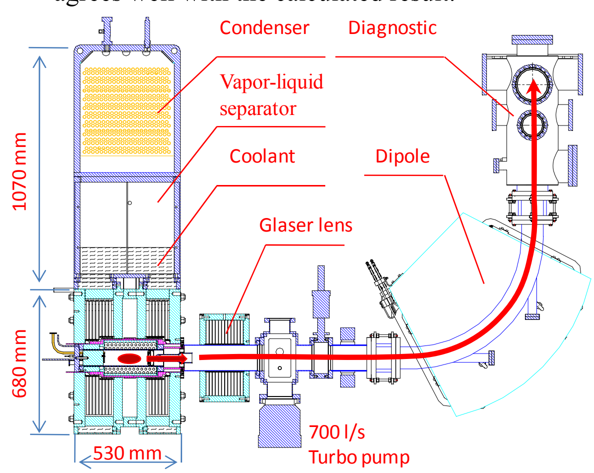

Figure 2:A schematic cross-section view of the LECR4 source body. No mechanical pumping at the injection side for simplicity.

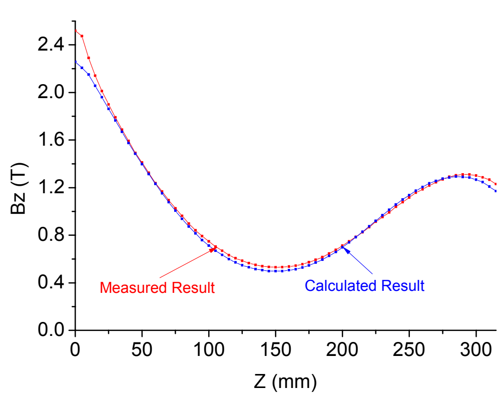

Figure 3: Axial magnetic field distribution of LECR4.

Preliminary Commissioning Results with Single 18 GHz Microwave Generator

A single 18 GHz CPI microwave generator with the maximum microwave power output of 1.2 kW was connected to the ion source through a HV DC-BREAK.

Two-electrode extraction system has been installed at the first commissioning phase. The insulation cover is made by PP material with a thickness of 3 mm. Extraction high voltage up to 28 kV has been tested. In the commissioning, the maximum applied high voltage was 25 kV, and the drain current was 5-10 emA depending on the operation conditions.

The first plasma was ignited on January 28th 2014 and the first analyzed ion beam was obtained on February 20th 2014. After about one week's continuous conditioning and outgassing, the plasma became comparably stable. With about 1.0 kW single rf power injection, 1.4 emA of O^{6+}, 285 euA of O^{7+} were obtained with the total drain current of about 7.6 emA. The extraction high voltage was 25 kV. Figure 4 shows the typical spectrum when O^{6+} optimized. In addition, the relationship between transmission efficiency and extraction high voltage has been tested. The preliminary results indicated that the efficiency was increased from 28.3 % to 82.5 % when extraction high voltage was increased from 10 kV to 20 kV, as shown in Fig.5.

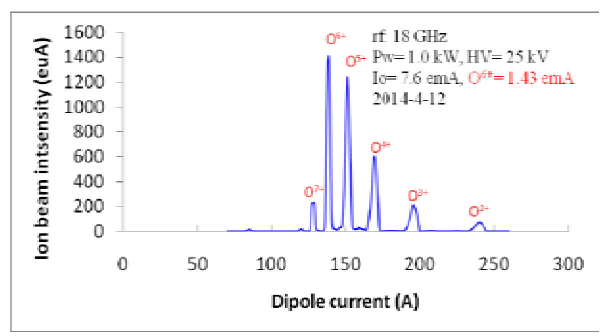

Figure 4: CSD spectrum with the source when optimized on O^{6+} at 1.0 kW with single rf generator.

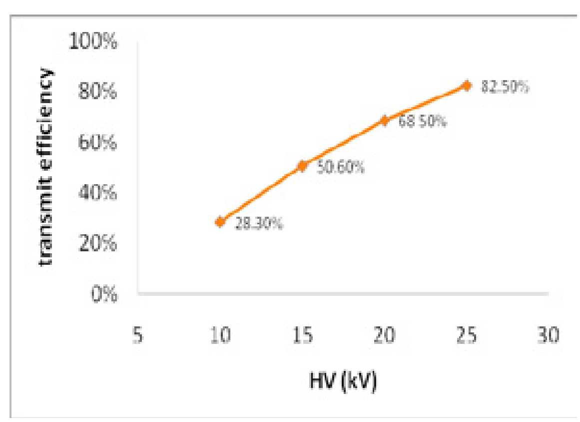

Figure 5: Transmit efficiency of Oxygen beam with different extraction high voltage.

ISBN 978-3-95450-158-8

Preliminary Commissioning Results with Double 18 GHz Microwave Generators

To get better results, certainly higher microwave power is necessary. Another 18 GHz CPI microwave generator was installed.

With total input power about 1.6 kW (0.8 kW+ 0.8 kW) from two 18 GHz microwave generators, some outstanding results were achieved in three month's tuning, such as 1.97 emA of O^{6+}, 1.71 emA of Ar^{8+}, 293 euA of Xe^{20+}, 118 euA of Bi^{28+}, and so on. 1.97 emA of O^{6+} was produced at microwave power of 1.45 kW with the field configuration as B_r= 1.0 T, B_{inj}= 2.5 T, B_{ext}= 1.01 T. Fig.6 shows the typical spectrum with the source optimized for O^{6+}. Fig.7 shows the axial magnetic field distribution. Fig.8 shows the typical spectrum when Ar^{9+} optimized at 1.4 kW. Figure 9 shows the typical spectrum when Xe^{20+} optimized at 1.5 kW. Table 1 gives the preliminary results of LECR4 in comparison with other high performance ECR ion sources: SECRAL [9], GTS and LECR3.

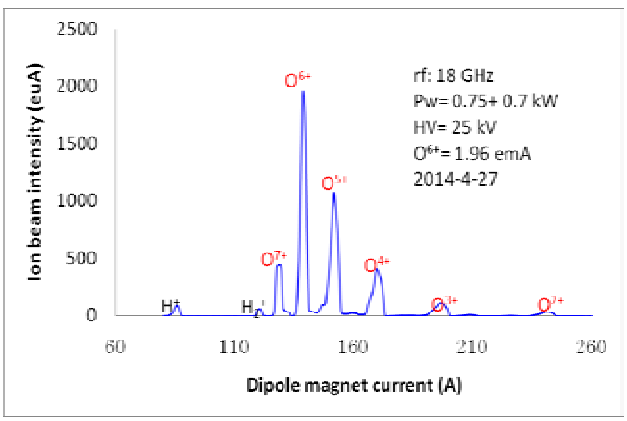

Figure 6: CSD spectrum with the source when optimized on O^{6+} at 1.45 kW.

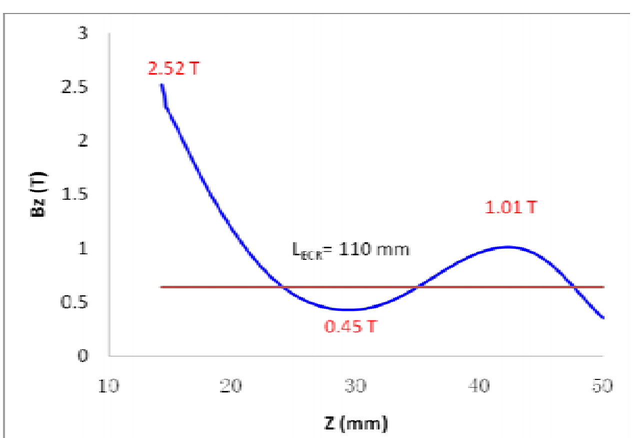

Figure 7: Axial magnetic field distribution when O^{6+} optimized.

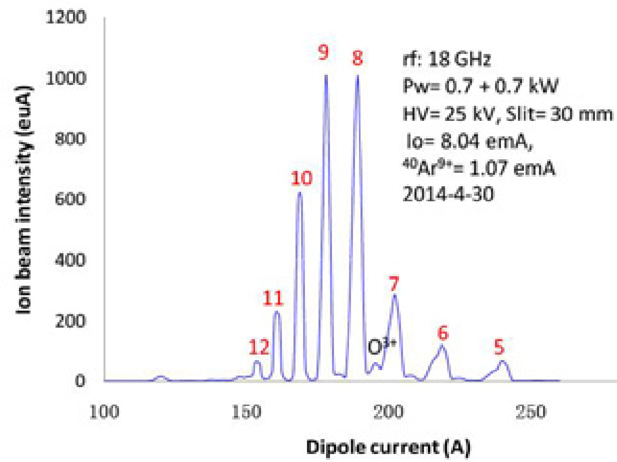

Figure 8: CSD spectrum with the source when optimized on Ar^{9+} at 1.4 kW.

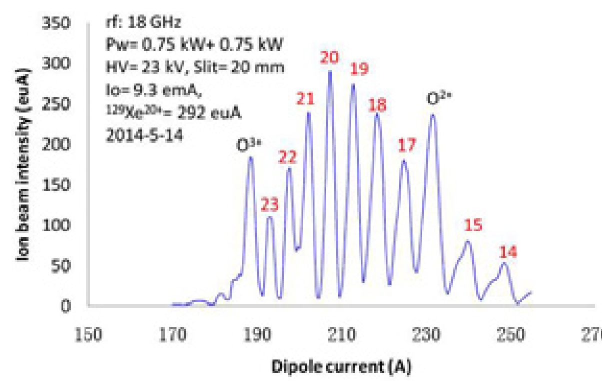

Figure 9: CSD spectrum with the source when optimized on Xe^{20+} at 1.5 kW.

Table 1: comparison of the preliminary results of LECR4 with other high performance ECR ion sources

f (GHz)		***SECRAL*** *18* *<3.2 kW*	***GTS*** *18* *>2 kW*	***LECR3*** *14 &18*	***LECR4*** *18* *<1.6 kW*
^{16}O	6+	2300	1950	780	1970
	7+	810		235	438
^{40}Ar	8+		1100	1100	1717
	9+	1100	920	720	1075
	11+	810	510	325	503
^{129}Xe	20+	505	310	160	293
	23+			130	143
^{209}Bi	28+	214			118
	30+	191			78

Commissioning with RFQ

The first commissioning with RFQ was performed on 4th April 2014. With only 0.1 kW microwave power injection and 11.92 kV extraction voltage, over 200 euA

ISBN 978-3-95450-158-8

of O^{5+} beam was produced and delivered to RFQ continuously for three days without breakdown. The second test was done with heavier Ar^{8+} beam on 21th May 2014. With 0.2 kW microwave power and 18.6 kV extraction voltage, about 210 euA of Ar^{8+} beam was delivered to RFQ. The transmission efficiency is better than 90% according to the test result. The normalized rms emittance of Ar^{8+} ion beam from LECR4 is 0.07 π.mm.mrad in horizontal direction and 0.13 π.mm.mrad invertical direction, respectively, as shown in Fig. 10.

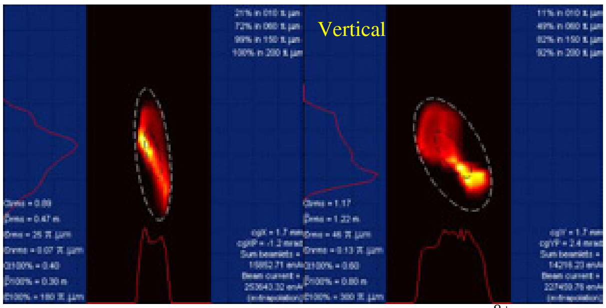

Figure 10: Normalized rms emittances of Ar^{8+} ion beam extracted from LECR4 ECR ion source.

CONCLUSION AND DISCUSSION

A high performance room temperature ECR ion source has been built successfully at IMP. Preliminary test results at 18 GHz demonstrated that LECR4 ECR ion source and its subsystems can operate with a nice reliability and stability. Many good results for intense medium charge state ion beams have been produced in three month's commissioning. Better results will be coming soon after further optimum tuning test and some technology improvements.

ACKNOWLEDGMENT

This project is under the support of the key basic research of Chinese Academy of Science. The authors also gratefully acknowledge the helpful advice from Dr. D. Xie and P. Spaedtke for their kind help and fruitful discussions during the design and commissioning of LECR4.

REFERENCES

[1] X. N. Li *et al,* CPC (HEP & NP), 36, 1126 (2012)
[2] Z. Q. Xie *et al*, RSI, 69, 625 (1998).
[3] T. Nakagawa *et al*, RSI, 75, 1394 (2004).
[4] Z. M. Zhang *et al*, RSI, 749, 238 (2005).
[5] D. Hitz *et al*, RSI, 75, 1403 (2004).
[6] L. Ruan*et al*, "The comparison of cooling effect between evaporative cooling method and inner water cooling method for the large hydro generator", Proc. of ICEMS, p. 67 (2007).
[7] W. Lu *et al*, RSI, 83, 02A328 (2012).
[8] W. Lu *et al,* RSI, 85, 02A926 (2014).
[9] H. W. Zhao *et al,* RSI, 79, 02A315 (2008).

ISBN 978-3-95450-158-8

DEVELOPMENT OF THE MAGNETIC SYSTEM FOR NEW DECRIS-PM ION SOURCE

V. Bekhterev, S. Bogomolov, A. Efremov, FLNR, JINR, Dubna, Moscow Reg., Russia
N. Konev, ITT-Group, Moscow, Russia

Abstract

Super-heavy-element factory is under development at the Flerov Laboratory for Nuclear Reactions, JINR, Dubna. The factory will include DC-280 cyclotron, which will be equipped with two 100 kV high voltage platforms. All-permanent magnet ECRIS will be installed on one of the platforms. The request for the source is a production of medium mass ions with A/q=4÷7.5 such as $^{48}Ca^{8+}$. Results of the detailed design of a magnetic structure for DECRIS-PM will be presented.

INTRODUCTION

One of the basic scientific programs which are carried out at the FLNR is a synthesis of new elements requiring intensive beams of heavy ions. To enhance the efficiency of experiments for next few years it is necessary to obtain accelerated ion beams with the following parameters:

Ion energy	4÷8 MeV/n
Ion masses	10÷238
Beam intensity (up to A=50)	10 pμA
Beam emittance	≤ 30 π mm×mrad
Efficiency of beam transfer	> 50%

These parameters have formed the base for the new cyclotron DC-280 [1]. The basic design features of the DC-280 cyclotron project are shown in Table 1.

Table 1: DC-280 Cyclotron - Basic Technical Parameters

Parameter DC280	Goals
High energy of the injected beam (up to 100 kV)	Shift of the space charge limits by a factor of 30
Large gap in a centre	Space for a long spiral inflector
Low magnetic field	Large starting radius. Good orbit separation. Low deflector voltage
High acceleration rate	Good orbit separation.
Flat-top system	Effective capture. Single orbit extraction. Beam quality.

The axial injection system of the DC-280 cyclotron will include two high voltage platforms which will allow for efficient injection of ions from helium to uranium with an atomic mass to charge ratio in the range of 4÷7. Each HV-platform will be equipped with the low power consuming ECR ion source. For production of ions with the medium masses (from He to Kr) the all permanent magnet (PM) ECR ion source will be used. In this paper we report the design of the magnetic system of the new DECRIS-PM ion source.

MAGNETIC STRUCTURE DESIGN

Many good performance all-permanent magnet ECRISs have been built around the world: NANOGAN series [2], BIE series [3], LAPECR2 [4] and others. The main advantages of all permanent magnet ECRISs are low power consumption, low pressure in the cooling water system, simplified operation, etc. However there are few significant drawbacks of all permanent magnet ECRISs. First of them is the fixed distribution of the magnetic field and comparatively low field strength. Thus, the designed magnetic configuration should be optimized for the desired operation mode from the very beginning. Another drawback is strong mechanical force acting on the individual parts of the system. As a result the correction of the magnetic field after the assembly of the magnetic system is practically impossible without the degaussing of it.

Some deviations from the required field distribution can occur for many reasons. The magnetic material itself has scatter in parameters of up to 5%. Furthermore, the magnetic rings that form the axial magnetic field consist of several blocks. In calculations of the magnetic field it is almost impossible to take into account the influence of gaps between individual blocks. Fig. 1 illustrates this problem. The figure shows the distribution of the magnetic field in front of one of the hexapole poles which is made of five blocks of identical magnetic material. With the gaps of about 0.1 mm the oscillations in the magnetic field measured at a distance of 3 mm from the pole are around 10%.

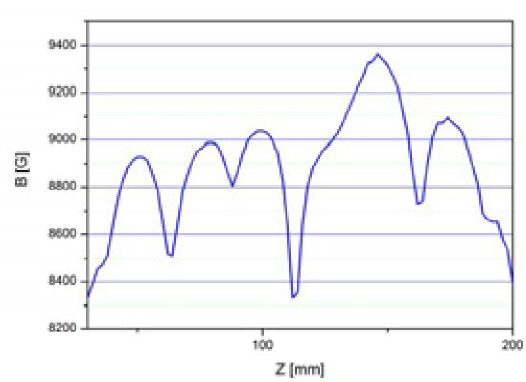

Figure 1: Measured magnetic field distribution along the hexapole pole.

ISBN 978-3-95450-158-8

For this reason it is desirable to provide a possibility for correction of the field distribution in the case of finding an inconsistency between the measured and desired magnetic fields.

The operating frequency selected to be 14 GHz for the source. The corresponding values of B_{inj}, B_{min} and B_r were chosen according to scaling laws for the axial magnetic field configuration [5]. The injection magnetic field maximum was chosen to be around 1.3 T to have a reasonable weight of the system and basing on the earlier experience of conventional ion sources. The desired parameters of the magnetic system of DECRIS-PM are listed in Table 2.

Table 2: Design parameters of DECRIS-PM

Frequency	**14 GHz**
B_{inj}	≥ 1.3 T
B_{min}	0.4 T
B_{extr}	1.0 ÷1.1 T
B_r	1.05÷1.15 T
Plasma chamber internal diameter	70 m

Preliminary calculations were made using the program of synthesis of axially symmetric magnetic systems [6]. It allows optimizing the following parameters of the magnetic system: number of sections, sizes of the sections, orientation and value of the magnetization. The result of this synthesis is shown in Fig. 2.

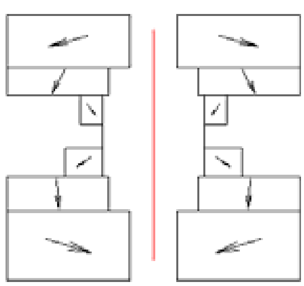

Figure 2: First version of the axial magnetic structure.

The synthesized system provides the desired distribution of the axial magnetic field. However, all magnets have different angular directions of magnetization which leads to a considerable increase in the cost of the magnets. In addition it is practically impossible to correct the field when the system is assembled. Nevertheless this magnetic structure is optimal in terms of weight (477 kg) and size (axial length of 460 mm, outer diameter of 500 mm) and can be used as a reference design.

By further consideration of the different magnetic structures we came to the version which fully satisfies the stated objectives. The structure is shown in Fig. 3. The magnetic structure consists of five large 36-segmented axial magnetic rings with corresponding axial or radial magnetization.

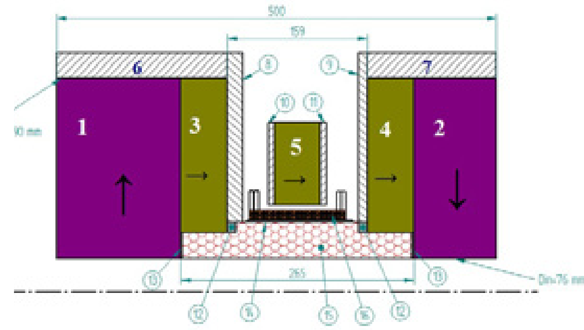

Figure 3: Magnetic structure of DERIS-PM. 1÷5 – PM rings; 6, 7 – soft iron rings; 8÷11 – soft iron plates, 12÷14, 16 - auxiliary elements, 15 – hexapole.

Two magnetic rings at the source injection side provide the injection magnetic field maximum up to 1.3 T, and other two magnetic rings at the extraction side provide the extraction field up to 1.1 T. Single central axial magnetic ring increases the B_{min} field up to 0.42 T. Permanent magnet (PM) rings at the extraction and at the injection sides are inserted into the soft iron rings which slightly increase the magnetic field peaks and strongly suppress the stray field around the source. The soft iron plates around the PM rings with the axial magnetization play an important role in the final magnetic field distribution. The effect of thickness of one of the plate on the B_{min} is shown on Fig. 4. By changing the thickness, it is possible to tune the minimum field when necessary.

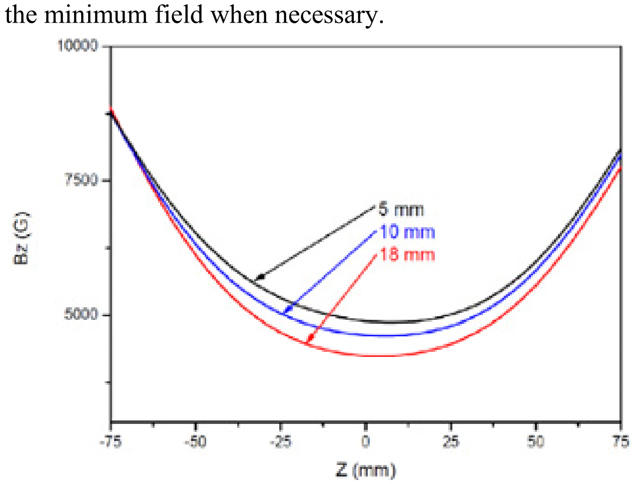

Figure 4: The effect of the soft iron plate thickness.

Figure 5 shows the axial magnetic field distribution of DECRIS-PM. A distance between the injection and extraction maxima is 24.5 cm. The field is changing its sign and reaching 0.8 T at extraction gap, which influences the ion beam extraction and transport.

The magnetic field of DECRIS-PM is the superposition of axial and hexapole fields similar to conventional ECRIS. The hexapole is a 24-segmented Halbach structure magnet which provides a radial field of 1.05 T at the inner wall of the Ø70 mm ID plasma chamber. The

ISBN 978-3-95450-158-8

result of 3D magnetic field calculation is shown in Fig. 6. The ECR zone length is around 7 cm, the $2B_{res}$ zone is closed according to the commonly accepted requirements.

The total weight of the permanent magnets is around 525 kg and total weight of the system is about 1000 kg.

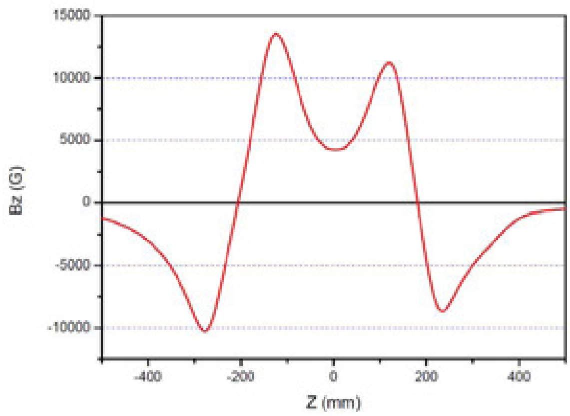

Figure 5: Axial magnetic field distribution of DECRIS-PM.

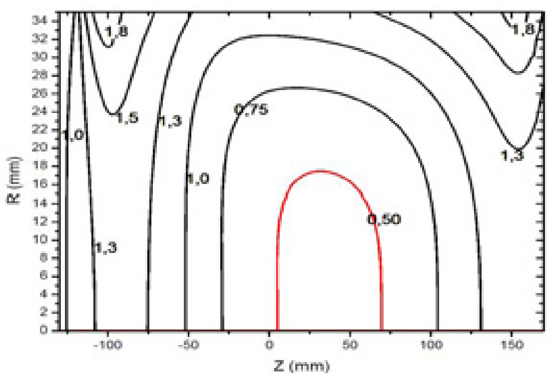

Figure 6: Total field contours.

Other specific feature of the source is an additional coil placed at the centre of the structure between the hexapole and central PM ring. The coil will be used to tune the Bmin value during the source operation. According to [7], the optimal value of Bmin depends on the level of the injected microwave power and it should be changed on-line. Use of such the tuning can assist in improving the source performance.

The coil consumes less than 1.5 kW of electric power and shares the cooling system with the plasma chamber. The influence of the coil on the Bmin value is shown in Fig.7. When the coil is excited to maximum current, the Bmin value is shifted by ±0.05 T depending on the current polarity.

The assembling procedure is planned to be the following: first, the extraction and injection groups of magnets are assembled, and then the axial magnetic field in each group is measured separately. The total magnetic field is calculated basing on the real magnet properties. When necessary, dimensions of soft iron component are defined as the final step.

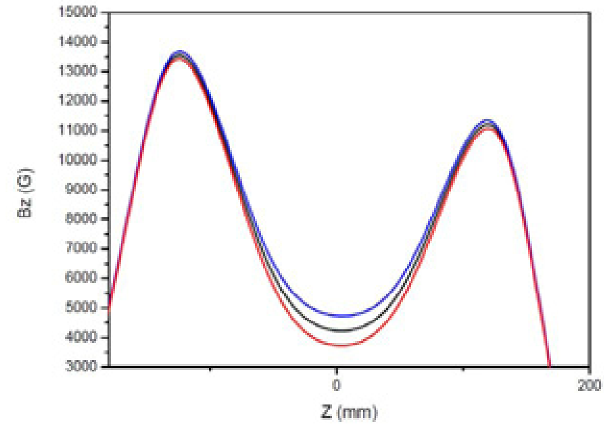

Figure 7: Coil effect.

CONCLUSIONS

A new all-permanent magnet ECR Ion source DECRIS-PM had been designed to be used at the high voltage platform of DC-280 cyclotron. Combination of the permanent magnet rings and soft iron plates makes the magnetic structure flexible. The additional electric coil in the structure centre makes the on-line tuning possible. Manufacturing of the system is planned to be finished in the end of 2014.

ACKNOWLEDGMENT

The authors acknowledge the assistance of N.I. Klevets in preliminary calculations of the magnetic structure. Useful discussions with V.E. Mironov are appreciated.

REFERENCES

[1] G. Gulbekyan et. al., Development of FLNR JINR heavy ion accelerator complex in the next 7 years. New DC-280 cyclotron project, Proceedings of IPAC 2011, San Sebastián, Spain, 2011, WEPS082, p. 2700.

[2] C. Bieth, J.L. Bouly, J.C. Curdy, S. Kantas, P.S Sole, and J.L. Vieux-Rochaz, Rev. Sci. Instrum. **71**, 899 (2000).

[3] Dan. Z. Xie, Rev. Sci. Instrum. **73**, 531 (2002).

[4] L.T. Sun et. al., Nucl. Instr. Meth., B **263** (2007) 503–512.

[5] 2. S. Gammino, G. Ciavola, L. Celona, D. Hitz, A. Girard, and G. Melin. Rev. Sci. Instrum. **72**, 4090 (2001).

[6] Nickolay I. Klevets, Optimal design of magnetic systems, Journal of Magnetism and Magnetic Materials **306** (2006) 281–291.

[7] T. Nakagawa, M. Kidera, Y. Higurasi, J. Ohnishi, T. Kageyama, T. Aihara, A. Goto, Y. Yano, Magnetic field configuration effect and new ECRISs for RIKEN RIBF project, Proceedings of the 17th International Workshop on ECR ion sources and Their Applications, IMP-Lanzhou, China, September 17 – 21, 2006, p. 23.

ISBN 978-3-95450-158-8

THERMAL DESIGN OF REFRIDGERATED HEXAPOLE 18 GHZ ECRIS HIISI

T. Kalvas, O. Tarvainen, H. Koivisto, K. Ranttila
University of Jyväskylä, Department of Physics, 40500 Jyväskylä, Finland

Abstract

A project is underway for constructing a new 18 GHz ECR ion source HIISI at University of Jyväskylä. An innovative plasma chamber structure with grooves at magnetic poles for larger chamber radius at poles. The hexapole will be refridgerated to sub-zero temperatures to boost the coercivity and the remanence of the permanent magnet material and to allow the use of high remanence, low intrinsic coersivity permanent magnet materials. The hexapole structure is insulated from high temperature solenoid coils and plasma chamber by vacuum. The thermal design of the structure has been made using a thermal diffusion code taking in account radiative, conductive and convective heat transfer processes. The heat flux distribution from plasma has been estimated using electron trajectory simulations. The electron simulations are verified by comparing the distribution to plasma chamber patterns from 14 GHz ECR. Thermal design efforts are presented together with an analysis of the demagnetizing H-field in the permanent magnets.

INTRODUCTION

A project is underway for constructing a new 18 GHz ECR ion source HIISI at the University of Jyväskylä. The minimum-B magnetic field configuration is created by normally-conducting solenoid coils and permanent magnet 24-segment Halbach-array hexapole. See figure 1 for a schematic presentation of the ion source and the magnetic field. An innovative plasma chamber structure with grooves at magnetic poles is being studied [1]. This allows large chamber radius at the poles, leading to the pole field necessary according to the scaling laws while using less permanent magnetic material than a conventional design would. The smaller radius between the poles makes space for chamber water cooling. The hexapole will be refridgerated to sub-zero temperatures to boost the coercivity and the remanence of the permanent magnet material. The hexapole structure is insulated from high temperature solenoid coils and plasma chamber by vacuum. See figure 2 for a cross section view of the ion source. The overall design of the ion source is presented elsewhere in detail [1], while this paper concentrates on the thermal modelling and engineering choices of the plasma chamber and the refridgerated hexapole and the analysis of the demagnetizing H-field in the permanent magnet structure.

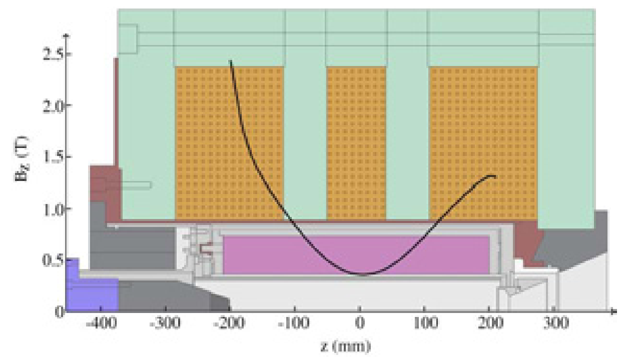

Figure 1: Schematic presentation of the 18 GHz ECRIS HIISI with the axial magnetic field overlaid.

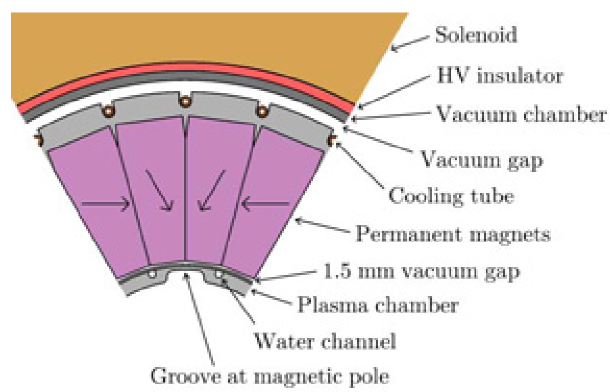

Figure 2: Cross section of the 18 GHz HIISI showing part of the refridgerated 24-segment Halbach permanent magnet hexapole and the vacuum gaps insulating it from the plasma chamber and the solenoid coils. The plasma chamber is grooved to increase the radius at the pole.

ELECTRON TRAJECTORY SIMULATIONS

An estimate of the heat flux distribution from the ion source plasma to the plasma chamber wall is needed for credible thermal studies of the plasma chamber and the permanent magnets. A computer code was devised for this purpose. The code tracks single electron trajectories in the ion source magnetic field using relativistic energy-conserving leapfrog-type Boris algorithm [2]. Electric fields and plasma processes are not considered. The particles are launched isotropically from random locations fullfilling the condition $B < B_{\mathrm{ecr}}$, where B_{ecr} is the resonance field for relativistic electrons with kinetic energy E . Thus, the simulated trajectories can be throught to represent electron trajectories after a collision process in the plasma. If the particle is in the loss-cone it will escape the magnetic bottle in a finite time and contribute to the heat flux on the plasma chamber. Otherwise it will remain confined in the plasma.

Magnetic Field Model

The magnetic field used in the simulations is a superposition of analytic models for the solenoid field in (r, z) coordinates and the hexapole field in (r, θ) coordinates. The solenoid field model is constructed by fitting a sixth order polynomial $B\ (z)$ to on-axis magnetic field data from FEMM simulation [3] from the bias disc to the plasma electrode. The evaluation of the solenoid field at off-axis locations is done using standard expansion, presented for example in [4]. The hexapole field model is constructed by fitting a linear combination of cylindrical multipoles

$$B\ (r,\theta) \;=\; \sum J \left(\frac{r}{r_{\mathrm{ref}}}\right)^{-1} \cos(i\theta) \qquad (1)$$

$$B\ (r,\theta) \;=\; \sum -J \left(\frac{r}{r_{\mathrm{ref}}}\right)^{-1} \sin(i\theta) \qquad (2)$$

to FEMM simulation field data. The parameters J_1, J_2, J_4, ... are zero due to hexapole symmetry. Therefore a six-parameter fit is acquired by fitting the non-zero parameters J_3, J_9, J_{15}, J_{21}, J_{27} and J_{33}. The reference radius r_{ref} corresponds to the plasma chamber radius at the pole (38 mm in case of JYFL 14 GHz ECRIS and 55 mm in case of 18 GHz HIISI).

Validation

The electrons are tracked until their trajectories intercept with the plasma chamber or the maximum tracking time of 1000 ns has elapsed. On average 70 % of the particles are time-limited when the electron energy is below 200 keV. Increasing the tracking time by a factor of 10 decreases the number of time-limited particles by less than 1 % (see figure 3). Therefore it seems that majority of the time-limited electrons are not in the loss cone of the magnetic field configuration. It is assumed that the electrons escaping the plasma during this time represent the electron flux of much longer tracking times with appropriate accuracy. Time-step $\Delta t = 1$ ps is used for the trajectory calculation. A few trajectories were studied in more detail and it was observed that the accumulation of error in the particle location is less than 1 mm during 1000 ns.

The code was first used to acquire the electron flux distributions to the plasma chamber of the JYFL 14 GHz ECRIS [5] (see table 1 for the characteristic numbers of the magnetic field) with electron kinetic energies of 10, 100 and 200 keV to test the validity of the simulation. At kinetic energy higher than 200 keV the ECR surface starts intersecting with the plasma chamber wall between the magnetic poles. In each case the number of simulated particles was 10^6. The distribution of electron fluxes in the simulations are presented in table 2 in percentages. A comparison of the electron flux distributions acquired with the simulations for radial direction against experimental results is presented in figure 4. The figure 4a shows a photograph [6] of an aluminium liner placed inside the plasma chamber during beam production with the MIVOC-method [7]. The carbon

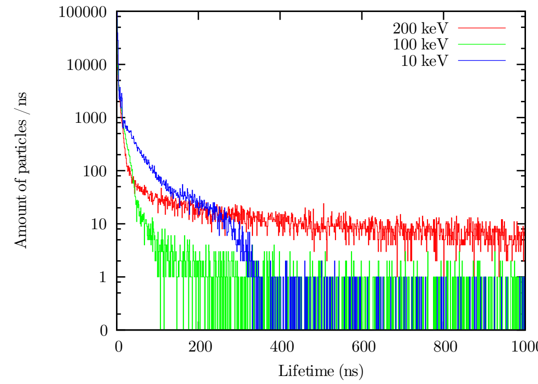

Figure 3: The lifetime of electrons in the electron trajectory simulations with the JYFL 14 GHz ECRIS magnetic field.

contaminants have left black marks at the poles, which are encircled by the red line in the figure. The same encircling has been transferred to the figures illustrating the electron tracking results to enable comparison of the flux patterns. It can be seen that the observed marks match well with the electron flux distribution with kinetic energy of 200 keV and that all the simulated patterns are within the observed marks. Even though the the observed marks are left by ions and the simulation tracks electrons, the comparison gives confidence in the simulations because it is known that ions and electrons occupy roughly the same spatial coordinates in ECRIS.

Table 1: Characteristics of the magnetic fields used in electron simulations. The 14 GHz ECRIS field corresponds to the typical operating point with 520 A solenoid currents.

	14 GHz ECRIS	**18 GHz HIISI**
B_{min}	0.37 T	0.36 T
B_{inj}	2.03 T	2.43 T
B_{ext}	0.94 T	1.31 T
B_{pole}	1.08 T	1.29 T
B_{btw}	0.69 T	0.95 T

18 GHZ HIISI ECRIS

The electron trajectory code was also used to acquire flux distributions for the 18 GHz HIISI ECRIS being designed (characteristic numbers of the magnetic field are presented in table 1). The flux distributions to different parts of the plasma chamber are presented in table 2. The radial flux patterns show similar characteristics as in the 14 GHz ECRIS case. The flux of higher energy electrons covers a wider area around the pole. 10 keV electrons are confined to an area ±5.5 mm around the pole, 100 keV electrons to ±9.4 mm and 200 keV electrons to ±12.7 mm. The grooves in the plasma chamber are ±8 mm wide. In the thermal modelling of the ion source it is important to consider the worst case scenario for the system. Therefore the 10 keV case with the highest electron flux density in the radial direction has been chosen as an input for the thermal model.

ISBN 978-3-95450-158-8

Table 2: Distribution of electron fluxes to different parts of the plasma chamber in simulations in percentages. The flux to the 8 mm diameter extraction aperture is also included in the total flux to the extraction end of the plasma chamber.

	Flux in 14 GHz ECRIS 10 / 100 / 200 keV	**Flux in 18 GHz HIISI 10 / 100 / 200 keV**
Injection flux	8.3 / 6.9 / 5.7	6.7 / 5.7 / 5.1
Extraction flux	27.1 / 23.5 / 22.6	12.4 / 10.4 / 9.1
Extraction aperture flux	5.1 / 3.4 / 2.6	2.2 / 1.5 / 1.0
Radial flux	64.5 / 69.7 / 71.7	80.8 / 83.9 / 85.8

The amount of power used to heat the plasma is estimated to be 6 kW at highest. According to the 10 keV simulation, the injection (bias plate) will receive a 400 W flux and the extraction a 750 W flux. These parts will be water cooled. The radial direction is more critical due to the refridgerated hexapole. Therefore this direction is analyzed more carefully. To gain some safety margin it is assumed that all of the 6 kW power is deposited radially to the plasma chamber. With this assumption 10 keV simulation yields the power density distribution shown in figure 5.

THERMAL MODELLING

The thermal modelling for the ion source parts is done in 3D using a computer code, which solves the discretized heat transfer problem in a Cartesian grid with a regular step size. The code takes in account conductive, radiative and convective processes and is capable of handling different materials with non-linear thermal conductances, heat capacities, mass densities, emissivities, absorptivities, etc. The radiative and convective transfer models assume thin gaps, which means that heat transfer takes place only in the direction of the surface normal. Therefore no dispersion of heat flux takes place. This approximation slightly emphasizes localized heat loads.

Plasma Chamber

The plasma chamber of the HIISI ECRIS is going to be constructed from two concentric aluminium cylinders. The ±8 mm grooves in the inner surface and the flow channels for the cooling water are machined to the inner cylinder. The outer cylinder is shrink fitted onto the inner cylinder to enclose the water channels. The cylinders are welded together at the ends. See figure 6 for a cross section view of the plasma chamber. Based on tests with similar structures, a thermal contact resistance of around 8000 W/(m^{2}K) is expected between the cylinders.

The temperature distribution of the plasma chamber has been calculated assuming the heat flux from the plasma shown in figure 5 and radiative and convective heat exchange with the surrounding hexapole structure at 263 K (−10°C). The water in the cooling channel is at 300 K. The highest temperatures of 405 K appear at the inner surface of the chamber at $z = 25$ (see figure 1 for the coordinates) as shown in a cross section view in figure 6. At the outer surface with a line-of-sight to the hexapole up to 360 K temperatures are observed. Therefore, it is critical to prevent contact between the hexapole magnets and the plasma chamber to avoid demagnetizing the permanent magnets. Careful engineering is required as the gap between the plasma electrode and the hexapole structure is nominally only 1.5 mm.

Refridgerated Hexapole

The Halbach-array hexapole is constructed inside a cylindrical aluminium shell with machined grooves on the outer surface for copper tubes with liquid coolant nominally at 263 K. At the ends of the cylindrical structure, the permanent magnets are confined by aluminium plates, which are bolted to the shell. This whole structure is under rough vacuum to minimize convective heat transfer with the other parts. It is expected that < 1 Pa is reached and therefore 1 Pa and 10 Pa cases have been simulated. The radiative heat transfer is a function of surface emissivities. In the simulations, the emissivity has been assumed to be same for all surfaces. The simulations have been done with 0.1, 0.5 and 1.0 emissivities. According to the material datasheets, it is expected that the surface emissivities are below 0.5, but the unity emissivity case is simulated as a worst case scenario. The permanent magnet structure is held in place by 6 PEEK insulated supports at each end, which are connected to plates at 300 K. These supports are the only conductive heat transfer channel from the hexapole transferring about 12 W of power in total. The vacuum tank surrounding the hexapole in the radial direction is assumed to be at 320 K due to the heat load of the surrounding solenoid.

A cross section view of the temperature distribution at the center of the hexapole ($z = 0$ mm) is shown in figure 7 for the worst case with 10 Pa pressure and 1.0 emissivity. The peak temperature is only 3 K higher than the coolant temperature. Therefore it is believed that there is margin for imperfections in the system as long as there is no contact between the hexapole and the surrounding parts other than the supports.

The thermal model assumes perfect contact between the magnets, which may not be the case in reality, but this is not be a problem because most of the heat flows radially from the inner surface towards the cooling circuit. It is more critical that a good thermal contact is ensured between the magnets and the aluminium cylinder. Therefore, the use of

ISBN 978-3-95450-158-8

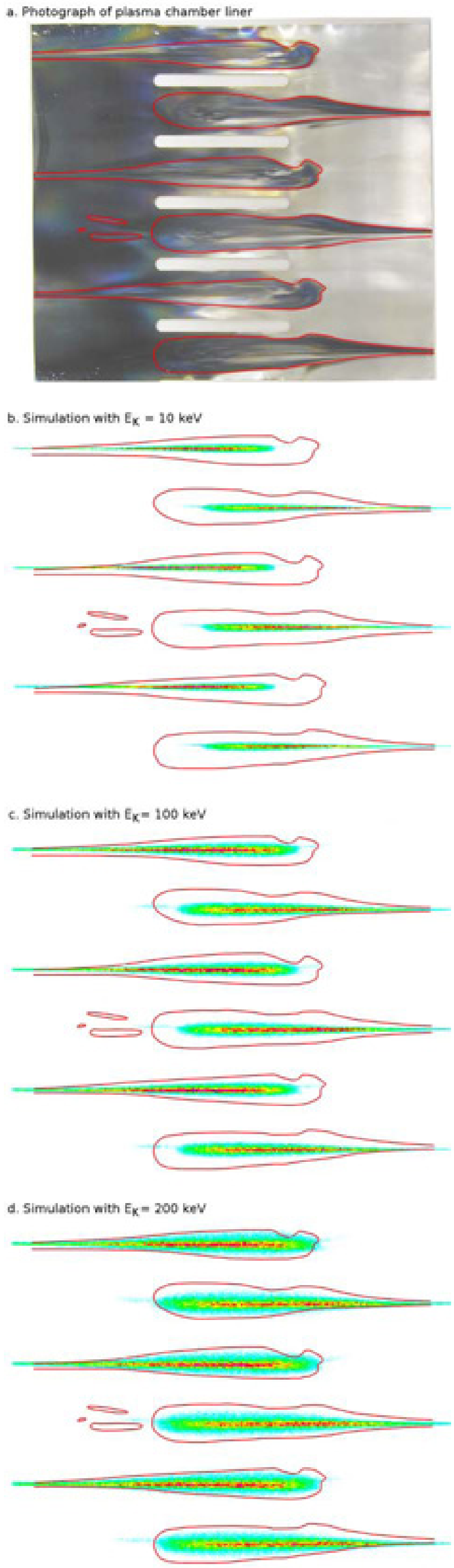

Figure 4: Comparison of the simulated electron fluxes to the marks left by carbon contaminants on the JYFL 14 GHz ECRIS plasma chamber liner.

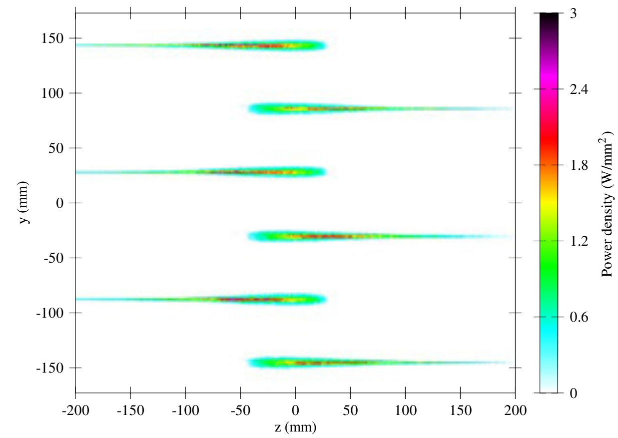

Figure 5: Power density deposited radially on the 18 GHz HIISI plasma chamber assuming 6 kW total power and distribution of the 10 keV electron trajectory simulation.

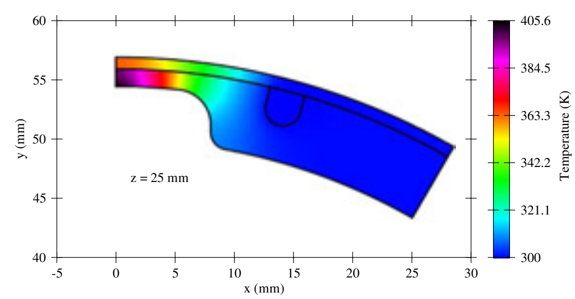

Figure 6: A section view of the plasma chamber temperature distribution.

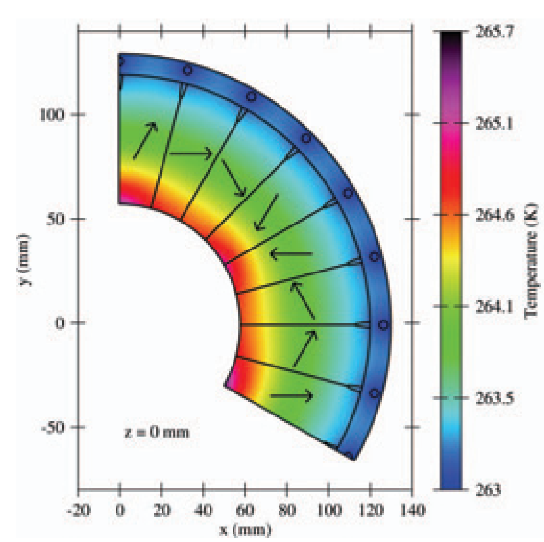

Figure 7: A section view of the hexapole temperature distribution.

ISBN 978-3-95450-158-8

vacuum compatible, heat conducting paste at this interface is under consideration.

The required cooling power depends strongly on the pressure and the emissivity of the system. The simulated cooling power requirements for different heat transfer components are presented in table 3. It has been planned that the refridgeration unit will be placed at ground potential, while the hexapole is at +30 kV at highest. The coolant piping needs to be long enough to withstand the potential difference and well insulated to avoid condensation of moisture. It has been estimated that about 15 W will be lost in the transport. For reaching −20°C in P = 10 Pa and ϵ = 1.0 conditions a cooling power of 402 W will be needed. Based on this data, a refridgeration unit with at least 300 W cooling capacity at −20°C is being considered even if the nominal design temperature is −10°C.

H-FIELD ANALYSIS

The magnetic field structure has been studied to ensure that the H-field does not cause significant demagnetization of the permanent magnets. The critical limits in different magnet temperatures can be seen in the demagnetization curves in figure 8 for the permanent magnet material N40UH (B = 1.29 T and H = 1990 kA/m) [8] designed to be used at first in HIISI 18 GHz ECRIS.

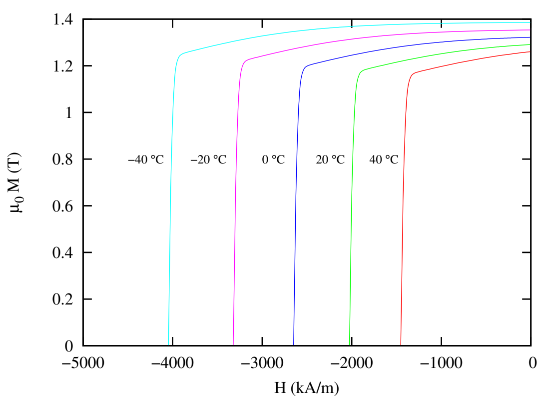

Figure 8: Demagnetization curves for the permanent magnet material N40UH in different temperatures.

The total H-field has been calculated as a superposition of the H-field from two separate 2D FEMM simulations of the hexapole and the solenoid field. Due to symmetries it is sufficient to analyze two of the 12 sectors, which form the 24-segment Halbach hexapole: one with magnetization M pointing inwards and one with M pointing outwards. The resulting 3D H-field maps were separated to field components $H_{\|}$ parallel to magnetization and $H_{\perp}$ perpendicular to magnetization. The $H_{\perp}$ values are less than 1600 kA/m everywhere. According to [9] the resistance to demagnetization in the perpendicular direction is almost double that compared to the parallel direction. Therefore the $H_{\perp}$ will not cause any problems at permanent magnet temperatures less than 50°C. The largest negative $H_{\|}$ values are 1800 kA/m, which are encountered in the hexapole at z = −106 mm and z = 104 mm planes at which the radial component of the solenoid field is strongest. See figure 9 for colormap representation of the H-field. To avoid the demagnetization at these regions, the permanent magnets should be kept below 20°C. Refridgeration of permanent magnets is therefore not necessary for avoiding demagnetization with the N40UH magnet grade. The refridgeration system makes it possible to use N42SH (B = 1.32 T and H = 1600 kA/m) and N48H (B = 1.42 T and H = 1350 kA/m) grades [8].

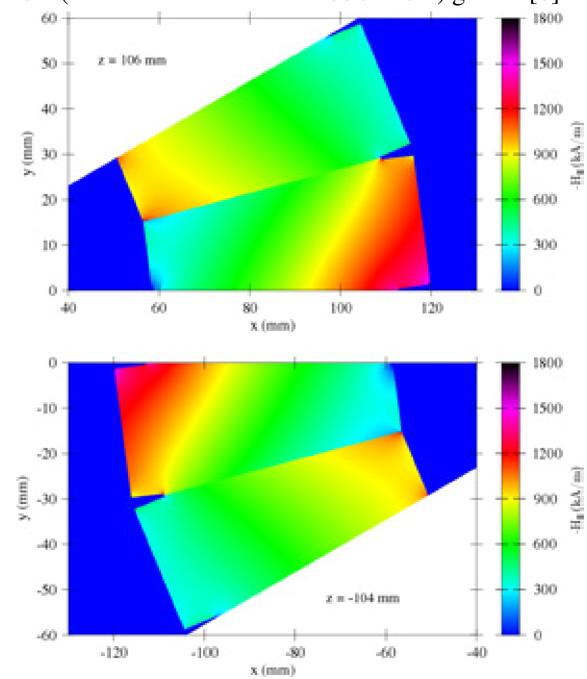

Figure 9: Colormap representation of $-H_{\|}$, the H-field component opposing the magnetization.

ACKNOWLEDGMENTS

This work has been supported by the EU 7th framework programme “Integrating Activities — Transnational Access”, project number: 262010 (ENSAR) and by the Academy of Finland under the Finnish Centre of Excellence Programme 2012–2017 (Nuclear and Accelerator Based Physics Research at JYFL) and Research Infrastructure Programme of the Academy of Finland.

Table 3: Heat flux components and total cooling power needed for reaching −10°C with different pressures P and emissivities ϵ. The numbers do not include 15 W loss in piping outside the ion source.

	P = 1 Pa ϵ = 0.1	P = 1 Pa ϵ = 0.5	P = 10 Pa ϵ = 0.1	P = 10 Pa ϵ = 0.5	P = 10 Pa ϵ = 1.0
Radiative	19.7 W	98.3 W	19.6 W	98.0 W	195 W
Convective	16.0 W	16.0 W	159 W	159 W	158 W
Conductive	12.0 W	12.0 W	12.0 W	12.0 W	12.0 W
Total	47.7 W	126 W	191 W	268 W	365 W

ISBN 978-3-95450-158-8

REFERENCES

[1] H. Koivisto, et. al., in these proceedings.

[2] J. P. Boris, Proceedings of the 4th Conference on the Numerical Simulation of Plasmas, Naval Research Laboratory, Washington D. C., 2–3 November 1970, pp. 3–67.

[3] D. C. Meeker, Finite Element Method Magnetics, Version 4.0.1. (3 Dec 2006 build), `http://www.femm.info/`.

[4] J. Rodney and M. Vaughan, IEEE Trans. Electron Devices **19**, 144 (1972).

[5] H. Koivisto, et. al., Nucl. Instrum. Meth. B **174**, 379 (2001).

[6] P. Suominen, "Modified Multipole Structure for Electron Cy clotron Resonance Ion Sources", Ph. D. Thesis, Department of Physics, University of Jyväskylä, Research Report No. 6/2006.

[7] H. Koivisto J. Ärje and M. Nurmia, Nucl. Instrum. Meth. B **94**, 291 (1994).

[8] Xiamen Dexing Magnet Tech. Co. Ltd., "Magnetic Properties of Sintered NdFeB Magnets", http://www.magneticalloy.com/sintered-NdFeB-magnet.htm

[9] S. Ruoho et. al., IEEE Trans. Magnetics **44**, 1773 (2008).

ISBN 978-3-95450-158-8

EXPERIMENTAL ACTIVITIES WITH THE LPSC CHARGE BREEDER IN THE EUROPEAN CONTEXT*

T. Lamy, J. Angot, T. Thuillier, LPSC, Université Grenoble - Alpes, CNRS/IN2P3, Grenoble, France
P. Delahaye, L. Maunoury, Grand Accélérateur National d'Ions Lourds (GANIL), CEA/DSM -CNRS/IN2P3, Caen, France
J. Choinski, L. Standylo, Heavy Ion Laboratory, University of Warsaw, Warsaw, Poland
A. Galatà, G. Patti, INFN/LNL, Legnaro (PD), Italy
H. Koivisto, O. Tarvainen, JYFL, Jyväskylä, Finland

Abstract

One of the Work Packages of the "Enhanced Multi-Ionization of short-Lived Isotopes at EURISOL" NuPNET project focuses on the ECR charge breeding. The LPSC charge breeder is used for experimental studies in order to better understand the fundamental processes involved in the 1+ beam capture by a 14 GHz ECR plasma. Some improvements, like symmetrisation of the magnetic field at the injection side and higher pumping speed, have been carried out on the PHOENIX charge breeder. The impact of these modifications on the efficiencies and charge breeding times are presented. In the same time, the new LPSC 1+ source developments performed in order to ease the efficiency measurements with various elements are presented.

CONTEXT

In Europe, several high energy radioactive ion beams (RIB's) facilities are under design, construction, or upgrade. At CERN (Geneva, Switzerland), the HIE-ISOLDE project (which uses an EBIS as a charge breeder) has the objectives to increase the energy and the beam intensity of the REX-ISOLDE facility by 2017 [1]. At GANIL (Caen, France), the SPIRAL2 phase2 aiming to produce high energy intense RIB's has been stopped for the moment; however, an upgrade of the SPIRAL1 facility will allow the delivery of new light condensable elements, by 2016, using a modified PHOENIX ECRIS charge breeder whose initial version was developed at LPSC [2].

At the 'Laboratori Nazionali di Legnaro' (Legnaro, Italy) of the Istituto Nazionale di Fisica Nucleare (INFN), the SPES facility (Selective Production of Exotic Species) [3] is under construction; its completion is foreseen in 2017. It will deliver mainly heavy radioactive ions up to an energy of 11 MeV/u, and will be equipped with a LPSC PHOENIX ECRIS charge breeder [4].

For long term science with accelerated radioactive ion beams, the EURISOL project aims to produce high intensities (10 to 100 times higher than the present facilities under construction) and should be equipped with an EBIS and an ECRIS charge breeder. ECR charge breeders with their high intensity acceptance, their fully cw or pulsed operation, are suitable to increase the charge state of the monocharged radioactive ions, as a beam line component located far from the highly radioactive environment of the production targets. LPSC, where ECR charge breeding has been first developed, has taken the responsibility of the design, the construction, and of the experimental qualification of European charge breeders.

Within the same time, the laboratories, authors of this publication, have gathered their research and development activities related to charge breeding in a collective project named '**E**nhanced **M**ulti-**I**onization of short-**L**ived **I**sotopes at **E**URISOL (EMILIE)', funded by the **E**uropean **R**esearch **A**ctivities - **NET**work for Nuclear Physics Infrastructures (NuPNET).

LPSC ACTIVITIES RELATED TO ECRIS CHARGE BREEDERS

SPIRAL2

A detailed mechanical design of the ECR charge breeder has been performed including the modifications studied at LPSC (for example, the suppression of the grounded tube for the slowing down of the 1+ beam). The definition of the operating conditions have been characterized on the LPSC test bench allowing the highest efficiencies maintaining a short charge breeding time (typically 10 ms per charge). The radioactive environment has been taken into account by optimizing the troubleshooting procedures of contaminated parts, allowing to respect the "**A**s **L**ow **A**s **R**easonably **A**chievable" principle. For the moment the SPIRAL2 phase 2 project has been suspended, so the LPSC charge breeding activities for this project, too.

SPIRAL1 Upgrade

The SPIRAL1 facility, after its upgrade including a modified ECR PHOENIX charge breeder, will have to deliver new light condensable radioactive elements. In this context, we have performed experiments with the original charge breeder to compare the charge breeding efficiencies of carbon ions when injecting either $^{13}C^{+}$, $^{13}CO^{+}$ or $^{13}CO2^{+}$ beams extracted from the miniaturized 2.45 GHz COMIC [5] source (see Fig. 1). The detailed

*Work supported by the ERA-NET NuPNET

ISBN 978-3-95450-158-8

results of these experiments [6] show that the best charge breeding efficiencies are obtained when injecting $^{13}CO2^{+}$ into the charge breeder and confirm the interest of using molecules, when available, to “make heavier” the atoms to be charge bred.

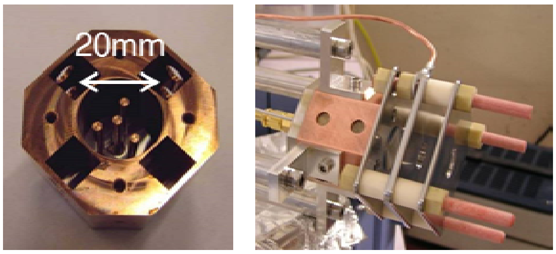

Figure 1: The 2.45 GHz COMIC source.

The next step, before the final setup of the upgrade at GANIL, will be the qualification of the SPIRAL1 charge breeder including its specific optics on the LPSC test stand, this should be performed in 2015.

SPES

The Physics case of the SPES project is detailed on the SPES website [7]. The main goal of the SPES Project is to produce neutron-rich radioactive nuclei with mass in the range 80-160 up to 11 MeV/u for A=130. The 1+ ion sources close to the production target will deliver beams with an emittance in the range 5÷50 π.mm.mrad extracted at a maximum voltage of 40kV. The charge breeder (CB) extraction voltage upper value will be 40 kV as well, the multi-ionization efficiencies on a specific ion with A/q<7 will be 10-15% for gaseous ions and 5-10% for metallic one [4]. In order to get rid of most of the impurities superimposed to the n+ beams, a -120 kV high voltage platform will be equipped with a spectrometer with a resolving power of ΔA/A~1/1000 at 10% of the peak's intensity (see Figure 2).

LPSC is in charge of the final design, the construction and the experimental qualification of the charge breeder which will be delivered to LNL in April 2015.

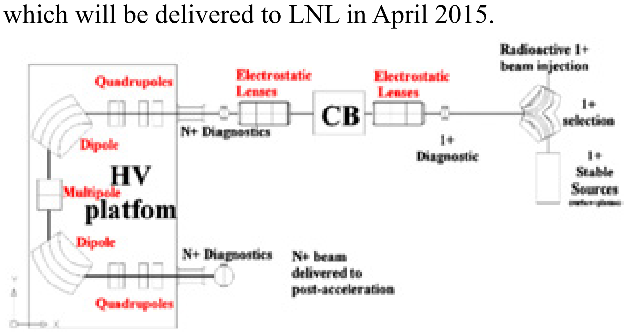

Figure 2 : Scheme of the charge breeding part of SPES

EUROPEAN R&D ACTIVITIES WITH THE ECR PHOENIX CHARGE BREEDER

Activities of The “EMILIE” Project

In a far future, the EURISOL facility may be equipped with both EBIS and ECRIS charge breeders which have been shown as complementary devices [8]. The R&D activities of the EMILIE project has the objectives of improving both Charge Breeding methods. Concerning ECRIS, we have the objective to improve the PHOENIX charge breeder. The main goals are to increase the breeding efficiency keeping the charge breeding times in the range of 4 to 10 ms/charge, to study the wall recycling effects and the possibilities to reduce the stable background mixed with the low intensity multicharged radioactive ion beams extracted from the charge breeder, and finally, to establish the reproducibility of the performances.

Until now, extensive and accurate experiments to evaluate the transmission, the capture, the charge breeding efficiencies and the charge breeding times, have been performed with Ar^{+}, Kr^{+}, Na^{+}, Rb^{+}, Cs^{+} beams. The influence of the support gas flux and nature, the benefits of fine frequency tuning and double frequency heating have been evaluated. The development of a hot 1+ source has been performed to evaluate wall recycling effects. In the following paragraphs different studies performed within the collaboration are presented.

Studies Performed

Wall recycling effects in low charge ion sources

We have developed a hot version (650°C) of the 2.45 GHz COMIC source to produce 1+ alkali ion beams with high stability and low emittance. The objective is to study its efficiency dependence with the temperature. This may give information about the interest of developing a charge breeder with a hot plasma chamber.

In order to control their temperature, the FeNdB permanent magnets have been installed in a water cooled support independent from the hot cavity (Fig. 3). The design criteria were to reproduce the magnetic field and the electric field of the COMIC source. RADIA-Mathematica and ANSYS allowed simulating magnetic field, RF coupling and thermal characteristics. The magnetic field induction is shown in Fig. 4 and the electric field intensity in Fig. 5

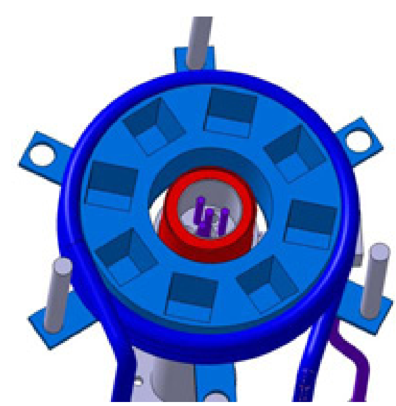

Figure 3 : Mechanical design of the hot COMIC source, purple: HF couplers, red: hot plasma cavity, blue: water cooled magnets support

ISBN 978-3-95450-158-8

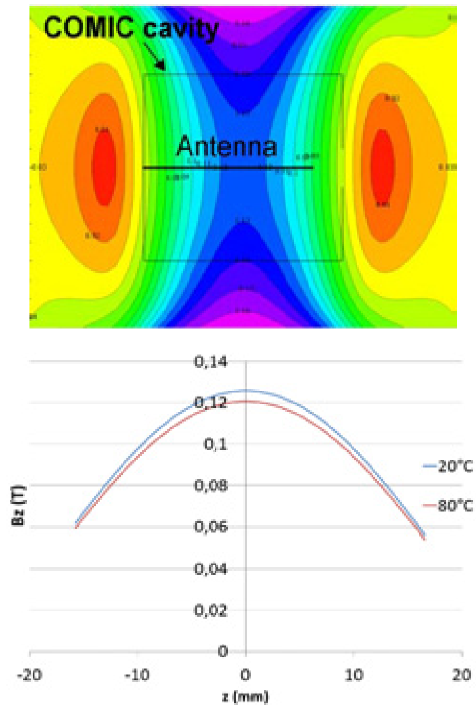

Figure 4: Magnetic field of the hot COMIC source (top: iso-B in the plasma cavity, bottom: magnetic induction on the axis).

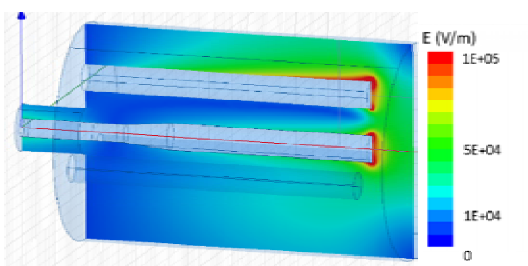

Figure 5: Electric field magnitude into the hot COMIC plasma cavity.

The source has been built (Fig. 6) and will soon be tested. A second version will be developed to reach 1200 °C, in order to extend the operation to metallic ion beams.

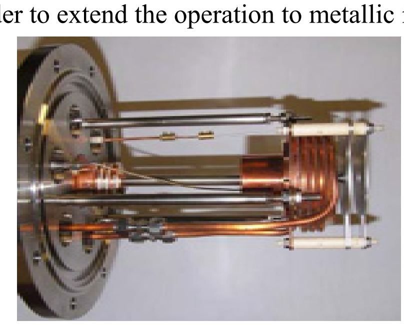

Figure 6: Hot 2.45 GHz COMIC ion source.

LPSC PHOENIX charge breeder improvements

- Vacuum improvement

The charge breeding efficiency is known to be highly dependent on the vacuum level [9]. We have added a 1000 l/s turbo molecular pump on the LPSC test stand, allowing reaching 3 E-07 mbar. Fig. 7 shows, for two different gas fluxes, the production efficiencies of argon charge states obtained with a specific tuning. The total efficiency (sum of the efficiencies for each charge state) drastically decreases with increasing pressures (from 60% at 3.3 E-07 to 20% at 6E-07 mbar).

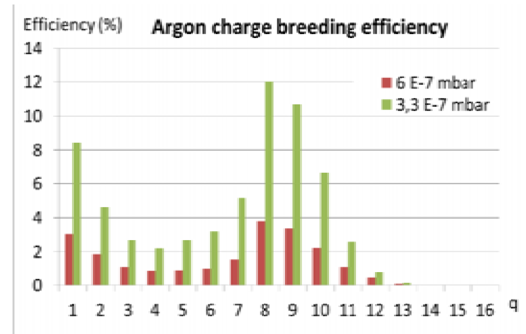

Figure 7: Efficiency for charge bred argon at different gas fluxes.

- Magnetic field symmetrization at the injection

The LPSC charge breeder has two HF ports in order to study the effect of double frequency heating, the electromagnetic waves being injected radially into the plasma chamber at 90° one from each other. The soft iron magnetic plug at the injection has two grooves (Fig. 8) to allow the passage of the two WR62 waveguides with water cooling tubes. These grooves produce a non-symmetric axial magnetic field at the injection, the region where the 1+ beam is decelerated.

Figure 8: Magnetic plug with cuttings.

We have simulated the 3D trajectories of a 20 keV $^{85}Rb^{+}$ beam injected into the charge breeder with such a magnetic configuration and at a potential of 19.99 kV. The initial condition is composed of 1000 ions in the emittance of the 1+ beam measured on the test stand, $\varepsilon(1\sigma) = 2\pi$.mm.mrad. The 3D magnetic field map has been calculated with RADIA-Mathematica and used in SIMION 3D in order to get the ions trajectories. In Fig. 9, that shows a cut view of the result of the simulation, the green rectangles are the positions of the two WR62 waveguides. One can see an important deflection of the beam on the opposite side of the two soft iron cuttings that may lead to a lack of capture of the 1+ beam by the plasma.

ISBN 978-3-95450-158-8

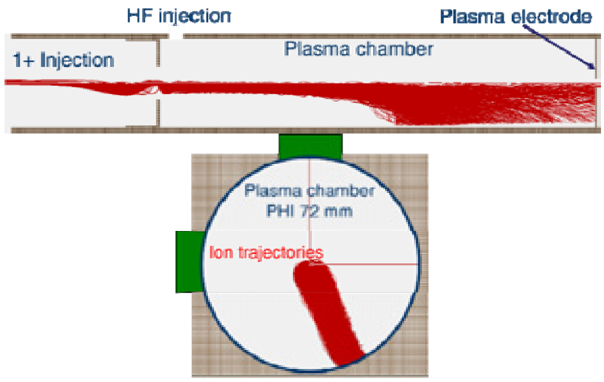

Figure 9: SIMION3D trajectories in the dissymmetric magnetic field ($^{85}Rb^{+}$, 20 keV, ε(1σ) = 2π.mm.mrad, charge breeder potential: 19990 V).

The injection magnetic plug was symmetrized by machining two additional grooves like shown in Fig. 10. The beam experiments with sodium have shown, for high charge states, a significant efficiency increase (see Table 1) maintaining the charge breeding time to 6 ms/charge. Moreover, we have experimentally noticed that the optics tuning was easier after the symmetrization and that there was no efficiency increase for rubidium.

Table 1: Sodium efficiencies measured before and after the symmetrisation of the magnetic field at the injection

Ion	Before sym.	After sym.
$^{23}Na^{6+}$	3%	3.7%
$^{23}Na^{7+}$	1.47%	3%
$^{23}Na^{8+}$	--	2.6%

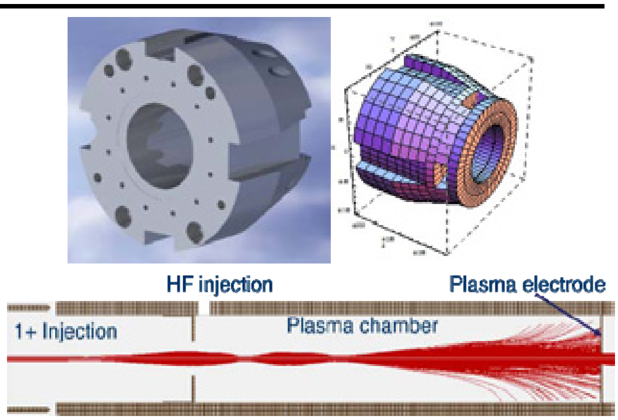

Figure 10: Symmetrized injection magnetic plug and its RADIA model, SIMION 3D trajectories.

- Magnetic field gradient modification

In the PHOENIX charge breeder, the axial magnetic field gradient can be adjusted by moving two soft iron rings placed around the hexapole. Since many years, various modifications were applied to the charge breeder,but the influence of the magnetic field gradient on the efficiencies was not checked. The position of the iron rings was changed, pushing them toward the extraction side. The initial position, the final one, the iso-B plots and the axial magnetic field for the two positions are shown in Fig. 11. We can see that the 14.5 GHz resonance zone (pink curve on the iso-B plots) is shifted towards the extraction and slightly deformed, however the magnetic field at the injection is almost unchanged.

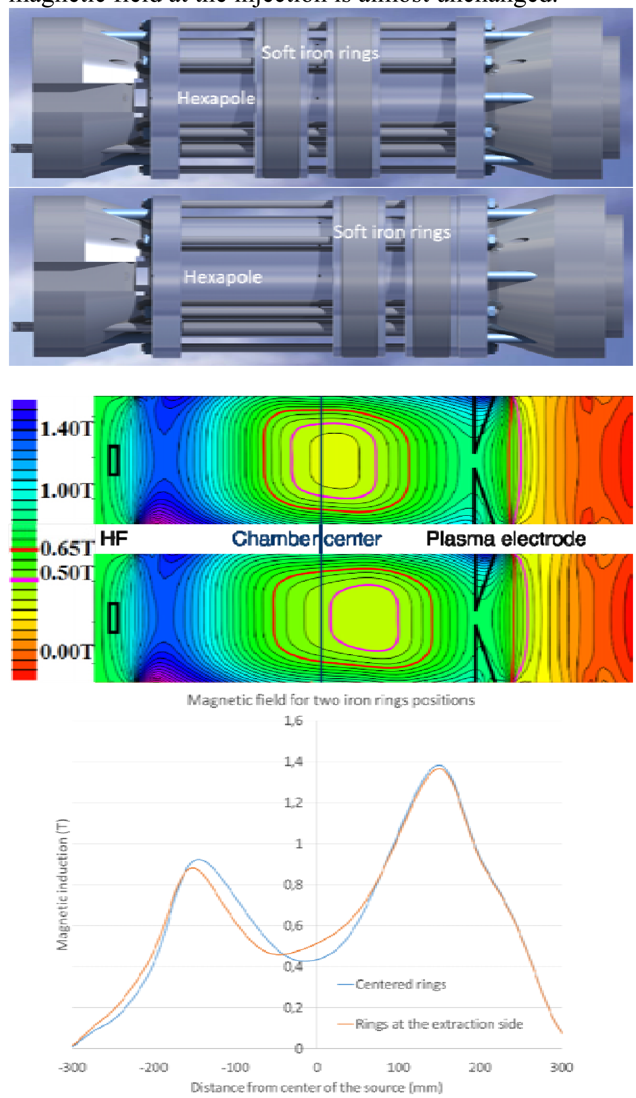

Figure 11: Magnetic field induction on axis for two different positions of the movable soft iron rings.

The efficiency yields have been measured for sodium beams. Results are shown in Table 2, one can see a significant improvement of the efficiencies for the multi-ionization of sodium to high charge states.

Table 2: Sodium efficiencies for two magnetic field gradients

Ion	Rings centered	Rings shifted towards extraction
$^{23}Na^{6+}$	3.7%	3.8%
$^{23}Na^{7+}$	3%	3.7%
$^{23}Na^{8+}$	2.6%	3.2%

ISBN 978-3-95450-158-8

Double frequency heating and fine frequency tuning in conventional and charge breeder ECRIS's

- Double frequency heating

Double Frequency heating has been tested with the JYFL 14 GHz ECRIS and the PHOENIX charge breeder. Ar, Kr and Xe have been used for these studies. The results have been published in [10]. It has been shown the same effect in both sources, double frequency heating improves the production efficiency of high charge states. Moreover, despite an axial magnetic field, at the injection, much lower in the charge breeder than in the conventional ECRIS (1.2 T versus 2.2 T), and despite the absence of bias disk, the ionization efficiency and the charge state distribution (CSD) of each source are very close one to each other.

- Fine frequency tuning

We have tested the fine frequency tuning in the LPSC charge breeder and compared the Ar^{11+} production efficiencies obtained when using a Traveling Wave Tube Amplifiers (TWTA) to vary the ECR frequency, or a klystron with a fixed frequency of 14.521 GHz. With the TWTA, we have noticed for some specific frequencies huge variations of the multi-ionization efficiency, and important plasma instabilities preventing us from measuring correct values. In any case, the klystron has given the best results with a highest value of 8.4% for Ar^{11+}. Even for other charges and ion species the best efficiencies have always been obtained with the klystron.

Our interpretation of this fact is like the one developed in [11]. The charge breeder has a direct injection of the microwaves into the plasma chamber through a WR62 waveguide brazed on it. When the plasma is established in the large volume of the plasma chamber, the coupling optimization is not effective due to multi-mode behavior and to the plasma absorption. In 'CAPRICE-like' sources, we have a waveguide to coaxial mode transition which is extremely sensitive, so in this later case, fine frequency tuning surely optimizes the transmission of waves through the transition.

New charge breeding results and potential application to ECR plasma physics

- Cesium

The 1+ beam was produced by a commercial ion gun (Heat Wave Labs) with an extraction optics simulated and designed at LPSC (Fig. 12).

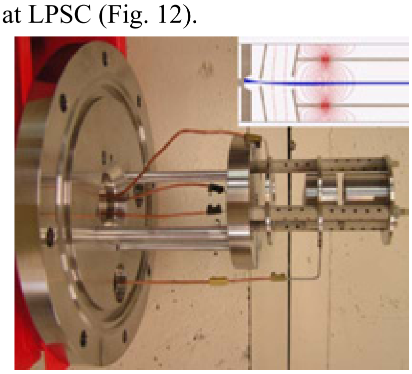

Figure 12: LPSC ion gun with its extraction optics.

We have studied the charge breeding efficiencies for the different charge states of cesium, varying the 1+ beam intensity between 50 nA up to 1.15 μA. In the range between 50 nA and 500 nA, the emittance (1σ) of the 1+ beam, increases from 1.7 to 2.7 π.mm.mrad and presents a plateau for higher intensities. The results are shown in Fig. 13. Except for the lowest 1+ beam intensity injected (~50 nA), where the highest multi-ionization efficiency is obtained (9.5% for $^{133}Cs^{27+}$), the CSD are peaked on the $^{133}Cs^{26+}$. They exhibit two maxima in the ranges from 1+ to 3+ and from 21+ to 31+. The 1+ charge breeding efficiency is the proportion of the incident 1+ beam which is not captured, propagating through the plasma. The 2 and 3+ ones have two components, one due to subsequent multi-ionization after capture, and one contribution of direct in-flight ionization without capture. Additional data supporting the given interpretation will be presented in a future publication.

In terms of breeding efficiency variation with the injected intensity, there are two kinds of behaviors depending on the charge state domain. For charge states in the range 4+ to 20+, there is almost no efficiency variation when increasing the 1+ intensity, whereas for the 1+ to 3+ and the 21+ to 31+ ranges, we observe a decrease of the efficiencies, more important for low charges. If we look at the sum of the efficiencies in the different charge states ranges (lower plot Fig.13), the decrease of the global capture is essentially due to the high charge states that decrease like the 1+ beam intensity transmitted by the plasma.

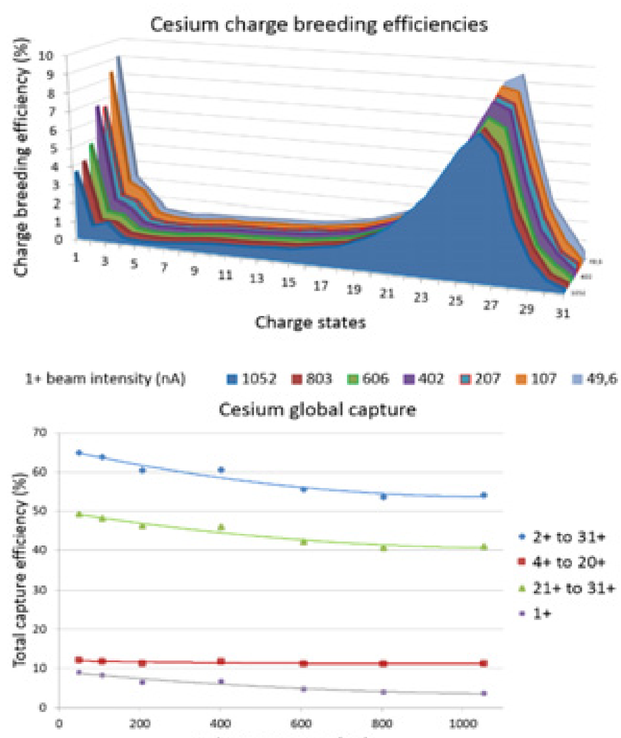

Figure 13: Charge breeding efficiencies for cesium charge states and global capture in different domains of charge states as a function of the 1+ beam intensity.

ISBN 978-3-95450-158-8

These results seem to show that the injection of the 1+ beam has a great influence on the plasma characteristics or on its electronic population. The high charge state decrease suggests that the high intensity 1+ capture reduces the ion confinement time or increases the neutral density in the chamber.The ΔV plots (Fig. 14) show the efficiencies for various charge states as a function of the incident 1+ beam energy. It is interesting to note that the high charge states are clearly obtained after the capture of the 1+ beam, that occurs in a narrow 1+ energy range, when the 2+ plot has almost the same behavior than the 1+ transmitted through the plasma, so we may consider that the majority of the 2+ is directly ionized in flight when crossing the plasma.

- Sodium

We have extensively studied the charge breeding of sodium to try to better understand the difficulty to capture light ions. The best efficiencies obtained have been detailed in the previous sections of this publication. Figure 15 shows the ΔV plots for $^{23}Na^{+}$, $^{23}Na^{2+}$ and $^{23}Na^{6+}$. It is very interesting to note that the 2+ plot seems to have two contributions, a similar shape to the 1+ plot for high energies (high negative values), but a maximum at the energy corresponding to the optimum of the 1+ capture (close to the 6+ which is obviously obtained after the capture process.). This result can be interpreted as follows: at low energy, 2+ ions are produced subsequent to a capture process, while at high energies, they are mainly in-flight ionized. Such effect (dual-peak) is not observed with heavier elements because the charge state distribution of the captured ions does not overlap with the low charge states being ionized in-flight.

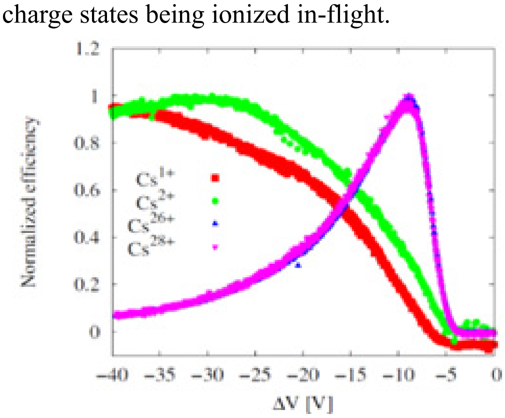

Figure 14: Relative efficiencies for cesium charge breeding as a function of the DeltaV.

The charge breeding times measurements (Fig. 16) for different charge states (1+, 2+, 3+, 6+) for ΔV= -11.4V, allowing the optimization of the capture, shows a classical behavior with a charge breeding time of about 10 ms/charge. If we set ΔV= -23 V, value outside of the 1+ beam energy capture window, we measure for the 2+ (green plot) a faster signal much closer to the 1+ one. This clearly shows that, in this condition, we have access, quantitatively, to the small part of the Na^{2+} which is directly produced during the flight of the uncaptured 1+ beam.

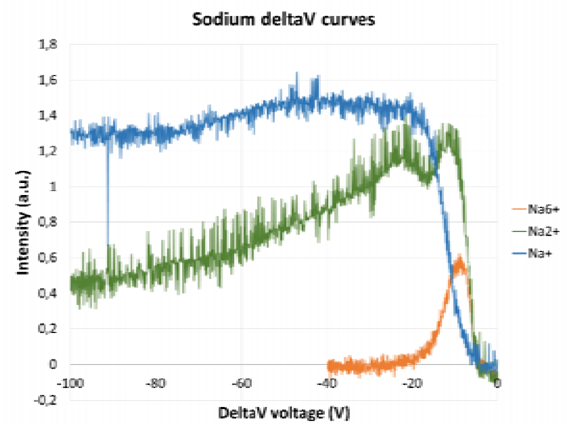

Figure 15: Relative efficiencies for sodium charge breeding as a function of the DeltaV

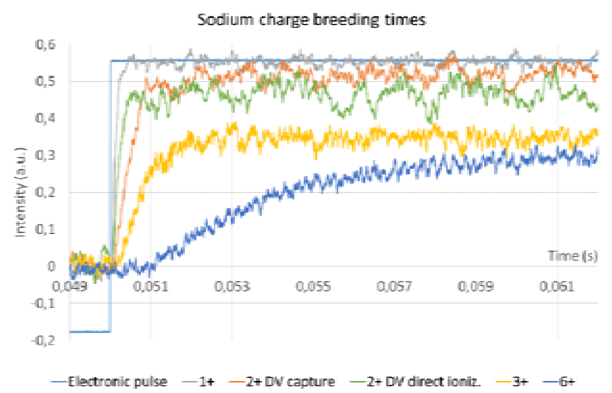

Figure 16: Charge breeding times for 1+, 2+, 3+ and 6+ charge states, two 1+ beam injection energies for the 2+.

- Plasma-beam interaction physics

We have seen, in the previous paragraphs, that the injection of a low intensity (with respect to the total current extracted) 1+ heavy ion beam into a dense ECR plasma may affect this latter. Such an effect was shown in [12] when injecting a Xe^{+} beam. We have performed the same experiment injecting a Cs^{+} beam, varying its intensity. We have measured the intensity variation of the buffer gas ions (oxygen) during the injection. The results are reported in Fig. 17. We see a huge decrease of the intensity, especially for multicharged ions and a slight increase of the monocharged ones. A plausible interpretation of the result could be based on momentum transfer in ion-ion collisions, often referred as ion cooling. In such a process, the average energy of the lighter ion species (O) increases due to Coulomb collisions with the heavier one (Cs). The increased energy in turn implies a shorter confinement time, which shifts the charge state distribution of the buffer gas towards lower charge states. Further experiments and/or simulations are required to confirm this hypothesis. The possible charge exchange process is not a dominant effect, the low charge ions being not repopulated significantly. So only a modification of the plasma equilibrium could be the cause of such an important phenomenon.

ISBN 978-3-95450-158-8

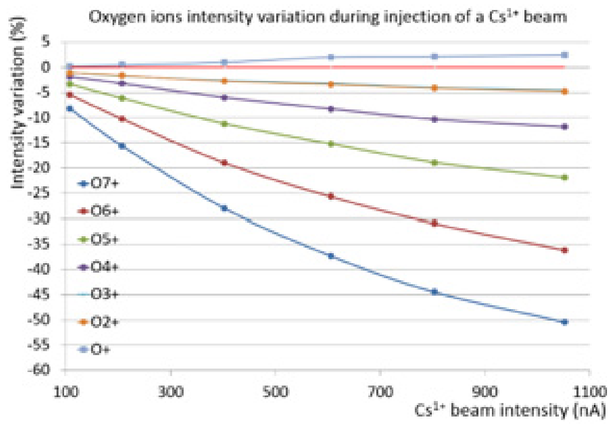

Figure 17: Intensity variation of buffer gas ions when injecting different Cs^{1+} beam intensities.

PROSPECT

The next stages of our activities will be the support of the present construction projects (SPES, SPIRAL1) and the reinforcement of fundamental studies of plasma physics made possible by the charge breeding method. We will soon explain, in a new publication, how powerful this method can be.

AKNOWLEDGEMENT

The authors would like to acknowledge the financial support of the ERA-NET NuPNET.

REFERENCES

[1] HIE-ISOLDE website: https://hie-isolde.web.cern.ch/hie-isolde/
[2] O. Kamalou et al., "GANIL operation status and upgrade of SPIRAL1", FR1PB04, proceedings of the 20th International Conference on Cyclotrons and their Applications, Cyclotrons'13, Vancouver, BC Canada, p. 470 (2013); http://www.JACoW.org
[3] SPES Technical Design Report website: https://web.infn.it/spes/index.php/characteristics/documents/tdr-2012.
[4] A. Galatà et al., "Design of a Charge Breeder for the SPES Project at INFN" Rev. Sci. Instrum. 85, 02B905 (2014).
[5] P. Sortais et al., "Ultracompact/ultralow power electron cyclotron resonance ion source for multipurpose applications" Rev. Sci. Instrum. 81, 02B314 (2010).
[6] L. Maunoury et al., "Future carbon beams at SPIRAL1 facility: Which method is the most efficient?" Rev. Sci. Instrum. 85, 02A504 (2014).
[7] SPES Physics case website: https://web.infn.it/spes/index.php/nuclear-physics
[8] P. Delahaye et al., "Evaluation of charge breeding options for EURISOL" Eur. Phys. J. A 46, 421-433 (2010).
[9] R. Vondrasek et al., "Results with the electron cyclotron resonance charge breeder for the ^{252}Cf fission source project „Californium Rare Ion Breeder Upgrade at Argonne Tandem Linac Accelerator System" Rev. Sci. Instrum. 81, 02A907 (2010).
[10] H. Koivisto et al., "Ionization efficiency studies with charge breeder and conventional electron cyclotron resonance ion source" Rev. Sci. Instrum. 85, 02B917 (2014).
[11] V. Toivanen et al., "Electron cyclotron resonance ion source plasma chamber studies using a network analyzer as a loaded cavity probe" Rev. Sci. Instrum. 83, 02A306 (2012).
[12] T. Lamy et al., "Fine frequency tuning of the Phoenix charge breeder used as a probe for ECRIS plasmas", proceedings of the International Workshop on Electron Cyclotron Resonance Ion Sources ECRIS2010, Grenoble, France website: accelconf.web.cern.ch/AccelConf/ECRIS2010/papers/wecobk03.pdf

INVESTIGATION ON THE ORIGIN OF HIGH ENERGY X-RAYS OBSERVED IN THIRD GENERATION ECRIS

T. Thuillier*, LPSC, Grenoble, France

Abstract

The operation of third generation ECR ion source heated with 24 or 28 GHz microwave frequency shows a high energy x-ray spectrum with a characteristic temperature much higher than the one observed at the usual heating frequencies (14-18 GHz). The behaviour of the x-ray spectrum is studied based on the review of a set of data previously done at LBNL [1]. The data reviewed shows that the hot x-ray temperature scales with the ECR frequency. The experimental data is compared with the prediction of a simple model of ECR heating developed for this purpose. A formula to estimate the ECR resonance thickness is calculated. The model explains nicely the experimental x-ray temperature variation when the central magnetic field of the ECRIS is changed. It demonstrates that such a magnetic field variation does not change the electron confinement time and that the change of the x-ray spectrum temperature is due to the change of the ECR zone thickness. The only way for the model to reproduce the fact that the x-ray temperature scales with the ECR frequency is to assume that the electron confinement time scales (at least) with the ECR frequency. This result brings new credit to the theoretical prediction that the hot electron RF scattering is decreasing when the ECR frequency increases.[2,3] The spatial gyrac effect, which can be considered as another possible origin of the very hot x-ray produced in ECRIS is recalled for convenience in this paper.

VENUS EXPERIMENTAL DATA

Extensive experimental x-ray measurements have been carried out on several third generation ECR ion sources. This paper focuses on data formerly measured with the VENUS ion source at LBNL. [1] The data considered in this paper is the one comparing the x-ray spectrum produced at 18 GHz and 28 GHz with a homothetic magnetic field (*i.e.* scaling the ECR frequency) and for 2 values of the axial median magnetic field intensity (B_{min}):

- steep Gradient configuration when B_{min}~0.47B_{ecr}
- shallow Gradient configuration when B_{min}~0.47B_{ecr}

The axial magnetic field configuration associated to these four tuning is shown on Figure 1. The red and blue plots respectively stand for 28 and 18 GHz operation. Solid lines are for shallow gradient, while dashed lines are for steep gradient. The magnetic calculation have been carried out with RADIA.[4] The VENUS radial magnetic field is considered to reach 2.1 T at wall (radius 70 mm) for the 28 GHz operation and 1.35T for the 18 GHz operation.

The experimental x-ray spectrum plotted in [1] have been fitted with the usual Boltzmann temperature profile:

$$\frac{dN}{dE} \sim N_0 e^{-\frac{E}{kT}} \qquad (1)$$

The fits are plotted on Figure 2, and the spectrum temperatures calculated are summarized in the Table 1. The same convention of color and line style is used in Fig. 1 and 2 for convenience.

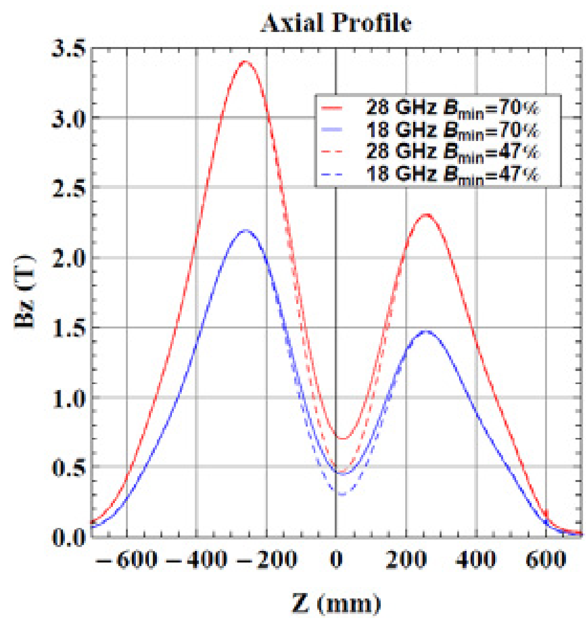

Figure 1: Axial magnetic field profiles used to study the x-ray spectrum dependence for 2 ECR frequencies and 2 B_{min} values.

Table 1: Experimental x-ray spectrum temperatures

f_{ECR}	Gradient type	kT
18 GHz	Steep	$47.7 \pm 2\ keV$
18 GHz	Shallow	$91.2 \pm 2\ keV$
28 GHz	Steep	$72.7 \pm 2\ keV$
28 GHz	Shallow	$139.5 \pm 2\ keV$

DATA ANALYSIS

A way to compare these spectrum is to normalize their values at the energy E=0 and consider that an individual x-ray population at a given dN/dE value undergoes an energy boost from E_1 to E_2 when the magnetic gradient changes from steep (kT_1) to shallow (kT_2), or when the frequency is changed from 18 to 28 GHz (with an appropriate homothetic magnetic field). This implies that:

*thuillier@lpsc.in2p3.fr

ISBN 978-3-95450-158-8

$$e^{-\frac{E_2}{kT_2}} = e^{-\frac{E_1}{kT_1}} \Rightarrow E_2 = \frac{kT_2}{kT_1} E_1 \qquad (2)$$

It is assumed next that when the magnetic gradient and/or the ECR frequency is changed, the plasma hot electron population undergoes an energy boost proportional to the x-ray temperature change. The experimental ratio of x-ray temperature between 28 and 18 GHz operation (for a homothetic magnetic field) and between shallow and steep gradients for a given ECR frequency are included in the Table 2. The experimental 28 to 18 GHz temperature ratio appears to be the same for the two gradients considered with a value of ~1.53. Since the ratio of the microwave frequencies 28 on 18 is 1.55, it is guessed that the hot x-ray temperature tail in an ECRIS is proportional to the microwave frequency (assuming a homothetic magnetic field configuration). A second interesting point comes from the fact that the shallow to steep gradient x-ray temperature ratio gives the same value for 18 GHz and 28 GHz. This time, the effect is expected to be due to the magnetic field.

Table 2: Experimental x-ray spectrum temperature ratios

f_{ECR}	Temperature ratio type	$\frac{kT_2}{kT_1}$
28/18 GHz	Shallow	1.52±0.11
28/18 GHz	Steep	1.53±0.06
18 GHz	Shallow /Steep	1.91±0.12
28 GHz	Shallow /Steep	1.92±0.08

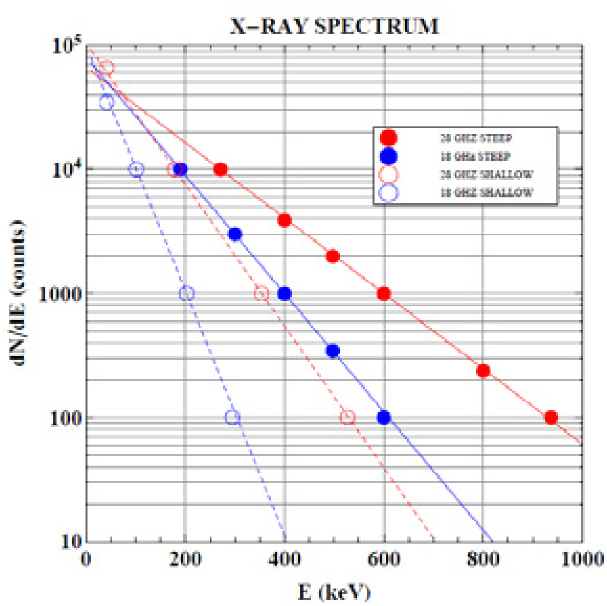

Figure 2: Fit of the x-ray spectrum extracted from [1]. Red curves are 28 GHz profiles. Blue curves are 18 GHz ones. Solid line are the "shallow" gradient tuning, dashed lines stand for "steep" gradient.

DISCUSSION

A higher temperature x-ray spectrum implies that the ion source generates much higher energy electrons. There are two obvious ways to increase the electron energy in an ECR ion source: either by increasing the electron confinement time or by increasing the mean energy gained when an electron passes through the ECR resonance area. This can be considered using a simple electron heating model:

$$W_\perp = \sum_{i=1}^{N} \epsilon_i \sim N\epsilon \qquad (3)$$

Where $W_\perp$ is the electron perpendicular energy, N is the electron mean number of passage through the ECR zone (before it is lost to the wall), and ϵ is the electron mean energy gained per passage. Thus, increasing the confinement time equals to increasing N which in turn increases $W_\perp$. This is the mechanism expected to occur using the hypothesis that the hot electron RF scattering phenomenon is decreasing when the ECR frequency increases. [3] Another way to explain a higher $W_\perp$ is to assume that $N\sim Constant$ and that instead ϵ increases. In this paper, we investigate the hypothesis that the electron energy could increase because of a change of the mean energy gain per passage ϵ through the ECR zone. To do so, a model to estimate ϵ is developed as a function of the ECR frequency.

ECR HEATING GAIN PER PASS

An estimate of an electron energy boost gained when crossing the ECR zone in a magnetic gradient is given by:

$$\epsilon \sim \frac{eE^2\Delta t^2}{2m} \qquad (4)$$

Where e is the electron charge, E the local microwave field intensity, m the electron mass and Δt the time to cross the resonance. Δt is not a convenient parameter to estimate ϵ. One can define the ECR zone thickness $\Delta l = v_{||}\Delta t$ where $v_{||}$ is the electron velocity parallel to the magnetic field. But Δl still depends on the local magnetic field gradient intensity $g = \frac{\partial B}{\partial l}$, gradient taken along the local magnetic field line crossing the ECR zone. Δl can be substituted by $\frac{\Delta B}{g}$ where ΔB is the intrinsic ECR zone magnetic thickness. The ECR angular frequency ω is finally introduced in ϵ by considering that $\frac{\Delta B}{B} = \frac{\Delta\omega}{\omega}$. So the expression for ϵ becomes:

$$\epsilon \sim \frac{mE^2\Delta\omega^2}{2ev_{||}^2 g^2} \qquad (5)$$

The question is now to estimate $\Delta\omega$ and study its possible dependences with physical parameters such as the ECR frequency ω_{ce} and the electrical field intensity E. This point is investigated in the next section.

ISBN 978-3-95450-158-8

ECR Peak Width Study

The intrinsic ECR thickness has been studied theoretically by solving the equation of motion (non-relativisitic cas) as a function of ω_{RF} , $\omega_{ce} = \frac{eB}{m}$ being considered constant:

$$\frac{d\vec{v}}{dt} = \frac{eE}{m} \cos \omega_{RF} t\, \vec{x} + \omega_{ce}\vec{z} \times \vec{v} \qquad (6)$$

The initial velocity considered is expressed as a function of a random phase angle ϕ: $\vec{v}(0) = v_0 \cos\phi\vec{x} + \sin\phi\vec{y}$ and the theoretical solution for the velocity is averaged on this angle. When $\omega_{RF} = \omega_{ce} + \Delta\omega$, an electron gains energy while $\Delta\omega \times t \leq \pi$. It then reaches an energy noted T_{max}. Next, the electron is out phased and eventually decelerates back to its initial velocity: the electron kinetic energy is thus increasing and decreasing periodically. This well-known effect [5] is shown on Fig. 3 for the particular case when $v_0 = 0$ for several values of $\Delta\omega$.

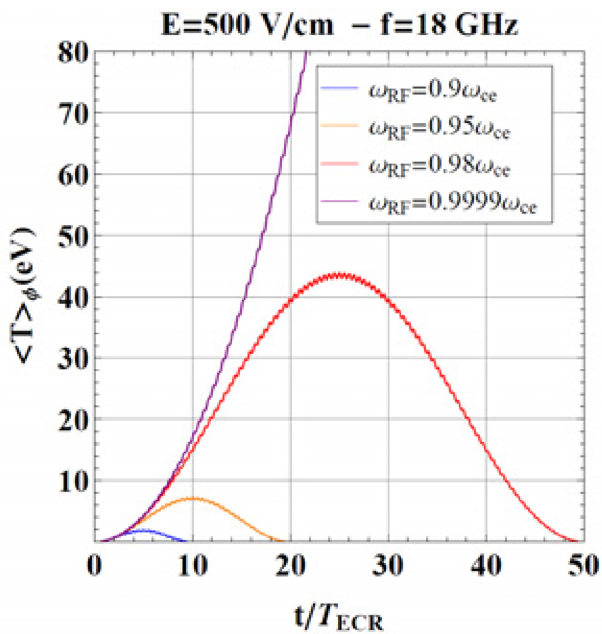

Figure 3: Evolution of the electron kinetic energy as a function of time for several values of $\Delta\omega$. The initial energy is taken as null here for convenience. The electron kinetic energy has a maximum as a function of time.

In order to build an estimator of the ECR frequency peak width, the maximum electron kinetic energy achievable T_{max} is plotted as a function of $\frac{\omega_{RF}}{\omega_{ce}}$ (see Fig. 4). The frequency width $\Delta\omega$ to be considered in Equation (5) is then the resonance width of the plot for a given kinetic energy allowing multi-ionization. One can note that the relative ECR peak width $\frac{\Delta\omega}{\omega}$ decreases with the ECR frequency. The reason is that the time to reach T_{max} is $t_{max} = \frac{\pi}{\Delta\omega}$, while on this plot the abscissa is $\frac{f_{RF}}{f_{ECR}} = 1 + \frac{\Delta\omega}{\omega}$. A fixed $\frac{f_{RF}}{f_{ECR}}$ ratio implies that $\Delta\omega \propto \omega$. Hence, $t_{MAX} \propto \frac{1}{\omega}$: for a given electrical field intensity and a given $\Delta\omega$, the higher the ECR frequency, the shorter the time for acceleration before an electron gets out phased, leading to a lower achievable kinetic energy. This study shows that the intrinsic ECR thickness is a constant independent of the ECR frequency. The phase averaged maximum of the electron kinetic energy for $\omega_{RF} = \omega_{ce} + \Delta\omega$ is:

$$T_{max} = \frac{2e^2}{m}\left(\frac{\omega_{ce}E}{\omega^2 - \omega_{ce}^2}\right)^2 + \frac{1}{2}m{v_0}^2 \cong \frac{e^2}{2m}\left(\frac{E}{\Delta\omega}\right)^2 \qquad (7)$$

provided $\frac{\Delta\omega}{\omega} \ll 1$ and $\frac{1}{2}m{v_0}^2 \ll \frac{e^2}{m}\left(\frac{E}{\Delta\omega}\right)^2$.

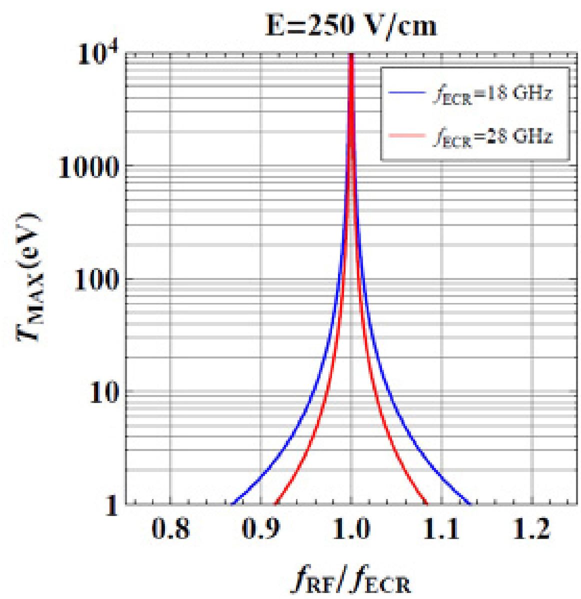

Figure 4: Evolution of the maximum kinetic energy that an electron can reach as a function of the RF frequency normalized to the ECR one, with an electrical field arbitrarily fixed to E=250 V/cm. The blue/red curves avec respectively the plots obtained for f_{RF}=18 and 28 GHz.

Model for the ECR Energy Boost per Passage

The Eq. 7 is eventually used to substitute $\Delta\omega$ in Eq. 5. This introduces the parameter T_{max} that is considered as a constant. In the following, a value of T_{max}~5 keV is considered to study the physics of ECR heating in the non-relativistic approximation. The energy kick per passage through the ECR zone is now:

$$\epsilon \sim \frac{eE^4}{4{v_{||}}^2 g^2 T_{max}} \qquad (8)$$

In the relativistic case, since the electron mass is γm, the resonance occurs on a different ECR surface, where $B \rightarrow \gamma B$, to keep the ECR condition $\omega_{ce} = \omega_{RF}$ valid. The study of $\Delta\omega = f(T_{max})$ can be extended by simulation to the relativistic case, when assuming that the magnetic field intensity automatically adjusts (by a factor γ) to the mass increase to match the ECR condition (gyrac effect). Simulation shows that the function $\Delta\omega = f(T_{max})$ does not change much in the relativistic case, apart from a relativistic boost occurring above ~10 keV. In the next

ISBN 978-3-95450-158-8

parts, the non-relativistic expression is assumed to represent the appropriate dimensional dependence of ϵ, even for relativistic electrons.

COMPARISON OF THE DATA WITH THE MODEL

The four magnetic configurations shown on Figure 1 have been simulated with RADIA and a 3 dimension magnetic field map was constructed.[4] For each configuration, the ECR zone is described by a network of $\sim 10^5$ points forming elementary surface triangles used to compute the magnetic gradient distribution over the ECR surface. A surface-weighted ECR gradient is next calculated. The ECR volume is estimated for each configuration on the basis of the ECR thickness:

$$\Delta l = \frac{m\Delta\omega}{eg} \cong \frac{\sqrt{m}E}{\sqrt{2T_{max}}\,g} \qquad (9)$$

An electrical field of 250 V/cm, and a kinetic energy $T_{max} = 5\,keV$ are used to estimate Δl. A summary of the ECR zone geometry is presented in Table 3 for the four VENUS plasma configurations presented in the first section of the paper.

Table 3: ECR zone geometry derived from the 4 magnetic configurations as on Fig. 1. Lengths, surfaces and volumes are expressed in cm, cm^2 and cm^3 respectively; magnetic gradients are in T/m.

	18 GHz Steep	18 GHz Shallow	28 GHz Steep	28 GHz Shallow
ECR Surface	530.3	389.8	519.2	382.8
ECR Thickness	3.5×10^{-3}	4.8×10^{-3}	2.2×10^{-3}	3.1×10^{-3}
ECR Volume	1.85	1.91	1.14	1.18
Min Gradient	6.7	5.1	10.4	8.0
Max Gradient	22.7	17.0	35.4	26.5
Mean Gradient	17.2	12.5	26.7	19.5

Shallow/Steep Gradient Comparison

For a given frequency (18 or 28 GHz), one can notice that increasing the axial gradient by reducing B_{min} increases greatly the ECR surface (by ~33-35%) but on the other hand it reduces the ECR thickness (by ~33-37%) which lets the ECR volume quasi unchanged. Because the RF power absorbed by the ECR mechanism is necessarily proportional to the ECR volume, it is reasonable to assume that the RF electrical field intensity is a constant for the two magnetic gradient configurations. It is thus possible to compare the mean energy boost ϵ for the two gradients and test the model presented earlier (see Table 4). It is noticeable that the ratio of the energy kick for the shallow and steep gradient closely fits the respective experimental x-ray temperature ratios. When the B_{min} value is changed, the electron energy boost closely fits with g^{-2}. So, in the framework of the simple electron heating model $W_{\perp} \sim N\epsilon$, the mean gain of electron energy is not due to a change of the electron confinement time, but mainly to a change in the ECR zone thickness. This result obtained was not obvious because the two magnetic gradients configurations have a significantly different axial magnetic mirror ratio which could have been thought as being able to modify the electron confinement time and thus the hot x-ray tail temperature.

Table 4: Comparison of experimental data with the model for a given ECR frequency

	18 GHz Steep	18 GHz Shallow	28 GHz Steep	28 GHz Shallow
ϵ (A.U.)	6.25	11.83	2.59	4.86
$\frac{\epsilon_{shallow}}{\epsilon_{steep}}$	1.89		1.87	
$\frac{kT_{shallow}}{kT_{steep}}$	1.91		1.89	

ECR Frequency Effect

The model developed to estimate the mean energy kick per passage ϵ through the ECR zone shows that the intrinsic ECR peak width $\Delta\omega$ is independent of the ECR frequency. Because in a given ECR ion source the magnetic gradient is increased proportionally to the ECR frequency ($g \propto f_{ECR}$), the ECR zone thickness goes like $\Delta l \propto 1/f_{ECR}$ and ϵ like f_{ECR}^{-2}. The comparison of the 18 and 28 GHz experimental results is not obvious because, as it can be seen in the table 2, the ECR volume scales with $1/f_{ECR}$, which implies that, for a given electrical field intensity, the total RF power absorbed by the ECR volume is $\propto 1/f_{ECR}$. So the equilibrium of the RF wave in the source cavity is different and one would expect a different quality factor Q of the cavity (the electromagnetic wave (EMW) being less absorbed per passage through the plasma, a larger number bounce in the cavity can be imagined for the wave). Thus, the electrical field to consider in the Eq. 8 is unlikely to be the same for different ECR frequencies.

If one assumes an equal electrical field intensity for both frequencies and a constant electron confinement time, the model of mean electron energy $W_{\perp} \sim N\epsilon$ scales like f_{ECR}^{-2}. But experimentally, we observe that the hot x-ray tail temperature is such that $kT \propto f_{ECR}$. Consequently, under this hypothesis, the discrepancy between the model and experimental measurements is proportional to f_{ECR}^{-3}. The only way for the model to match the experimental measurements is to assume that the confinement time scales with f_{ECR}^{3}, which is unlikely to be real.

ISBN 978-3-95450-158-8

If now one assumes that, for the same RF power injected, the electrical field intensity is changing with the RF frequency (because the power absorbed by the ECR mechanism in a magnetic gradient scales with f_{ECR}^{-1}), we can at least estimate the maximum theoretical electrical field reached in the cavity for a given ECR frequency. The RF power injected in the ion source can either be absorbed by the ECR zone (plasma), reflected or lost to the cavity wall:

$$P_{injected} = P_{ECR} + P_{reflected} + P_{wall} \qquad (10)$$

If we assume a perfect cavity wall and a null reflected power, one can consider the perfect case when all the RF is absorbed by the ECR mechanism:

$$P_{injected} = P_{ECR} \sim \frac{E_Q{}^2}{2\epsilon_0} V_{ECR} \propto \frac{E_Q{}^2}{2\epsilon_0} \frac{1}{f_{ECR}} \qquad (11)$$

Where $E_Q = QE$ is the RF field intensity in the cavity with a quality factor Q at the frequency f_{ECR} and E the original electrical field of the propagating RF wave in the section of the cavity. This leads to $E_Q{}^2 \propto f_{ECR}$. So in this theoretically perfect cavity, because $\epsilon \propto \frac{E^4}{g^2}$ we get, at best, $\epsilon(f_{ECR}) \sim Const$ and the energy per passage does not scale with the ECR frequency. So, in the case of a frequency increase, the model fit to the data implies that $W_\perp \sim N\epsilon \sim f_{ECR}$ which is only fulfilled if $N \propto f_{ECR}$: the higher energy x-ray observed are then understood as a consequence of a higher electron confinement time proportional to the ECR frequency, leading to higher energy electrons. This study is consistent with the explanation that the higher electron energies observed at higher ECR frequency are due to the electron RF scattering reduction expected by theory.[2]

SPATIAL GYRAC EFFECT

Another possible track for the high energy x-ray observed in ECRIS is the so-called spatial gyrac effect.[6] The ECRIS magnetic field structure is a minimum-B with field lines along which the magnetic intensity change is important. See for instance on Fig.1 the axial magnetic profile of VENUS where the axial field line evolves from $B_{max} = 3.4\,T$ down to $B_{min} = 0.5\,T$ for the 28 GHz steep gradient configuration, while the ECR is located at $B = 1\,T$. This extended magnetic gradient can favour a thick ECR condition for electrons propagating along a field line with an appropriate parallel velocity $v_{||}$ such that the relativistic mass increase (due to the perpendicular velocity increase) equals to the magnetic field increase:

$$\omega_{RF} = \frac{eB(t)\uparrow}{\gamma(t)m\uparrow} = Const \qquad (12)$$

In this case, an electron can reach a relativistic energy in a single passage through the magnetic gradient going from B_{ecr} to B_{max}. The maximum theoretical relativistic factor reachable when the electron goes up the magnetic mirror peak is $= B_{max}/B_{min}$. The calculation for the VENUS source heated at 28 GHz gives ~1.2 MeV which is consistent with what is experimentally observed in the x-ray energy spectrum. On the other hand, no ECR frequency effect is *a-priori* expected on the spatial gyrac effect in an ECRIS because the magnetic field structure is changed with a homothetic ratio leading to the same value of B_{max}/B_{min}.

REFERENCES

[1] D. Leitner, J. Y. Benitez, C. M. Lyneis, D. S. Todd,T. Ropponen, J. Ropponen H. Koivisto, and S. Gammino, Rev. of Scient. Instrum., 79, 033302 (2008).
[2] A. Girard, C. Pernot, and G. Melin, Phys. Rev. E, Vol. 62, No. 1, 2000, p.1182.
[3] C. Perret, A. Girard, H. Khodja, and G. Melin, Phys. Plasmas, Vol. 6, No. 8, 1999, p. 3408.
[4] RADIA, magnetic-field simulation code, © ESRF, Grenoble, France, portions © Wolfram Research Inc., http://www.esrf.fr/machine/groups/insertion_devices/Codes/Radia/Radia.html
[5] R. Geller, Electron Cyclotron Resonance Ion Sources and ECR plasmas, Institute of Physics Publishing, Bristol., CRC Press, 1996, p. 110.
[6] R. Geller, Electron Cyclotron Resonance Ion Sources and ECR plasmas, Institute of Physics Publishing, Bristol., CRC Press, 1996, pp. 112, 184.

ISBN 978-3-95450-158-8

BORON ION BEAM PRODUCTION WITH THE SUPERNANOGAN ECR ION SOURCE FOR THE CERN BIO-LEIR FACILITY

J. Stafford-Haworth, CERN, Geneva, Switzerland
John Adams Institute at Royal Holloway, University of London, Egham, United Kingdom
D. Küchler, R. Scrivens, V. Toivanen, CERN, Geneva, Switzerland
J. Röhrich, Helmholtz-Zentrum Berlin für Materialien und Energie GmbH, Berlin, Germany

Abstract

To deliver B^{3+} ions for medical research the compounds decaborane and m-carborane were tested using the metal ions from volatile compounds (MIVOC) method with the Supernanogan 14.5 GHz ECR ion source. Using decaborane the source delivered less than 10 μA intensity of B^{3+} and after operation large deposits of material were found inside the source. Using m-carborane 50 μA of B^{3+} were delivered without support gas. For m-carborane, helium and oxygen support gasses were also tested, and the effects of different source tuning parameters are discussed. The average consumption of m-carborane was 0.1 mg/μAh over all operation.

INTRODUCTION

Over the last fifty years the field of ion beam therapy has developed from its first tests at the Lawrence Berkeley National Laboratory to, amongst other things, a powerful tool for the treatment of cancer tumours [1]. While the majority of treatments are conducted with protons, heavier ions provide different radiobiological properties and could be more useful in some cases [2]. Different ion species may hold specific advantages for treatment however, a comprehensive study of different viable species has not been completed. Ion beam therapy has been pioneered using carbon ions while helium, boron, lithium, oxygen and other light ion species require further studies to determine their radiobiological properties. No facility currently existing has been designed to deliver this range of ions from protons to neon exclusively for medical research. After discussion at CERN with many representatives of the radiobiological community a strong desire for such a facility has been expressed. Such a facility would allow for fundamental research in this field with new ion species, delivery techniques, and diagnostic tools [3].

The ion injection chain for the LHC starts with a 4.2 MeV/u ion Linac, followed by the Low Energy Ion Ring (LEIR) where the beam is multi-turn injected, and its emittance reduced with an electron cooling scheme. The ions then continue to the LHC through the PS and SPS synchrotrons. The energy range of LEIR (as the LHC lead injector it accelerates Pb^{54+} to 72 MeV/u) does not match the 430 MeV/u carbon beams that are delivered at for medical treatment, however with upgrades to the machine this should be achievable [4]. In the period between LHC fills, it could be envisaged to use LEIR for the delivery of different ion types. Regardless of how the beam is accelerated for injection into LEIR, an ion source is needed. The chosen source must be capable of delivering most of the ions from protons to neon. The Supernanogan is a commercial, permanent magnet, 14.5 GHz ECR ion source currently being used at Heidelberg Ion Therapy Center, the Centro Nazionale di Adroterapia Oncologica (CNAO) and MedAustron to deliver carbon and protons [1]. The Supernanogan is capable of being operated with a micro-oven and gas mixing [5]. Of the ions up to neon, four ions present difficulties for producing ion beams. Beryllium, boron, lithium, and fluorine have not been routinely delivered from ECR ions sources and so production techniques for these ions require verification. Boron was selected to be investigated first using the Helmholtz-Zentrum Supernanogan, Berlin [6].

EXPERIMENT SETUP

Previously boron has been produced using the MIVOC technique at the University of Jyväskylä [7] and at the Flerov Laboratory for Nuclear Reactions (FLNR) in Dubna [8]. Both experiments used the same compound, m-carborane $C_2H_{12}B_{10}$, to deliver between 100 – 200 μA of $^{11}B^{3+}$. For this work a second compound, decaborane, was also chosen as an alternative source of boron material in case problems arose with m-carborane. The relevant properties of decaborane and m-carborane are given in Tables 1 and 2.

Table 1: M-carborane Properties.

Property	*Value*
Atomic Formula	$C_2H_{12}B_{10}$
Mass Ratio	24 : 12 : 110
Melting Point	546 K
Vapor Pressure	0.05 mbar (at 300 K)
Phase at 300 K	Crystalline Solid

Table 2: Decaborane Properties.

Property	*Value*
Atomic Formula	$H_{14}B_{10}$
Mass Ratio	14 : 110
Melting Point	373 K
Boiling Point	486 K
Vapor Pressure	0.269 mbar (at 300 K)
Phase at 300 K	Crystalline Solid

ISBN 978-3-95450-158-8

To utilise the MIVOC technique, the Supernanogan oven was removed and the bias tube, which is used to mount the oven bayonet inside the chamber and act as a port for the coaxial RF transport line into the plasma chamber, was attached to a valve separating it from the MIVOC vacuum section. A vacuum chamber was attached to this, with two valves going to the MIVOC chamber and an ion pump respectively. The MIVOC chamber itself was separated from the rest of the vacuum system by a needle valve with a maximum flow of 1600 cm^3s^{-1}. This configuration is shown in Fig. 1. For both compounds the ampoule containing the compound was filled under an argon atmosphere, sealed with the needle valve closed and then attached to the vacuum system. Prior to operation some vacuum pumping was done in the MIVOC vacuum section to remove most of the argon before opening the valve to the plasma chamber. Throughout the experiment source pressure measure-

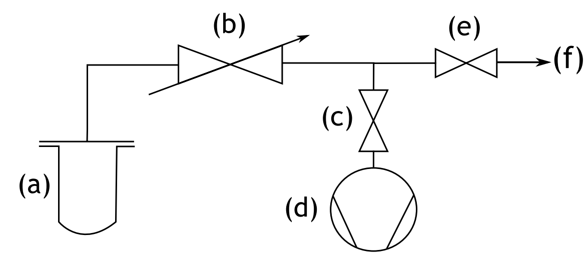

Figure 1: Diagram of the MIVOC setup attached to the injection end of the Supernanogan source. (a) Glass ampoule containing compound. (b) Needle valve with max 1600 $cm^{-3}s^{-1}$ flow. (c) Valve. (d) Vacuum Pump. (e) Valve to source bias tube, open for operation. (f) Source bias tube to plasma chamber.

ments were taken near the gas inlet, inside the RF matching cavity which attaches the RF waveguide to the source plasma chamber. Charge state intensities were measured using a Faraday cup after ion species separation through a spectrometer magnet.

DECABORANE

Decaborane was the first compound investigated. The needle valve was opened gradually until boron ions began to be extracted from the plasma. The minimum valve opening which allowed for $^{11}B^{3+}$ to be extracted corresponded to a source pressure of 3.36×10^{-6} mbar. Up to 480 μA of H^+ could be extracted while operating with decaborane. Over 24 hours the source conditions were varied however even after 24 hour conditioning of the source only 10 μA of $^{11}B^{3+}$ could be extracted. When the source was dismantled after operation, a macroscopic amount of material was found deposited inside the bias tube, and throughout the source. It is suspected that the decaborane underwent pyrolysis as described in [9]. Decaborane pyrolysis results in hydrogen and non-reactive hydrides, which would account for both the material deposited inside the source and the high H^+ intensity measured. No further analysis was performed on the deposited material.

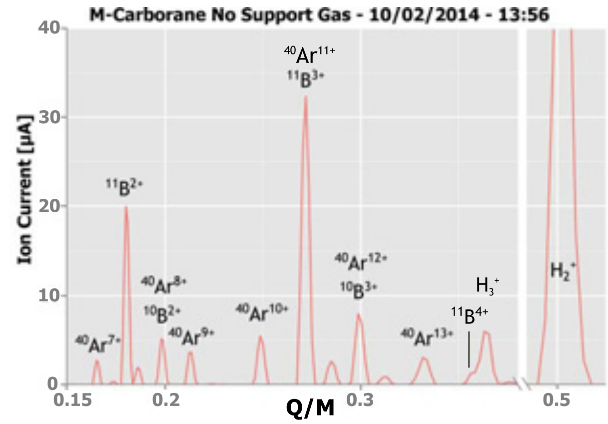

Figure 2: M-carborane charge state distribution without upport gas. 11 W injected RF power, 3.4×10^{-4} mbar at gas inlet valve, −50 V bias voltage, 15 kV extraction voltage. The observed Argon peaks come from filling the MIVOC container under an Argon atmosphere. The H_2^+ peak reaches 190 μA.

M-CARBORANE

The experiment setup for m-carborane was identical to hat of decaborane. The source was started without support gas, with injected RF power of 50 W, needle valve allowing pressure of 2×10^{-6} mbar, and bias voltage of −50 V. These conditions were arbitrary, and resulted in an immediate extracted current of $^{11}B^{3+}$ of 35 μA. Lowering the injected RF power to 30 W increased this to 45 μA. Fig. 2 shows a harge state distribution for 35 ± 1 μA of $^{11}B^{3+}$, however ome argon contamination is included. The argon distribuion implies that this contamination is on the order of 5 μA.

The extracted intensity of $^{11}B^{3+}$ showed a strong sensitivity to the injected RF power. The most stable intensity was achieved with the minimum possible 11 W of injected power which produced 38 ± 1 μA. The maximum intensity achieved was 56 ± 1.5 μA and was achieved with higher gas pressure in the source, with 30 W of injected RF power. Fig. 3 shows the initial source tuning. The sensitivity to the RF power was a limit on the extracted intensity during inial tuing as once the power was increased above 50 W the plasma became very unstable, with very large variations in the extracted intensity of $^{11}B^{3+}$.

A further investigation into the intensity and injected RF power relationship is shown in Fig. 4. This secondary investigation was at fixed pressure of 3.5×10^{-7} mbar which during previous tuning had given the best stability of extracted $^{11}B^{3+}$ intensity. Higher injected power caused a reduction in extracted intensity of $^{11}B^{3+}$ without any decrease in stability. While Fig. 4 shows this trend the intensity peaks at 30 W. The data point at 30 W may be anomalous and verification would be required in further work. Higher powers than 70 W were not investigated as the extracted $^{11}B^{3+}$ intensity fell to 0 μA past 70 W at this pressure. At higher pressures the intensity did not fall to 0 μA but the stability became very poor with variations in extracted intensity of up to 10 μA on a second-to-second timescale. A long term

ISBN 978-3-95450-158-8

stability test was conducted over 21 hours. During this test the intensity fell by 5 μA and the short-term stability remained constant at ± 1 μA.

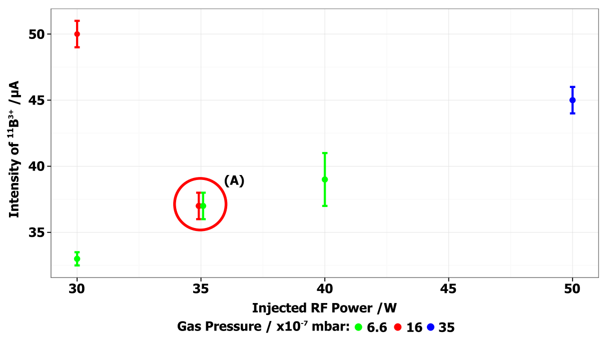

Figure 3: For these tests the extraction voltage was fixed at 15 kV and the bias voltage at -70 V. During initial tuning at 16×10^{-7} mbar an inverse relationship between injected RF power and extracted intensity was observed. (A) Note these two points are different pressure but the same intensity and instability, they have been separated for visibility but are both at 35 W. The error bars indicate the second-to-second variation in the observed intensity.

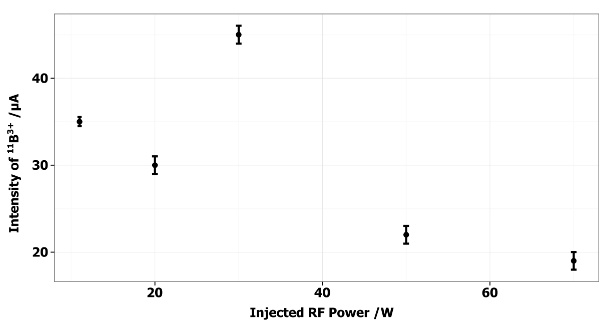

Figure 4: A follow up test to Fig. 3. The extraction voltage was fixed at 15 kV, and the bias disk at -70 V. Constant pressure of 3.5×10^{-7} mbar was maintained to observe the inverse power and extracted intensity relationship. The error bars indicate the second-to-second variation in the observed intensity.

Two support gases were investigated with m-carborane, helium and oxygen. With helium support gas up to 40 μA of $^{11}B^{3+}$ could be extracted at 1.36×10^{-6} mbar of pressure in the source, compared with 6×10^{-7} mbar without support gas. With this increased pressure in the source the plasma could tolerate up to 70 W of injected RF power before becoming unstable. This was 20 W more than it could tolerate without support gas. At lower injected RF power (50 W) the extracted intensity of $^{11}B^{3+}$ was lower compared to operation without support gas. Oxygen was also investigated however, much lower boron intensities (around 15 μA) were extracted than operation with helium or without support gas.

Over the 4 days of operation with m-carborane a consumption rate of 0.1 mg/μAh was observed being converted into $^{11}B^{3+}$. This is higher previously observed at JYFL and FLNR where 0.02 mg/μAh was converted into $^{11}B^{3+}$. Additionaly up to 235 μA of $^{11}B^{3+}$ were observed with the JYFL source compared with 56 μA from the Supernanogan.

CONCLUSIONS

In conclusion, using m-carborane, the Supernanogan is capable of delivering up to 50 μA of $^{11}B^{3+}$ varying by up to 1 μA on a second-to-second timescale. The long term stability tests suggest this intensity can be sustained over 24 hour periods limited only by the size of the ampoule containing the material, with a consumption rate of 0.1 mg/μAh. Both helium and oxygen support gases were tested with m-carborane which allowed for higher injected RF power of 70 W before instabilities arose, however the extracted intensity was not higher than operation without support gas. Increasing the pressure of just m-carborane did not allow for increased extraction intensity either. Further investigation into the intensity–RF dependence could be done to try to understand why increased injected power reduced the extracted intensity.

Decaborane was also investigated but delivered a very low intensity of $^{11}B^{3+}$. This is suspected to be caused by pyrolysis of decaborane during diffusion through the bias tube into the plasma chamber. If decaborane were to be reinvestigated, cooling of the diffusion channel should be considered. The decaborane pyrolysis deposited macroscopic amounts of boron compounds throughout the source.

ACKNOWLEDGEMENTS

The authors would like to thank the Helmholtz-Zentrum for the use of their Supernanogan, and the technicians Winfried Hahn and Uwe Müller for their assistance.

REFERENCES

[1] A. Kitagawa et al., "Review on heavy ion radiotherapy facilities and related ion sources", Rev. Sci. Instrum., 81, 02B909, (2010).

[2] H. Suit et al., "Proton vs carbon ion beams in the definitive radiation treatment of cancer patients", Journal of Radiotherapy and Oncology, 95, p.3-22, (2010).

[3] M. Dosanjh et al., "A possible biomedical facility at the European Organization for Nuclear Research (CERN)", BIR, British Journal of Radiology, (2013).

[4] D. Abler et al., "Feasibility study for a biomedical experimental facility based on LEIR at CERN", Journal of Radiation Research, (2013).

[5] Pantechnik website: `http://www.pantechnik.com/#!sources/vstc2=supernanogan`, (2014).

[6] P. Arndt et al., "Status of the ISL's ECR Ion Source Injectors for the K=132, Proc. of the 15th International Workshop on ECR Ion Sources, p.165-168, (2002).

[7] H. Koivisto et al., "The first results with the new JYFL 14 GHz ECR ion source", Nucl. Instrum. Meth. B, 174, p.379-384, (2001).

[8] S. Bogomolov et al., "Production of ions of metals with an ECR ion sources at FLNR (JINR) cyclotrons", *Proceedings of the 14th International Workshop on ECR ion sources* CERN, Geneve, Switzerland (1999).

[9] B. Siegel et al., "Pyrolysis of Decaborane", Journal of Physical Chemistry, Vol. 62, 3, p.373-374, (1958).

ISBN 978-3-95450-158-8

APPLICATION OF AN ECR ION SOURCE FOR IONIC FUNCTIONALIZATION OF IMPLANT MATERIALS ON THE NANOSCALE

R. Rácz#, S. Biri, P. Hajdu, A Csik, K. Vad, Institute for Nuclear Research, Hungarian Academy of Sciences (Atomki), Hungary, H-4026 Debrecen, Bem tér 18/C
S. Kökényesi, I. Csarnovics, University of Debrecen, Department of Experimental Physics, Hungary, H- 4026 Debrecen, Bem tér 18/A
Cs. Hegedűs, T. Radics, J. Bakó, University of Debrecen, Department of Biomaterials and Prosthetic Dentistry, Hungary, H-4032 Debrecen, Nagyerdei krt. 98
V. Hegedűs, University of Debrecen, Department of Pediatric Dentistry and Orthodontics, Hungary, H-4032 Debrecen, Nagyerdei krt. 98
J. Pálinkás, Institute for Nuclear Research, Hungarian Academy of Sciences (Atomki), Hungary, H-4026 Debrecen, Bem tér 18/C and University of Debrecen, Department of Experimental Physics, Hungary, H- 4026 Debrecen, Bem tér 18/A

Abstract

Surface modification by variously charged heavy ions plays an increasingly important role since functionalization of surfaces and/or deeper layers at micro- and nanoscopic scale can be biologically useful for materials of medical implants. The functionalized surfaces have a huge potential in the field of nanotechnology, sensor devices as well.

Our group explores the physical and biological effect of such treatments. In the recent phase of the research work the implantation of titanium and zirconium-dioxide samples by calcium, gold and silicon ions is required.

The 14.5 GHz Electron Cyclotron Resonance Ion Source (ECRIS) of Atomki - a classical room-temperature ion source - was used in this study as an ion implanter to deliver low energy particles from wide range of elements.

A new vacuum chamber and a sample holder for effective irradiation and the production of the beam itself were developed. The technical details of the irradiation and the first result of the physical investigations are described in this paper.

INTRODUCTION

Plasma processing is a frontier technology and discipline born out of the need to control a group of parameters in materials processing unattainable by strictly chemical process. Materials treated by the plasma, or by the ions of the plasma have a huge area of the possible application field e.g. industry and biomedicine. The field is multidisciplinary involving and combining plasma physics, atomic and molecular physics, surface science and (depending on the final aim of the process) biomedical and engineering disciplines.

Plasmas and ion beams provided by an ECR ion source have some unique future which makes it one of the best candidates to carry out such surface treatment experiments. Due to the high gas efficiency, ECRISs can produce ion beams from a variety of materials, even from solid. By changing the extraction voltage of the source and/or of the charge state distribution (CSD) of the plasma the implantation depth of the ions into the materials can be varied easily. Usually it must be around 10 nm, which is available applying standard terminal voltage. Last but not least there is another remarkable advantage: as an additional irradiation parameter the effect of the charge state of the ions can also be investigated.

The Atomki ECRIS [1,2] is highly suitable device for this task, because it is an independent ion source (there is no post acceleration) offering beam time more freely. Furthermore, the modularity of the source opens the possibility to change the configuration within reasonable time.

MOTIVATION

Our main efforts have been and steel are being made to accelerate and increase bone formation around dental and orthopaedic implants and to improve lifetime and mechanical stability. Modification of the medical implant and material surfaces by variously charged ion beam extracted from ECR ion source are investigated. We have started three subtopics (A-B-C) aiming different goals and requiring different irradiation conditions and ion beams. In the recent phase of the research work the implantation of titanium (the surface is always oxide) and zirconium-dioxide (ceramic) samples by calcium, gold and silicon ions is required. Those attributes are listed in the table 1 and the topics are described shortly below.

Table 1: This table shows the three subtopics started in the Atomki ECR Laboratory

	A	B	C
Target material	TiO_2	TiO_2	ZrO_2
Beam	Au	Ca	Si

#rracz@atomki.hu

ISBN 978-3-95450-158-8

A. The material of the target surface is titanium-dioxide (TiO_2) having good properties e.g. corrosion resistance and also bioinertness. These properties make this material suitable for medical applications. Gold nanoparticles (GNP) in the TiO_2 can be produced by forming gold atomic layers on the surface (and/or close to the surface) by applying heat treatment afterward [3]. GNPs can chemically bond many types of biomolecules which may be able to assist to reach more stable bond to bone [4]. The other favorable property of the GNPs is comes from the plasmon-effect. The energy transfer between the implants covered by GNPs and the light with appropriate wavelength may be able to destroy the bacteria molecules around the implants.
B. The implanted Ca ions may increase and accelerate the adherence of the human tissue due to diffusion.
C. Recently the ZrO_2 (non-silica-) based restorations have become very popular in the dentistry. It can be suitable choice for fix partial dentures and for implants in esthetic area. In order to bond polymer molecules to the ceramic silicon implantation into and/or close to the surface are necessary to increase the cementation of the dental prosthesis.

REQUIREMENTS AND DIFICULTIES

It is clearly visible in table 1 that metallic (gold, calcium and silicon) ion beams are necessary for the planned treatments. Since there is no stable gas phase of these atoms in standard conditions the production of the ion beam from solid had to be realized in case of the gold and calcium.

The implantation depth of the ions must be around 10 nm. At first we should characterize and precisely control of that. It requires physical investigation i.e. depth profile analysis of the samples made e.g. by SNMS (Secondary Neutral Mass Spectrometer) and requires theoretical calculation for realistic prediction.

After the physical investigation of the samples clinical test to investigate the effect of the treatment must be done. Such rigorously controlled actions require a series of the samples (at least 60 pieces) in order to conclude by significant statistic. The high number of the samples and their relatively big size (10 mm x 10 mm) indicate technical developments of the irradiation system (chamber, sample holder) to achieve the treatments in reasonable time.

Another difficulty is to fulfill the dose requirements: from 10^{16} ion/cm^2 up to 10^{18} ion/cm^2 must be produced by the ECRIS.

The implantation process in case of an insulation target (e.g. ZrO_2 in subtopic C.) is not trivial. During the irradiation the sample surface can be charged up the sample which affects the incident beam, causing indefinite dose and implantation depth.

The requirements and difficulties are listed in this chapter indicated the technical and ion beam developments of the ion source.

ION BEAM DEVELOPEMENTS

The three different kinds of ion beams were produced by three different methods. Note that the application mainly require high intensity, low charged ion beams.

For gold ion beam production the sputtering technique [5] was chosen. Instead of the biased disc a movable sputtering electrode was mounted on the axis of the plasma chamber. This holder equipped with a thermocouple [6], allowing to measure the temperature of the pastille during operation (Figure 1). Oxygen plasma was generated and the oxygen ions of it were used to sputter the metal pastilles. The pastille was negatively biased with respect to the plasma up to 2kV and about 2 mA current was measured on it. The optimal distance between the samples and injection plate was around 80 mm.

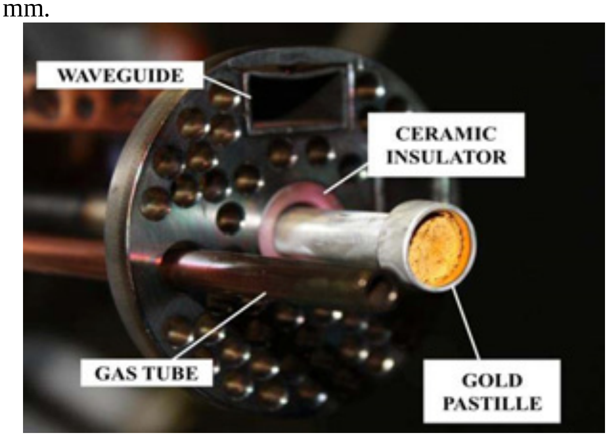

Figure 1: The movable sputtering electrode mounted axially instead of biased disc. The thermometer (not visible) is placed inside the mounting tube.

Remarkable parts of the mass spectra come from the support gas. Typical CSD of the extracted beam can be seen in the Figure 2. During the irradiation process the terminal voltage of the ion source was 2 kV (in order to reach the ~10 nm implantation depth).

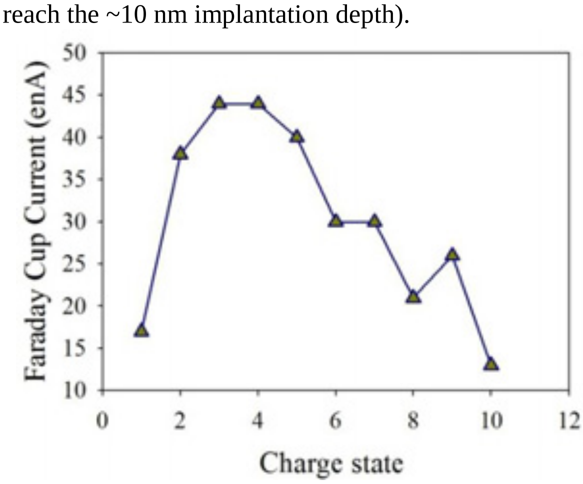

Figure 2: Typical CSD of the extracted gold ion beam used for irradiation. The plasma was tuned for Au^{3+}.

Calcium ion beam was produced by the well-known oven technique [7]. The large capacity oven developed

ISBN 978-3-95450-158-8

by the Pantechnik Company was used. It is an ohmic resistor allowing controlling the temperature from 300°C up to 1700°C. The head was placed on the axis of the plasma chamber and filled by pure calcium. Due to the vapor pressure of the calcium the optimal operation temperature was found between 500°C and 700°C. We have used helium as support gas. Just before the optimal operation point very strong getter effect was observed. This effect causes very clear calcium spectra showing almost only calcium related peaks and the peaks of the support gas (Figure 3).

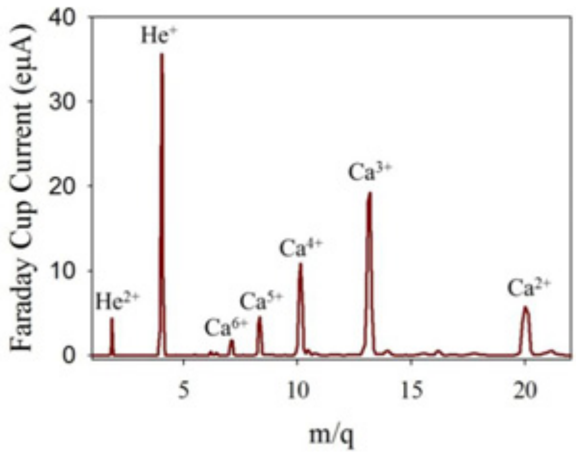

Figure 3: Calcium ion beam spectra. The extraction voltage and the temperature of the oven were 5 kV and 700°C respectively. The purity of the spectra is caused by the strong getter effect. The plasma was optimized Ca^{3+}.

In order to obtain silicon ion beam we used SiH_4 (silane) gas. Special care was applied. A concentration of 1.37% is the lower flammable limit for this material in air under conditions of normal temperature and pressure. Between 1.37% and about 4.5%, mixtures can react if an ignition source is provided. Over this concentration mixture is metastable and will undergo auto ignition.

Therefore special gas handling system was designed to transfer the silane gas from high volume high pressure (2 dm^3 and 50 bar) gas bottle to a smaller (50 cm^3 and 1.5 bar) one. The small bottle was connected to the ion source through a gas dosing valve and silicon ion beam was produced. Due to the safety arrangements the risk was reduced to the normal operation level.

Typical silicon ion beam spectra can be seen in Figure 4. For low and middle charge states (Q=1-8) beam currents between 25 and 100 eμA were easily obtained (Figure 5) with good stability.

TECHNICAL DEVELOPMENTS

Over the requirement referring the ion beam production itself, technical developments were indicated by the reasons listed above.

A new irradiation facility was developed: a vacuum chamber to change the samples easily without breaking the vacuum of the ion source and with a relatively big sample holder in it (Figure 6). The sample holder can handle 3 x 14 = 42 pieces of 10 mm x 10 mm size samples. It is possible to irradiate 14 samples at the same time. The samples are connected to the vertical copper holder by special conductive glue.

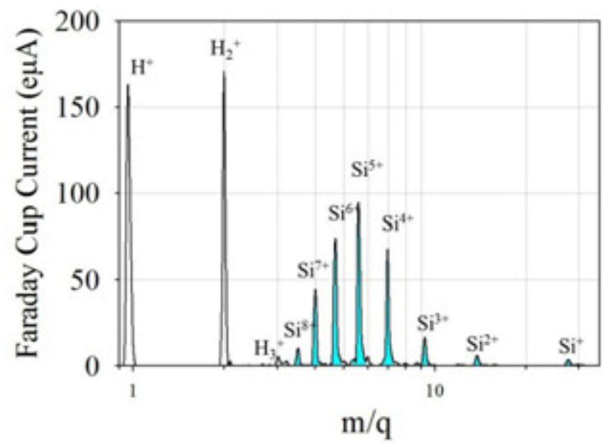

Figure 4: Typical silicon ion beam spectra (optimized for Si^{5+}). The extraction voltage was 10 kV.

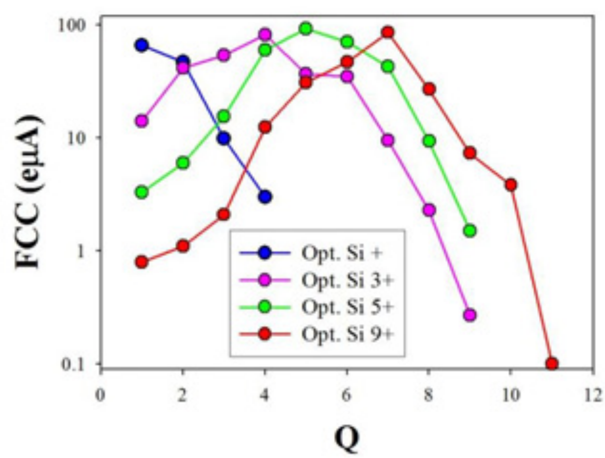

Figure 5: CSDs of the silicon ion beam spectra as a function of the optimized charge state.

To control parameters of the relatively big beam spot a simple beam diagnostic system (profile meter) was also developed. It is an improved version of the 5-segments sample holder already published in ECRIS08 workshop [2]. It was supplemented by four concentric segments to set the size and check the homogeneity of the beam.

In order to reach as high dose as possible, the irradiation facility was built in the primary (zero degree) beamline. In that case, of course all the extracted components of the plasma reach and hit the samples. Instead of the 90 degree line irradiation (with analyzed beam), this method allows to use all the charge states of the produced plasma and the losses of the beam caused by transportation are avoided. During irradiations the analyzed (90 degrees) beamline was only used to estimate the composition of the beam, before, after and several times during an irradiation.

ISBN 978-3-95450-158-8

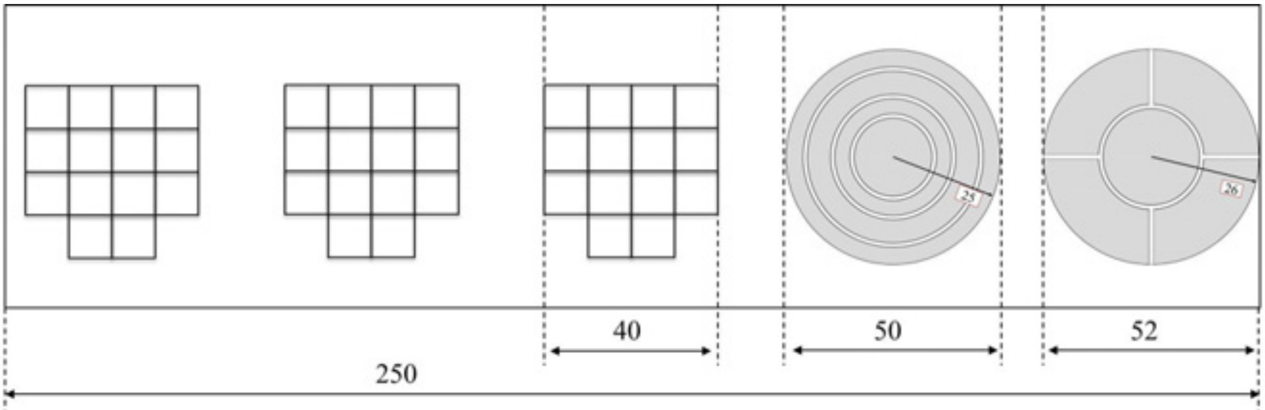

Figure 6: The drawing of the new sample holder constructed by 5 mm thick copper plate. The 5-segment profile monitor helps to set the x-y position of the beam, while the 4-segments concentrical monitor helps to set the size and the homogeneity of the beam spot.

RESULTS OF THE FIRST INVESTIGATIONS

Firstly, as the starting point of the projects (A-B-C) a small number of the samples were irradiated by the beams developed (Table 2).

Table 2: The parameters of the irradiations: name of the project, ionic piece, average charge state, irradiated dose, irradiation time.

Project	Ion	$\overline{Q}$	Dose (ion/cm^3)	Time (hour)
A	Au	1.3	10^{16}	8
B	Au	2.2	10^{17}	4.5
C	Si	3.1	10^{17}	1.25

In order to avoid the charging up effect of the ZrO_2 sample, it was covered by 25 nm thick carbon layer and for comparison a sample without this layer was also irradiated.

The depth profiles of the treated samples were investigated. After such implantation the depth distribution of the irradiated materials are Gaussian like or can be handled by the superposition of Gaussian curves. The well-known SRIM (Stopping and Range of Ions in Matter) code [8] was used to make sense of the curves measured experimentally by an SNMS device (type INA-X, SPECS, Berlin).

The depth, where the density of the ions reaches the maximum (called implantation depth) was used as a representative parameter to compare the calculated and measured profiles. The data are summarized in Table 3.

In case of the titanium (oxide) target (project A and B) the implantation depth of the incident ions were well predicted by the computer code. However in case of the ZrO_2 sample (which is an insulation material) the sample can charge up, as we supposed, which affects the kinetic energy of the incident beam causing indefinite (lower) implantation depth. This uncertainty can be avoided by evaporating carbon layer on the surface of the target. In this way the implantation depth becomes easy to be predicted (see last row in Table 3). The added carbon layer can be removed by heating the sample applying 800^{o}C over 6 hours in a furnace.

Table 3: Comparison of the calculated and measured implantation depths.

Ion	Target	Depth (nm)	Calc. depth (nm)
Au	TiO_2	1-10	7
Ca	TiO_2	8	9
Si	ZrO_2	6	25
Si	ZrO_2 + C layer	25	25

SUMMARY

In the frame of a long term multidisciplinary scientific project the Atomki ECR ion source was used to produce specific heavy ion beams and plasmas for materials research and to explore the possibility of medical applications of such ions. We are focusing to the medical implants and materials since functionalization of such material's surfaces and/or deeper layers at micro- and nanoscopic scale can be biologically useful.

The requirements and difficulties of this field listed in this paper evoked technical and ion beam developments of the Atomki ECR ion source. New vacuum chamber and sample holder (new irradiation facility) for effective irradiation were designed and constructed. Calcium, gold and silicon plasmas and beams were produced by different techniques. Two different types of materials (TiO_2 and ZrO_2) were irradiated by three kinds of ion species.

The implantation depth of the incident ions was measured and compared with the calculated one. As a result, we can control and allocate this parameter even in case of insulation target material.

ISBN 978-3-95450-158-8

As the logical continuation of this work, high number of samples will be treated by using the new irradiation facility presented in this paper. In the near future (before the clinical phase) further physical and biomedical studies of those samples are planned.

ACKNOWLEDGEMENT

This work supported by the TAMOP 4.2.2.A-11/1/KONV-2012-0036 project, which is co-financed by the European Union and European Social Fund. The research leading to these results has received funding from the European Union Seventh Framework Program FP7/2007-2013 under Grant Agreement No. 262010 - ENSAR. The EC is not liable for any use that can be made on the information contained herein. Work was also partly supported by a Hungarian-Taiwan bilateral research program No NKM-92/2014.

REFERENCES

[1] S. Biri, R. Rácz and J. Pálinkás, *Status and special features of the Atomki ECR ion source,* Review of Scientific Instruments **83** (2012) 02A341 (3 pp).

[2] S. Biri, I. Iván, Z. Juhász, B. Sulik, Cs. Hegedűs, A. Ifj. Jenei, S. Kökényesi, J. Pálinkás, *Application of the Atomki-ECRIS for materials research and prospects of the medical utilization,* Proceedings of the 18th Int. Workshop on ECRIS Chicago, Ill. USA, 15-18 Sept., 2008. 41-47.

[3] S. Kökényesi, S. Biri S, Cs. Hegedűs, I. Csarnovics, A. Csik, Functionalization of amorphous chalcogenide and titanium oxide layers by gold nanoparticles, Advanced Materials Research **747** (2013) 289-292.

[4] Y.C. Chai, A. Carlier, J. Bolander, S.J. Roberts, L. Geris, J. Schrooten, H. Van Oosterwyck, F.P. Luyten, Current views on calcium phosphate osteogenicity and the translation into effective bone regeneration strategies Acta Biomaterialia 8 (2012) 3876–3887.

[5] Brown, I. G., (ed.), The physics and technology of ion sources WILEY-VCH Verlag GmbH. 2004.

[6] R. Rácz, S. Biri, I. Csarnovics, I. Kökényesi, Gold and calcium ion beams for materials research by the Atomki ECR Ion Source Acta Physica Debrecina **46** (2012) 133-141.

[7] C. Barue, C. Canet, M. Dupuis, J. L. Flambard, R. Frigot, P. Jardin, T. Lamy, P. Lemagnen, L. Maunoury, B. Osmond, C. Peaucelle, P. Sole, T. Thuillier, Metallic beam developments for the SPIRAL 2 project, Review of Scientific Instruments **85** (2014) 02A946 (4 pp).

[8] J. F. Ziegler, M. D. Ziegler, J. P. Biersack, SRIM – The stopping and range of ions in matter, (2010), Nucl. Instrum. Methods Phys. Res. B **268** (2010) 1818.

ISBN 978-3-95450-158-8

A POINT-LIKE SOURCE OF EXTREME ULTRAVIOLET RADIATION BASED ON NON-EQUILIBRIUM DISCHARGE, SUSTAINED BY POWERFUL RADIATION OF TERAHERTZ GYROTRON*

A.V. Sidorov#, S.V. Golubev, M.Yu. Glyavin, I.V. Izotov, A.G. Litvak, A.G. Luchinin, D.A. Mansfeld, S.V. Razin, V.A. Skalyga and A.V. Vodopyanov, Institute of Applied Physics RAS, Nizhny Novgorod, 603950, Russia

Abstract

It is proposed in this paper to use discharge plasma supported by terahertz radiation as a source of EUV light for high-resolution lithography. In this report we discuss the experimental investigation of two types of EUV sources based on discharge, supported by powerful gyrotron radiation. Following investigation results are described:

-a series of experiments that demonstrate the generation of EUV light from the vacuum-arc discharge plasma in tin vapor in the magnetic trap heated by gyrotron radiation with a frequency of 75 GHz under electron cyclotron resonance (ECR) conditions;

-a numerical modelling of the plasma emissivity in the EUV range, depending on the parameters of the heating radiation is performed;

-experimental studies of EUV emission from plasma discharge sustained by strong terahertz powerful radiation in inhomogeneous gas flows are started.

INTRODUCTION

Today micro- and nano- electronics industry requires a source of extreme ultra-violet (EUV) radiation with a wavelength of 13.5 ± 1 % nm for high resolution projection lithography. The power of the source must be at a level of 1 kW at the size of the emitting region of less than 1 mm.

One of the most promising sources of EUV light is considered to be a source that uses a pulsed CO2 laser radiation focused on a specially formed stream of drop-lets of tin with dimensions of the order of 0.1 mm [1]. However, along with tangible achievements in these light sources have a number of fundamental flaws that do not allow us to consider the problem of creating a EUV light source to be solved.

We propose to use discharge plasma supported by terahertz radiation as a source of EUV light for high-resolution lithography. In this report we discuss the experimental investigation of two types of EUV sources based on discharge, supported by powerful gyrotron radiation. Following investigation results are described:

- a series of experiments that demonstrate the generation of EUV light from the vacuum-arc discharge plasma in tin vapor in the magnetic trap heated by gyrotron radiation with a frequency of 75 GHz under electron cyclotron resonance (ECR) conditions;
- a numerical modelling of the plasma emissivity in the EUV range, depending on the parameters of the heating radiation is performed;
- experimental studies of EUV emission from plasma discharge sustained by strong terahertz powerful radiation in inhomogeneous gas flows are started.

ELECTRON CYCLOTRON RESONANCE HEATING EXPERIMENTS

The experimental scheme is following: tin ions injected into the magnetic trap from a vacuum-arc dis-charge. Low-pressure discharge sustained in a magnetic trap by the high-power millimetre-wave radiation (200 kW @ 75 GHz) under ECR conditions. Multiply charged ions are efficiently generated and excited in such a discharge and emit line radiation in the desired wave-length range [2]. Experimental layout is in the Fig. 1.

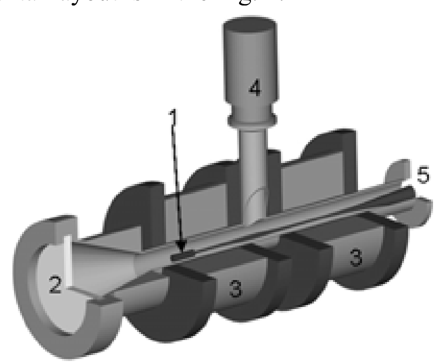

Figure 1: Experimental setup 3d-scheme. 1 – plasma generator, 2–window for microwaves, 3 - coils, 4 – EUV detector, 5 – flange for plasma analysis or EUV detector.

The charge state distribution of tin ions achieved in these experiments is shown in Fig. 2. A radiation power of 50 W in a wavelength range of 13.5 nm ± 1% and an efficiency of about 1% for the conversion of the micro-wave radiation absorbed in the plasma to the extreme ultraviolet radiation were achieved in the experiments.

NUMERICAL SIMULATION

The efficiency of the source of the EUV radiation was estimated as follows. The system of the rate equations for the densities of the charged particles in various ionization states was solved. The initial mean charge of the tin ions in the injected beam was 2. The microwave-radiation

*Work supported by RSF within grant No 14-12-00609
#alexsv@appl.sci-nnov.ru

ISBN 978-3-95450-158-8

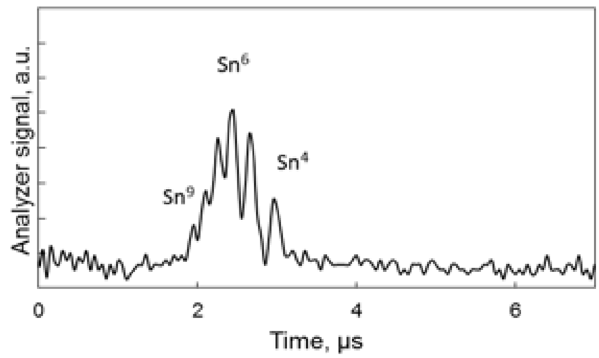

Figure 2:Tin-ion distribution over the degree of ionization in the vacuum-arc plasma heated by microwaves.

power necessary to sustain plasma with a certain electron temperature T_e (the power absorbed by the plasma) was calculated as the sum of the energy carried out from the trap mirrors by the plasma and the energy spent for the ionization and excitation of the ions followed by emission. The radiative losses from the plasma were calculated as follows. Density of the plasma and the resulting ion distribution over charges were calculated for a given flow of plasma in a trap (defined by vacuum arc current I_{arc}) and a fixed T_e. Then EUV light power was estimated using the averaged constants for the excitation rate of multiply charged tin ions [3]. The most impressive results are plotted in Fig. 3.

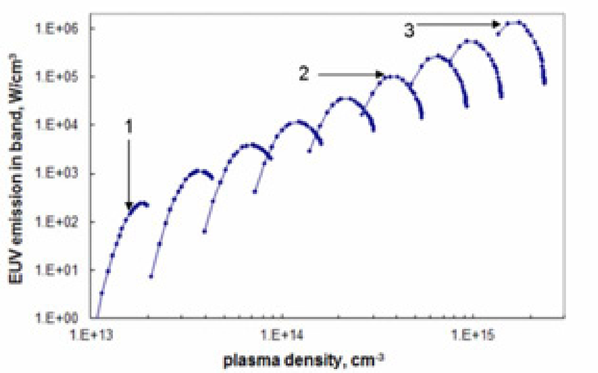

Figure 3: Radiation power calculations in the range of 13.5 nm ±1% into a solid angle of 4 π sr for the predetermined Te and Iarc. Resulting points calculated for fixed I_{arc} and different T_e are connected by lines.

Arrow 1 shows the calculation for the parameters of the experiment described above. Performance of the EUV light source could be improved by increasing the plasma density. For example, the use of plasma heating waves with frequency of 170 GHz will make it possible to reach plasma density values up to $4\cdot10^{14}$ cm^{-3}. And the longitudinal size of the emitting region will be less than 5 mm. This example marked with arrow 2 in Fig. 3. To reach desired 1 kW of light power in desired band and size of the source less than 1 mm further increase of the frequency of the heating radiation is needed. 300 GHz will make it possible to reach plasma density values up to 10^{15} cm^{-3}. And the longitudinal size of the emitting region will be about 1 mm. In this case conversion efficiency and total EUV light emission could be 5 % and 1 kW. This example is marked by the arrow 3 in Fig. 3.

TERAHERTZ WAVE HEATING EXPERIMENT

An increase in plasma density with increasing frequency of the heating wave to the value of 10^{15} cm^{-3} and above makes a plasma resonance heating mechanism effective with small plasma size [4, 5]. This removes the need to use high magnetic fields. The main idea of creating of a point discharge with high emissivity in the required wavelength band is the realization of a breakdown in a non-uniform gas jet with the scale of the inhomogeneity of the order of 1 mm. In this case, breakdown conditions fulfilled only in a small region of space and discharge cannot go beyond it. General view of the experimental setup (without gyrotron) is shown in Fig.4. The plasma was ignited by gyrotron radiation with a frequency of 0.67 THz and power up to 200 kW in pulses lasting from 20 to 50 μs [6].

Figure 4: Photo of the experimental setup. 1 - discharge vacuum chamber, 2 – manipulator with the gas inlet and an additional focusing mirror, 3 - vacuum pump, 4 – microwave beam mode converter, 5 - additional focusing parabolic mirror with a nozzle to form a non-uniform flow of gas.

Gyrotron radiation transformed into Gaussian beam by quasi-optical converter was directed into the discharge vacuum chamber, where was additionally focused by a parabolic mirror (5), maximum value of the THz wave power density was of about 40 MW/cm^2 that ensured stable gas breakdown for the pressure values of about 20 Torr. A small nozzle (150 μm in diameter) connected to a buffer volume was drilled in the centre of the mirror (5) for producing an inhomogeneous gas flow. Neutral gas flow was about 10^{20} particles/sec at a gas pressure of 2-3 atm in buffer volume, which corresponds to approximately atmospheric pressure at the nozzle outlet. The pumping system allowed to maintain background pressure on the level of 10^{-2} – 10^{-3} Torr. Argon was used as a gas in the first experiments (expedience of using xenon gas in real sources is obvious). In spite of the lack of emission lines into the required band for the projection lithography this gas seems optimal for the demonstration of principal opportunity to use terahertz gas discharge as

ISBN 978-3-95450-158-8

an effective point-like UV source. Terahertz wave beam power and gas inlet parameters were chosen to fulfil breakdown conditions near the focus of the parabolic mirror and ignite the discharge. Discharge glow diagnostics was performed using a several photomultipliers (“Photon-1” in the wavelength range of 200 - 650 nm and PMT-142 with the MgF_2 window and removable quartz filter in the vacuum ultraviolet range – 112-400 nm). The boarder of the quartz filter free pass was close to the wavelength of 180 nm.

The main purpose of this work is to study the possibility of obtaining a point-like discharge plasma with size less than 1 mm and parameters (T_e, $N_e\tau$) providing VUV radiation by using a non-uniform gas flow. It is necessary to provide the breakdown conditions near and only near the nozzle to localize the discharge (gas pressure in this area should be about atmospheric pressure which corresponds to the minimum of the breakdown curve for quasi-optical beam of terahertz radiation [5]), which requires steep gas pressure gradient, that is, effective pumping. To illustrate the Figure 5 shows photographs of the discharge for different values of background gas pressure in the vacuum chamber.

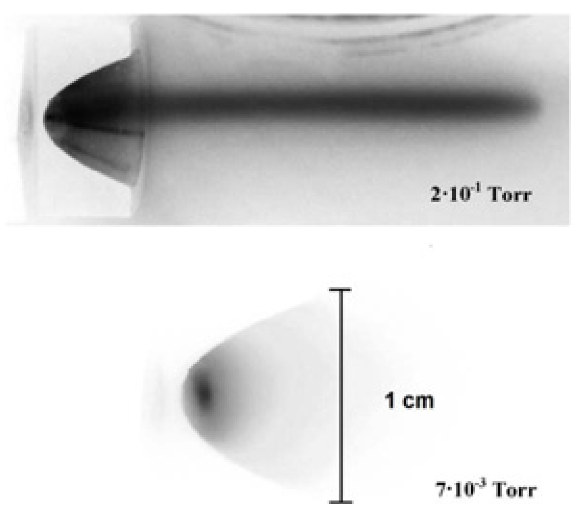

Figure 5: Discharge glow photographs at the values of the background gas pressure $2{\cdot}10^{-1}$ Torr (upper) and $7{\cdot}10^{-3}$ Torr (lower).

It is clearly seen that at relatively high background pressures (10^{-1} Torr) discharge emerged at the high-pressure region near the nozzle extends towards radiation and ends in the area where the breakdown conditions are not fulfilled. The same could be seen from the Figure 6 showing the discharge optical scan obtained by a streak camera FER-27. Discharge existence in the region with initial field intensity less than the breakdown value apparently could be realized due to the electric field normal component amplification in inhomogeneous plasma at the plasma resonance point [7].

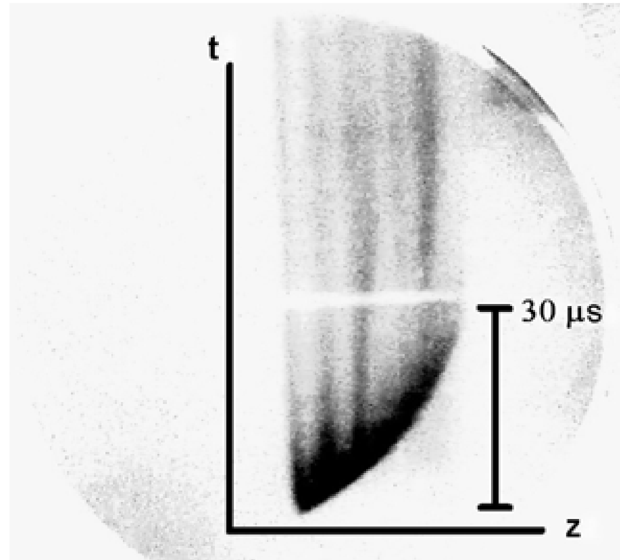

Figure 6: Streak camera FER- 27 scan-image of the discharge glow. Vertical axis represents time, horizontal axis is the coordinate directed to the electromagnetic radiation source.

With the background gas pressure decrease discharge reduced its dimensions and at the pressure less than $5{\cdot}10^{-2}$ Torr it became localized near the nozzle. Light emission of such point-like discharge was studied in the wavelength range from 650 nm to VUV region. Figure 6 shows the waveforms of photomultiplier signals obtained at background pressure of $3{\cdot}10^{-2}$ Torr.

Time evolution of the discharge glow comes into notice: it is clearly seen that the intensity of the discharge glow in the VUV range increased right after the end of the THz radiation pulse and the glow in the visible range increased only after hundreds of microseconds together with the decay of the VUV emission. This behaviour can apparently be explained as follows. During the terahertz radiation pulse when electron temperature is relatively high formation and excitation of multiply charged ions by electron impact takes place together with subsequent de-excitation in the VUV band. After the pulse end electron temperature decreases which leads to sharp increase of the rate of radiative recombination in three-body collisions (it is proportional to $T_e^{-9/2}$) and rapid increase of recombination radiation intensity. Then, the plasma ionization degree decreases down to the level where only low-charged ions remain, plasma recombination luminescence spectrum shifts from the VUV to the visible range (Fig . 7). We assume that the excitation of multiply charged ions by electron impact during the THz radiation pulse is changed to their excitation by impact-radiation recombination. It should be noted that radiation intensity in the optical band increase with the gas pressure in opposite with the radiation intensity behaviour in the VUV region: for the pressure values of about 10^{-1} Torr discharge hardly radiated in the VUV band. This fact could be noticed after the comparison of the PMT-142 signals with and without quartz filter (for relatively low

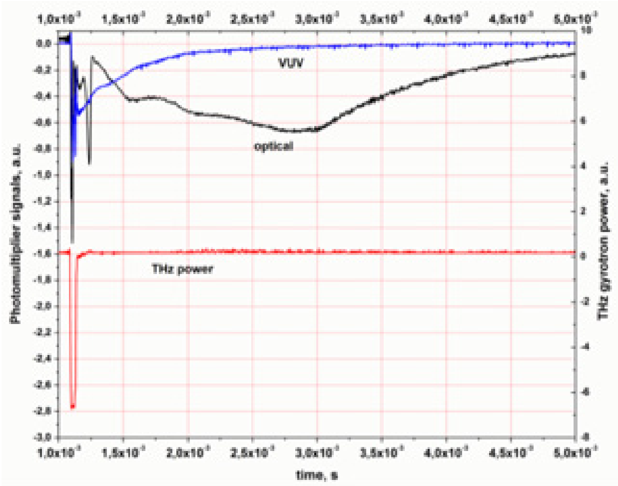

Figure 7: Signals from photomultipliers in optical and VUV regions (upper). Lower signal – THz radiation power pulse. Background gas pressure $3 \cdot 10^{-2}$ Torr.

pressures signal without filter was in several times more, for high pressures they were close). The value of the VUV radiation power can be estimated from the low bound using a data of PMT-142 sensitivity. Comparison of the PMT-142 signals at low pressures with quartz filter (that cut off the radiation with the wavelength low than 180 nm) and without it demonstrated that in assumption of the isotropic radiation 10 kW of radiation total power fell on the range of 112-180 nm.

These results demonstrate the feasibility and prospects of EUV point-like source creation on the basis of a discharge in a non-uniform gas flow sustained by a powerful terahertz radiation. It should be noted that the first experiments were carried out using cheap and available noble gas Argon. Argon does not have as many emission lines in the desired wavelength range as Xenon does (it was shown that xenon discharge emission efficiency in the range of 13.5nm ± 1% could be up to 1%, and in the range of 11.2 nm ± 1% up to 4 % of energy absorbed by the plasma [8]). THz gyrotron with 50 kW CW power at 1 THz should be enough to create 13.5 or 11.2 nm EUV source of such type with output power at the level of 0.5 kW assuming the reasonable level of terahertz radiation absorption efficiency (dozens of percent as it was mentioned above). Last developments in gyrotron technologies offer possibility of such generators production [9].

ACKNOWLEDGMENT

The work was supported by RSF within grant No 14-12-00609.

REFERENCES

[1] G. Schriever et al., J. Micro/Nanolith. MEMS MOEMS, 11(2), 021104 (2012).
[2] N. Chkhalo et al., J. Micro/Nanolith. MEMS MOEMS, 11(2), 021123 (2012).
[3] J. White et al., J. Appl. Phys., 98(11), 113301 (2005).
[4] A. D. Piliya, Sov. Phys. Tech. Phys. 11, 609 (1966).
[5] V. Bratman et al., Phys. Plasmas, 18, 083507 (2011).
[6] M.Yu. Glyavin, A.G. Luchinin, G.S. Nusinovich, J. Rodgers, D.G. Kashyn, C.A. Romero-Talamas, and R. Pu, Appl. Phys. Lett. 101, 153503 (2012)
[7] Yu. Ya. Brodskii, S.V. Golubev, V.G. Zorin, G.M. Fraiman, Sov. Phys. JETP 61, 453-458 (1985).
[8] E. R. Kieft, K. Garloff, and J. J. A. M. van der Mullen, Phys. Rev. E 71, 036402 (2005).
[9] V.L. Bratman, A.G. Litvak, E.V. Suvorov, Physics-Uspekhi 54, 837–844 (2011).

ISBN 978-3-95450-158-8

CLOSING REMARKS FOR ECRIS'14

T. Thuillier#, LPSC, Grenoble, France

Abstract

A scientific overview of the ECRIS14 workshop is proposed in this paper. The workshop content demonstrated that the ECR community is still very active and that research is of high interest for future accelerator projects. A selection of new results and development presented during the workshop is proposed.

INTRODUCTION

The XXIst ECR Ion Source conference was hosted by the Institute of Applied Physics of the Russian Academy of Science in Nizhny Novgorod, Russia, from August 24th to August 28th 2014. The number of attendees was 60. The workshop atmosphere was relaxed, studious and suitable to discussion. Many new ion sources have been presented, many new developments were announced and interesting new results shown. The paper proposes selected highlights from the workshop. Because it is not possible to present every single contribution, the author apologies for those works which are not mentioned there.

NEW RESULTS

The know-how on the use of high ECR frequency in superconducting ECR ion sources keeps on improving with new results from MSU, IMP Lanzhou and RIKEN.

At IMP Lanzhou, impressive high intensities Bi beams were produced: 710 μA of Bi^{30+} (1.4 kW 18 GHz+4.7 24 GHz), 100 μA of Bi^{41+} and 10 μA of Bi^{50+}.

The RIKEN 28 GHz SC-ECRIS, demonstrated the production of high intensity U beam using the sputtering method: 225 μA of U^{33+} and 180 μA of U^{35+}.

At MSU, the commissioning of SUSI started at the 24 GHz frequency. 860 μA of Ar^{12+}, 530 μA of Ar^{14+} have been obtained (with 5.5 kW of RF power). It is noticeable that these intensities are equivalent to the records of VENUS (LBNL) obtained at 18+28 GHz, with quite a different plasma chamber volume (7.6 litre for VENUS and 3.5 for SUSI). Another insight from MSU studies is that beam intensities obtained at high power 18 GHz compare with the ones obtained with a pure 24 GHz frequency. The so-called "ECR frequency scaling law" implying a current extracted proportional to the frequency to the square is not quite observed here. Results look like the higher intensities obtained with the 24 GHz emitter for Ar^{11+} to Ar^{14+} could be due to the higher RF power available rather than the frequency change, since the current gain per RF power is very similar for both frequencies. Nevertheless, a net gain in current performance at 24 GHz has been obtained for high charge state (Ar^{16+}). A last interesting information from SUSI comes from the plasma chamber return temperature which happens to be higher at 24 GHz than at 18 GHz for the same RF power level.

At LPSC Grenoble, the first 60 GHz high power pulses have been injected into SEISM, a room temperature magnetic CUSP having a closed ECR resonance. Record beam current densities have been measured up to 600 mA/cm^2 (5 mA extracted from a Ø1 mm extraction electrode). Another very interesting point is that intense afterglow peaks of low charge states have been observed. This implies that such a simple axisymmetric structure features non trivial plasma confinement properties: interesting physics is hidden behind.

NEW DEVELOPMENTS

This workshop edition featured many new ion sources projects or major upgrades of existing ones. Because the detailing all the contributions would be too long to be included in these closing remarks, the reader is invited to look into the proceedings for uncovered new developments.

First ECRIS Plasma and Commissioning

The commissioning of the ECRIS-LECR4 at Lanzhou gave excellent results at 18 GHz : 1.9 mA O^{6+}; 1.7 mA Ar^{8+}, 0.29 mA Xe^{20+} with a radial magnetic intensity at wall of 1T only. The source uses a set of original evaporative cooling coils to generate its axial magnetic field.

The KBSI team of Busan presented the first plasma of their new 28 GHz SC-ECRIS dedicated to the production of Li beam. The SC solenoids reached their nominal current design, while the hexapole coils reached 83% of design so far. Further training of the hexapole is planned.

The Fraunhofer Institute and the Dreebit company presented the development of an original ECR ion source including an inverted cylindrical sputter magnetron to produce intense 1^+ aluminum beams for ion implantation.

New ECRIS Project

IMP CAS is building an upgrade of the SECRAL source named SECRAL II, to be operated at 18+28 GHz. The source has an upgraded cryogenics. The cold mass has been built and the coils ramped together to 90% of the design within 8 quenches.

IMP CAS presented the HIAF accelerator complex project requiring the challenging production of pulsed U^{34+} with a peak intensity of 1.7 mA and a duration of 400 μs. The design of a 4th generation high frequency ECR is under progress in the institute to tackle this objective.

INFN-LNS team reported the design of a new hybrid ion source named AISHa dedicated to hadrontherapy. The source features a permanent hexapole and a set of 3 He-free coils. The talk also included the presentation of

thuillier@lpsc.in2p3.fr

ISBN 978-3-95450-158-8

the ESS microwave 2.45 GHz proton source featuring a flexible axial magnetic field to investigate classical flat, simple mirror and magnetic beach profiles.

JYFL is developing a new room temperature ECRIS named HIISI with a chamber volume and a magnetic field topology very similar to the SUSI ion source. The source has 3 coils for the axial magnetic profile and a refrigerated hexapole including permanent magnets.

Metallic Beam Developments

Several contribution included new developments in metallic beams. The use of dedicated low temperature metallic ovens, initiated by LBNL, spread to other facilities (MSU, IMP Lanzhou). The advantage of such an oven technique is that it is insensitive to the level of power feedback from the plasma (or microwave), providing higher reliability and tunability of the ion source. New ^{50}Ti MIVOC beams (Metal Ions from Volatile Organic Compounds) have been developed at JINR Dubna (82 µA $^{50}Ti^{5+}$) and GANIL (25 µA $^{50}Ti^{11+}$). A technique to produce pure rare earth metal sample from oxydized state has been successfully developed at MSU and used to produce Yb and Sm beams.

PLASMA, BEAMS INVESTIGATIONS, SIMULATIONS

At CERN, the demand to increase luminosity at LHC requires an improvement of the whole LINAC3 performance. As a first step, a Pb beam extraction simulation study was performed on the CERN's GTS-LHC ion source. The IBsimu freeware used was able to reproduce the experimental emittances and characteristic beam shapes.

Systematic emittance measurements of high charge state uranium beam have been performed with the RIKEN 28 GHz SC-ECRIS as a function of its axial magnetic profile intensity. The team measured an emittance decrease by ~50% when the magnetic injection intensity peak Binj was reduced from 3.1 to 1.5 T. This effect was not pointed out in the past: similar measurements in other ECRIS would be of high interest. Another emittance measurement was done as a function of the magnetic extraction peak intensity B_{ext}. The results show that the beam emittance decreases with the B_{ext} intensity. At first sight , this measures looks contradictory with the well-known fact that the emittance in a ECRIS is driven by the magnetic emittance. But, on the other hand, there are evidences that high charge state ions are extracted very close to the ion source axis which limits *de facto* the magnetic emittance contribution. Again, it would be great to cross check this original study in another ion source.

The Jyväskylä team in collaboration with IAP RAS Nizhny Novgorod presented an interesting study on beam current oscillations driven by electron cyclotron instabilities in ECRIS. The study included a careful temporal analysis of microwave reflection, x-ray, light emission and ion beam intensity to capture information on the instability. The study was completed by a theoretical approach by D. Mansfield who presented a theoretical work on the development of kinetic instabilities in ECR plasma due to the anisotropy of the electron energy distribution function.

At LPSC, experimental hot electron x-ray spectrum data from the VENUS source was revisited. The investigation tends to show that the hot energy tail temperature is proportional to the ECR heating frequency. A fact which is of bad omen for future 60 GHz SC-ECRIS which would endure even stronger x-ray flux toward the coils cold mass. A simple ECR heating model developed allows to correlate the change of x-ray temperature (when the B_{med} field is varied) for a given ECR frequency as a direct geometrical change of the ECR surface.

V. Mironov from JINR used a particle in cell code to test the ECRIS scaling laws. Helped with simple assumptions and an effective model, the code can reproduce many features from ECRIS like charge state distribution or some variation of beam current with magnetic field intensity.

CONCLUSION

The ECRIS 2014 workshop demonstrated once again that the ECR community is still very alive. The development of new ECR ion source remains an important activity in many laboratories and the workshop was, as usual, a great place to share valuable information together. The performance and know-how of 3rd generation ECRIS is still improving. The existing projects of future generation accelerators featuring challenging performances require to increase again the performance of ECR ion sources. So ECRIS research and development must go on to explore even higher RF frequencies to improve beam intensities and charge states. The author, on behalf of the attendees, wishes to express his warmest congratulation to the chairman V. Skalyga and to the local organizing committee for organizing such a high quality level workshop. The XXIInd edition of the Electron Cyclotron Resonance Ion Source workshop will be hosted by the Korean Basic Science Institute in Busan, Republic of Korea. Hope to see you all there!

ISBN 978-3-95450-158-8

ISBN 978-3-95450-158-8

List of Authors

Bold papercodes indicate primary authors

— A —

Aleev, A.A. MOPPH017
Andrianov, S.L. MOPPH017
Angot, J. MOOMMH02, WEOBMH01
Arredondo, I. MOPPH018
Asfari, Z. MOPPH015
Ayala, J.M. MOPPH003

— B —

Bahng, J. MOPPH011
Bakó, J. THOMMH02
Bakulin, M.I. MOOMMH02, **TUOBMH01**
Barue, C. MOPPH002
Basu, T.K. MOPPH005
Becker, R. MOPPH006
Beijers, J.P.M. MOOAMH03
Bekhterev, V. **MOPPH016**, WEOMMH03
Bellodi, G. MOOAMH01
Belver, D. MOPPH018
Bhang, J.B. WEOMMH01
Biri, S. **MOOAMH05**, THOMMH02
Bogard, D. MOPPH003
Bogomolov, S.L. **MOPPH015**, MOPPH016, WEOMMH03, WEOBMH02
Bondarchenko, A.E. MOPPH015
Brandenburg, S. MOOAMH03
Bustinduy, I. MOPPH018
Bykov, Yu.V. TUOBMH02

— C —

Canet, C. MOPPH002
Cao, Y. **MOPPH008**
Castro, G. TUOMMH02
Cee, R. MOPPH004
Celona, L. **TUOMMH02**
Chalykh, B.B. MOPPH017
Chauvin, N. MOPPH003
Chen, J. MOOBMH04
Chen, J.E. MOOBMH04
Chirkov, A.V. TUOBMH01
Choi, S. MOPPH011, WEOMMH01
Choinski, J. WEOBMH01
Choo, W.I. **MOPPH012**, MOPPH013, MOPPH014
Ciavola, G. TUOMMH02
Ciric, D. MOPPH016
Cole, D.G. MOOMMH03, MOPPH019
Comunian, M. MOPPH017
Corres, J. MOPPH018
Csarnovics, I. THOMMH02
Csik, A. THOMMH02

— D —

Debray, F. MOOMMH02
Delahaye, P. WEOBMH01
Denisov, G.G. TUOBMH01, **TUOBMH02**
Dobrosavljevic, A.S. MOPPH016
Dumas, J.M. MOOMMH02

— E —

Echevarria, P. MOPPH018
Efremov, A.A. MOPPH016, **WEOMMH03**, WEOBMH02
Eguiraun, M. MOPPH018
Eremeev, A.G. MOOMMH02, TUOBMH01, TUOBMH02

— F —

Faure, H. MOPPH015
Feng, Y.C. MOPPH010, WEOMMH02
Filliger, M. MOPPH015
Flambard, J.L. MOPPH002
Frigot, R. MOPPH002
Fujita, T.F. TUOMMH01
Fukushima, K. TUOMMH01

— G —

Gachev, I.G. TUOBMH02
Galatà, A. MOPPH017, TUOMMH02, WEOBMH01
Gall, B.J.P. MOPPH002, MOPPH015
Gammino, S. TUOMMH02
Garmendia, N. MOPPH018
Gasajniev, Z.Sh. TUOBMH01
Ghosh, J. MOPPH005
Girardot, P. MOPPH003
Glyavin, M.Yu. TUOBMH02, THOMMH03
Gobin, R. **MOPPH003**
Golubev, S. MOOAMH02, MOOAMH04, THOMMH03
González, P.J. MOPPH018
Grandclement, C. MOOMMH02
Guan, M.Z. TUOMMH03
Guiho, P. MOPPH003
Guo, J.W. MOPPH010
Guo, S.Q. WEOMMH02
Guo, Z.Y. MOOBMH04

— H —

Haberer, Th. MOPPH004
Hajdu, P. THOMMH02
Hamm, R.W. MOPPH006
Harrault, F. MOPPH003
Hartung, U. TUOMMH04
Hegedus, Cs. THOMMH02
Hegedus, V. THOMMH02
Heikkinen, P. M.T. TUOMMH05

ISBN 978-3-95450-158-8

Higurashi, Y. **MOOBMH02**
Holland, K. MOOMMH03
Holoptsev, V.V. TUOBMH02
Hong, J.G. MOPPH011, WEOMMH01
Hu, Q. TUOMMH03

— I —

Izaola, Z. MOPPH018
Izotov, I. MOOMMH02, MOOBMH01, MOOAMH02, MOOAMH04, TUOMMH05, WEOBMH04, THOMMH03

— J —

Jacob, J. MOOMMH02
Jang, S.O. MOPPH012, **MOPPH013**, MOPPH014
Jardin, P. MOPPH002

— K —

Kalagin, I.V. MOPPH015
Kalvas, T. MOOBMH01, MOOAMH02, TUOMMH05, **WEOMMH04**
Kamigaito, O. MOPPH007
Kanjilal, D. MOOBMH03, MOPPH006
Kase, M. MOPPH007
Kasughai, A. MOPPH003
Kato, Y. TUOMMH01
Kim, E.-S. MOPPH011
Kim, S.J. MOPPH011, WEOMMH01
Kitagawa, A. **TUOMMH01**
Koivisto, H. A. MOOBMH01, MOOAMH02, **TUOMMH05**, WEOMMH04, WEOBMH01
Kokenyesi, S. THOMMH02
Komppula, J.P.O. MOOBMH01
Konev, N.N. WEOMMH03
Kopte, T. TUOMMH04
Kostyukhov, Yu.K. MOPPH016
Kotaka, Y. MOPPH007
Kreller, M. **TUOMMH04**
Kremers, H.R. **MOOAMH03**
Kronholm, R.J. MOOBMH01
Küchler, D. MOOAMH01, THOMMH01
Kuibeda, R.P. MOPPH017
Kulevoy, T. **MOPPH017**
Kumar, N. MOOBMH03
Kuzmenkov, K.I. MOPPH015

— L —

Lamy, T. **MOOMMH02**, MOPPH002, TUOBMH01, **WEOBMH01**
Lang, R. MOOAMH05
Laulainen, J.P. MOOBMH01
Lebedev, N. MOPPH015, MOPPH016
Lebedev, V.Ya. MOPPH015
Lee, B.S. **MOPPH011**, WEOMMH01
Leitner, D. MOOMMH03, MOPPH019
Lemagnen, F. **MOPPH002**
Li, X.X. MOPPH010
Litvak, A.G. THOMMH03
Loginov, V.N. MOPPH015
Loiseau, D. MOPPH003
Lombardi, A.M. MOOAMH01
Lu, W. TUOMMH03, **WEOMMH02**
Luchinin, G. THOMMH03

— M —

Ma, B.H. WEOMMH02
Ma, H.Y. MOPPH009, MOPPH010, WEOMMH02
Ma, L.Z. TUOMMH03
Machicoane, G. **MOOMMH03**, MOPPH019, TUOMMH05
Mäder, J. MOOAMH05
Maimone, F. MOOAMH05
Makwana, R.J. MOPPH005
Mal, K. MOOBMH03
Manchanda, R. MOPPH005
Mansfeld, D. MOOBMH01, **WEOBMH04**, THOMMH03
Mascali, D. TUOMMH02
Maslennikova, A.V. MOOAMH02
Mathur, Y. MOOBMH03
Maunoury, L. MOPPH002, WEOBMH01
Mei, E.M. TUOMMH03
Miracoli, R. **MOPPH018**
Mironov, V. **WEOBMH02**
Morris, D. MOOMMH03
Mostako, A.T.T. **MOPPH005**
Movshevich, B.Z. MOOMMH02, TUOBMH01
Muguira, L. MOPPH018
Muramatsu, M. TUOMMH01

— N —

Naas, B. MOPPH004
Nagatomo, T. **MOPPH007**
Nakagawa, T. MOOBMH02, MOPPH007
Neben, D.E. MOOMMH03, **MOPPH019**
Neri, L. TUOMMH02
Nešković, N. MOPPH016
Ni, D.S. TUOMMH03
Nikitin, A.A. MOPPH017

— O —

Ohnishi, J. MOOBMH02
Ohshiro, Y. MOPPH007
Ok, J.W. MOPPH011, WEOMMH01
Okumura, Y. MOPPH003
Osmond, O. MOPPH002
Ozeki, K. MOOBMH02

— P —

Pálinkás, J. THOMMH02
Park, J.Y. MOPPH011, WEOMMH01
Patti, G. WEOBMH01

ISBN 978-3-95450-158-8

Peaucelle, C. MOPPH002
Peng, S.X. MOOBMH04
Peters, A. MOPPH004
Piot, J. MOPPH002

— Q —

Qian, C. MOPPH010

— R —

Rácz, R. MOOAMH05, **THOMMH02**
Radics, T. THOMMH02
Ranttila, K. TUOMMH05, WEOMMH04
Rao, C.V.S. MOPPH005
Razin, S. MOOAMH02, MOOAMH04, THOMMH03
Ren, H.T. MOOBMH04
Ritter, E. MOPPH004
Rodrigues, G.O. **MOOBMH03**, **MOPPH006**
Röhrich, J. THOMMH01
Rogozhkin, S.V. MOPPH017
Roy, A. MOOBMH03
Ruan, L. WEOMMH02
Rueda, I. MOPPH018

— S —

Sala, P. MOOMMH02
Samsonov, S.V. TUOBMH02
Sasaki, N. TUOMMH01
Schlei, B.R. MOOAMH05
Schreiner, J. MOPPH004
Scrivens, R. MOOAMH01
Senée, F. MOPPH003
Shin, C.S. MOPPH011, WEOMMH01
Shmelyov, M.Y. TUOBMH01
Sidorov, V. MOOAMH02, **MOOAMH04**, **THOMMH03**
Silze, A. TUOMMH04
Skalyga, V. MOOMMH02, MOOBMH01, **MOOAMH02**, MOOAMH04, TUOMMH05, WEOBMH04, THOMMH03
Sole, P. MOOMMH02, MOPPH002
Soluyanova, E.A. TUOBMH02
Spädtke, P. MOOAMH05
Stafford-Haworth, J.T. MOOAMH01, **THOMMH01**
Standylo, L. WEOBMH01
Sun, L.T. MOOMMH01, MOPPH009, MOPPH010, **TUOMMH03**, WEOMMH02

— T —

Tai, E.M. TUOBMH02
Takahashi, K. TUOMMH01
Takasugi, W. TUOMMH01
Tarvainen, O.A. **MOOBMH01**, MOOAMH02, TUOMMH05, WEOMMH04, WEOBMH01, WEOBMH04
Thuillier, T. MOOMMH02, MOPPH002, TUOMMH05, WEOBMH01, **WEOBMH03**, **THOBMH01**
Tinschert, K. MOOAMH05
Tobos, L. MOOMMH03, MOPPH019
Toivanen, V. MOOBMH01, **MOOAMH01**, THOMMH01
Torrisi, G. TUOMMH02
Trajic, I.M. MOPPH016
Trophime, C. MOOMMH02
Tzoganis, V. MOPPH007

— V —

Vad, K. THOMMH02
Vaganov, R.E. MOPPH015
Vala, S.J. MOPPH005
Viktorov, M. WEOBMH04
Virani, N. MOPPH005
Vodopyanov, A. MOOAMH04, THOMMH03
Volovecky, A. MOOAMH02
Vujović, V. MOPPH016
Vukosavljevic, Lj. MOPPH016

— W —

Weichsel, T. TUOMMH04
Winkelmann, T.W. **MOPPH004**
Won, M. MOPPH011, **WEOMMH01**
Wu, B.M. TUOMMH03
Wu, Q. **MOPPH009**, MOPPH010
Wu, W. TUOMMH03

— X —

Xie, D. TUOMMH05
Xiong, B. WEOMMH02
Xu, Y. **MOOBMH04**

— Y —

Yang, T.J. TUOMMH03
Yang, Y. MOPPH009, TUOMMH03
Yoon, J.H. MOPPH011, WEOMMH01
You, H.J. MOPPH012, MOPPH013, **MOPPH014**

— Z —

Zhang, A.L. MOOBMH04
Zhang, H.J. MOPPH010
Zhang, J.F. MOOBMH04
Zhang, T. MOOBMH04
Zhang, W.H. **MOPPH010**, TUOMMH03
Zhang, X.Z. MOPPH009, MOPPH010, TUOMMH03, WEOMMH02
Zhang, Z.M. MOPPH009, MOPPH010
Zhao, B. TUOMMH03
Zhao, H.W. **MOOMMH01**, MOPPH009, MOPPH010, TUOMMH03, WEOMMH02
Zhao, J. MOOBMH04
Zheng, S.J. TUOMMH03
Zhu, L. TUOMMH03
Zschornack, G.H. TUOMMH04

ISBN 978-3-95450-158-8

Institutes List

AEC
Chiba, Japan
- Fukushima, K.
- Sasaki, N.
- Takahashi, K.
- Takasugi, W.

ATOMKI
Debrecen, Hungary
- Biri, S.
- Csik, A.
- Hajdu, P.
- Rcz, R.
- Vad, K.

CEA/DSM/IRFU
France
- Bogard, D.
- Chauvin, N.
- Girardot, P.
- Gobin, R.
- Guiho, P.
- Harrault, F.
- Loiseau, D.
- Senée, F.

CERN
Geneva, Switzerland
- Bellodi, G.
- Küchler, D.
- Lombardi, A.M.
- Scrivens, R.
- Stafford-Haworth, J.T.
- Toivanen, V.

CNAO Foundation
Milan, Italy
- Ciavola, G.

CNS
Saitama, Japan
- Ohshiro, Y.

Dreebit GmbH
Großröhrsdorf, Germany
- Kreller, M.

DREEBIT GmbH
Dresden, Germany
- Ritter, E.
- Silze, A.
- Zschornack, G.H.

ESS Bilbao
Bilbao, Spain
- Arredondo, I.
- Belver, D.
- Bustinduy, I.
- Corres, J.
- Echevarria, P.
- Eguiraun, M.
- Garmendia, N.
- González, P.J.
- Izaola, Z.
- Miracoli, R.
- Muguira, L.
- Rueda, I.

Fraunhofer FEP
Dresden, Germany
- Hartung, U.
- Kopte, T.
- Weichsel, T.

FRIB
East Lansing, Michigan, USA
- Holland, K.
- Leitner, D.
- Morris, D.

GANIL
Caen, France
- Barue, C.
- Canet, C.
- Delahaye, P.
- Flambard, J.L.
- Frigot, R.
- Jardin, P.
- Lemagnen, F.
- Maunoury, L.
- Osmond, O.
- Piot, J.

Graduate University, Chinese Academy of Sciences
Beijing, People's Republic of China
- Zhang, A.L.

GSI
Darmstadt, Germany
- Lang, R.
- Mäder, J.
- Maimone, F.
- Schlei, B.R.
- Spädtke, P.
- Tinschert, K.

ISBN 978-3-95450-158-8

GYCOM Ltd
Nizhny Novgorod, Russia
- Bakulin, M.I.
- Gasajniev, Z.Sh.
- Soluyanova, E.A.

HIL
Warsaw, Poland
- Choinski, J.
- Standylo, L.

HIT
Heidelberg, Germany
- Cee, R.
- Haberer, Th.
- Naas, B.
- Peters, A.
- Schreiner, J.
- Winkelmann, T.W.

HZB
Berlin, Germany
- Röhrich, J.

IAP/RAS
Nizhny Novgorod, Russia
- Bykov, Yu.V.
- Chirkov, A.V.
- Denisov, G.G.
- Eremeev, A.G.
- Gachev, I.G.
- Glyavin, M.Yu.
- Golubev, S.
- Holoptsev, V.V.
- Izotov, I.
- Litvak, A.G.
- Luchinin, G.
- Mansfeld, D.
- Movshevich, B.Z.
- Razin, S.
- Samsonov, S.V.
- Shmelyov, M.Y.
- Sidorov, V.
- Skalyga, V.
- Tai, E.M.
- Viktorov, M.
- Vodopyanov, A.

IAP
Frankfurt am Main, Germany
- Becker, R.

IEE
Beijing, People's Republic of China
- Ruan, L.
- Xiong, B.

IFMIF/EVEDA
Rokkasho, Japan
- Ayala, J.M.
- Okumura, Y.

IMP
Lanzhou, People's Republic of China
- Cao, Y.
- Feng, Y.C.
- Guan, M.Z.
- Guo, J.W.
- Guo, S.Q.
- Hu, Q.
- Li, X.X.
- Lu, W.
- Ma, B.H.
- Ma, H.Y.
- Ma, L.Z.
- Mei, E.M.
- Ni, D.S.
- Qian, C.
- Sun, L.T.
- Wu, B.M.
- Wu, Q.
- Wu, W.
- Yang, T.J.
- Yang, Y.
- Zhang, H.J.
- Zhang, W.H.
- Zhang, X.Z.
- Zhang, Z.M.
- Zhao, B.
- Zhao, H.W.
- Zheng, S.J.
- Zhu, L.

IN2P3 IPNL
Villeurbanne, France
- Peaucelle, C.

INFN/LNL
Legnaro (PD), Italy
- Comunian, M.
- Galatà, A.

INFN/LNS
Catania, Italy
- Castro, G.
- Celona, L.
- Gammino, S.
- Mascali, D.
- Neri, L.
- Patti, G.
- Torrisi, G.

Institute for Plasma Research
Bhat, Gandhinagar, India
- Basu, T.K.

ISBN 978-3-95450-158-8

- Ghosh, J.
- Makwana, R.J.
- Manchanda, R.
- Mostako, A.T.T.
- Rao, C.V.S.
- Vala, S.J.
- Virani, N.

IPHC
Strasbourg Cedex 2, France
- Asfari, Z.
- Faure, H.
- Filliger, M.
- Gall, B.J.P.

ITEP
Moscow, Russia
- Aleev, A.A.
- Andrianov, S.L.
- Chalykh, B.B.
- Kuibeda, R.P.
- Kulevoy, T.
- Nikitin, A.A.
- Rogozhkin, S.V.

ITT-Group
Moscow, Russia
- Konev, N.N.

IUAC
New Delhi, India
- Kanjilal, D.
- Kumar, N.
- Mal, K.
- Mathur, Y.
- Rodrigues, G.O.

Japan Atomic Energy Agency (JAEA), International Fusion Energy Research Center (IFERC)
Rokkasho, Kamikita, Aomori, Japan
- Kasughai, A.

JINR
Dubna, Moscow Region, Russia
- Bekhterev, V.
- Bogomolov, S.L.
- Bondarchenko, A.E.
- Efremov, A.A.
- Kalagin, I.V.
- Kostyukhov, Yu.K.
- Kuzmenkov, K.I.
- Lebedev, N.
- Lebedev, V.Ya.
- Loginov, V.N.
- Mironov, V.
- Vaganov, R.E.

JYFL
Jyväskylä, Finland
- Heikkinen, P. M.T.
- Kalvas, T.
- Koivisto, H. A.
- Komppula, J.P.O.
- Kronholm, R.J.
- Laulainen, J.P.
- Ranttila, K.
- Tarvainen, O.A.

KNU
Deagu, Republic of Korea
- Kim, E.-S.

Korea Basic Science Institute
Busan, Republic of Korea
- Choi, S.
- Hong, J.G.
- Kim, S.J.
- Lee, B.S.
- Ok, J.W.
- Park, J.Y.
- Shin, C.S.
- Won, M.
- Yoon, J.H.

KVI
Groningen, The Netherlands
- Beijers, J.P.M.
- Brandenburg, S.
- Kremers, H.R.

Kyungpook National University
Daegu, Republic of Korea
- Bahng, J.
- Bhang, J.B.

LBNL
Berkeley, California, USA
- Xie, D.

LNCMI
Grenoble Cedex, France
- Debray, F.
- Dumas, J.M.
- Grandclement, C.
- Sala, P.
- Trophime, C.

LPSC
Grenoble Cedex, France
- Angot, J.
- Jacob, J.
- Lamy, T.
- Sole, P.
- Thuillier, T.

ISBN 978-3-95450-158-8

National Institute of Radiological Sciences
Chiba, Japan
- Fujita, T.F.
- Muramatsu, M.

NFRI
Daejon, Republic of Korea
- Choo, W.I.
- Jang, S.O.
- You, H.J.

NIRS
Chiba-shi, Japan
- Kitagawa, A.

Nizhny Novgorod State Medical Academy
Nizhny Novgorod, Russia
- Maslennikova, A.V.
- Volovecky, A.

NSCL
East Lansing, Michigan, USA
- Cole, D.G.
- Leitner, D.
- Machicoane, G.
- Neben, D.E.
- Tobos, L.

Osaka University, Graduate School of Engineering
Osaka, Japan
- Kato, Y.

PKU
Beijing, People's Republic of China
- Chen, J.E.
- Chen, J.
- Guo, Z.Y.
- Peng, S.X.
- Ren, H.T.
- Xu, Y.
- Zhang, J.F.
- Zhang, T.
- Zhao, J.

R&M Technical Enterprises
Pleasanton, California, USA
- Hamm, R.W.

RIKEN Nishina Center
Wako, Japan
- Higurashi, Y.
- Kamigaito, O.
- Kase, M.
- Kotaka, Y.
- Nakagawa, T.
- Ohnishi, J.
- Ozeki, K.

RIKEN
Saitama, Japan
- Nagatomo, T.
- Tzoganis, V.

SHI Accelerator Service Ltd.
Tokyo, Japan
- Kotaka, Y.

The University of Liverpool
Liverpool, United Kingdom
- Tzoganis, V.

University Debrecen
Debrecen, Hungary
- Bakó, J.
- Csarnovics, I.
- Hegedus, Cs.
- Hegedus, V.
- Kokenyesi, S.
- Pálinkás, J.
- Radics, T.

University of Chinese Academy of Sciences
Beijing, People's Republic of China
- Yang, Y.

Universitá Mediterranea di Reggio Calabria
Reggio Calabria, Italy
- Torrisi, G.

VECC
Kolkata, India
- Roy, A.

VINCA
Belgrade, Serbia
- Ciric, D.
- Dobrosavljevic, A.S.
- Nešković, N.
- Trajic, I.M.
- Vujović, V.
- Vukosavljevic, Lj.

ISBN 978-3-95450-158-8

Participants List

Bakulin	Michael	RU	GYCOM Ltd
Basu	Tejen	IND	Institute for Plasma Research
Biri	Sandor	Hungary	Institute for Nuclear Research (Atomki), Hungarian Academy of Sciences
Bogomolov	Sergei	RU	Joint Institute for Nuclear Research
Bondarchenko	Andrey	RU	Joint Institute for Nuclear Research
Cao	Yun	PRC	Chinese Academy of Sciences
Celona	Luigi	Italy	Istituto Nazionale di Fisica Nucleare
Choo	Wonil	KOR	National Fusion Research Institute
Delferriere	Olivier	F	Commissariat à l'Energie Atomique (CEA/IRFU)
Denisov	Gregory	RU	Institute of Applied Physics, GYCOM Ltd
Efremov	Andrey	RU	Joint Institute for Nuclear Research
Gasajniev	Zakhar	RU	GYCOM Ltd
Gaubert	Gabriel	F	PANTECHNIK
Gobin	Raphael	F	Commissariat à l'Energie Atomique (CEA/DSM/IRFU) Direction des Sciences de la Matière Institut de recherche sur les lois fondamentales de l'Univers
Golubev	Sergey	RU	Institute of Applied Physics
Higurashi	Yoshihide	japan	RIKEN Nishina Center
Hong	In-Seok	KOR	Institute for Basic Science
Izotov	Ivan	Russia	IAP RAS
Jang	Soouk	KOR	National Fusion Research Institute
Janke	Swetlana	D	VACOM Vakuum Komponenten & Messtechnik GmbH
Jardin	Pascal	F	GANIL
Kalvas	Taneli	Finland	University of Jyvaskyla
Kitagawa	Atsushi	Japan	National Institute of Radiological Science
Kreller	Martin	Germany	Dreebit GmbH
Kremers	Herman	NL	Kernfysisch Versneller Instituut
Kuchler	Detlef	France	European Organization for Nuclear Research (CERN)
Kulevoy	Timur	RU	Institute of Theoretical and Experimental Physics
Kuzmenkov	Konstantin	RU	Joint Institute for Nuclear Research
Lamy	Thierry	F	Laboratoire de Physique Subatomique et de Cosmologie
Lee	Byoung Seob	KOR	Korea Basic Science Institute
Lemagnen	Frederic	F	GANIL
Lu	Wang	PRC	Chinese Academy of Sciences
Machicoane	Guillaume	USA	Michigan State University
Mansfeld	Dmitriy	RU	Institute of Applied Physics
Miracoli	Rosalba	Spain	ESS Bilbao
Mironov	Vladimir	RU	Joint Institute for Nuclear Research
Nagatomo	Takashi	Japan	Nishina Center for Accelerator-Based Science
Nakagawa	Takahide	Japan	RIKEN, Nishina center for accelerator based science
Neben	Derek	USA	Michigan State University
Peaucelle	Christophe	F	Institut de Physique Nucleaire de Lyon

ISBN 978-3-95450-158-8

Peng	Shixiang	PRC	Peking University
Racz	Richard	Hungary	Institute for Nuclear Research (Atomki), Hungarian Academy of Sciences
Razin	Sergey	RU	Institute of Applied Physics
Rodrigues	Gerard	IND	Inter University Accelerator Centre
Roehrich	Joerg	Germany	Helmholtz-Zentrum Berlin für Materialien und Energie
Sidorov	Alexander	RU	Institute of Applied Physics
Skalyga	Vadim	RU	Institute of Applied Physics
Stafford-Haworth	Joshua	CH	European Organization for Nuclear Research
Sun	Liangting	PRC	Chinese Academy of Sciences
Tarvainen	Olli	FIN	University of Jyvaskyla
Thuillier	Thomas	FRANCE	Laboratoire de Physique Subatomique et de Cosmologie
Toivanen	Ville	CH	European Organization for Nuclear Research (CERN)
Vala	Sudhirsinh	IND	Institute for Plasma Research
Viktorov	Michael	RU	Institute of Applied Physics
Winkelmann	Tim	Germany	Heidelberg Ionenstrahl-Therapie Centrum
Won	Mi-Sook	KOR	Korea Basic Science Institute
Xu	Yuan	PRC	Peking University
Zhao	Hongwei	PRC	Institute of Modern Physics,Chinese Academy of Sciences

ISBN 978-3-95450-158-8